Università degli Studi di Ferrara

DOCTORAL COURSE IN
ENVIRONMENTAL HEALTH SCIENCES

CYCLE XXXVIII

COORDINATOR Prof. Luisa Pasti

Study of biodegradable polyesters as materials for applications in the fishing industry

Scientific/Disciplinary Sector (SDS) CHEM/04/A

Candidate
Dott. Matteo Calosi

Supervisor
Prof. Monica Bertoldo

Co-Supervisor
Dr. Elena Buratti

Year 2022/2025

1. General introduction 6

1.1 The fishing industry and plastic pollution 6

1.2 Overview of bioplastics 7

1.3 Perspectives on bioplastics substitution of selected materials 20

1.4 Aim of the thesis 28

2. Preparation of high-solid poly(lactic acid) waterborne dispersions with PEG-PLA-PEG block copolymer as surfactant and their use as hydrophobic coating on paper 31

2.1 Introduction 31

2.2 Materials and methods 35

2.3 Results and discussion 40

2.4 Conclusions 63

2.5 Supporting information 64

3. Production of aquaculture socks from recycled poly(lactic acid) and study of their biodegradation properties 74

3.1 Introduction 74

3.2 Materials and methods 77

3.3 Results and discussion 80

3.3 Conclusions 90

4. Foaming of amorphous blends of poly(lactic acid) and poly(3-hydroxybutyrate-*co*-4-hydroxybutyrate) with supercritical CO_2 and study of the biodegradation properties of the foamed materials 92

4.1 Introduction 92

4.2 Materials and methods 94

4.3 Results and discussion 98

4.4 Conclusions 114

4.5 Supporting information 115

5. Foaming of blends of semicrystalline poly(lactic acid) and amorphous poly(3-hydroxybutyrate-co-4-hydroxybutyrate) with supercritical CO_2 and study of the biodegradation properties of the foamed materials 119

5.1 Introduction 119

5.2 Materials and methods 121

5.3 Results and discussion 123

5.4 Conclusions....138
5.5 Supporting information....140
6. Evaluation of cytocompatibility and osteoinductivity of peptide-functionalized poly(lactic acid)-based scaffolds obtained from waterborne dispersions using an in vitro model of Human Adipose-derived stem cells....143
6.1 Introduction....143
6.2 Matherials and methods....146
6.3 Results and discussion....154
6.4 Conclusions....163
7. Biodegradable poly(lactic acid)/graphene oxide platform obtained from waterborne dispersion for biomolecules sensing....165
7.1 Introduction....165
7.2 Materials and methods....167
7.3 Results and discussion....170
7.4 Conclusions....183
8. General conclusions....185
9. References....187

Abstract

Mass plastic production for short-term use has caused widespread pollution including in the oceans. Plastic pollution related to the fishing industry - nets, ropes, and expanded polystyrene (EPS) foam packaging - constitutes ~10% of marine litter and dominates marine macroplastics. Lost or discarded gear causes ghost fishing while EPS fragments into microplastics. Such materials are made almost entirely of fossil-derived non-biodegradable polymers with a heavy environmental impact. The use of bioplastics, plastics that are bio-based, biodegradable, or both, could reduce these impacts. Poly(lactic acid) (PLA) is the most produced bioplastic, widely used in packaging. It is strong but brittle and biodegrades slowly except in industrial composting. Blending with other biodegradable polymers can enhance biodegradation and performance. Polyhydroxyalkanoates (PHAs) are biopolyesters produced by bacteria as intracellular granules for energy storage which biodegrade rapidly in soil, compost, and marine environments, unlike PLA, making them valuable blend partners.

This thesis focuses primarily on the evaluation of biodegradable polyesters as replacement materials for fishing gear and packaging but also deals with spin-off applications of the technologies developed for this purpose in different application fields, namely biomedical and sensors. For fishing gear, the direct replacement of non-biodegradable polymers with biodegradable polymers was tested, while in the packaging sector, focusing on the replacement of EPS fish boxes, we explored both the option of using cardboard with a waterproof biodegradable coating and direct replacement of EPS foam with a biofoam.

To obtain sustainable waterproof biodegradable polymer coatings for paper packaging we prepared waterborne dispersions of PLA using a PEG-PLA-PEG triblock copolymer as the main surfactant. We achieved formulations with good stability over a 6-month period and high solids content (~40 wt%). The waterborne dispersions underwent analysis by dynamic light scattering (DLS), size exclusion chromatography (SEC), gravimetric tests, and rotational rheology with and without xanthan gum (0.2–0.8 wt%) as a thickener. Subsequently, the thickened dispersions were coated at 60 °C onto a paper substrate. SEM analyses revealed the formation of a polymer layer on the paper surface with thickness and morphology dependent on the processing conditions. Partial interpenetration between the coating and the paper fibers was observed, resulting in excellent adhesion between the layers. The coated paper exhibited good barriers to liquid and water vapor, with Cobb60<5 g/m^2 and water vapor transmission rate (WVTR)<100 g/(m^2 day) for coating weights ≤15 g/m^2, comparable to the performance of solvent-based PLA paper coatings. The surface energy of the coating was approximately 50 dyne/cm, higher than that of neat PLA, making it suitable for printing with common inks, without the need of any additional treatment.

Furthermore, the coated paper was able to be fully pulped in water, indicating that it can still be recycled in the paper stream.

In the field of fishing gear, the fabrication of aquaculture nets for mussel farming made from recycled PLA instead of the conventional polypropylene (PP) polymer was carried out. The potential thermal degradation of this secondary PLA in further processing was studied and a thorough analysis of the biodegradation of the nets in industrial compost, in seawater and in soil in simulated laboratory tests was carried out. PLA nets with similar mechanical properties to conventional nets were obtained and were found to be biodegradable within 3 months by industrial composting. Testing in a simulated marine environment found no loss of weight or visible degradation of net samples within 4 months. Biodegradation testing in soil found only a small loss in weight within a year. Thus, the nets were found to be potentially useful for the purpose of aquaculture but not biodegrade quickly in the environment.

For the objective of obtaining insulating foams for packaging purposes, we obtained blends of amorphous PHA with, respectively, amorphous and semicrystalline PLA. In both cases, the morphology of the blend was studied by TEM, DSC, Dynamic Mechanical Analyses (DMA) and rotational rheology. The blend components were found to be immiscible but well dispersed. The foaming was carried out by a batch process using supercritical CO_2 as the physical foaming agent. After process optimization, low density foams were obtained for all studied amorphous compositions, with PHA content up to 30%, and for semicrystalline blends up to 20% PHA. The recrystallization of PLA in the semicrystalline blends was found to be strongly accelerated by the dispersed PHA phase, which added challenges to the foaming process. The biodegradation capabilities in a home composting setting of the blend foams were analyzed and found to be superior to the ones of pure PLA foams, although in semicrystalline foams degradation was still very slow, with the degradation of the PHA phase being slowed down by being dispersed in the crystalline PLA phase.

The waterborne dispersions were further used in two spin-off studies: first to obtain composites with graphene oxide by direct film casting for applications as biodegradable electrochemical sensing platforms with possible employment in smart packaging. We successfully verified that these composites were industrially compostable. The composites were laser scribed to form conductive pathways in the insulating material and successfully tested for the electrochemical detection of model analytes such as adrenaline and ascorbic acid. Secondly peptides capable of osteogenic promotion were encapsulated into films prepare from the dispersions and used to promote the specialization of stem cells into osteoblasts when used as tissue culture surfaces. The efficacy of the functionalization was quantified by the expression of the RUNX2 gene as measured by PCR and osteocalcin as measured by ELISA test. The combined results of the tests allowed the identification of the

most promising peptide/film combination for the further objective of using the material as coating for titanium bone implants.

1. General introduction

1.1 The fishing industry and plastic pollution

The mass production of polymers from fossil sources in the past century, mostly for short-term applications, has led over time to a constant increase in the presence of the discarded synthetic plastic in the environment. Of all plastics ever produced and then discarded, it is estimated that only 10% has been recycled and 14% has been burned, leaving 76% of the total to constitute various forms of plastic pollution.[1] The dispersal into the sea to form marine litter is one of the main destinations of discarded plastic materials. While approximately 80% of marine plastic litter is estimated to come from land-based sources, mostly packaging, fishing gear used for fish capture is also an important source of marine pollution. The portion of gear that is damaged or has reached its end of life often ends up in the ocean through accidental loss or deliberate disposal. This abandoned, lost, or discarded fishing gear (ALDFG) is considered the largest sea-based source of marine plastic pollution. A wider definition of fishing gear is also useful in understanding how to mitigate this problem, by including within the term ancillary items such as the packaging used for the transport of the caught seafood.[2]

Plastics are currently the main materials used for fishing gear and as result this accounts for 10% of marine plastic litter and a higher proportion of macroplastics (> 50 cm size) found floating. As an example of a major marine macroplastic pollution area, studies of the Great Pacific Garbage Patch have identified materials connected with the fishing industry to be its main component at around 80% of mass, with just under half being made up of nets and ropes and the remainder of other fishing-connected items, with fish boxes being a major component.[3,4] Fishers use a combination of nets, ropes, lines and poles to catch marine organisms. The aquaculture industry also uses a similar combination of materials to artificially farm seafood. Nets are generally made from woven polymer fibers, mostly made from polyamide (PA or nylon), polyethylene (PE) and polypropylene (PP). Ropes and lines are typically made from PA, PP or poly(ethylene terephthalate) (PET).[2]

In general, food packaging is critical in ensuring food safety from contamination, preserving quality and facilitating distribution, thus reducing food waste. Fish and seafood face particular challenges in maintaining quality throughout the supply chain and have a rather large 36% rate of food waste in Europe.[5] The predominant packaging material for transporting and storing fish, from fishing vessels to the final sale, is expanded polystyrene

(EPS). EPS ranks among the most common elements of marine plastic pollution, both floating at sea and on coastlines due to accidental losses from fishing vessels, and mismanagement of waste in coastal areas. It is an attractive material because of its combination of low density, good mechanical properties and thermal insulation that make it possible to effectively store 10 kg of fish in only 0.34 kg of EPS.[6]

Fishing industry waste has major impacts on marine organisms and ecosystems. The accumulation of macroplastic ALDFG leads to entanglement which may result in starvation or injury of the caught organisms, a phenomenon known as “ghost fishing”. Nets, lines and ropes are the materials primarily involved in ghost fishing. Accidental consumption of plastic litter can also lead to blockage of the digestive tract.[7]

Moreover, microplastic particles, which are < 5 mm in size and are typically created by mechanical degradation, can persist within organisms and enter the food chain. These particles can be harmful both because of their particulate nature and because they can absorb and carry contaminants, such as heavy metals and hydrophobic chemicals. The biggest sources of microplastics, both in the ocean and on land, are synthetic clothing which sheds microfibers through use and washing and the abrasion of car tires. Many marine organisms exhibit limited growth, inflammation and reduced cognitive function upon exposure to higher levels of microplastic particles.[8] EPS can be an important contributor to microplastic pollution in coastal areas with important fishing activity due to its relatively easy breakdown into small fragments.[9]

The substitution of these materials employed by the fishing industries with more sustainable bio-based or biodegradable alternatives offers a possible solution to the listed problems.

1.2 Overview of bioplastics

Plastic is a term which still does not have a single agreed-upon definition. In the widest meaning, plastics are any polymer-based materials, composed of one or more organic polymers plus any additives and fillers. The capability of the material of being shaped by flow, and thus be a thermoplastic, at some point of its processing is also generally accepted as a necessity.[10] Bioplastic is also a term that is quite debated and is tied to the presence in a plastic material of either bio-based polymers, meaning that they are produced from renewable natural resources rather than fossil sources, or biodegradable polymers, which are able in certain conditions of being used as food source by microbes and reduce their molecular weight through this process. A distinct definition is the one of biopolymer, which is any macromolecule that is produced by living organisms.

Two main definitions of bioplastic may then be found: In the industry definition “a plastic material is defined as a bioplastic if it is either biobased, biodegradable, or features both properties”[11]. This definition is illustrated in figure 1.1. However, by the IUPAC definition, a bioplastic is a “Biobased polymer derived from the biomass or issued from monomers derived from the biomass and which, at some stage in its processing into finished products, can be shaped by flow.”[10] Thus, by the IUPAC definition the lower right corner of figure 1.1 is not considered to be part of bioplastics. IUPAC also generally discourages the use of term as misleading into a positive perception of the material and argues in favor of only using bio-based polymer. In addition to these contrasting definitions it is also quite common to find that “old economy” bioplastics, those biopolymer-based materials preexisting the widespread adoption of petrochemical-based polymers, such as cellulose acetate, natural rubber, regenerated cellulose etc. are excluded from bioplastic production statistics altogether despite meeting criteria.[12] The “de-facto” currently used definition of bioplastics is thus a type of plastic that:

- Has started being commercialized in the modern age of plastics (since the 1950s)
- Is bio-based and/or biodegradable.

As found in the definitions, not all bio-based polymers are biodegradable, and not all biodegradable polymers are bio-based. Non-biodegradable bio-based polymers include modified natural polymers such as cellulose acetate, as well as polymers such as bio-PE or bio-PET that are identical to their fossil-based versions but are built from bio-based monomers such bio-ethylene. Biodegradability can be a characteristic of both bio-based and non-bio-based plastics. For example, polycaprolactone (PCL) and poly(vinyl acetate) (PVAc) are non-bio-based and biodegradable while poly(lactic acid) (PLA) and polyhydroxyalkanoate (PHA) are bio-based and biodegradable. The bio-based nature of a given polymer is actually often dependent on the technical and economic viability of competing fossil-based and bio-based production processes; for example succinic acid and 1,4 butanediol, the building blocks of poly(butylene succinate) (PBS), have been historically mostly produced by fossil-based routes, but the growth of bio-based production makes it so PBS is increasingly considered a bio-based polymer.

The definition of biodegradable polymer is also something that needs to be clarified. Any polymer that is capable of being used as a food source by naturally occurring microorganisms and lose molecular weight through this action meets the general definition.[10] However, this does not specify either the time-scale, the degree or the kind of environmental conditions where this degradation may happen. From a regulatory and commercial perspective, a certification process was created in the 1990s, as new biodegradable polymers started being commercialized, to define which polymers may be classified as biodegradable. No general definition was adopted. Instead test methods were

specified to quantitatively test biodegradation in a given test environment of which common examples include ISO-14855 (Industrial composting) or ASTM D-6691 (seawater). These norms lay out the conditions and methods where the testing is to take place and can be used to measure either the disintegration (breakdown into particles below a certain size) and/or ultimate biodegradation, as measured by CO_2 (aerobic) or CH_4 (anaerobic) emissions of tested polymers. These testing standards do not necessarily include biodegradability definitions, which are often left to other industry norms. For example, the heavily used EN 13242 standard for compostable packaging specifies that a material can be defined as compostable if it has a mass loss of at least 90% within 3 months as measured by the ISO-14045 method and an ultimate biodegradation of at least 90% within 6 months as measured by ISO-14855. Other standards, for other kinds of material or for different environments (seawater, soil, home composting) follow a similar route of defining a biodegradation threshold, a maximum time where this needs to be met and a test method to follow.[13]

Another possible classification of bioplastics is the one from a process perspective, as bio-based polymers can be produced by three routes. First, the chemical modification of biopolymers (e.g. thermoplastic starch); second, the production of monomers or their building blocks by biomass conversion followed by one or more further chemical synthesis steps to obtain the polymerized product (e.g. PLA, PBS); third, the direct production of polymers from biomass that are used as-is after purification and processing (e.g. PHA).

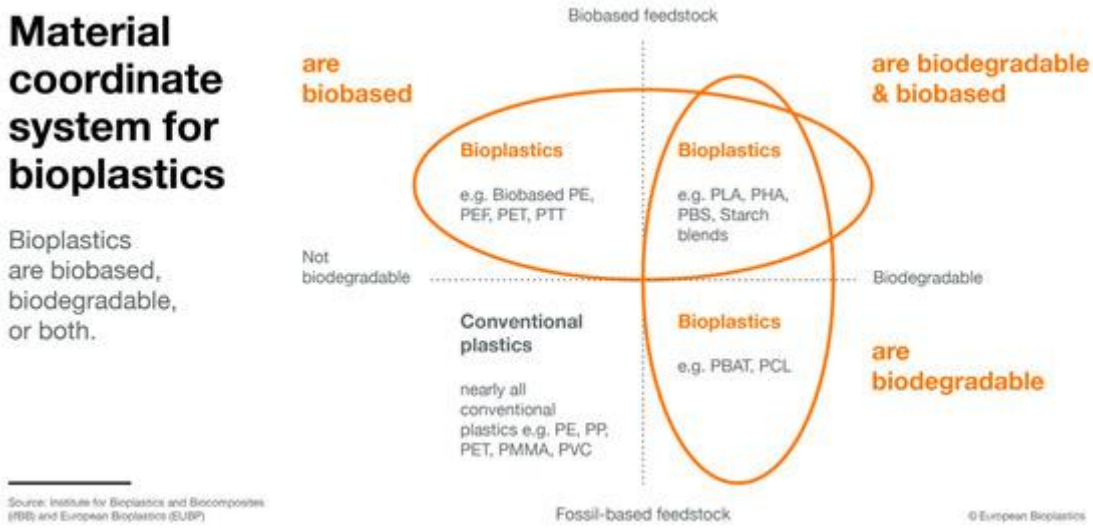

Figure 1.1 Classification of bioplastics according to Bioplastics Europe[11]

Bioplastics represent a small but constantly increasing fraction of plastics, amounting to 2.5 million tons in 2024, 0.5% of global plastics production, which is expected to double in the next 5 years. PLA is the most widely produced bioplastic as of 2024, making up 37% of bioplastics production and 66% of biodegradable bioplastics production and is especially

predominant in the packaging sector. PHAs represent a much smaller fraction of this production (4% of bioplastics as of 2024) but are the fastest growing biodegradable plastic. While PLA production is expected to double by 2029, PHA production is projected to increase tenfold and these two polymers together are currently projected to make up the great majority of bio-based biodegradable plastics production (Figure 1.2).[14]

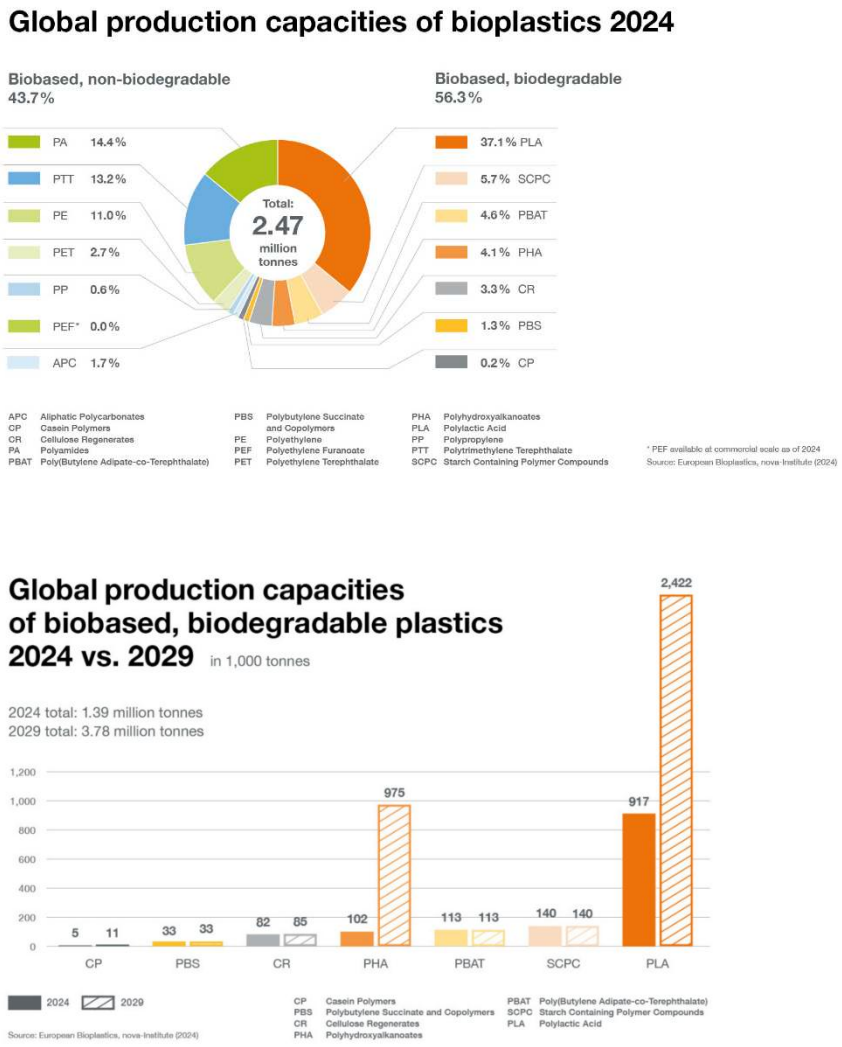

Figure 1.2 Production capacities and near future production outlook of bioplastics according to Bioplastics Europe[14]

1.2.1 PLA

The starting point of PLA production is lactic acid, its basic monomeric unit, a naturally occurring hydroxy acid characteristic of fermentation processes (dairy being the most prominent) that is also bulk produced as a food additive. Lactic acid has been produced on an industrial scale by fermentation processes since the 1880s. Synthetic routes by the lactonitrile route from petrochemical precursors were competitive with this process in the

mid- to late 20th century, but currently lactic acid is obtained almost exclusively (over 90%) by industrial fermentation biotechnological processes rather than chemical synthesis.[15]

PLA is a thermoplastic polymer with glass transition above room temperature and has a rigidity and transparency similar to polystyrene (PS) or poly(ethylene terephthalate) (PET). PLA started being produced on a limited scale by polycondensation in the 1970s and the 1980s for medical applications. After the lactide route was optimized in the 1990s, it started being employed in general polymer applications, the first leading producers being Natureworks (which started as a joint venture of Cargill and Dow and is today owned by Cargill and Thai state-owned PTT) and global production has been growing constantly. The well-optimized nature of both monomer production and the polymerization route mean that PLA currently has a cost advantage over other biodegradable polyesters that have started being produced on an industrial scale and commercialized much later. Its main current uses are in packaging (both rigid and flexible), single use food items (cups, cutlery, bottles), extrusion coating, injection molded products and 3-D printed products, as well as more specialized applications in the medical field (sutures, drug delivery etc.). While PLA can be produced directly by condensation polymerization of lactic acid, the most common industrial routes utilize the more efficient route of the polymerization of lactide - the cyclic dimer of lactic acid- via ring opening polymerization (ROP), most commonly catalyzed by a tin-based catalyst. The starting point is in any case lactic acid, produced by industrial bacterial fermentation, that must first be carefully purified because crude lactic acid contains many impurities such as acids, alcohols, esters, and traces of nutrients. The lactide is then obtained from the bulk condensation of lactic acid into short PLA chains under vacuum at high temperature followed by catalytic depolymerization under reduced pressure. Purified lactide is then used for the ROP reaction, which is also conducted in bulk at temperatures above the melting point of the lactides (100-130°C) and below temperatures that cause thermal degradation of PLA (around 200°C).[15,16]

The crystallization properties, processing ability and degradation behavior of PLA depend primarily on the structure and composition of the polymer chains, particularly the ratio of the L- to the D-isomer of the lactate repeating unit. The stereochemical structure of PLA (figure 1.3) depends on the mixture of L- or D-lactide as well as meso- or rac-lactide used in the feed and results in an amorphous or semicrystalline polymer with a melting point in the range from 130 to 185°C and a glass transition temperature from 45 to 70 °C. As L-lactic acid is the principal naturally occurring isomer, lactic acid is produced mainly in the L- form or as a racemic mixture, with D-lactic acid being rare and costly. Thus, the isotactic PLA homopolymer that is industrially produced is effectively PLLA – made up from pure L-lactide only – instead of PDLA. Isotactic PLA is a semicrystalline material with the highest degree of crystallinity and melting point out of the PLA homopolymers. PLA copolymers with higher

D-isomer content are obtained by the addition of rac-lactide in the monomer feed and exhibit lower melting points and slower crystallization behavior as D- content increases, becoming amorphous due to crystallization being slow enough that crystallinity is negligible in most recrystallization conditions at D- contents higher than 10%. Blending or block copolymerization of PLLA and PDLA results in the formation of a stereocomplex between isotactic polymer chains with opposite configurations, with a crystalline structure different from that of each homopolymer and with a very high melting point around 230 °C.[15,17]

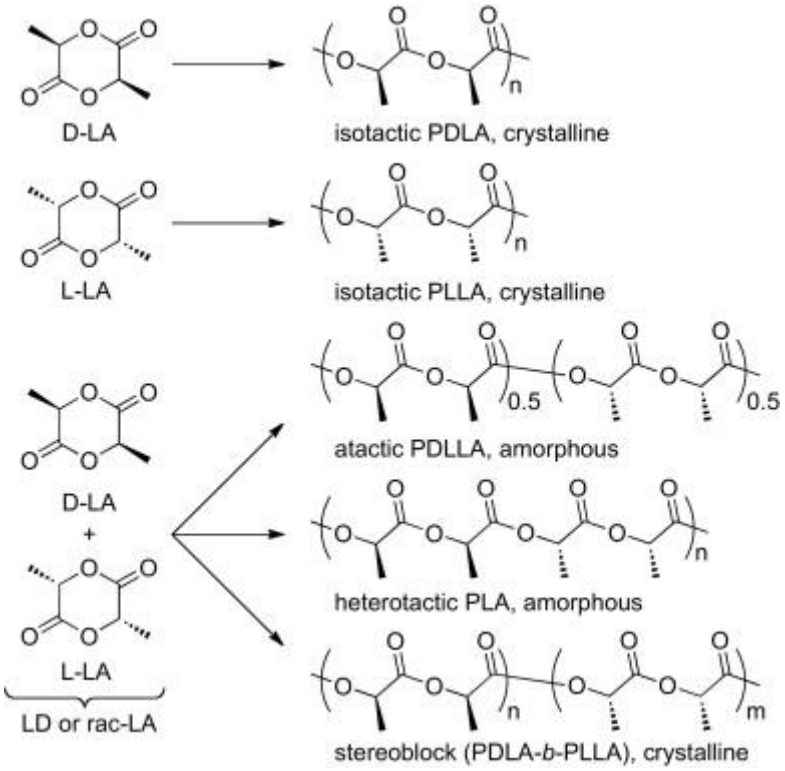

Figure 1.3 Possible enantiomeric structures of lactide and their influence on the nature of PLA.

Mechanically, PLA is a brittle polymer with a high modulus (3-4 GPa), a high tensile strength (50-70 MPa), low elongation at break (2-10 %) and low toughness. The brittleness is caused by glass transition being 30-40 °C above room temperature and may be countered by the addition of plasticizers or blending with less brittle polymers. PLA's crystallization kinetics are fairly slow, and proper crystallization is necessary for applications at temperatures above 40-50 °C. The objects obtained from high-temperature processing such as injection molding are mostly amorphous unless also subjected to an annealing process or made into a composite with components which enhance crystallization properties.[18] PLA is generally considered only a moderately effective barrier polymer and its permeability towards low-molecular weight gases and vapors is higher than several conventional polymers used for packaging. For example the water permeability of PLA is higher than the one of PE, PP, PS

and PET while the oxygen permeability is lower than the one of PE, PP and PS but higher than PET or Nylon 6,6. These properties can be improved by the use of fillers and nanofillers, most prominently clay, as well as the use of stereocomplex PLA or blending with polymers with better barrier properties.[19]

As laid out above, blending with other polymers is often key to improving certain properties of PLA for a given use. The research on this subject has mostly concentrated on the improvement of mechanical, barrier and biodegradation properties. Simple blends of PLA and other polymers are commonly thermodynamically disfavored and result in an immiscible blend. These multiphase structures present in the blend can be identified from studying the morphology, rheology, and glass transition. Miscible polymers are characterized by a single amorphous phase and a single thermal transition while immiscibility creates several phases, which generates more complex rheological properties and independent glass transitions. Often, immiscible polymer blends have low interfacial adhesion leading to poor mechanical performance. The phase structure of immiscible blends can be observed by microscopy (SEM, TEM, AFM) and is determined by the respective ratios of the blend partners (Figure 1.4). In a two-polymer blend, when one of the two polymers constitutes only a small fraction of the blend, the common morphology is the droplet microstructure, when with the cooling of the melt the minor blend partner loses miscibility and coalesces in dispersed droplets within a matrix of the major blend partner. This is the morphology commonly found when one polymer is used as a modifier of mechanical properties of another and is commonly regarded as effective at improving elastic performance when the droplets are below 1 μm in size. Smaller particle sizes and narrower size distributions are indicative of better surface interaction and low surface tension.[20,21]

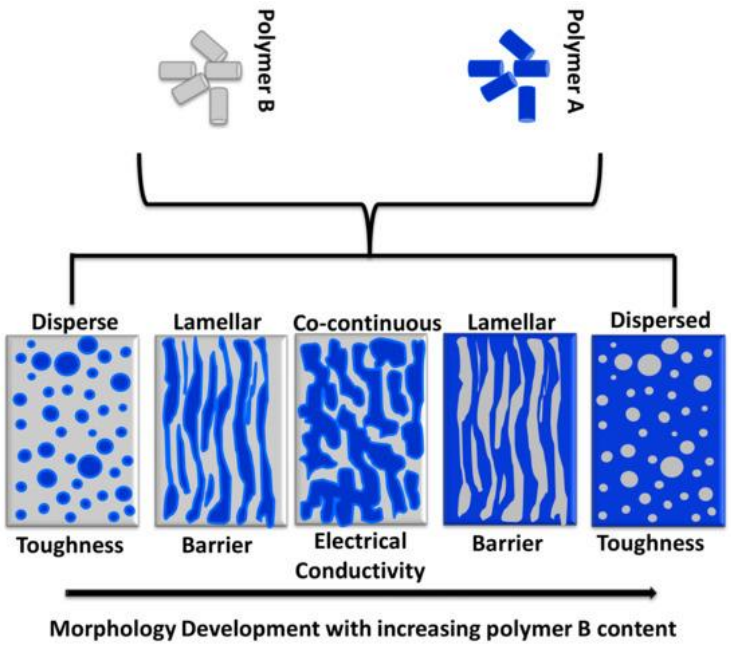

Figure 1.4 General scheme of common immiscible polymer blend morphologies depending on blend ratios. Adapted from ref[22]

The use of non-biodegradable polyolefins such as PE and PP as blend partners for PLA is promising because of their low cost and the potential mechanical and barrier improvements. However, such blends are characterized by poor dispersion due to the differences in surface energy between the phases and a loss of biodegradability of the blend. Among other non-biodegradable polymers, poly(methyl methacrylate) (PMMA) has shown miscibility with PLA in low PMMA ratios and in certain processing conditions and such blends are of particular interest in the biomedical field due to the high biocompatibility of both polymers. Other biodegradable polymers are also often used as blend partners for PLA, which is ideal to maintain or sometimes even enhance biodegradability of the blends compared to pure PLA. Biodegradable PVAc and its hydrolysis product Poly(vinyl alcohol) (PVA) have shown miscibility with PLA at low weight ratios when pure or only slightly hydrolyzed PVAc is used and are effective at improving PLA's mechanical properties.[23] PVA with a higher degree of hydrolysis (around 90%) which is water-soluble has also been obtained in a blend with PLA by using water-based techniques of mixing with PLA dispersions, avoiding both high-temperature processing and use of organic solvents.[24] Other biodegradable polyesters are, despite structural similarities, invariably immiscible with PLA but do generally have a degree of compatibility which limits the loss of phase adhesion, especially since high-temperature processing during blend processing encourages transesterification between different polymer chains. PCL is a very common blend partner as it is a soft and flexible polymer with low glass transition (-60°C) and melting point (55-70 °C) and thus blending allows both polymers to overcome their limitations.[25] Blends with PHAs are also popular as these

polyesters also have a low T_g combined with desirable environmental biodegradability and will be described in detail later.

When exposed to environmental conditions PLA may undergo degradation through a number of pathways. These mainly include hydrolytic, photo-oxidative, enzymatic and microbial degradation.[26]

Photodegradation of PLA is caused by the absorption of UV radiation by the carbonyl functionality of the ester group which causes Norrish-type radical reactions that result in chain cleavage and the formation of double bonds, as well as anhydride groups.[27]

Hydrolysis cleaves the ester links of the backbone chain of PLA and leads to a loss of molecular weight, as well as the release of water-soluble monomers and oligomers. Both alkaline and acid pH of water will increase the rate of the reaction, which may thus be autocatalyzed by the formation of acid groups that follow hydrolysis. Under acidic conditions, chain-end unzipping is the prevalent mode of hydrolysis while under basic conditions random ester cleavage prevails. Hydrolysis results in the erosion of PLA materials which, depending on the diffusion rate of water within the PLA particle, may be surface, or heterogeneous erosion or bulk, or homogeneous erosion.[28]

Enzymatic degradation acts by inducing the hydrolysis of the ester bond through enzyme catalysis: various depolymerases that are part of the α/β hydrolase family, mainly cutinases, esterases, lipases and proteases have been identified as active for this reaction. Active enzymes must be capable of accepting a large hydrophobic substrate and facilitate the cleavage of the ester link. The various enzymes differ in stereoselectivity, with different activities towards PLLA and PDLA polymers as some enzymes, such as proteases, will only accept the L enantiomer of the repeating unit and have reduced activity as D-content increases, while other enzymes make no such distinction. Enzymatic degradation mostly acts through a random scission mechanism that may occur throughout the polymer chain rather than attacking the chain ends.[29,30]

Microbial degradation begins first by exploiting enzymatic degradation by secreting extracellular depolymerases that break down PLA chains into soluble products that may then be transported within the cells where they are metabolized into carbon dioxide, water or methane. Most of the microorganisms capable of degrading PLA are actinomycetes, a phylum of gram-positive bacteria mostly found in the soil, while only a small fraction are fungal or belonging to other bacterial phyla.[31]

All the listed types of degradation take place preferentially in the amorphous region of PLA; as a result polymer crystallinity is usually observed to increase as degradation takes place.[32]

The temperature and kind of environment where PLA is located both play key roles in determining its biodegradation rate. PLA-degrading organisms are frequently found in soil and compost but are absent from freshwater and seawater environments. Thus, PLA immersed in aqueous environments degrades by simple chemical hydrolysis of the ester bonds without enzymatic catalysis. In most studies, ambient temperature testing has found little change in PLA's average molecular weight or the properties of PLA objects even after 1-2 years of immersion. Temperature is the most important factor in determining PLA hydrolysis rate, as accelerated aging can be obtained by raising the temperature to 40°C or above, which results in heavy molecular weight decrease in a matter of months, due to a combination of simple reaction rate increase combined with the increased mobility of the PLA chains as glass transition is approached. However, no precise estimate of the average hydrolysis rate of PLA in natural aqueous environments is yet available.[33,34]

The presence of PLA-biodegrading microorganisms also does not necessarily mean that the biodegradation is fast. The ideal conditions for PLA degradation are those found in an aerobic high-temperature (50-70 °C) industrial composting plant. In this case, it is well-verified that the complete biodegradation of PLA down to CO_2 is achieved in 1-3 months.[35] However, the reduction of temperature causes a severe slowdown in the biodegradation process, despite the presence of biodegrading microorganisms, due to the lack of availability for hydrolysis of the rigid polymer below glass transition. Aerobic biodegradation testing of PLA in compost or soil at temperatures below 50°C has shown little biodegradation for at least a year, although the loss of molecular weight and mechanical properties is faster in these conditions than the one observed in natural aqueous environments.[36–38] Under typical anaerobic landfill conditions it has been estimated that the full biodegradation of semicrystalline PLA would take more than 100 years.[39]

The risk of PLA breaking down into persistent microplastics (MPs) in the environment is also a potential concern due to its slow degradation. Both the degree to which this kind of breakdown may happen, and the potential harmful effects of such MPs are currently highly uncertain, as due to the relative novelty of the material PLA MPs are very rare in real environments. Preliminary research in the matter has found that PLA MPs may serve as transport for a significant number of pollutants and are potentially harmful to invertebrate organisms but cause no clear damage to plants or to soil quality.[40] Since PLA is capable of being quickly hydrolyzed and metabolized in warm-blooded animals and humans, and has been approved for medical uses such as a suture and implant material, the risk posed by PLA MPs within the human body is likely limited.[41]

The acceleration of PLA biodegradation properties has been the object of intense research. The addition of specific biostimulants has been shown to enhance PLA degradation in soil or wastewater.[42,43] However, this approach does not solve the issue of PLA dispersed in the

environment. Engineered enzymes can be encapsulated in the PLA itself and this can significantly accelerate PLA biodegradation at home composting temperatures (30-45 °C).[44] The most common technique however is the blending of PLA and more readily biodegradable polymers or the mixing with easily biodegradable fillers to make composites. The degradation of the more readily biodegradable phase has been shown to not only accelerate the biodegradation of the overall plastic but possibly accelerate the degradation of the PLA phase itself. This is explainable by a number of mechanisms, mainly by the increase of the exposed surface area due to the formation of microvoids as the more degradable phase is destroyed, as well as the easier formation of biofilms on these surfaces and, if the non-PLA phase is more hydrophilic, by increasing water permeation within the material and thus hydrolysis. Starch, cellulose and PHAs are the most common materials blended with PLA for this purpose.[45,46]

Despite PLA being a bio-based polymer, its mechanical recycling conducted in a way that is analogous to fossil-based polymers is also a potentially attractive end of life option, as it is durable enough to still be useful after multiple melt processing steps. This is for now not an option followed by plastic recycling plants, mostly due to the scarcity of PLA in the plastic waste stream but it is studied as an option for the future when PLA may be more prevalent. A careful drying of the collected PLA waste and separation from other polymers is crucial to obtain usable secondary PLA.[47]

1.2.2 PHA

PHAs are polyesters with the general structure illustrated in scheme 1.1. Although they can also be obtained from chemical synthesis, the unifying characteristic of PHAs is being a class of biopolymers produced by bacteria as intracellular granules. Chemical production, on the other hand, is commonly conducted by the ring opening polymerization of the corresponding cyclic lactone or by the copolymerization of epoxides and carbon monoxide. The microbial production is carried out by prokaryotic organisms, bacteria and archaea, which obtain the polymer mostly from 3-hydroxyacid (x=1) monomers through polymerization catalyzed by PHA synthase enzymes. PHAs are produced in the form of intracellular granules which are used for energy storage by the organisms. A feast-famine regime where the producing biomass is alternatively fed abundant nutrients and starved is used to induce this formation. Around 150 monomers can be used by the biosynthetic route, differentiated by the alkyl sidechain, and may be obtained both as homopolymers or as copolymers of two or more monomers. Biosynthetic PHAs are highly isotactic, containing exclusively the (R) configured stereoisomers, while chemically synthesized polymers can be obtained with different degrees of tacticity. Since microbially produced PHAs are stored

inside cells, they must be extracted and purified. This is one of the major obstacles to the commercialization of PHAs because this requires organic solvents (commonly halogenated ones) that are toxic and must be disposed of properly and also requires a high energy input. From 30 % to more than 50 % of PHA production costs are attributable to the purification steps rather than to feedstock and production process. More sustainable methods, based on cell digestion rather than solvent extraction are being developed.[48–51]

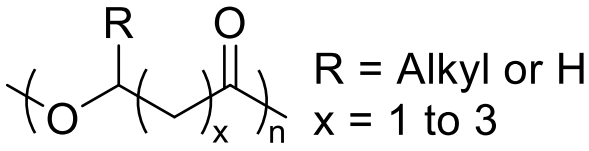

Scheme 1.1 General structure of PHAs.

PHA homopolymers are categorized on the basis of the number of carbon atoms constituting their monomeric units. Short-chain-length PHAs (scl-PHAs) have at most five carbon atoms, medium-chain-length PHAs (mcl-PHAs) have between six and fourteen and long-chain-length PHAs (lcl-PHAs) have more than fourteen carbon atoms. Scl-PHAs have a melting point in the 130-180°C range while mcl-PHAs have much lower melting points of 40-60°C. Glass transition temperatures are below room temperature and may be found in a wide range between -50 and 10 °C depending on PHA composition.[52]

The first PHA to be industrialized, and still the most produced is poly(3-hydroxybutyrate) (PHB). This homopolymer is characterized by a high crystallinity degree, which leads to high brittleness and low elongation at break. Another drawback is the lack of thermal stability. The onset of complete degradation to volatile compounds is at 220-240°C while the melting temperature of PHB is 170-180°C, and at the latter temperature the polymer already experiences a significant loss in molecular weight during processing.[53] One of the main techniques used to improve PHB properties is by inducing the biosynthesis of copolymers of PHB with other monomers, the most common being 3-hydroxyvalerate (PHBV copolymer), 3-hydroxyhexanoate (PHBH) and 4-hydroxybutyrate (P3HB4HB). The addition of these comonomers causes a lowering of crystallinity and melting temperature which results in a more easily processable and more flexible material.[54]

PHAs containing 4HB as a comonomer were first discovered in the late 1980s and later on were developed so as to tune the 4HB content as well as being able to obtain the P4HB homopolymer. The properties of P34HB range from a hard semi-crystalline plastic to an elastic amorphous rubber, depending on the content of 4HB. With the increase of 4HB content, the Young modulus, glass transition temperature, and melting point of the copolymer decrease, and the elongation at break and thermal decomposition temperature

increase.[55] The amorphous polymer (with 4HB content around 30-40% is of particular interest as a modifier for other polymers.[56]

PHA biodegradation takes place thanks to a wide array of bacteria and fungi and is mediated by extracellular enzymatic attack by lipases and hydrolases. Soluble oligomers and monomers are then transported inside the cell and metabolized. PHA degradation rates depend on both crystallinity and copolymer ratios: a greater amount of amorphous region results in faster biodegradation, while on the other hand comonomers with longer side chains are known to have lower enzyme affinity than 3HB which has the highest.[57] PHAs are degraded by a much wider array of bacteria compared to other biodegradable polyesters like PLA. PHA-degrading bacteria have been identified not only in soil and compost but also in freshwater, hot springs and marine environments.[58] PHAs are as a result the only class of bio-based polyesters displaying thorough biodegradability in marine environments. Full mass loss or mineralization in seawater is generally observed in a time scale varying from 3 months to a year depending on testing conditions and polymer nature.[57] In comparison with PLA, PHAs generally have a much faster biodegradation speed in every environment except in industrial composting, as a combination of better availability of biodegrading bacteria and greater chain mobility due to the 50-100 °C difference in T_g.

Due to PHA's environmental biodegradation capabilities, their use as blend partners with other biodegradable polymers lacking these capabilities have been studied to enhance the capability of the overall blend to biodegrade while having a lower cost and different mechanical properties than pure PHA. PLA and PHA generally form immiscible blends but ones which have a good degree of compatibility, which can be further enhanced by the addition of compatibilizers.[59]

The biodegradation properties of such blends with PLA specifically have been investigated in different environmental contexts. In particular, blends of PLA and 30% PHBV were measured to have a similar rate of biodegradation in soil to pure PHBV,[60] blends of PLA and PHBHH have marine biodegradation capabilities that increase with PHBHH content[61] and the rate of disintegration in soil of blends of PLA and P34HB (10% 4HB) was tested finding that blends with 50% or greater PHA content were able to completely disintegrate within 5 months.[62] Han and colleagues measured the home composting properties of PLLA and P34HB (30% 4HB) blends at 30 °C and found that after 45 days the addition of 30% P34HB resulted in 72% biodegradation and the addition of 50% aPHA resulted in 83% biodegradation, and these materials could thus be considered home compostable. However, the recrystallization by annealing of the PLA in the blends led significantly slower overall biodegradation.[63] Thus, the blending of the polymers and the crystalline status of the PLA both play an important role in determining the final biodegradability. On the other hand, compostability testing of PLA/PHA blends at 58 °C has shown that under these conditions

PLA and PHA have similar biodegradation properties, as the blends degrade at the same speed, or even slower, than pure PLA.[57]

1.3 Perspectives on bioplastics substitution of selected materials

1.3.1 Nets

Many commercially available biodegradable plastics are viable for the manufacture of fishing and aquaculture nets, the main ones being PBS, poly(butylene adipate-*co*-terephthalate) (PBAT), PLA, and PHAs. Tensile strength is the main mechanical property that must be considered for netting materials as the fibers must withstand high tensile loads. The tensile strengths of the listed polymer fibers are ranked: PBS > PLA > PBAT > PHA.[64]

The most studied biodegradable materials for fishing nets try to combine the mechanical resistance of PBS with the greater flexibility and marine biodegradability of PBAT. This is most often done by using the copolymer poly(butylene succinate-*co*-adipate-*co*-terephthalate) (PBSAT). Field testing of gillnets made from this copolymer has usually shown a moderate decrease in catch efficiency compared to polyamide (PA) gillnets.[65–69] Blends or composites of PBS and PBAT are also used for similar purposes: a blend of 82% PBS and 18% PBAT has shown similar performance to conventional driftnets while starting to biodegrade after 24 months in seawater[70]. The use of PBAT fibers coated with PBS, which combines the tensile strength of PBS with an increased biodegradability and flexibility has also been reported for aquaculture.[71]

PLA has seen comparatively less research as a potential material for use in fishing nets, with only two papers tackling the issue recently. A study on the use of PLA monofilaments in trammel nets showed that catch efficiency was similar to conventional PA materials, making PLA a potential substitute material.[72] On the other hand, a study on the use of PLA in gillnets found a slightly lower catch number and a lower fishing efficiency than PA.[73] Both papers measured inferior mechanical properties of PLA compared to the conventional fishing nets and the different mechanical strains experienced in the different fishing techniques probably explain the diverging results, highlighting that PLA can only be used as a substitute material in a subsection of possible fishing and aquaculture types. PLA is also a fully bio-based material, while PBS and PBAT are currently only in part manufactured from bio-based sources.

The significantly higher costs of any of the previously mentioned fibers compared to PA are the main barrier to adoption, combined with the drop in fishing efficiency this means that strong subsidies currently need to be adopted to incentivize the use of biodegradable netting.[68]

The materials used for fishing gear should maintain its mechanical properties for its service life, which for fishing nets is generally 3-12 months.[70] Ready biodegradation in seawater, such the one that PHAs are capable of, is thus ultimately undesirable as it would lead to a quick drop in the properties of the net. This means that common seawater-biodegradable certifications that require materials to reach 90% biodegradation after 6 months (such the one defined by TÜV for packaging)[74] are not really useful for the case of fishing gear, but alternative standards are not yet available. The ideal polymer used for fishing nets would be one that starts to biodegrade after over a year of immersion in seawater. PBSAT nets have demonstrated the capability of maintaining their mechanical properties without notable biodegradation for 18-24 months of immersion and then start biodegrading. Degradation over such long periods is generally measured by means of mass loss, loss of mechanical properties, and visual observation, as measurements of ultimate polymer biodegradation are challenging.[70,75] However, it is still unclear to what extent this slow biodegradation is an improvement over fishing nets made of traditional materials in terms of diminishing ghost fishing or other forms of marine pollution.

1.3.2 Fish boxes

Several alternatives to expanded polystyrene (EPS) fish boxes have been tested and are already commercially available. The objectives of these materials are to reduce the environmental impact of fish packaging both by making its disposal easier though either more effective recycling or compostability, as well as using materials that may biodegrade more in case of dispersal in the ocean. Three main types of alternative material may be identified.

- Reusable plastic fish boxes
- Corrugated cardboard packaging
- Bio-based foams

Reusable plastic boxes are made of polyolefins, mainly high-density-polyethylene (HDPE) or polypropylene (PP). Unlike EPS these materials can be disinfected for reuse and also offer greater mechanical recyclability, at the price of greater density and inferior thermal insulation.[5]

Corrugated cardboard is made up of two outer linear cardboard layers named liners and an inner fluted cardboard layer. The main impulse towards sustainability is that cardboard is a very recyclable material. For use as fish boxes, it is also necessary to coat the outer cardboard with a waterproof coating. Fossil-based polymers such as low-density-polyethylene (LDPE) and PET are commonly used materials for such coatings. These are not normally separated before disposal, meaning that a low quantity of coating material needs to be used to maintain recyclability. Environmentally sustainable liner materials such as wool, hemp or bio-based foams can be used around the fish to improve the lacking thermal insulation properties of cardboard.[6]

Substituting EPS wholesale with a bio-based and biodegradable foam (biofoam) is also a possibility, although bio-based foams can also be used to add insulation to a cardboard box as explained above. Most of the main commonly used bio-based polymers have been studied for use in expanded materials, quite often in the form of blends or composites to achieve more desirable properties and many such materials have reached the commercialization stage. Cellulose-based foams are quite used in non-food sectors such as construction and automotive but are currently limited in food-contact applications due to concerns with stability and safety.[76] Starch-based foams have similarly been developed in many forms and are commercially available, their main limitations being a lack of water resistance that limits properties and often forces the use of heavy chemical modification or extensive blending with more hydrophobic polymers.[77,78]

Biodegradable polyesters are one of the main studied kinds of polymers from which to obtain biofoams. PLA, alone or in blend, is the polymer for which the technique is better studied and developed and will be discussed extensively later. Of the other polyesters the only one to reach the commercial stage is PHA, as marine biodegradable PHA foam made out of PHBH is sold by Mitsui.[79] Other polyesters such as PBS and PBAT have been foamed on a research scale but have still not been optimized on a larger scale, the main issues being a low melt strength combined with a glass transition below room temperature which lead to severe foam shrinkage unless helped by chain extension or other kinds of reinforcement such as nanofillers.[80,81]

1.3.3 PLA paper coating

Polymer coatings, both bio-based and fossil-based, can be applied to paper by several techniques, the most prominent being extrusion coating, solvent coating and waterborne dispersion.

Extrusion is the most widespread and established technology. The polymer is processed in the melt and extruded in a way similar to a flat film, then the film is drawn between rolls that force it onto the paper substrate which moves faster than the film and draws it to the desired

thickness (Figure 1.5). It has the advantage of providing a continuous and solvent-free process to provide a uniform coating. However, it also has limitations. The melt strength of the polymer limits the extent to which it can be stretched during application, and this applies a lower bound to the thickness of the applied coating. For polyolefins with good melt strength, such as the most applied on paper, which is PE, very thin coatings in the order of 10 µm can nevertheless be obtained. However, the lower melt strength of PLA means that it is limited to a higher coating thickness when melt extruded, in the 20-30 µm range.[82,83] Another potential issue with extrusion coating on paper substrates is the poor adhesion between coating and substrate, which is particularly an issue with thinner coatings.[84]

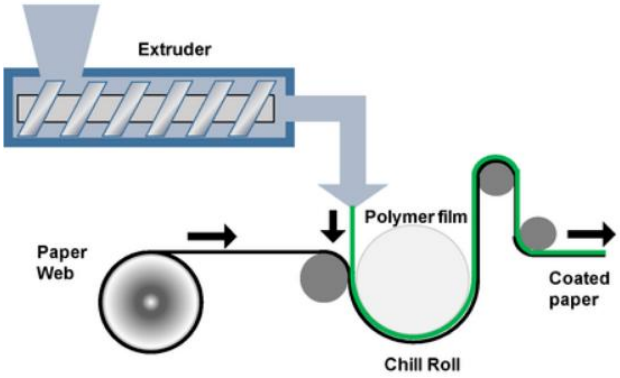

Figure 1.5 Illustration of paper coating by extrusion technique. Adapted from[85]

The limitations of extrusion coating for the application of thin layers of polymeric material can be surpassed by the use of “wet” techniques, where the polymer is deposited on the surface dissolved or dispersed in an appropriate liquid medium which is then removed by evaporation. Thickness in this case is not limited by mechanical properties and even nanometric coatings can be achieved. Adhesion is mostly regulated by the wettability of the surface by the coating liquid; a high wettability will generally result in a strong adhesion between the two layers.[86] From a technical perspective, various batch and continuous techniques can be used for the application of waterborne and organic solvent-dissolved polymers (Figure 1.6). Surface sizing is a continuous coating technique where the polymer solution is gathered by a roll which then applies the polymer to the substrate. This method is widely used but runs into issues when the polymer solution has high viscosity. Rod coating is a batch technology that allows for a good control of coating thickness over a wide range of viscosities, but it is hard to scale for industrial applications. Dip coating is a simpler batch technology that quickly coats surfaces but allows little control over thickness.[85]

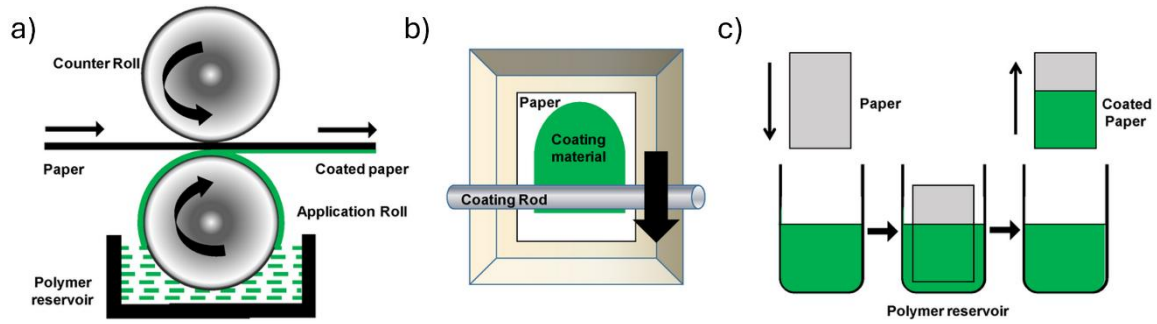

Figure 1.6 Illustration of paper coating by a) Surface sizing b) Rod coating c) Dip coating. Adapted from[85]

For environmental and safety reasons, the use of water-based mediums is preferable to the use of generally fossil-derived and often toxic organic solvents. Polymer dispersions and emulsions (which may collectively be defined as polymer latexes) are widely used to obtain surface coatings used as paints, adhesives, inks, and packaging. Both are colloidal systems: emulsions are mixtures of immiscible liquids (e.g., oil in water), while dispersions are suspended solid particles in a liquid. Typical polymer latexes contain particles of 10 nm – 10 µm, prepared either by solvent evaporation or emulsion polymerization. Stability is crucial for storage, as emulsions and dispersions need to have a shelf-life sufficient for their application. Stability may be evaluated through simple visual observation, or more advanced techniques such as light scattering methods that measure droplet size and distribution and can measure the change of these properties over time.

To successfully coat a material, an unbroken film of polymer needs to be formed on its surface (Figure 1.7). For polymer latexes, film formation generally follows three steps: water evaporation (drying), particle deformation, and coalescence into a continuous film. The minimum film formation temperature (MFFT), typically near the polymer's glass transition, dictates success; below it, brittle films and discontinuous films form. Plasticizers and coalescing agents lower T_g and facilitate particle merging. Surfactants also influence final film properties: compatible ones dissolve in the polymer, while incompatible ones migrate or remain at interfaces, affecting barrier and surface properties.

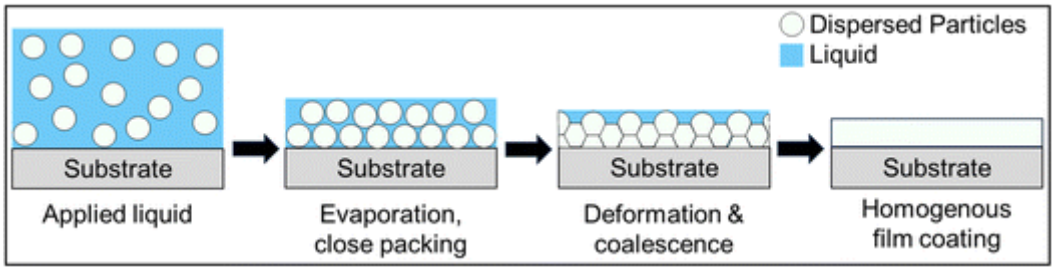

Figure 1.7 Illustration of the mechanism of film formation from a solid polymer dispersion in a liquid medium. Reproduced from[87]

Waterborne polymer coatings currently make up the majority of the formulations employed as durable protective coatings (architectural and automotive paints, wood varnishes etc.) but are far less used in the packaging sector. Fossil-based non-biodegradable polymers (mostly polyurethanes and polyacrylates) dominate the waterborne coating sector with very few polymers used being bio-based.[87] Techniques to obtain biodegradable polyester dispersions have been studied for decades but this has not generally been focused on obtaining coatings but on the use of the dispersed particles for biomedical uses, mostly drug delivery, where the use of bioabsorbable polymers such as PLA, PCL, and PHB is of great interest. Preparation methods include nanoprecipitation, salting-out, emulsification–diffusion, and double emulsion–solvent evaporation. These usually yield low polymer concentrations (<5 wt.%) and focus on nanoparticle isolation rather than dispersion stability over time.[88]

1.3.4 PLA foams

PLA is one of the most studied bio-based polymers for foamed applications. It is particularly considered a promising replacement for polystyrene for commodity applications due to the similar properties of the obtained foams. A plastic foam can generally be defined as a multi-phase plastic material with a cellular structure, with a gas phase organized in cells dispersed in a polymer matrix. Cell size and structure have a fundamental influence on material properties and foams may be generally classed into closed cell or open cell. In a closed cell foam each cell is completely enclosed by a cell wall and the gas used for expansion is trapped inside, though it will slowly permeate through the cell walls. This can offer superior insulation properties if the trapped gas is favorably comparable to air. In open cell foams the cells are connected with each other and the exterior, the gas phase will thus be air. Intermediate morphologies with a certain percentage of open cell content are also possible. Foams can also be classified by cell size and density. Macrocellular or conventional foams have a cell size > 10 μm, or > 100 μm in other definitions, microcellular foams have a cell size between 1 and 10-100 μm and nanocellular foams have a cell size < 1μm.[89,90] Finally, by density, foams may be classed on the basis on their volume expansion ratio (VER), the density of the foam relative to the one of the polymer. A low-density foam has a VER > 10, a medium density one a VER of 4-10 and a high density one a VER < 4.[90]

Foaming agents can generally be distinguished in chemical or physical agents. Chemical foaming agents are materials that are stable and non-volatile at storage conditions but under different conditions, generally at a higher temperature, will decompose in a way that yields at least a gaseous species. For example, the most widely used chemical foaming agent, azodicarbonamide, will evolve N_2 when heated. In self-blown foams the monomer

itself is also a form of chemical foaming agent, e.g. isocyanates in polyurethane foams that evolve CO_2 in reactions with water. PLA foams, however, have mostly been obtained by physical foaming agents, which are dissolved within the polymer matrix and physically transition to gaseous state and cause the consequent material expansion through cell nucleation and growth after a change in conditions. The instability of the foaming agent can be induced through temperature increase or pressure drop methods. As temperature reaches below the glass transition of the polymer, the overall structure is stabilized. The typical foaming agents are either low-boiling liquids, pentane being a common choice, which become gases when heated or supercritical fluids such as N_2 or CO_2, which turn into gases either when heated or by a pressure drop (Figure 1.8).[91]

Regardless of the foaming agent used, the formation of thermoplastic foam involves three steps:

- 1) The dissolution of the foaming agent in the polymer matrix
- 2) The nucleation of gas bubbles
- 3) The growth and stabilization of cells within the matrix

The dissolution of the foaming agent is achieved in the melt, for chemical foaming agents generally by directly feeding agent and polymer into an extruder at the foaming temperature, while physical foaming agents may be injected within the polymer matrix in batch processes as well as extrusion. To achieve a controlled cell structure, a homogenous polymer-gas solution needs to be achieved and thus the two phases need to reach equilibrium. This is harder to achieve with chemical foaming agents which will generally give a less uniform cell structure.

Phase separation then happens when the gas supersaturates the polymer matrix, and the equilibrium is broken by the nucleation of bubbles. The nucleation may happen heterogeneously around a nucleating agent, a solid within the polymer melt that forms a liquid-solid interface where bubbles easily form. This may be as an added component (e.g. talc) or may happen around polymer crystals as part of melt recrystallization. Nucleation may also happen homogenously by bubble self-nucleation. Nucleation density, the number of formed bubbles per volume unit, is thus influenced by the nucleation capability of the supersaturated gas, the number of nucleation sites and its interactions with them.

The formed bubbles will grow as long as the resistance from the matrix is lower than gas pressure. The radius of the bubble will increase, and nearby bubbles will coalesce into each other if they meet. As the polymer matrix cools, the resistance to expansion increases as viscosity does until the structure is stabilized and the cellular structure is formed. The nature of the polymer and the process temperature are both vital parameters for this process. At one extreme, most the bubbles will expand into each other, and the formed gas will largely

escape the polymer matrix as it collapses. At the other extreme, the polymer will resist expansion from the start, and no cells will be formed. Parameters such as cell size, cell wall thickness and open cell content are determined by the extent of bubble growth and stabilization. The viscoelastic properties of the polymer matrix thus need to be regulated through process temperature and choice of additives to achieve the desired structure.

The main drawback of PLA in this process is its limited melt strength which can limit foamability to low volume expansion ratios. This may be improved by modification techniques or by enhancing crystallization. Achieving a good crystallization during foaming can also increase the service temperature of PLA foams.[92]

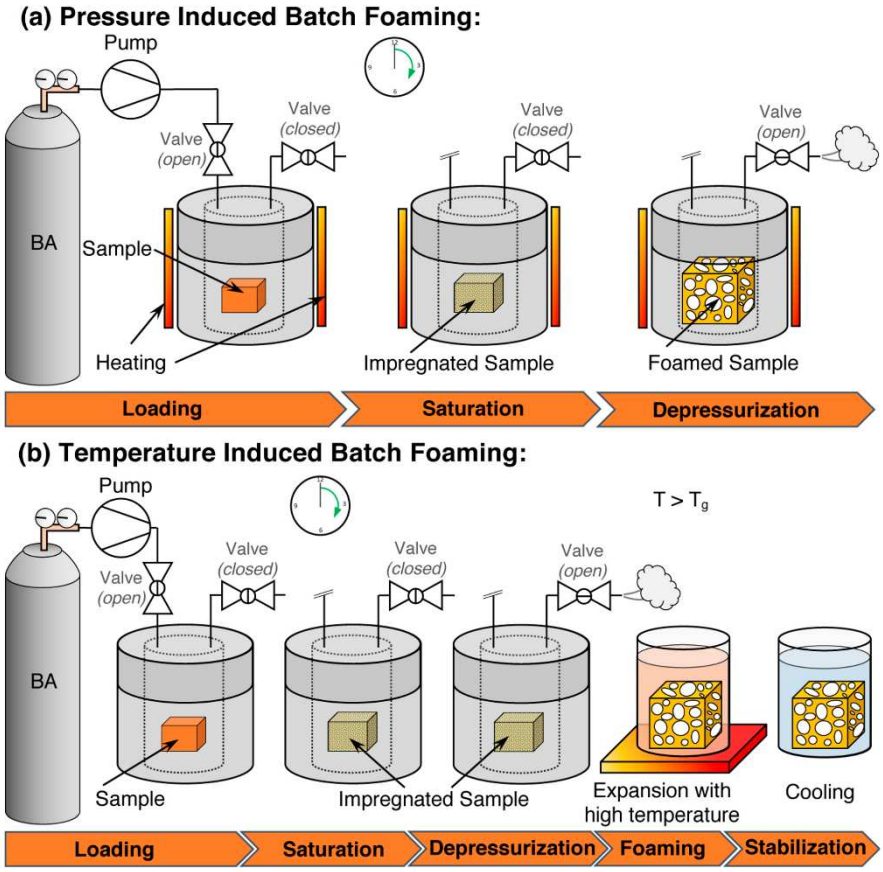

Figure 1.8 Scheme of batch foaming of a polymer with a physical foaming agent by a) pressure drop or b) temperature raise. Reproduced from[93]

The influence of PLA crystallinity on foaming behavior is complex and has been well studied in relation to foaming using supercritical CO_2. The interaction between CO_2 and PLA's microstructure is critically dependent on the polymer's crystallinity. CO_2 solubility in crystalline regions of a polymeric material is far lower than in the amorphous regions, leading to a reduction of the fraction of the sample in which bubble formation takes place. Crystalline regions also contribute to a higher overall viscosity of the polymer matrix by acting as physical crosslinking sites, which further hinders cell growth[94]. On the other hand,

the interfaces between the amorphous and crystalline phases serve as bubble nucleation sites.[95] Thus, overall, a polymer with higher crystallinity has the potential of forming smaller and more uniform cells upon foaming, but this effect is undermined by the challenges of obtaining a high volume expansion ratio. The foaming of semicrystalline PLLA requires a careful selection of processing conditions and results across studies are often not easily reproducible or scalable due to the many factors contributing to final foam morphology and properties.[96] CO_2 pressure also influences PLA crystallization itself, as the dissolved CO_2 molecules act as plasticizers enhancing chain mobility and weakening interchain interactions, with a complex effect on crystallization. In general, at higher foaming temperatures chain mobility is increased so much that it makes it harder for polymer chains to fix into the lattice and crystallization rate is decreased, while at lower foaming temperatures the enhanced mobility will counter the effect of high viscosity and enhance the crystallization rate.[97]

As PLA is a biodegradable polymer, it is interesting to analyze the possible effects of a cellular structure on a material's biodegradability. The surface area of a plastic structure is a key element in determining its biodegradation rate. For example, smaller particles are commonly found to be more biodegradable than larger ones due to the greater surface area exposed to the formation of biofilms.[98] Foamed structures have a much larger surface area compared to bulk structures, which may accelerate their biodegradation. However, this is heavily dependent on foam nature, as an open-cell structure allows microorganisms and enzymes full access to the entire surface area while a closed-cell structure will block this access to anything except the external surfaces and thus similar in nature to a bulk material. Pore size also plays a role, as microcellular foams with pores below 10 μm in size would block access to many bacteria, although extracellular enzymes would only be blocked by the finer nanofoams.[99] It needs to be mentioned that these extrapolations are made on theoretical grounds as no thorough investigation on the influence of foam structure on biodegradation seems to exist.

1.4 Aim of the thesis

The aim of the present work is to analyze the potential of bioplastics as alternative materials in three areas of employment closely related to the fishing industry

- The use of waterborne dispersions of PLA for paper coating
- The use of blends of PLA and PHAs to obtain insulating foams
- The use of recycled PLA in nets

In the case of waterborne PLA dispersions, the thesis also includes follow-up research presenting results regarding their employment in sectors not directly related to fishing industry, namely biomedical and sensors.

In all cases special attention has been paid to study the biodegradation properties of the obtained materials and their effect on their potential uses.

In chapter 2, the preparation of hydrophobic paper coatings made from waterborne dispersions of an amorphous PLA is described. A PEG-PLA-PEG triblock copolymer was tested for use as surfactant in the waterborne systems and the formulation of the dispersion was optimized so as to maximize both its stability over time and its solids content. For application on paper the viscosity of the system itself and with the addition of xanthan gum used as thickener was studied and exploited to obtain the best results as barrier against liquid water and water vapor while minimizing coating weight and thus helping in the recyclability of the overall system.

In chapter 3, the fabrication of aquaculture nets for mussel farming made from recycled PLA instead of the conventional PP polymer is described. The potential thermal degradation of this secondary PLA in further processing was studied and a thorough analysis of the biodegradation of the nets in industrial compost, in seawater and in soil in simulated laboratory tests was carried out.

In chapters 4 and 5, the fabrication of blends of an amorphous PHA with, respectively, amorphous and semicrystalline PLA is described with the objective of obtaining insulating foams for packaging purposes, such as potentially fish boxes, from the blends. In both cases, the morphology of the blend was studied by microscopy and thermal analysis, and the foaming is carried out by a batch process using supercritical CO_2 as the physical foaming agent. For semicrystalline blends the influence of the PHA component on the crystallization of the PLA, both in the blend and in the ultimate foam, was also analyzed. The morphology of the resulting foams was analyzed in order to describe the effect of different blend ratios and optimize the process conditions to obtain low density foams. Finally, the biodegradation capabilities in a home composting setting of the blend foams were analyzed and compared to foams made from pure PLA. For the amorphous blend foams the biodegradation capabilities in a simulated marine environment were also tested.

In chapter 6, the functionalization of films obtained from waterborne PLA by the encapsulation of peptides is described. Three different peptides, two known for osteogenic and one for angiogenic capabilities, were encapsulated by a wholly waterborne technique. The cytocompatibility and the capability of the functionalized films of promoting the specialization of human stem cells into osteoblasts was studied with the ultimate objective of using the material as coating for titanium bone implants.

In chapter 7, the use of the previously described waterborne dispersions to obtain composites with graphene oxide and the biodegradation properties of these composites in industrial composting environments is studied. The composites can be laser scribed to form conductive pathways in the insulating material and by this process can be formed into biodegradable electrochemical sensing platforms that were validated to test bio-analytes.

2. Preparation of high-solid poly(lactic acid) waterborne dispersions with PEG-PLA-PEG block copolymer as surfactant and their use as hydrophobic coating on paper

This chapter is mostly adapted from the research article: Calosi, M.; D'Ilorio, A.; Buratti, E.; Cortesi, R.; Franco, S.; Angelini, R.; Bertoldo, M. Preparation of High-Solid PLA Waterborne Dispersions with PEG-PLA-PEG Block Copolymer as Surfactant and Their Use as Hydrophobic Coating on Paper. Progress in Organic Coatings ***2024****, 193, 108541. https://doi.org/10.1016/j.porgcoat.2024.108541.*

2.1 Introduction

Paper-based packaging is enjoying a resurgence, as bans on single-use plastics and consumer preference for paper over plastic packages are leading the industry towards using paper preferentially whenever viable due to its inherent biodegradability and recyclability.[100,101] Since paper itself is a hydrophilic and porous material with poor barrier properties and low resistance to water and grease, when used for packaging it is often coated or treated so as to improve its properties. The materials most commonly used as coatings are petroleum-based polymers such as polyethylene (PE), poly(vinyl chloride) (PVC), poly(ethylene vinyl alcohol) (EVOH) and many others depending on the application. These materials are a cause of concern to environment and health due to their lack of biodegradability, potential release of dangerous substances (e.g. microplastics or polyfluoroalkyl substances), use of volatile organic compounds (VOCs) during application and limitations to the recyclability of the final paper product.[102–104]

Two of the most important developments of the recent decades in the coating industry have been on the one hand the turn towards bio-based and biodegradable coatings in place of classic fossil-based non-biodegradable polymers, on the other hand the increasing use of water-based technologies for coating applications in alternative to extrusion coating and solvent-based coating.

A variety of biodegradable alternatives to fossil-based polymers are used for coating purposes. Natural biopolymers such as polysaccharides (e.g. starch, chitosan, modified cellulose) or proteins (e.g. zein) have been widely tested but they often run into limitations due to their inherent hydrophilicity limiting water barrier and resistance properties.[102,105] More desirable barrier properties can often be obtained by coating with biodegradable aliphatic polyesters such as polyhydroxyalkanoates (PHAs), polycaprolactone (PCL), poly(butylene-succinate) (PBS) and poly(lactic acid) (PLA), which have a significantly higher degree of hydrophobicity.[106]

PLA in particular can be considered a moderately hydrophobic material as it is water-insoluble and has a surface contact angle with water of 65-80°. However, it possesses poor gas barrier properties against both water vapor and oxygen compared to many fossil-based polymers.[107–109] At the moment, this makes PLA most interesting in the paper coating field for the purpose of reducing water absorptiveness and thus increase resistance to humidity rather than as barrier packaging,[110,111] though many potentially interesting PLA composites with improved barrier properties are being tested.[112] PLA has a slow biodegradation when dispersed in the environment but it is fully degradable in appropriate composting conditions.[113]

The recyclability of coated paper is an issue apart from its biodegradability. Coating biodegradability makes no difference to the paper recycling industry, as “rejects” from the repulping process are not separable from each other and are disposed of together. In general, the lower the coating weight, the better the coated paper will be recyclable, although no universal coating weight value above which paper is no longer recyclable exists. The current guidelines of the UK Confederation of Paper Industries, as an example, call for coating weight not to exceed 10% of total pack weight and aspire to reach 5% in the future.[114] Thus, minimizing the amount of coating weight, apart from the general advantages of using less plastic, is also preferable for paper recycling purposes. The biodegradability of paper used for packaging is nevertheless still an important factor as it reduces the environmental impact in case of incorrect disposal or littering, as well allowing for the overall compostability of food-contaminated packaging.

The most common technique for obtaining polymer-coated paper is extrusion coating. This has a limit in the minimum thickness of produced films that depends on the polymer melt strength. Thicknesses down to 10-15 µm may be obtained with PE films, but not with most

bio-based polymers such as PLA or PHAs (minimum thicknesses 20-30 μm) owing to their lower melt strengths.[115] Adhesion to the paper substrate is also reduced when thinner films are extruded.[84] These issues are reduced with “wet” methods that allow the production of very thin coatings; the polymers are deposited on the paper substrate by being dissolved or dispersed in a liquid phase, which is then evaporated. Organic solvent-based coatings cause high consumption of VOCs, with negative effects on the environment and severe concern for operators’ health. Thus, water is the preferred non-toxic and environmentally sustainable solvent for coatings, but most polymers, especially hydrophobic ones, are insoluble in water.

The polymers most commonly applied as paper coatings via water-based technologies are currently obtained from radically polymerizable fossil-based monomers such as styrene and acrylates by directly polymerizing in emulsion and thus obtaining high-solid content formulations.[116,117] This route is not available for polyesters and biodegradable polymers in general, which need to be dispersed in the aqueous phase after synthesis. To be of industrial interest, the waterborne formulations obtained need to fulfil several requirements: stability over time, high (> 40%) solid content, as well as ease of application. Interest in obtaining these formulations is increasing, as evidenced by the recent reports of the first such examples using PBS[118] and PHAs.[119]

PLA waterborne formulations have been the most researched among the various biodegradable polyesters. At the time of this writing, a commercial PLA waterborne product line exists, sold by Miyoshi Oil & Fat Co. (Tokyo, Japan).[120] These formulations have a particle size between 1 and 5 μm and 40% solid content and are sold for adhesive and paper coating applications. Industrial research is active on this subject, as is evident from patent literature. As examples, recently publicly available patents describe formulations of waterborne PLA using low-molecular weight plasticizers as dispersants for cosmetic use[121] and formulations using poly(vinyl alcohol) (PVA) in combination with polymeric surfactants and thickeners.[122]

Scientific literature has been lagging behind industrial research, the first high-solid stable PLA latex (a composite containing montmorillonite with 25 wt% solid content) being reported in 2016 by Bandera and colleagues.[123] This was tested as paper coating and showed 85% reduction in WVTR compared to the original paper at 20 g/m^2 coating weight. Our research group more recently tested the stability and filmability of waterborne dispersions of PLA, finding a range of ionic and non-ionic surfactants that were able to form stable dispersions.[88] We then measured the rheological properties of such dispersions using xanthan gum (XG) as thickener, in order to obtain a formulation more easily usable for coating and paint applications compared to the original dispersions.[124] We also used waterborne PLA dispersions to achieve blends of this polymer with PVA.[24] Most recently, Abdenour and

colleagues,[125] reported the properties of paper coated using XG-thickened aqueous PLA dispersions using commercial non-ionic surfactants. This formulation was intentionally low-solid (3-4 wt%) to limit the volume of organic solvents used per volume of water and a reduction in WVTR above 90% was obtained at 15 g/m^2 coating weight, while water absorption was not tested.

The PLA used for coatings may be amorphous or semi-crystalline, the degree of crystallinity depending on the quantity of D-lactide used in the polymerization. While semi-crystalline PLA confers materials more desirable mechanical properties, its solubility in organic solvents is more limited and the most commonly used ones are chlorinated solvents such as dichloromethane and chloroform, which are toxic and environmentally harmful. Amorphous PLA, on the other hand, is readily soluble in a wider array of solvents, allowing for the use of greener, but still cheap alternatives such as ethyl acetate.[126]

In our group's previous research,[88] we found that Synperonic PE/F68, a commercial poly(ethylene glycol)-*b*-poly(propylene glycol)-*b*-poly(ethylene glycol) (PEG-PPG-PEG) triblock copolymer by Croda was an effective surfactant for the formation of waterborne dispersions of PLA. In this work we aim to improve on the properties of these dispersions by synthesizing and using for this purpose a structurally analogous PEG-PLA-PEG triblock copolymer, in which PLA serves as the hydrophobic component of the surfactant in place of PPG. The hydrophilic-lipophilic balance (HLB) of the block copolymer was aimed to be similar to the one of the commercial product by using a similar overall ratio between the hydrophilic PEG component and the hydrophobic PLA component.

PLA-PEG block copolymers have been reported since the late 1980s;[127,128] since then they have been used extensively in drug delivery research due to their biocompatibility and easy possibilities of functionalization that make them versatile drug carriers.[129] Very little research has comparatively been carried out on the use of these copolymers outside the biomedical field, although in recent years they have been reported as possible plasticizers for PLA,[130] as well as crystallization and toughness enhancers.[131]

Our aim in this work is thus to use this kind of copolymers as surfactants, with the ultimate purpose of obtaining stable waterborne dispersions of PLA with high solid content, and to study their use in coating applications. To achieve this, the oil-in-water methodology of our previous work was used, the resulting dispersions were characterized and their stability over time was assessed. The filmability of the samples, the level of plasticization conferred by the surfactant and the consequent changes in film forming temperature were also evaluated. Different formulations were prepared to find the optimal surfactant content to achieve long-term (> 6 months) stable dispersions with minimal phase separation. We also analyzed the hydrolytic stability of PLA itself when stored as a waterborne dispersion at 4°C, an aspect for which there is little reference as PLA hydrolysis research has been mostly

concerned with the accelerated degradation of the polymer at higher temperatures (≥ 37°C).[132–134]

Concentration by water evaporation was used to maximize the solid content of the dispersions, as far as these could be kept stable. XG was then used to thicken the PLA dispersion and allow its use for paper coating through hand coater application on a heated surface. The resulting coated paper was studied using scanning electron microscopy (SEM) and its barrier properties against liquid water and water vapor were assessed by measuring water absorptiveness and water vapor transmission rate (WVTR). In the interest of ensuring recyclability of coated paper, we aimed to minimize coating weight by optimizing the coating formulation and application process and we studied the repulpability of samples at different coating weights.

2.2 Materials and methods

Materials

Poly(lactic acid) Ingeo PLA 4060D (PLA) was kindly provided by NatureWorks LLC (Minnetonka, MN). PLA 4060D is an amorphous polymer with a L-lactide content around 88 wt %. Xanthan gum Satiaxane CX2QD (XG) was supplied by Cargill Deutschland GmbH (Krefeld, Germany). Methoxypolyethyleneglycol (mPEG), with a nominal $\overline{M_n}$ of 2000 g/mol and dispersity index of 1.06, L-lactide, sodium dodecyl sulphate (SDS), hexamethylene diisocyanate (HDI) and 4 Å molecular sieves were purchased from Sigma-Aldrich (St. Louis, MO). Stannous octoate ($Sn(Oct)_2$) and acid red 87 were purchased from TCI chemicals (Tokyo, Japan). Analytic-grade solvents (toluene, ethyl acetate, dichloromethane, diethyl ether) as well as HPLC-grade solvents (chloroform) were purchased from Carlo Erba (Milan, Italy). mPEG was dehydrated by azeotropic distillation under nitrogen flow using anhydrous toluene and a Dean-Stark apparatus and then dried under reduced pressure before use. Anhydrous toluene and ethyl acetate were obtained by storing the solvent for at least 3 days and no more than a month over 20 % weight/volume of 4 Å molecular sieves, activated by 200 °C heating for a day. L-lactide was recrystallized twice from anhydrous ethyl acetate, dried under vacuum and stored under nitrogen. Ultrapure water was obtained using an Arium® Mini (Sartorius Lab Instruments GmbH & Co. KG, Göttingen, Germany) water purification system fed with pretreated deionized water. Standard printing paper (Copy paper, Indonesia) used for coating had 98 ± 2 µm of thickness, 71 ± 1 g/m^2 grammage, 100 ± 10 g/m^2 water absorptiveness as measured by Cobb60 test.

Synthesis of mPEG-PLA-mPEG block copolymers (ELE)

15.010 g of mPEG (7.51 mmol), 3.000 g of L-lactide (20.83 mmol) and 45 mL of anhydrous toluene were heated to reflux under dry nitrogen atmosphere and 0.12 g of $Sn(Oct)_2$ (0.3 mmol) was then added. After 24 h the reaction mixture was cooled to 60 °C and 0.600 g (3.57 mmol) of HDI was added dropwise. After leaving the reaction overnight, 0.100 g, (0.43 mmol) of HDI was further added in 20 mg increments until no further reduction in the dispersity value by SEC was noticed. The mixture was cooled to room temperature and precipitated twice into diethyl ether. The precipitate was finally dried under reduced pressure (0.2 mbar) until constant weight was reached. 16.983 g of product was obtained (91% yield).

Preparation of aqueous dispersions of PLA

3.740 g of PLA was dissolved in 34 mL of ethyl acetate at 50 °C and the appropriate weight of surfactants (ELE from 0.260 to 0.780 g and SDS from 0 to 0.520 g) was dissolved into 26 mL of ultrapure water. The organic phase was added to the aqueous phase in a 100 mL glass beaker at room temperature and was homogenized using a Hielscher UP200St ultrasonicator (Hielscher Ultrasonics, Teltow, Germany) equipped with a 14 mm diameter probe, set at 50 % intensity for 30 seconds and then at 80 % intensity for 90 seconds. The resulting emulsions were mechanically stirred under a fume hood for at least 18 h or in any case until complete removal of the organic solvent. The PLA dispersions were stored at 4 °C.

To obtain high-solid aqueous dispersions of PLA, the necessary water was removed from the originally prepared aqueous dispersions by using a rotary evaporator and a 40 °C water bath, periodically weighing the sample until overall weight was in the desired range.

Characterization of aqueous dispersions of PLA

Solid content of PLA dispersions was measured by comparing the original weight of a 200-400 mg sample with the same sample after heating for 3 hours at 150 °C. Dispersions were manually shaken for 10 seconds prior to sampling.

Dynamic light scattering (DLS) measurements were carried out using a Malvern Zetasizer Nano S90 (Malvern Panalytical, Malvern, UK). Samples were diluted to approximately 0.1 mg/mL of PLA using ultrapure water. Measures were carried out in triplicate at 25 °C and an average ~~result~~ correlogram was generated using Zetasizer 8.02 software. The Z-average diameter derived from this average correlogram was generally reported as particle diameter. Intensity size distribution was generated by the same software by the non-negative least squares (NNLS) inversion method.

The Z-potential of the dispersions was determined by phase analysis light scattering (PALS) at 25 °C using a NanoBrook Omni Particle Size Analyzer (Brookhaven Instruments

Corporation, Holtsville, USA) equipped with a 35 mW red diode laser (nominal 640 nm wavelength). The analyses were carried out on samples at ~0.25 wt %, and the reported data are the average over five repeated measurements, the standard deviation between measurements was taken as the uncertainty value.

Size-exclusion chromatography (SEC) analyses were performed with an instrument set comprised of a Jasco PU-4180 pump (JASCO Corporation, Tokyo, Japan) operating at 0.4 mL/min, two in series PLgel miniMIXED-D columns (Agilent, Santa Clara, USA), a Jasco CO-4060 column oven, a 20 μl injector, a Jasco RI-4030 refractive index detector, and a Jasco UV-4075 multi-channel UV-Vis detector. The column oven was set at 30 °C and the eluent used was HPLC-grade chloroform. Polystyrene standards were used for calibration.

^{1}H Nuclear Magnetic Resonance (NMR) measurements were carried out on a Varian Mercury Plus 400 (Varian Inc., Palo Alto, USA) equipped with an Oxford NMR AS400 MHz autosampler (Oxford Instruments, Abingdon, UK) at room temperature. Sample concentration was approximately 30 g/L. Chemical shifts were referred to TMS as external standard by using solvent peak as the internal standard.

PLA films were obtained by pouring 3g of dispersion in a Petri dish (∅ 55 mm) and drying for 2 h at 60 °C in an oven, while covering the dish with filter paper to slow down evaporation and avoid surface cracking.

MFFT was measured by pouring 200 µL of dispersion on an aluminum plate that was pre-heated and kept at the desired temperature for 20 minutes while observing the film formation. Tests were performed at 1 °C intervals and the MFFT was considered as the minimum temperature at which a mostly transparent and continuous film to the naked eye was obtained, as opposed to a white and heavily cracked one.

DSC measurements were carried out on a PerkinElmer DSC 8000 calorimeter equipped with an IntraCooler II cooling device (PerkinElmer Inc., Shelton, USA). 5-7 mg of sample in an aluminum open pan was first heated up from room temperature to 240 °C, held isothermally for 5 minutes, cooled down to -60 °C, held isothermally for 5 min and heated up again up to 240 °C. Heating and cooling steps were performed at 10 °C/min.

Rheological measurements were performed with a rotational rheometer Anton Paar MCR 102 (Anton Paar Group AG, Graz, Austria) equipped with a cone-plate geometry (plate diameter = 24.964 mm, cone angle = 1998◦, truncation = 104 µm) both with a Peltier temperature controlling unit to keep the temperature constant at T=25°C, an evaporation control system and an isolation hood to prevent solvent evaporation and sample drying. Flow curves were measured in the shear rate range $\dot{\gamma}$ = (10^{-1}–10^{4}) s^{-1}. A pre-shear of $\dot{\gamma}$ = 100 s^{-1} for 60s, followed by a rest of 300s before each measurement, was applied to erase

any mechanical history. The experimental curves were obtained from averaging three different repetitions with standard deviation as error bars.

Coatings preparation and application

The appropriate quantity of xanthan gum (0.2, 0.4, or 0.8 wt %) was added to the aqueous PLA dispersions as thickener. Acid red 87 (0.01 wt %) was also added as coloring agent in some formulations to visually estimate the coating uniformity. This mixture was then gently stirred magnetically (concentration 0.2 and 0.4 wt %) or mechanically (concentration 0.8 wt %) overnight.

Coatings on paper were obtained using close wound wire bar hand coaters with nominal wet film deposit thicknesses of 4 or 15 μm. The paper sheet was set up on a film coater pre-heated at 60 °C (T_{MAX} Battery Equipment, Xiamen, China) and therein kept for at least 30 min after coating for drying.

Characterization of coated paper

Water absorptiveness of coated paper was measured by a 60 second Cobb test (Cobb60). The procedure was adapted from the Tappi T441 method using lab equipment. A 25 cm^2 testing sample of coated paper was laid, coated side up, on an impermeable surface and a glass cylinder with 10.8 cm^2 of internal surface area was tightly clamped on this surface. 10.8 mL of ultrapure water were added within the cylinder and left there for 60 seconds. The coated surface was covered with a sheet of blotting paper and dried using a wooden roller. The sample was then immediately weighed on an analytic balance (0.1 mg precision). The Cobb60 (g/m^2) value was obtained by:

$$\mathrm{Cobb60} = \frac{m_w - m_d}{A} \qquad (1)$$

Where m_w and m_d are the wet and dry weight, respectively, A is the sample area equal to 0.00108 m^2. Tests were carried out in triplicate and the standard deviation of data was used as the uncertainty value.

Scanning electron microscopy (SEM) analyses were accomplished with a Zeiss EVO 40 microscopy (Carl Zeiss Microscopy Ltd., Cambridge, UK) equipped with a LaB_6 source. Samples in the form of coated paper or film were gold sputtered (15 nm coating thickness) before observation with a Quorum Q150R sputter coater (Quorum Technologies, Laughton, UK).

Paper sheet thickness was measured using a digital micrometer with 1 μm accuracy, by taking the average measurement of 4 points. Standard deviation was used as the uncertainty value for coated and uncoated paper thickness. Coating layer thickness was measured by SEM by selecting 4 representative points within a cross-section view of coated paper where the dividing line between PLA and cellulose fiber was clearly visible, measuring

for each point the distance to the coating surface and taking the average distance as coating thickness. Standard deviation was used as the uncertainty value.

Cross-cut adhesion testing of prepared coatings was carried out as per ASTM D-3359 using an engraving tool and adhesive tape. The blade was run on the coated films in such a way that it should form a grille (1.5 cm × 1.5 cm) on the film. Then, adhesion tape was applied and pressed up to complete the adhesion on the surface of the coating, which was pulled off rapidly at an angle of 180° after 60 s. The sample portion that adhered to the tape was then observed to determine the degree of adhesion.

Water vapor transmission rate (WVTR) was measured by using the desiccant method according to the ASTM E96 standard. 20 g of anhydrous calcium chloride was placed in an aluminum cup closed with a test sample. The coated side of the sample was faced out and the bottom edges were sealed onto the cup with vinyl glue. Molten wax was poured onto the edge top so that 0.00385 m^2 surface area (A) was exposed to air. The samples were incubated at 22 ± 2 °C and 51 ± 3 % relative humidity (by saturated $Mg(NO_3)_2 \cdot 6\ H_2O$ solution) and their weight variation (0.1 mg precision) was monitored at time intervals that allowed for at least 20 mg of weight change. The analysis was over when at least 6 experimental points taken over at least 2 different days resulted in a R^2 value ≥ 0.998 by a linear fit. WVTR was calculated by the following equation:

$$WVTR = \frac{r}{A} \quad g/(days \cdot m^2) \qquad (2)$$

where r is the slope of the linear plot (in g/day) and A is the exposed surface area (in m^2). Water vapor permeability (WVP) was calculated from WVTR by the following equation:

$$WVP = \frac{WVTR \cdot L}{P} \quad g/(days \cdot Pa \cdot m) \qquad (3)$$

where L is the thickness of the sample (in m) and P is the water vapor pressure differential (in Pa) between the two sides of the sample (at 22 °C and 51 % RH, P = 1348 Pa). Tests were carried out in duplicate and the standard deviation between samples was used as the uncertainty value.

Surface energy measurements were carried out by the Dyne Test method according to ASTM D2578. Test inks (Ferrarini e Benelli, Romanengo, Italy). The reported surface energy is the one of the ink which separated into droplets after approximately 2 seconds when applied on the surface, or an interval between a fully wetting and a fully non-wetting ink when no available ink displayed such a property.

Repulpability was tested by weighing accurately around 0.4 g of 2.5x2.5 cm square samples and soaking them in water at a 5 g/L concentration at ~ 20-25 °C for 72 h and then stirring the samples magnetically at 450 rpm at 40 °C. In one variant the sample was stirred until

no individual fragment was visible to the naked eye and the time was recorded, and this was then verified by observing that in each case no sample was retained on a 5 mm sieve. In the other variant, the sample was stirred for 2 h and passed through the sieve, the elements remaining on the sieve were considered as rejected and weighed after drying (60 °C overnight and 2 h at 100 °C) and this weight was compared to the dry weight of the original sample to obtain the reject rate.

2.3 Results and discussion

Synthesis of PEG-PLA-PEG triblock copolymers

mPEG-PLA-mPEG triblock copolymers (ELE) were synthesized using the one-pot, two-step diisocyanate coupling technique first reported by Jeong and colleagues (Scheme 1).[135] Methoxy-PEG (mPEG) is used as initiator for lactide polymerization and the resulting ω-hydroxyl diblock copolymer is then coupled with a diisocyanate to obtain the triblock structure. We aimed for a HLB value similar to the one reported for the commercial Synperonic PE F/68 (SYN) surfactant that we used in previous research.[88] By assuming a similar hydrophobicity of PLA and PPG repeating units, we regulated the amount of lactide in the feed so as to reach similar mass ratios between blocks as the ones reported for SYN (82 ± 2% ethylene oxide content).[136] Commercial mPEGs with nominal $\overline{M_n}$ of 2 and 5 kDa were tested. When the higher molecular weight mPEG was used, the resulting triblock copolymer was insoluble in water at the desired concentrations of 1-3 % wt/v. We hypothesize this is due to the greater crystallization properties of the PLA block (18 repeating units) leading to excessive amounts of PLA crystalline phase that could not adequately arrange in a surfactant-like manner in water. Thus, the highest molecular weight mPEG was discarded and only mPEG with $\overline{M_n}$ of 2 kDa was then used. The produced triblock copolymer had a 2.8/1 molar ratio of L-lactide to mPEG (Scheme 1).

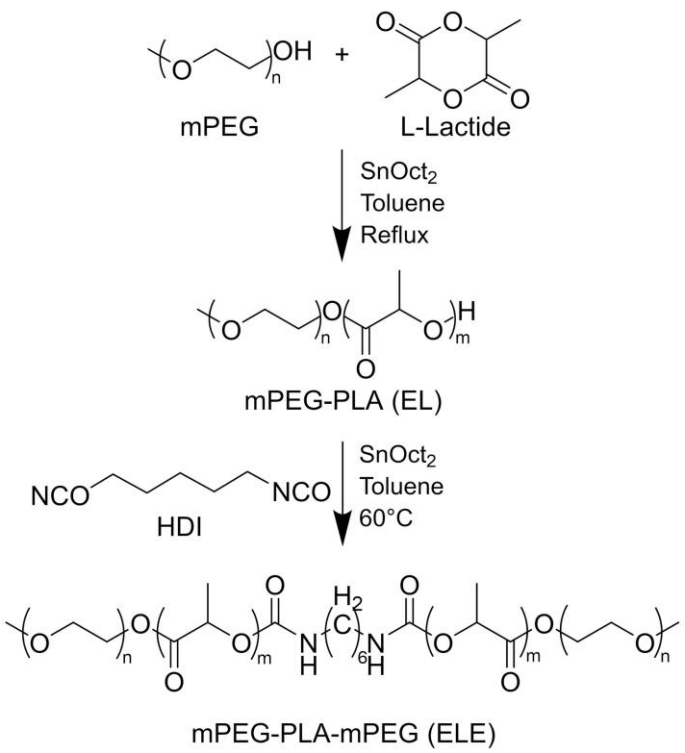

Scheme 2.1. Reaction for the synthesis of ELE copolymer surfactants.

The obtained ELE triblock copolymers show a single peak by SEC analysis with $\overline{M_n}$ of 9.2 kDa, approximately double the one of the EL diblock precursor (4.3 kDa) and a similar dispersity index of 1.06 (Figure 2.1). The presence of a peak at 3.14 ppm in the ^{1}H NMR spectrum of ELE, attributable to the urethane-adjacent CH_2 by NMR analysis (Figure 2.2, full spectrum in Figure 2.S1) confirms the coupling mechanism shown in Scheme 2.1. The number of repeating units of lactic acid in the EL precursor was approximately 4.7 when calculated by comparing the signal of the esterified terminal mPEG methylene (4.2-4.4 ppm) and the signal of repeating unit methines (4.9-5.3 ppm). This value is in reasonable agreement with the feed (2.8/1 lactide to mPEG) once the actual lactide conversion is taken into account (approximately 90%). The hydrophobic component, counting both the PLA segment and the HDI coupling agent, thus accounted for around 17 wt % in the ELE triblock copolymer and it is very similar to the one aimed for as analogous to the one of SYN (16-20%), although the molecular weight of ELE is lower (5.2 vs 9 kDa). The HLB is also similar, at the same Davies HLB value of 29 if the lactate repeating unit can be assumed to have similar hydrophobicity to the propylene oxide one or at 17 *vs* 16 if HLB is calculated via the simplified Griffin method.[137]

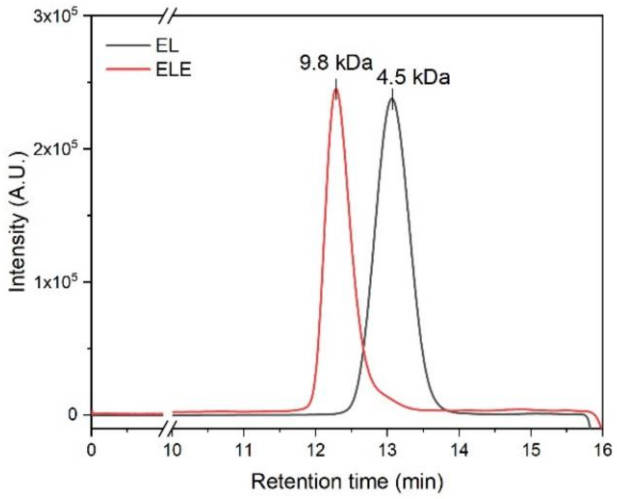

Figure 2.1 Comparison of SEC chromatograms of the triblock ELE (red) and the diblock EL (black) copolymers. Signals by RI detector arbitrarily normalized to the same height. Peak molecular weight value shown.

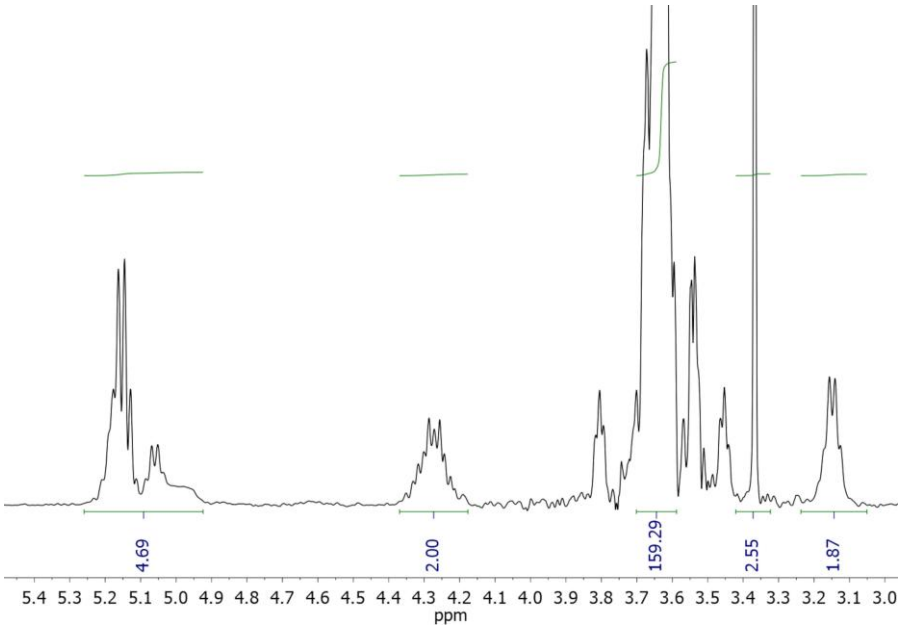

Figure 2.2 Relevant 1H NMR spectrum portion of ELE surfactant in $CDCl_3$

Preparation and characterization of PLA dispersions

The preparation of waterborne PLA dispersions was carried out using an oil-in-water method analogous to the one we used in previous research.[88] We used ethyl acetate as the organic solvent in which amorphous PLA was dissolved. We homogenized the two phases via ultrasonication and removed the organic solvent by evaporation at atmospheric pressure and room temperature.

A range of different formulations were prepared using the ELE copolymer as surfactant alone or in combination with SDS. The PLA concentration in the organic phase was kept constant at 11 wt % and the surfactants' concentration varied (Table 2.1). Samples are denominated ELEx-SDSy where x is the concentration of the ELE surfactant (% weight/volume) and y is the concentration of SDS multiplied by 100 in the aqueous phase, and thus in the waterborne formulation.

In the initial formulations, we tested ELE as the lone additive, in 1.8-3.0 wt % concentration (Table 2.1). The 3% upper bound in concentration was chosen so as to limit the ratio of surfactant/polymer ratio in the dry film coatings to a maximum of 1/5. The result was a homogenous milky emulsion, which was stable in the period immediately following preparation. Solid content of these dispersions was in the 13-17 wt % range, while particle size by DLS analysis was around 600 nm for formulations using 2 wt % (or less) ELE as surfactant, decreasing then with increasing surfactant quantity to 512 nm for ELE2.4 and 380 nm for ELE3.0. The particle size distribution was in all cases multimodal and polydispersity decreased along with size (Table 2.S1 for full data and Figure 2.S2 for examples of correlograms and their relative size distributions).

Table 2.1 Properties of aqueous dispersions of PLA using ELE and SDS as surfactants. All samples were prepared using 34 mL of organic phase containing 11% wt/vol PLA and 26 mL of aqueous phase.

Disper-sion	ELE[1] (wt %)	SDS[1] (wt %)	D (nm)[2]	Solid content (wt.%)	SC-6 (%)[3]	Filming ability at 60°C	MFFT (°C)	ξ (mV)[4]
ELE1.8	1.8	0	590	13	-	-	-	-
ELE2.0	2	0	670	14	-	-	-	-
ELE2.4	2.4	0	510 ± 40[5]	17 ± 3[5]	-	Good	-	-
ELE3.0	3.0	0	380 ± 40[5]	16 ± 1[5]	67	Good	38	-49 ± 1 (-36 ± 1)
ELE3.0-SDS5	3.0	0.05	290 ± 10[5]	16 ± 1[5]	83	Good	46	-62 ± 3 (-34 ± 1)
ELE2.4-SDS5	2.4	0.05	340 ± 20[5]	18 ± 2[5]	72	Good	41	-65 ± 3 (-38 ± 2)
ELE1.5-SDS5	1.5	0.05	370	17	67	Good	49	-72 ± 2 (-48 ± 2)
ELE1.0-SDS5	1.0	0.05	450	15	62	Good	47	-45.8 ± 0.2
ELE3.0-SDS10	3.0	0.1	260	15	93	Good	44	-67 ± 1 (-50 ± 1)
ELE3.0-SDS40	3.0	0.4	220	20	95	Opaque	46	-61 ± 2 (-31 ± 1)
ELE3.0-SDS200	3.0	2	190	18	94	Cracked	n.d.	-46 ± 1 (-36 ± 2)

1) Concentration in water phase; 2) D = hydrodynamic diameter as Z-average value by DLS analysis; 3) Solid content after 6 months as % of the original value; 4) Value after 6 months in brackets; 5) Average value across 3 separate preparations

Long-term stability of these dispersions was limited. ELE1.8 and ELE2.0 displayed the formation of evident precipitates within a week from preparation, a sign of phase separation of part of the solid from the dispersion and its sedimentation due to the density of PLA being

greater than water. Concentration of surfactant higher than 2 wt % led to stabler dispersions, in accordance with the reduced particle size, but dispersions still displayed polymer precipitation after 1 and 2.5 months in the case of ELE2.4 and ELE3.0, respectively. The solid content of ELE3.0 after 6 months was 67 % of the original, that is, 33% of the solid had precipitated. While, given the displayed trend, a dispersion stable over long term (>6 months) could probably be obtained by further increasing the surfactant content, we decided not to test this option as it would have led to unacceptably high hydrophilic surfactant content (above 20 wt % in the dried film).

Instead, we decided to add a quantity of sodium dodecyl sulphate (SDS) as an anionic co-surfactant together with ELE. We had already observed that SDS with starch was capable of stabilizing waterborne PLA dispersions, but that these dispersions were unable to film satisfactorily due to immiscibility with PLA.[88] Our aim was to add a small enough quantity of SDS that could stabilize the dispersion while not being too much to compromise the properties of films and coatings that may be obtained from them. We thus tested SDS in 0.05 to 2 wt % concentrations while keeping ELE concentration fixed at 3 wt % and ELE in concentrations from 1 to 3 wt % while keeping SDS fixed at 0.05 wt % (Table 2.1).

The stabilizing effect was successful even when using just 0.05 wt % SDS. For example, ELE1.0-SDS5 was stable for two months before precipitate formed, while ELE2.0, which contained double the quantity of neutral surfactant and no SDS, was only stable for a few days.

A reduction in particle size likely played the major role in improving dispersion stability. Figure 2.3a displays particle diameter as a function of SDS content when ELE concentration was fixed at 3 wt %. Indeed, addition of SDS in the smallest amount (0.05 wt %) was sufficient to reduce particle diameter from 380 to 290 nm, while further additions had a lesser but still relevant effect, with the minimum diameter of 188 nm being reached at the highest SDS concentration, 2 wt %. A logarithmic (R^2 = 0.98) dependence of the diameter on SDS concentration was identified, accordingly with what already observed in literature for polymer latexes resulting from emulsion polymerizations.[138–140] It is well known that surfactant molecules arrange themselves at the interface between the organic phase and the aqueous phase, therefore in an emulsion the greater the quantity of surfactant, the smaller the droplets of the organic phase dispersed in water, since the molecules are then able to stabilize a higher surface area, resulting in our case in smaller PLA particles after solvent removal. However, the stabilized droplet surface area reaches a maximum value above which a further increase of surfactant concentration does not affect the particle size but the exceeding surfactant molecules are dispersed in water,[139] thus explaining the logarithmic trend observed in Figure 2.3a. Increased ELE concentration also had the effect of reducing particle size as shown in Figure 2.3b. We noticed that when SDS content was

fixed at 0.05 wt %, the dependence of particle size on ELE content was near-linear (R^2 = 0.92), with higher ELE content resulting in smaller particle size. A linear dependence was also possible when no SDS was used, but the correlation was less clear in this case, probably due to the multimodal and quite polydisperse nature of large particles making such a trend harder to detect for low surfactant content. Indeed, DLS polydispersity index (PDI) was generally observed to increase along with particle size. When Z-average diameter was above 350 nm PDI was > 0.25 and the size distribution by intensity analysis was multimodal, on the other hand when it was below 350 nm, PDI was < 0.25 and the size distribution was monomodal, with a peak close to the Z-average value.

The particle size distribution also proved to be more reproducible when SDS was added. ELE2.4-SDS5 and ELE3.0-SDS5 formulations were replicated three times each and relative standard deviation of particle diameter across these preparations was small in both cases (5 and 7 %, respectively). ELE3.0 formulation without SDS, on the other hand, had a relative standard deviation (SD) of 11 % across three replications.

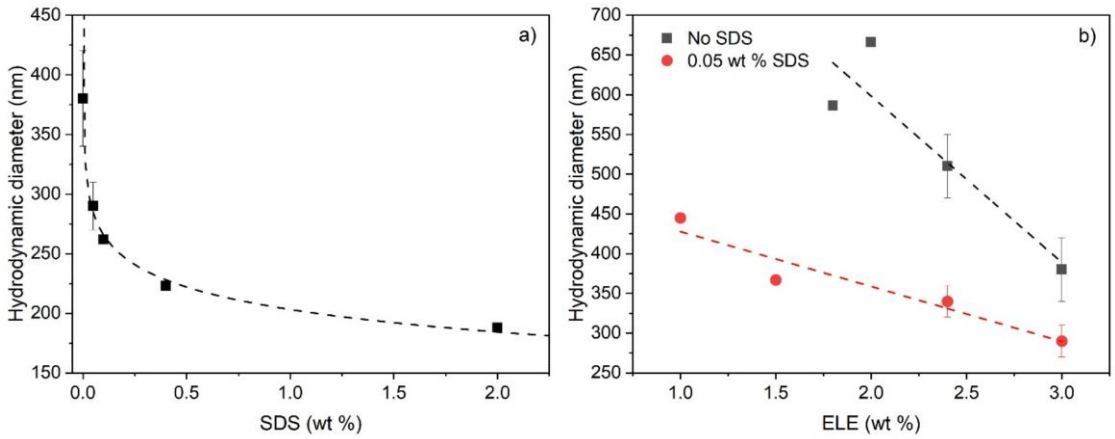

Figure 2.3 Hydrodynamic diameter (as measured by Z-average) of the particles in waterborne PLA dispersions versus: a) SDS content when ELE content was fixed at 3 wt %, b) ELE content when SDS was absent (black) or fixed at 0.05 wt % (red). Possible logarithmic (a) and linear (b) fit curves are also shown.

Qualitative observation of dispersion stability proved difficult when extended over a period of several months as buildup of precipitate can be very gradual. Thus, ultimately, stability over time was evaluated quantitatively by measuring solid content after 6 months and comparing it to the one of freshly prepared dispersions (Table 2.1). Figure 2.4 shows the dependence of dispersion stability on the content of the two surfactants. The trends observed for stability were quite similar to the ones previously laid out for particle size, supporting the correlation between these two properties. Addition of SDS even in small quantities had a dramatic effect on stability: the residual solid content increasing from 67 to

93% between ELE3.0 and ELE3.0-SDS10. On the other hand, the addition of SDS beyond 0.1 wt % did not cause a further increase in stability, as a decrease of ~5% in solid was noticed even when high quantities of SDS (up to 2 wt %) were added. When SDS content was fixed at 0.05 wt % and ELE content was varied from 1 to 3 wt % we, once again, noticed an almost linear (R^2 = 0.94) increase in dispersion stability with a trend that is similar to the one observed for particle size (Figure 2.4).

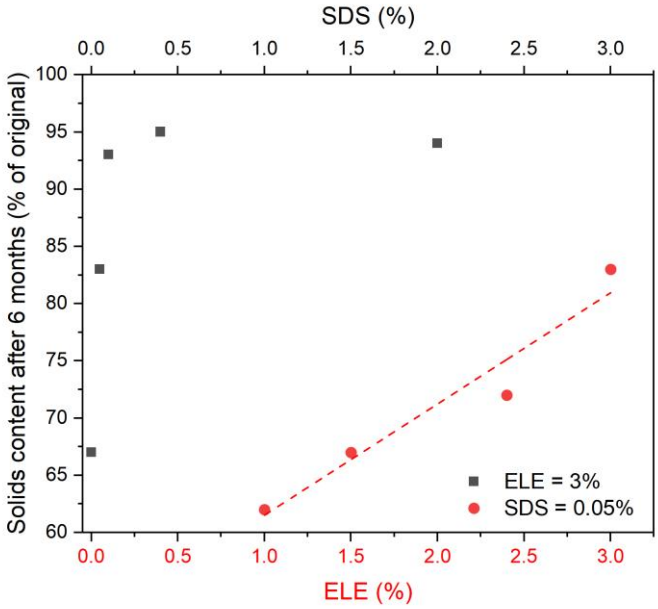

Figure 2.4 Stability of prepared PLA waterborne dispersions as evaluated by the percentage ratio of solid content after 6 months to the original solid value versus the surfactant content. Values shown in black are for an ELE content fixed at 3 wt % and SDS content varying in the 0-2 wt % range while values shown in red have an SDS content fixed at 0.05 wt % and an ELE content varying in the 1-3 wt % range. A possible linear fit is also shown for the latter.

Apart from the stability of PLA dispersions, the hydrolytic stability of the polymer itself in the aqueous dispersion is also a potential concern, as the backbone ester groups are vulnerable to hydrolysis, causing a reduction in molecular weight and thus potentially negative effects on the properties of the final polymer coating.[141] We monitored the molecular weight of ELE3.0-SDS5 for up to 10 months during storage at 4°C. SEC analysis of the dispersions shows two main peaks, the first due to the high molecular weight PLA (HMW) and a second at lower molecular weight due to both the ELE surfactant and hydrolyzed shorter PLA chains (LMW) (Figure 2.5a). In order to follow the degradation of PLA the area decrease of the HMW contribution above 28 kDa was monitored (Figure 2.5a). Indeed, as the degradation goes on the polymer molecular weight decreases and the chains are eluted at higher retention time. As results, the HMW area (A_{HMW}) decreases and the

LMW one (A_{LMW}) increases. The reduction over time of the normalized HMW areas was thus assumed as hydrolysis index (HI):

$$HI = \frac{A_{HMW,t}/(A_{HMW,t}+A_{LMW,t})}{A_{HMW,0}/(A_{HMW,0}+A_{LMW,0})} \qquad (4)$$

Where $A_{HMW,0}$ and $A_{LMW,0}$ are the areas of the SEC peaks above and below 28 kDa, respectively, in the chromatogram of a freshly prepared dispersion. $A_{HMW,t}$ and $A_{LMW,t}$ are the same area in the chromatogram of a dispersion stored for t time. As this value is defined, it is equal to 1 at the beginning of storage and tends to 0 over time as the quantity of HMW polymer decreases; HI=0 being a completely degraded PLA with no HMW fraction present.

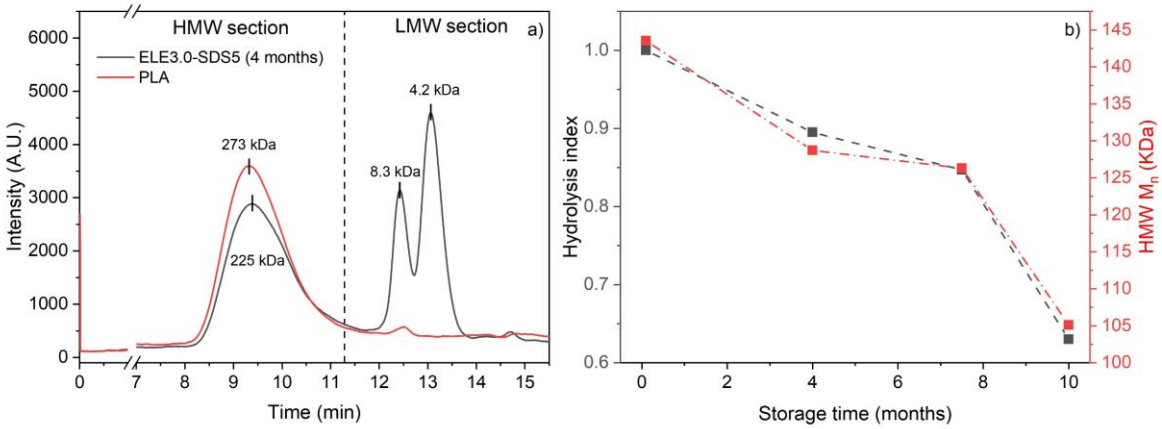

Figure 2.5 Left: SEC chromatograms (RI detector, chloroform eluent) of commercial PLA 4060D (red) and dried ELE3.0-SDS5 waterborne PLA dispersion after 4 months of storage at 4 °C (black). Peak molecular weight values shown; Right: hydrolysis index (in black) and $\overline{M_n}$ (in red) in the HMW-section of ELE 3.0-SDS5 as a function of storage time at 4°C.

Figure 2.5b shows the evolution of HI over time and compares it to the $\overline{M_n}$ calculated within the HMW section after the same storage time. As the two values change in similar ways, this supports the assumption that the molecular weight lost within the HMW area is transferred to the LMW area through PLA hydrolysis. PLA hydrolysis develops linearly and slowly for the first 7.5 months with the loss of ~2% of the HMW mass for each month in storage. Hydrolysis rate then strongly increases after this period with a loss of 18% of HMW mass within the next 2.5 months. This acceleration is attributed to the autocatalytic effect of carboxylic acid groups that form upon hydrolysis.[132]

Storage for up to a 7-month period of the dispersions should limit polymer degradation within parameters acceptable for most applications, but storage over a longer period is unadvisable due to the acceleration of hydrolysis. A typical validity period of many commercial polymer emulsions is 6 months; therefore, the observed stability is compatible with actual industrial practices.

Observing the SEC chromatograms, we also found that apart from the ELE peak, an additional well-defined peak was present at 4.2 kDa after 4 months of storage (Figure 2.5a). The most likely attribution for this peak is the splitting of the ELE surfactants in two portions; indeed, it may be noticed that its molecular weight is approximately half the one of ELE, and very similar to the one of the EL diblock prepolymer obtained before the isocyanate-promoted coupling (Scheme 2.1). The ester groups of ELE are more likely to have been hydrolyzed as compared to the more stable urethane bonds. The surfactant is in more intimate contact with the aqueous phase compared with the PLA itself and this should expose more the short PLA section of ELE to hydrolysis compared to the homopolymer chains. The hydrolysis of both PLA and ELE results in the formation of carboxylic groups, which was confirmed by pH measurements. Freshly prepared dispersions have a pH around 4, the acidity being probably attributable to carboxyl end groups of PLA; assuming each PLA chain contains a carboxyl group the concentration of these groups would be around 1 mM which would result in a pH of 3.5 assuming the pK_A of lactic acid and complete availability for proton exchange. After 6 months of storage the pH of the dispersions was around 3, thus being increased by surfactant and polymer hydrolysis.

Measurements of the Z-potential (ξ) of PLA dispersions may also help to better elucidate their structures and understand their stability over time. Freshly prepared dispersions had negative ξ in the -46 to -72 mV range (Table 2.1), with most of the samples having ξ values below -60 mV. This range of values is typical of stable colloids.[142] No clear relationship could be found between ξ values and the type and quantity of additives. For comparison, Abdenour and colleagues[125] also obtained negatively charged stable PLA dispersions with a ξ value of -39 mV using commercial non-ionic surfactants. While they attributed this property to the capability of non-ionic surfactants to selectively absorb OH^- ions from water, we consider the negatively charged character of the particles to be instead primarily attributable to the carboxyl end-groups of the PLA chains, which may be more or less exposed on the particle surface depending on surfactant and dispersion preparation. Interestingly, testing after 6 months of storage showed a significant increase in ξ for all samples, ranging from a 20 to a 50 % decrease in absolute value. This is most likely tied to the decrease in pH over time as previously described, which would in general cause an increase in ξ values, as well as to gradual particle aggregation. The decrease in absolute value of ξ to a range typical of moderate rather than good colloid stability may be a cause of the limitation in long-term stability of dispersions previously described. However, it cannot fully explain it, as samples with high stability with regards to suspended solid (95% solid retained after 6 months) still had similar ξ values to the ones with lower stability.

Properties of films obtained from waterborne PLA dispersions

The minimum film forming temperature (MFFT) of a waterborne formulation is one of its most important properties; above this temperature the coating is continuous due to particle coalescence, while below it a heavily cracked and discontinuous surface is formed, and particles generally remain separated from each other. MFFT is closely related to the glass transition temperature (T_g) of the waterborne polymer, but this relationship is not a simple one as, depending on the polymer/surfactant system and other additives; MFFT may have values either lower or greater than the T_g of the dried polymer. It is however generally accepted that plasticization of the waterborne polymer will lower MFFT along with T_g.[143–145]

PLA waterborne formulations were in general capable of forming a semi-transparent (74-86% transmittance at 600 nm) and continuous film when heated to 60 °C (Table 2.1, transmittance data reported in Table 2.S2, sample film in Figure 2.S3), slightly above the glass transition temperature of pristine PLA (54 °C). The only exceptions happened when SDS was added in the largest concentrations: 0.4 wt % SDS led to an opaque but still continuous film, while the dispersion containing 2 wt % SDS was unable to satisfactorily form a film due to macroscopic effects of polymer-surfactant immiscibility that leads to a discontinuous surface. Films cast from ELE3.0-SDS5 at various temperatures were observed by SEM to better discern the influence of temperature on film formation (Figure 2.6). Drying the dispersion at room temperature (23 °C) resulted in a heavily cracked and opaque surface. However, from SEM imagery we observed, not the single particles from the dispersion but still a heavily irregular and discontinuous surface (Figure 2.6a). This suggests that some particle coalescence still happened at room temperature, creating local continuous domains (< 10 μm wide) but that only a subset of dispersed particles was able to fuse with its neighbors, resulting in the overall discontinuity. Increasing the casting temperature, we observed that the surface became composed by two different kinds of large (> 100 μm wide) domains (Figure 2.6b-e), on the one hand some distinguished by a continuous homogenous surface, on the other hand by an irregular one, similar to that observed when dried at room temperature. The ratio of continuous film domains to the overall surface increased with temperature.

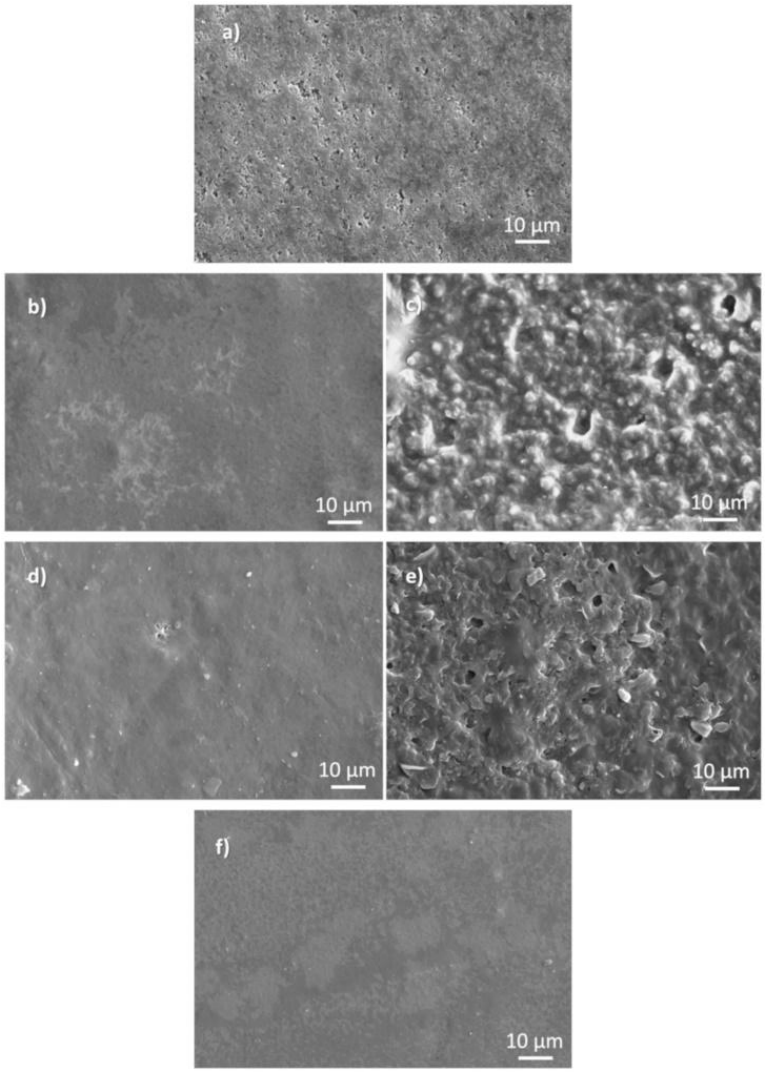

Figure 2.6 SEM images (3000x magnification) of PLA films cast from ELE3.0-SDS5 at: 23 °C (a), 45 °C (b and c), 47 °C (d and e), 60 °C (f). Side-by-side images display different regions of the same film displaying different morphology, continuous on the left and discontinuous on the right.

Macroscopically, we observed that at 47 °C the cast dispersion was mostly transparent, while at 45 °C it was opaque. This corresponded with a marked increase in the film to surface ratio observed by SEM. At 60 °C the entire surface of the dried dispersion was composed of a continuous film, with no particle or particle separation visible (Figure 2.6f). For some selected formulations (see Table 1), we thus carried out qualitative determination of film forming by drying dispersions at 1 °C intervals to find the temperature at which the surface became transparent, defined as MFFT (Figure 2.S4).

This qualitative observation is indeed the most common technique to determine MFFT.[146] The obtained values (Table 1) ranged from 38 to 49 °C, below the T_g of pristine PLA (54 °C) but above room temperature. ELE3.0 had a MFFT of 38 °C, which increased to 46 °C when 0.05 wt % SDS was added, but no further increase in MFFT was noticed as SDS content

was further increased. This seems to indicate that the presence of the anionic surfactant causes an increase in MFFT, but this is not then dependent on SDS concentration within the tested range.

The attempt to analyze the T_gs of dried polymer films and relate this to MFFT was complicated by the presence of surfactant melting peaks within the DSC thermograms (Figure 2.S5). The existence of non-miscible surfactant domains in films and coatings obtained from waterborne polymers is rather common and may cause diminished adhesion and water resistance properties as such hydrophilic domains migrate to the film surface.[147–149] In our case, we identified the frequent appearance of a peak around 50 °C in DSC thermograms with the presence within the sample of crystallized ELE domains, as the melting peak of the pure block copolymer was observed at 51 °C (Figure 2.S5). The presence of this peak influenced the nearby T_g transition by shifting the inflection point of the transition, thus making apparent T_g values higher (sample thermograms with and without this peak within a single film are shown in Figure 2.S5). It also made these values unreliable, as different regions of the films displayed different apparent T_g values with variations reaching over 10 °C within the same film, thus making comparison between formulations hard to do. It is however worth noting that even the apparent T_g values (reported in Table 2.S3), which ranged from 20 to 40 °C, were always lower than the one of pristine PLA, meaning that the ELE surfactant was effective as plasticizer of the polymer, and they were also lower than the observed MFFT value of the corresponding formulation. In particular, the addition of 3 wt % ELE and SDS below 0.1 wt %, which corresponds to a 20 % surfactant/polymer weight ratio, resulted in a T_g of 23-27 °C when the surfactant melting peak did not interfere with the measurement. This is in accordance with our previous research, which showed rather similar apparent T_g values when a PEG-PPG-PEG copolymer was used as surfactants, while the T_g of the SDS-based formulation was unchanged from pristine PLA.[88] PEG oligomers alone are good plasticizers for PLA. A 10 wt % PEG content has been shown to reduce the T_g of PLA to 30 °C and the same is also true for PLA-PEG-PLA triblock copolymers, which have been reported in literature and have been shown to have a similar effect when added in a 20 wt % ratio to the polymer.[130]

High-solid PLA dispersions

The solid content of the dispersions directly obtained by the oil-in-water technique was lower than 20 wt %. Attempts to increase this value by either increasing the ratio of organic to aqueous phase during preparation or the concentration of PLA in the organic phase run into physical limitations or issues of excessive solvent use.[88] Thus, the most accessible way to increase solid content is to remove water from the prepared dispersions until the desired

content is reached. Indeed, water evaporation already happens to a limited degree concurrently with the one of the organic solvent during the initial dispersion preparation, leading to solid content slightly higher compared to the theoretical value. This process can be accelerated by removing water under moderate reduced pressure.

The quantity of surfactant used proved to be decisive in determining how far the concentration process may be taken forward until macroscopic particle coalescence takes place. ELE1.5-SDS5 became unstable when dispersion volume was reduced to 60 % of the original (~ 25 % solid), while ELE3.0-SDS5 only became unstable at 33 % of the original volume (~ 50 % solid). When solid content was fixed at 40 ± 5 wt %, this latter formulation was found to be dimensionally unchanged when analyzed by DLS (diameter was 290 ± 10 nm across 3 replicates, the same as the original value). It was also stable by visual inspection for at least a month as no sedimentation or creaming occurred. Quantitatively, solid content of a concentrated ELE3.0-SDS5 sample that originally was 40 wt % after 6 months was found to still be 33 wt %, that is 83% of the original. Stability properties were thus only slightly worse than the ones of the unconcentrated corresponding sample. This formulation was next adopted as the model high-solid dispersion for coating studies.

Viscosity of PLA dispersions

Viscosity as a function of shear rate of ELE3.0-SDS5 PLA dispersions at low-solid (16.0 ± 3.0 wt %) (PLA15) and high-solid (40.0 ± 5.0 wt%) (PLA40) concentrations is reported in Figure 2.7. At low shear rates, PLA40 shows a viscosity plateau value two orders of magnitude greater than the one of PLA15, due to the greater number of particles per volume in the former sample that act as obstacles to flow. With increasing shear rate, both samples show a non-Newtonian shear thinning behavior well described by the Cross model (fitting of the various samples according to the Cross, equation (2.1), or power law, equation (2.2) models is described in the chapter annex and table 2.S4). The viscosity trend of PLA15, within error bars, is in good agreement with previous measurements on a similar sample (15.0 ± 0.1 wt %).[124]

Waterborne dispersions of polymers generally need the addition of a thickening agent to be coated on paper, as the pristine viscosity is usually very low, and particles permeates into the pores of the paper substrate instead of forming a layer on the top of the fiber network.

As thickener we chose xanthan gum (XG), a microbial polysaccharide that is widely used in a variety of industries, including as food additive. XG aqueous solutions have a pseudo-plastic behavior with high viscosity even at low concentrations and are quite stable to temperature and pH changes.[150] In our testing we primarily focused on the high-solid formulation, we previously obtained by concentration (40 ± 5 wt %) while varying XG

concentration in the aqueous phase from 0.2 to 0.8 wt/vol %. For comparison purposes we also tested a low-solid formulation (16 ± 3 wt %) with 0.4 wt/vol % of XG. This was because a high solid content avoids the thickener becoming an important component of the coating. For a 40 wt % solid content the addition of 0.2, 0.4 and 0.8 wt/vol % of XG in the aqueous phase results respectively in a 0.5, 1 and 2 wt % content of XG in the dry film, while in the low-solid alternative all these values are 2.5-fold larger.

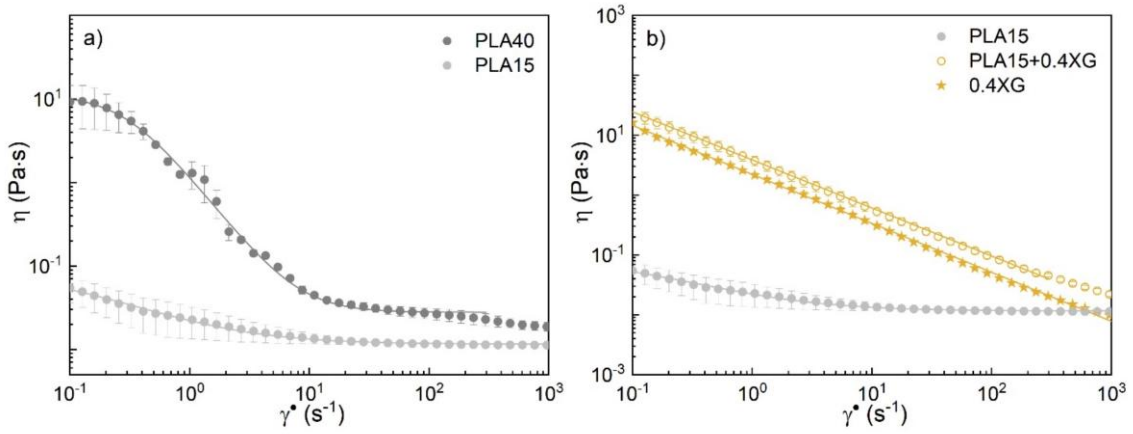

Figure 2.7 a) Viscosity of ELE3.0-SDS5 as a function of shear rate for low-solid (PLA15) and high-solid (PLA40) samples. Lines are fits through the Cross model. b) Viscosity as a function of shear rate for PLA15 with and without XG, and the reference XG solution at concentration 0.4 wt %. Lines are fits through the power law and Cross models (fitting parameters in Table 2.S4).

The viscosity behavior of XG alone was also evaluated while varying XG concentration from 0.2 to 0.8 wt/vol % in water (Figure 2.S6). At all concentrations, the solutions showed a shear thinning behavior without an evident low shear rate plateau. Viscosity increases with concentration as expected and data are well fitted through a power law equation (Table 2.S4). Figure 2.8 shows the comparison among the flow curves of the high-solid concentrated PLA sample (40.0 ± 5.0 wt %) with and without XG and the reference XG solution at three different weight concentrations of XG 0.2, 0.4 and 0.8 wt/vol %.

All curves show a shear thinning behavior and indicate that the addition of XG to the PLA dispersion hinders the formation of a Newtonian plateau at low shear rates. The viscosity of the samples increases by an order of magnitude compared to both the high-solid PLA without XG and to the XG solution. For comparison, in Figure 2.7b we report the viscosity of the low-solid formulation at 0.4 wt/vol % XG concentration as an example. In this case, the addition of XG modifies the shape of the curve as well. However, in contrast to the case of the high-solid sample, the viscosity of the low-solid one with 0.4 wt/vol % XG appears very similar to that of the XG reference solution, indicating that at low PLA concentration,

XG is the main significant component that affects rheological behavior, while at high solid-content both the PLA and the XG components have a contribution. This demonstrates that we are able to obtain the desired rheological behavior and thus optimize the coating formulation by both the addition of a small amount of XG and by changing the solid content in the waterborne PLA dispersion.

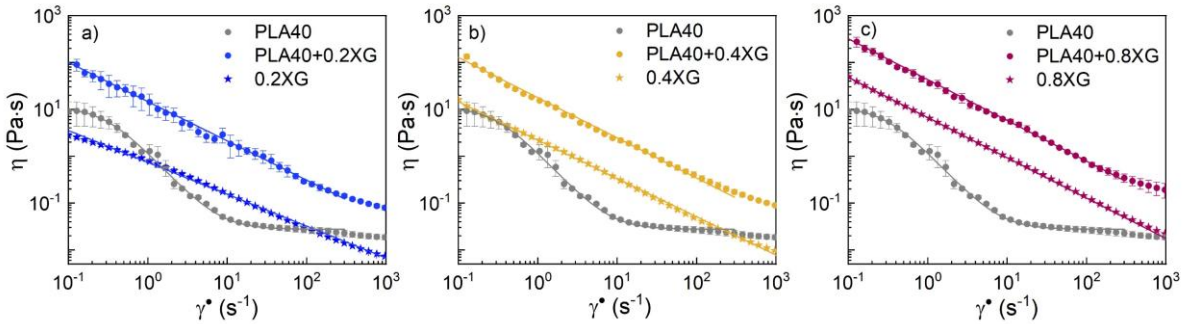

Figure 2.8 Viscosity as a function of shear rate for the high-solid sample (PLA40) with and without XG, and the reference XG solution, at XG concentrations (a) 0.2 wt/vol %, (b) 0.4 wt/vol % (c) 0.8 wt/vol %. Lines are fits through the power law and Cross models.

Application and properties of PLA paper coatings

The substrate used for testing was standard printing paper. This paper was coated using bars capable of applying two different nominal thicknesses of liquid layer, 4 and 15 μm (Table 2.S5). The coating was applied at 60 °C to work above MFFT. We anticipated from previous literature on the subject[118,123,125] that more than one application of the coating would be necessary to obtain satisfactory surface coverage and thus properties, so, for each formulation, a number of applications varying from 1 to 4 was tested (Table 2.S5). We also aimed to limit coating weight due to recyclability issues of the final product.

SEM micrographs in Figure 2.9 show surface views of paper sheets coated with successive applications of a 4 μm liquid film with PLA40 and 0.8 wt/vol % XG. By observing, the surface of the sample with a single application (6 g/m^2 of coating weight, Figure 2.9b) it is noticeable that the pulp fibers making up the paper sheet (Figure 2.9a) were not completely covered by the coating but were visible on the surface. On the other hand, when the film was applied twice (10 g/m^2 of coating weight, Figure 2.9c), the surface was completely covered by the coating and the fibers were not visible anymore. All other samples on which at least two layers of coating were applied, with any high-solid formulation, also displayed a continuous coated surface where the underlying cellulose fiber network was not visible.

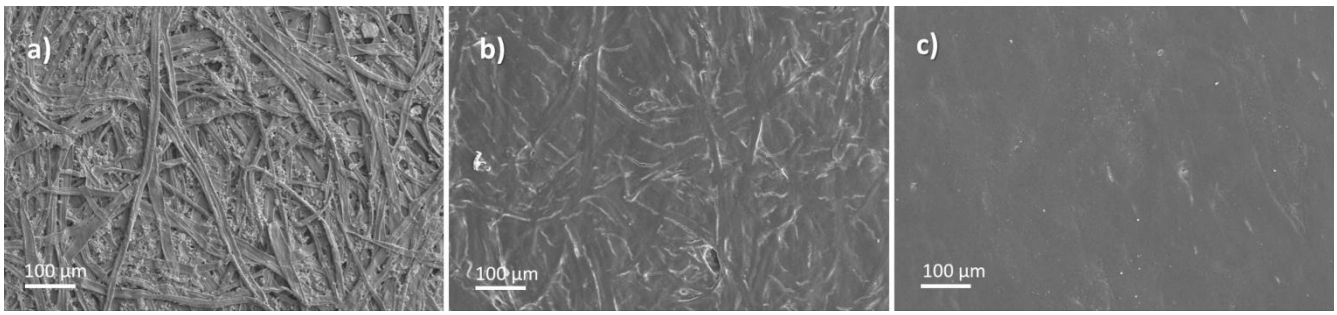

Figure 2.9 SEM pictures (400x magnification) of a: uncoated paper b-c: paper coated respectively with 1 and 2 applications of 4µm film of PLA40 with 0.8 wt/vol % XG content.

Figure 2.10 shows, in the first row, cross-section images of coatings produced with the same formulation with an increasing number of applied 4µm layers. With a single application (Figure 2.10b) the surface is smoother than pristine paper (Figure 2.10a), but the coating is not clearly visible as a separate element from the cellulose. With increasing applications of the same liquid film (Figure 2.10c, d and e corresponding to 10, 12 and 15 g/m^2 coating weight) a separate PLA coating layer becomes visible, and the images illustrate its increasing thickness and that its homogeneity is maintained with no visible separation within it being visible as successive layers are applied.

Further observations highlight the effect of different viscosities of the waterborne dispersion that was coated on the paper surface. Images f, g and h in Figure 2.10 show cross-section views of paper sheets coated with PLA40 containing 0.4 wt/vol % XG, respectively with 10, 15 and 21 g/m^2 coating weight. A PLA coating layer is still clearly visible and fully covers the paper surface, but it is harder to distinguish the separating line between this layer and the paper underneath. This suggests that a greater part of the dispersions enters paper pores rather than forming a surface layer. The effects of a further reduction in XG content to 0.2 wt/vol % are shown in images i and j in Figure 2.10 (respectively corresponding to 10 and 15 g/m^2 of coating weight). With 10 g/m^2 of coating weight, the PLA layer was not distinguishable as a separate element from the cellulose fibers, while at 15 g/m^2 the overlap between the cellulose fibers and the coating was even more evident than previous observation, with PLA being observed filling paper pores to a depth > 5 µm from the paper surface. Thus, a reduction in the viscosity (from 36 to 14 Pa·s at 1 s^{-1} shear rate, Table 2.S4) of the applied waterborne dispersion results in its deeper penetration within the paper and the formation of a thicker intermediate layer composed by paper with pores filled by the coating.

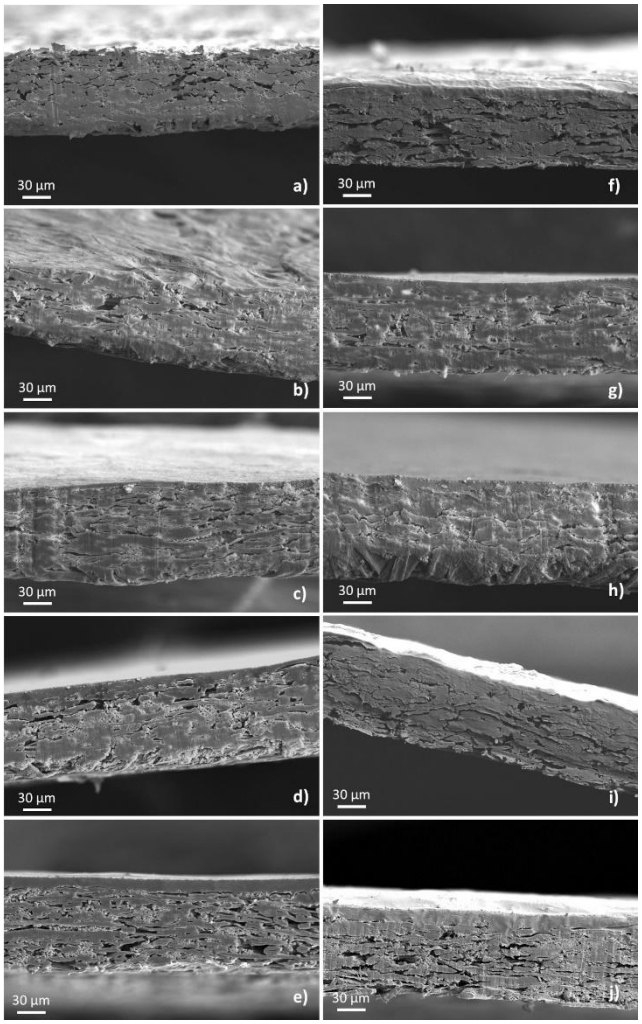

Figure 2.10 SEM images (1000x magnification) of the cross-section of paper samples. In the first row, uncoated paper (a) followed by paper coated with PLA40 with 0.8% XG in an increasing number of 4 µm applications from 1 to 4 (b-e). The coating weight of these samples is, in order, 6, 10, 12 and 15 g/cm^2. In the second row, paper coated with PLA40 under different conditions (XG content, applications and coating weight): (f) 0.4% XG, 2x4 µm, 10 g/m^2, (g) 0.4% XG, 3x4 µm, 15 g/m^2, (h) 0.4% XG, 3x15 µm, 21 g/m^2, (i) 0.2% XG, 2x4 µm, 10 g/m^2, 0.4% XG, 4x4 µm, 18 g/m^2.

Another observation is that the surfaces of coated paper samples made with 0.2 wt/vol % XG were significantly more irregular than the ones made with higher XG amount (Figure 2.11). This can be due to lower flattening ability of the formulation having low viscosity, which does not form a compact layer on top of the fiber network but rather cover the single fibers.

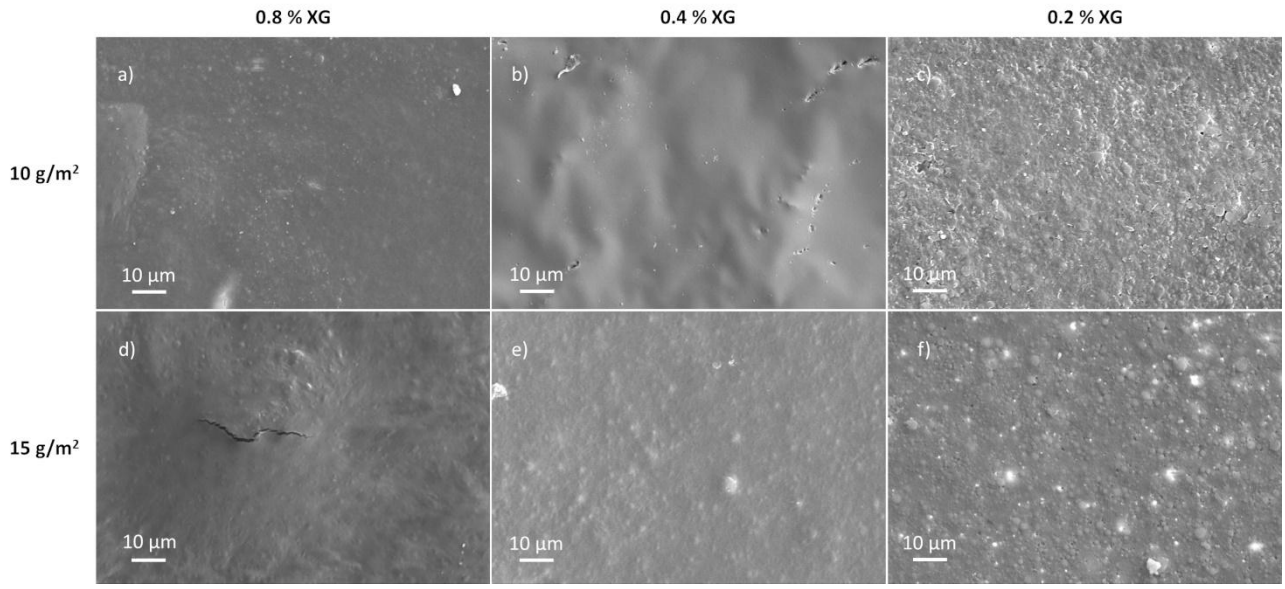

Figure 2.11 SEM images (3000x magnification) of coated paper using PLA40 formulation with different contents of XG (0.2, 0.4 or 0.8 wt/vol %) and at two different coating weights, 10 and 15 g/cm^2.

The partial penetration of the polymeric coating within the fibers of the paper we observed, which is promoted by the use of waterborne technology, should improve adhesion to the substrate compared to extrusion coating, in particular in the case of thin film layers.[151,152] Indeed, we achieved a good adhesion to the substrate with all tested formulations and under all application conditions: the PLA coating could not be removed in any way by mechanical means. When a scotch tape cross-cut peel test was tried, this resulted in either no detachment or in the removal of a significant amount of paper fibers in the cross-cut area rather than the coating itself, thus indicating that the adhesion energy of the coating to the paper substrate was higher than the internal cohesion energy between the paper fibers.[153,154]

The water resistance of paper coated under the different conditions was studied by Cobb60 tests and the results showed (Figure 2.12, Table 2.S5) that the application of a single layer was ineffective in conferring water resistance with any formulation with which it was tested. This result agrees with SEM observation that showed no full coverage in these cases. The coating resulting by the first application acted as a primer that did not reduce water absorptiveness compared to pristine paper but rather smoothed out the surface to allow for more effective coating layers in further applications. In Figure 2.12a we highlight the results obtained using only the high solid formulation (PLA40) with multiple applications, divided into 3 groups depending on the XG content present. Coating weight increased, as expected, both with the number of applications and liquid layer thickness deposited and had values

ranging from 9 to 21 g/m^2. Water absorption across these tests was always reduced compared to the one of pristine paper (100 ± 10 g/m^2) but varied strongly, from 50 to 2 g/m^2.

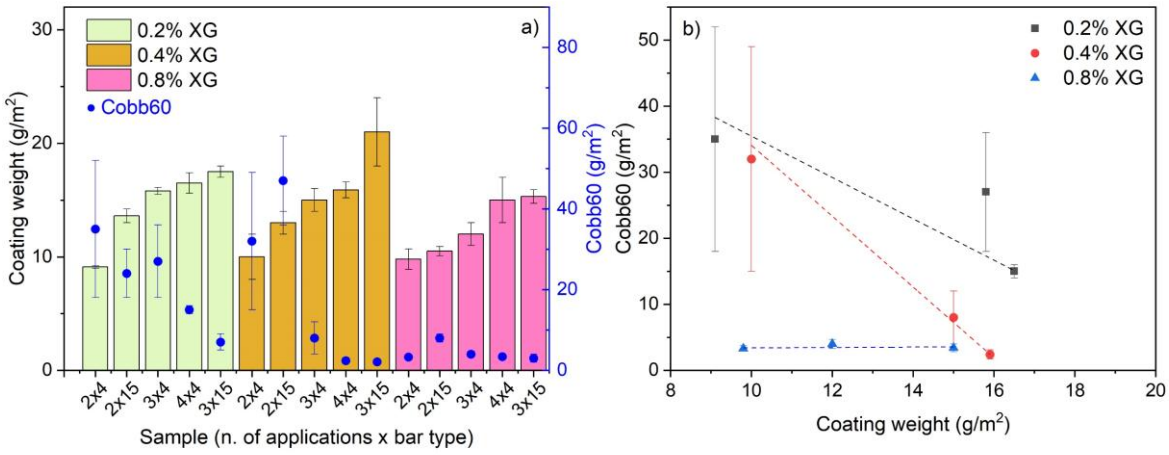

Figure 2.12 a) Coating weight and Cobb60 index of PLA-coated paper obtained with PLA40 formulation (solid content 40 ± 5%). Each column describes a coating obtained by multiple (2 to 4) applications of liquid film using a 4 or 15 µm bar. Different colors indicate different XG concentrations. b) Cobb60 index as a function of coating weight by 2 to 4 applications of liquid film using a 4µm bar, linear fits are shown as dashed lines.

XG content was crucial in maximizing water absorption as a function of coating weight on the surface: to obtain a Cobb60 value under 10 g/m^2, a coating weight of 18 g/m^2 with 0.2 wt/vol % XG, of 15 g/m^2 with 0.4 wt/vol % XG, and of 10 g/m^2 with 0.8 wt/vol % XG were needed (Figure 2.12a). The effect is highlighted in Figure 2.12b that shows Cobb60 as a function of coating weight for samples obtained using the 4 µm bar. Similar and very low Cobb60 values of 3-4 g/m^2 were obtained with 0.8 wt/vol % XG thickened dispersion irrespective of the coating thickness. On the other hand, using 0.4 wt/vol % XG resulted in a constant decrease in Cobb60 as coating weight increased, eventually reaching values similar to the ones obtained with 0.8 wt/vol % XG. Using 0.2 wt/vol % XG led to a similar trend to 0.4 wt/vol % XG but with higher Cobb60 values.

We hypothesize that coating weight as regards water absorptiveness may be divided in two fractions: a) effective fraction, due to the polymer in the film layer located on the top of the pulp fibers network; b) ineffective fraction, attributable to polymer chains that are into the pores of the fiber network. This latter portion is not continuous, and thus it is poorly effective in conferring barrier properties against liquid water. Low viscosity values of the dispersion result in an easier penetration into the pore and increase the ineffective coating fraction in proportion to the total coating weight. Thus, the greater viscosity obtained with greater thickener concentration (Table 2.S4) is crucial to maximizing water resistance per weight of coating applied on paper. When a certain effective coating weight is obtained, as seems to

already be the case for 0.8 wt/vol % XG from 10 g/m^2 on, water absorption is minimized and little reduction in Cobb60 takes place with further increases in coating weight.

When dispersions with low solid content (PLA15; solid content = 16 ± 3%) were used, water absorptiveness values below 10 g/m^2 could not be obtained. A Cobb60 of 14 g/m^2 was reached at 15 g/m^2 of coating weight. Notice that 8 g/m^2 absorptiveness was instead obtained at the same coating weight with the high-solid dispersion with 0.4 wt/vol % XG. This may be attributed to the lower viscosity (3.7 vs 15.5 Pa·s at 1 s^{-1} shear rate, Table 2.S4) of the low-solid dispersion and to the higher content (2.5-fold) of hydrophilic XG.

Water absorption values have been previously reported for PLA coatings on paper obtained using various techniques. Two papers report the values of classically solvent-borne semi-crystalline PLA coating: one used the Cobb120 index and reported values ranging from 12 to 0.2 g/m^2 for coating weights in the 3-90 g/m^2 range,[110] while the other used the Cobb30 index and reported values of 9 to 3 g/m^2 for coating weights in the 6-9 g/m^2 range;[111] in both cases water absorption constantly decreased with increasing coating weight. Electrosprayed solvent-borne semicrystalline coatings in the 3-8 g/m^2 range have been reported to have a Cobb120 index of 2 g/m^2, in this case not changing with coating weight.[155] The coatings we obtained differ from these experiments, not only in coating technique, but also for the presence of various additives (surfactants and thickener) and for the amorphous nature of the PLA used. Despite this, the values of 2-3 g/m^2 we obtained at 10-15 g/m^2 coating weight in the best formulations are quite similar to those observed by the various authors. Indeed, a study on the effect of the addition of PEG as plasticizer in PLA coatings found that it did not change water absorption up to 10 % weight content and then had a moderate hydrophilic effect with increasing content.[156] This finding is in agreement with our results. In fact, the hydrophilic components in the coatings are PEG and XG. The former is present in ~10 % by weight and the former in 0.5-2 % by weight and these combinations were found to not have a significant hydrophilic effect on the overall coating. Thus, the waterborne dispersion technique can substitute the use of harmful organic solvents successfully while achieving similar results. Compared to recently reported waterborne biodegradable coatings obtained with other polyesters, the water resistance performance of PLA coatings was superior to that of both PBS and PHBV, despite these polymers being used in much thicker layers (> 30 µm).[118,119]

Barrier properties against water vapor were also analyzed for coated paper by testing the WVTR of two selected samples both obtained with PLA40 and 0.8 wt/vol % XG. The samples have a coating weight of 10 and 15 g/m^2. These correspond to samples 2x4 and 4x4 illustrated in Figure 2.12a. These tests were carried out at 22 °C and 51 % relative humidity, aiming to emulate normal indoor conditions. The values of WVTR (Table 2.2) show that the PLA coating strongly reduces the WVTR of paper, by 60 % and 75 % when 10 and

15 g/m^2 coating weights are applied, respectively. This value may be normalized by thickness and water vapor pressure for easier comparison to other materials to obtain the water vapor permeability (WVP) of the coated paper which was reduced by 56 and 70 % respectively compared to pristine paper.

Table 2.2 Water vapor barrier properties of PLA40-coated and uncoated paper sheets, recorded at 22 °C and 51 % relative humidity.

Coating weight	**Thickness (µm)[1]**	**L_{PLA} (µm)[2]**	**WVTR (g/(m^2 × days))**	**WVP x 10^6 (g/(m×days×Pa))**	**WVP_{PLA} x 10^6 (g/(m×days×Pa))[3]**
Uncoated paper	98 ± 2	-	310 ± 20	22 ± 1	-
10 g/m^2	104 ± 3	5.1 ± 0.3	127 ± 2	9.7 ± 0.2	0.81 ± 0.07
15 g/m^2	110 ± 3	14 ± 1	83 ± 3	6.7 ± 0.3	1.2 ± 0.1

[1] Paper + coating as measured by micrometre [2] Measured on SEM images (Figure 2.S7) [3] $WVP_{PLA} = (WVP \cdot WVP_{paper} \cdot L_{PLA})/(WVP_{paper} \cdot L - WVP \cdot L_{paper})$

The coated paper could be considered a double-layer material made up of a paper layer and a PLA layer on top. The overall permeability of such material in this case may be obtained from the ones of the single layers by the following:

$$WVP = \frac{L}{\frac{L_{paper}}{WVP_{paper}} + \frac{L_{PLA}}{WVP_{PLA}}} \quad (5)$$

Where L_x is the thickness of the *x* layer and WVP_x is its WVP. As all other values were measured, this equation can be used to calculate the WVP of the PLA coating layer (WVP_{PLA}) which was found to be in the 0.8-1.2 10^6 g/(m×days×Pa) range (Table 2.2).

The WVP of PLA has been reported to be 1.4-1.6·10^{-6} g/(m·days·Pa) in similar humidity and temperature conditions to our tests[157]. The values of WVP_{PLA} obtained from the two samples were somewhat lower than this reference. This is probably because the actual structure of the multilayer material obtained by coating the paper using the waterborne technique is not simply a paper layer overlaid by a PLA one but includes a transitional layer of paper with pores filled by the polymer. Thus, the actual effective thickness of the PLA layer is probably higher than the one that may be directly measured by SEM and was used for calculation. This is confirmed by the WVP_{PLA} value of the 15 g/m^2 sample being higher and close to the theoretical one, as the transitional layer has comparatively less impact as the PLA layer

gets thicker. The PLA layer is also not composed of pure PLA, but it is a blend including two other main components, the ELE surfactant and the XG thickener. These components however are both hydrophilic, thus it would be surprising if they conferred the material higher water vapor barrier properties. Thus, the coated paper can overall be conceptualized as a two-layer paper-PLA material, with barrier properties to water vapor directly derived from the ones of the layers.

While a marked improvement in WVTR was achieved in comparison to pristine paper, due to the inherently mediocre water vapor barrier properties of PLA compared to fossil-based polymers (for example the commonly used LDPE has a WVP more than an order of magnitude lower than PLA)[158], the water vapor barrier properties of the coated paper are still inadequate for applications where a low WVTR is needed, and more appropriate for packaging where moderate water transmission is desired. This is in line with the results obtained by other researchers on paper coated with PLA.[110,125]

The surface energy of the PLA-coated paper was measured by the Dyne Test ink method and the values measured ranged between 42 and 56 dyne/cm (Table 2.S6). This range of surface energy values is higher than the one of neat PLA materials (38 dyne/cm), [159] a variation which is attributed to presence on the surface of surfactants more polar than PLA itself. As the coated paper thus has higher wettability by polar formulations, such as most inks and paints, compared to a pure PLA material, it is expected to be more easily printed on and dyed, as well as being somewhat less hydrophobic than paper coated with PLA by extrusion.[160] Indeed, the surface energy of our PLA coating is similar to the one of PLA modified for this purpose by plasma treatment.[161]

In order to determine the effect of PLA coating on the recyclability of the coated paper, we carried out preliminary repulpability tests. In one test, we observed the time it took for a paper sample, pre-soaked in cold water for 72 h, to be completely reduced to pulp by agitation at 40 °C. Pristine paper, as reference, was pulped in 1 hour. Three coated papers with 10, 12 and 15 g/m^2 of coating (PLA40, 0.8 wt/vol % XG, entries 2x4,3x4 and 4x4 in Figure 12a) were tested: the 10 g/m^2 sample was pulped in 5 hours while the others were both pulped overnight (between 8 and 18 hours). These preliminary tests thus indicate that even if slower, repulpability of the coated paper is possible. In another test, the rate of rejects (pieces of sample unable to pass through a sieve) to overall coated paper weight was measured after 2 hours of stirring at 40 °C. The reject rate for the same three samples after this time was respectively 15, 14 and 32 % in increasing order of coating weight. For comparison, Zhang and colleagues found a 21% reject rate for the repulpability of PLA-coated paper, thus in a similar range albeit using a somewhat different method.[162] Overall, this data confirms the importance of limiting coating weight in order to achieve easier recycling and indicates significantly better repulping for coating weights below 15 g/m^2.

The biodegradation in industrial composting conditions of films cast from waterborne dispersions was also studied to determine if the overall compostability of coated paper could be damaged by the addition of the coating. The results of these tests may be found in chapter 7, as a comparison with composite films and are not repeated here for brevity's sake. The film cast from the ELE3.0 formulation was found to be fully compostable at 58°C and the coated paper can thus be assumed to be compostable.

2.4 Conclusions

In the present work we have presented the use of PEG-PLA-PEG triblock copolymers (ELE) as surfactants to obtain waterborne PLA dispersions. To this aim, we exploited an oil-in-water ultrasonication methodology previously used with commercial surfactants. The dispersions obtained through this method using 2-3 % ELE had a particle size of 400 to 700 nm and solid content of 13-18 wt % . They were stable in the short term but displayed increasing phase separation beyond 2-8 weeks from preparation. The addition of SDS as co-surfactant in minor quantities (0.05-0.1 %) with similar solid content as previous proved effective in decreasing particle size below 300 nm and increasing long-term stability properties of the dispersions. In particular, dispersions with 3% ELE and 0.1% SDS were observed to retain more than 90% of dispersed solid after 6 months in storage. The hydrolytic stability of PLA in waterborne formulations stored at 4 °C was observed to proceed constantly but slowly by hydrolysis for the first 7.5 months in storage (loss of around 2% mass per month of high-molecular weight polymer), followed by an acceleration in hydrolytic degradation after this period. All formulations with an SDS content lower than 0.4 wt % could be cast into transparent films at 60 °C, displayed glass transition temperatures below 40 °C and minimum film formation temperatures in the 38-49 °C temperature range. Formulations with solid content above 40 wt % could be obtained by concentrating the original dispersions when at least 3 wt % ELE and 0.05 wt % SDS were used, with little change in particle size and dispersion stability. This is the first report in scientific literature of the preparation of such high solid content for PLA dispersions, it is similar to some industrial formulations but with significantly reduced particle size.

Dispersions using 3 wt % ELE and 0.05 wt % SDS as surfactants were thickened using XG reaching a viscosity of 14-15 Pa s (at shear rate of 1 s^{-1}) and 36 Pa s with 0.2-0.4 wt % and 0.8 wt % of XR, respectively. All formulation showed shear-thinning behavior and the viscosity plots could be well fitted by power-law or Cross models. Once applied as coating on paper, the most viscous formulation was found to be the most effective in reducing water

absorption even at low coating weight (~ 10 g/m ^{2}) thanks to the reduced capability to penetrate into the paper pores. In fact, the high viscosity reduces percolation and thus promotes the buildup of a layer on the top of the fiber network, as confirmed by SEM observation. Some penetration within the pores was, however, observed with all formulations, resulting in very good adhesion of the coating to the paper substrate, from which it could not be mechanically detached. Using 40 wt % PLA dispersion with 0.8 wt/vol % XG as thickener, a Cobb60 value of 3-4 g/m^2 was obtained at 10-15 g/m^2 coating weight, a >95% reduction from the original paper that is similar to the one that may be obtained using coatings cast from organic solvents. The water vapor transmission rate (WVTR) of paper was reduced by 75 % with 15 g/m^2 coating weight, corresponding to the reduction expected by the PLA layer based on literature data, thus indicating no or negligible effect of the additives (PEG blocks in ELE and XG). The surface energy of the coating was higher than the one of PLA itself (42-56 dyne/cm instead of 38) because of a greater presence of polar groups on the surface, probably caused by the surfactant additives. Such a surface is thus less hydrophobic but more easily dyable compared to PLA. Paper coated with 10-15 g/m^2 of PLA could be repulped even though it needed more time than pristine paper, furthermore the ease of repulpability decreased with the thickness of the PLA coating layer.

2.5 Supporting information

Fitting of viscosity plots

Fits reported in Fig. 2.7 and Fig. 2.8 were performed through two different models, the first is the Cross model:

$$\eta(\dot{\gamma}) = \eta_\infty + \frac{(\eta_0 - \eta_\infty)}{1+(\tau_c \dot{\gamma})^n} \qquad \text{(Equation 2.1)}$$

where η_0 and η_∞ are the zero-shear viscosity and the infinite shear viscosity approached at very low and very high shear rate, respectively; the parameter τ_c is a characteristic time of the system, and *n* is a power exponent. The second one is the Power law model:

$$\eta(\dot{\gamma}) = k\,\dot{\gamma}^{n-1} \qquad \text{(Equation 2.2)}$$

where k is the flow consistency index and *n* the dimensionless flow behaviour index . All the fit parameters are reported in Table 2.S4 for each investigated sample.

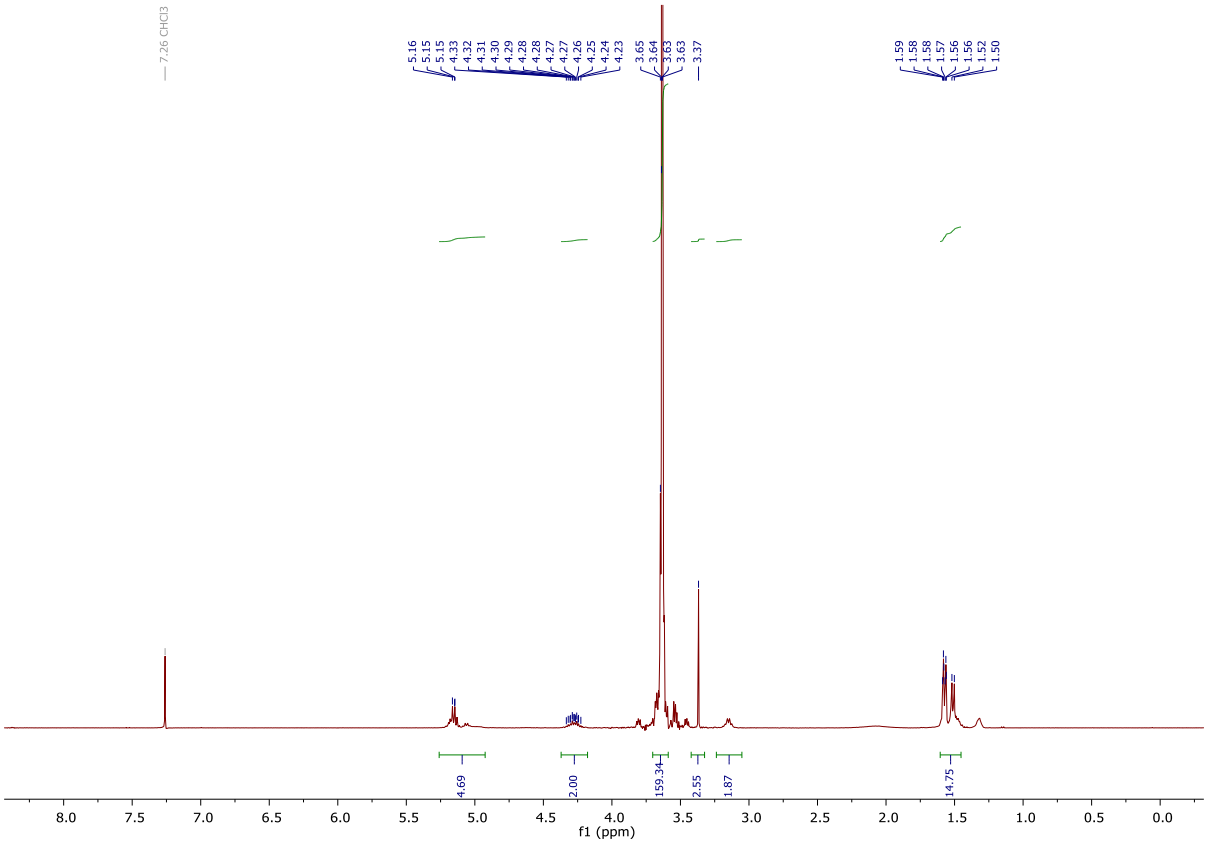

***Figure 2.S1**. [1]H NMR spectrum of ELE surfactant in $CDCl_3$*

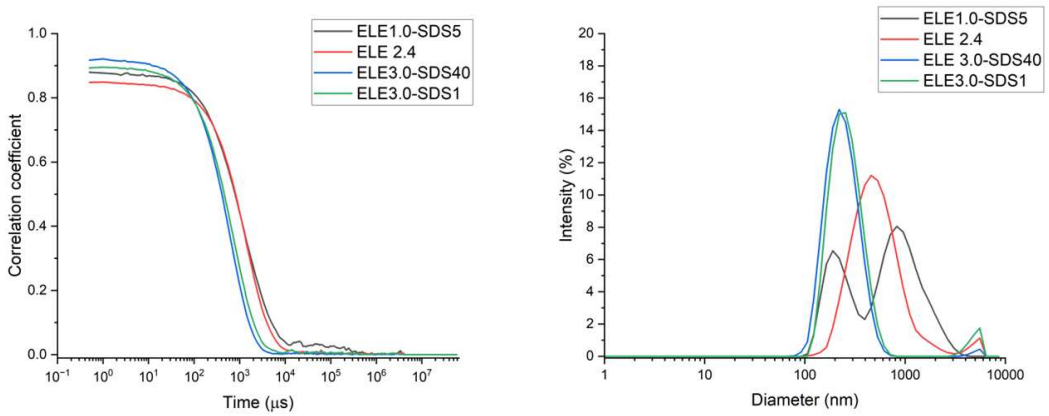

***Figure 2.S2**. Correlograms (left) and intensity-weighted size distributions (right) of a selection of 4 dispersions with different surfactant contents.*

Figure 2.S3. *Picture of a film cast from ELE3.0-SDS5 at 60°C.*

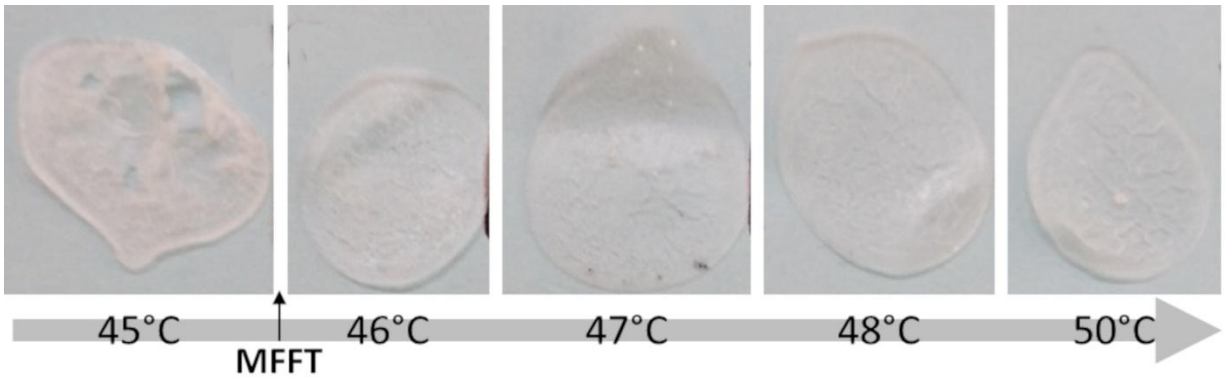

Figure 2.S4. *Pictures of film samples, detached from the aluminum plates, of the MFFT measurements of ELE3.0-SDS5.*

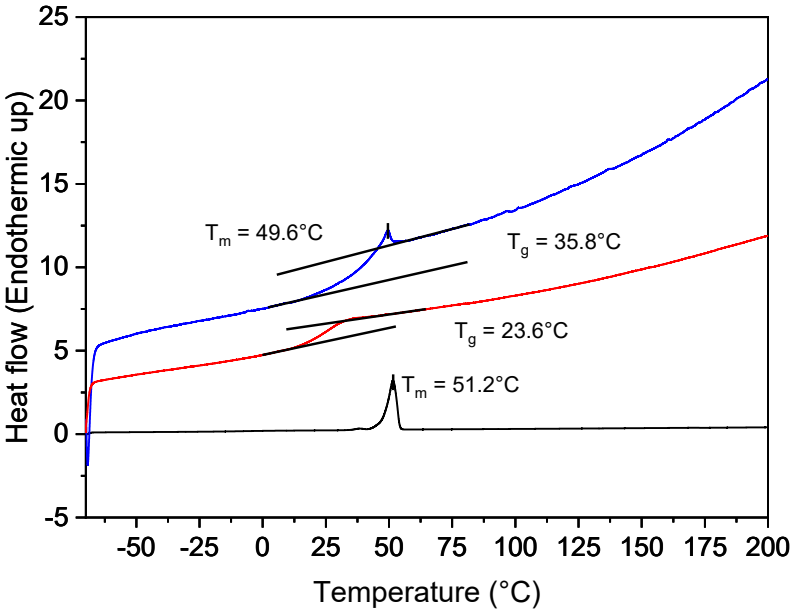

Figure 2.S5. *DSC thermograms of ELE surfactant (black) and PLA film cast at 60 °C from ELE3.0 dispersion, tested in two different regions of the same film (red and blue). Thermograms were shifted and normalized along the y-axis for display purposes.*

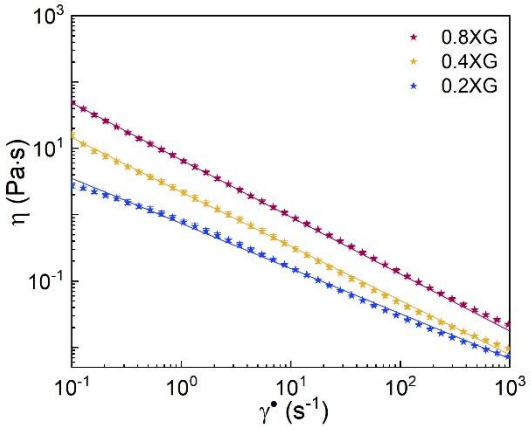

Figure 2.S6. *Viscosity as a function of shear rate for water solutions of xanthan gum (XG) at three different concentrations (wt/vol %), as indicated in the legend. Lines are fit through the Carreau-Yasuda model.*

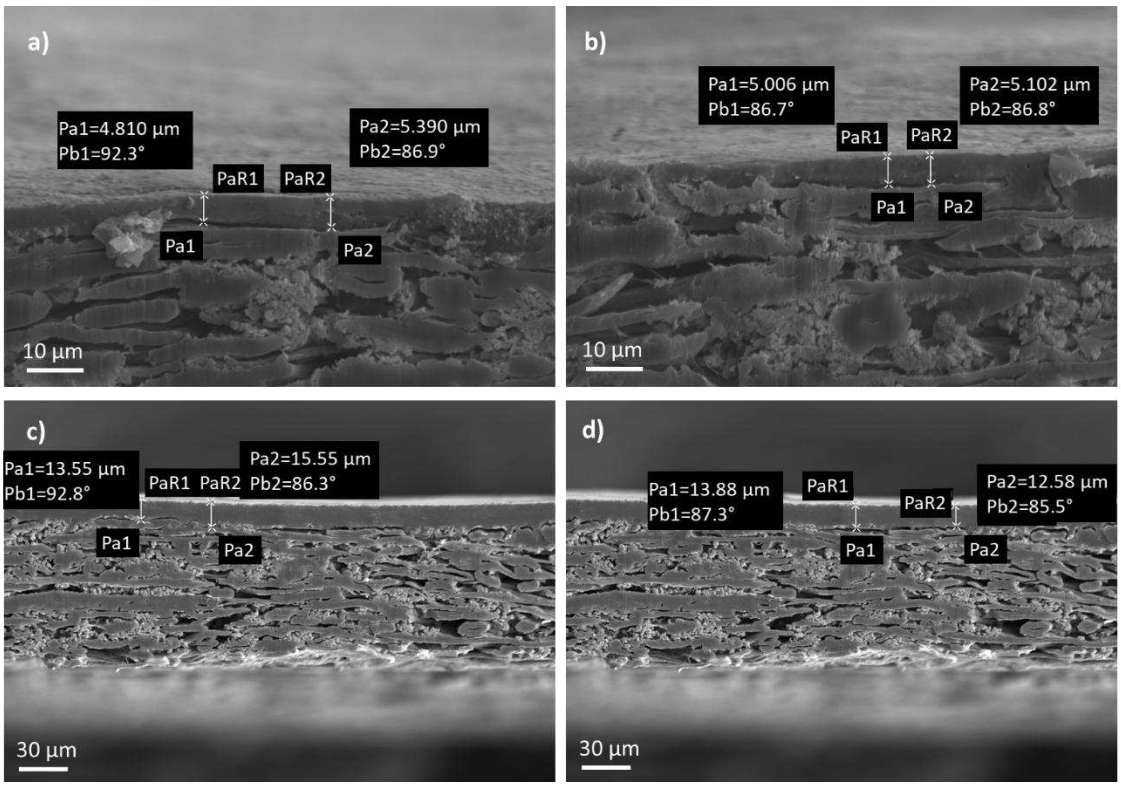

Figure 2.S7. *SEM images of the cross-section of coated paper samples showing the coating thickness measurements used to obtain the values of L_{PLA} reported in Table 2.*

Table 2.S1. *Intensity distribution and polydispersity by DLS analysis for PLA waterborne dispersions*

Sample	D_Z (nm)[1]	D_i (nm)[2]	PDI[3]
ELE1.8	590	-	0.526
ELE2.0	670	-	0.419
ELE2.4	510	-	0.339
ELE3.0	380	-	0.296
ELE3.0-SDS5	290	310	0.201
ELE2.4-SDS5	340	340	0.234
ELE1.5-SDS5	370	-	0.319
ELE1.0-SDS5	450	-	0.416
ELE3.0-SDS10	260	270	0.217
ELE3.0-SDS40	220	250	0.146
ELE3.0-SDS200	190	210	0.144

[1] Diameter by Z-average; [2] Diameter by average value of intensity distribution peak, left blank if multimodal; [3] Polydispersity index.

Table 2.S2. *Optical transmittance at 600 nm for films cast at 60 °C from PLA dispersions.*

Sample	Transmittance (%)
ELE3.0-SDS40	< 5
ELE3.0-SDS10	79
ELE3.0-SDS5	80
ELE3.0	74
ELE2.4-SDS5	86
ELE1.5-SDS5	86
ELE3.0 + 0.4% XG	32
ELE3.0-SDS5 + 0.4% XG	10

Table 2.S3. *Apparent glass transition temperatures by DSC analysis of films cast at 60 °C from waterborne PLA.*

Sample	ELE (wt %)[1]	SDS (wt %)[1]	Apparent T_g (°C)[2]
ELE2.4	2.4	0	23.4
ELE3.0	3	0	23.6
ELE3.0-SDS5	3	0.05	26.6
ELE2.4-SDS5	2.4	0.05	35.9
ELE1.5-SDS5	1.5	0.05	38.7
ELE1.0-SDS5	1.0	0.05	40.3
ELE3.0-SDS10	3	0.1	24.6
ELE3.0-SDS40	3	0.4	32.5

[1] Concentration in water phase; [2] When measurements were repeated on the same film, the lowest value is reported.

Table 2.S4. *Parameters from the Power law (eq. 2.1) and Cross (eq. 2.2) fits to the experimental viscosity plots of xanthan gum solutions (XG), ELE3.0-SDS5 as prepared (PLA15) and after concentration (PLA40) by water evaporation, and combination of these samples.*

Model	Sample	K (Pa s^n)	τ(s)	n	η_0 (Pa·s)	η_∞ (Pa·s)	η ($\dot{\gamma}$=1) (Pa·s)
Power law	XG 0.2	6.72±0.02		0.140±0.001			0.78±0.07
Power law	XG 0.4	2.21±0.02		0.180±0.005			2.15±0.21
Power law	XG 0.8	0.80±0.01		0.320±0.004			6.46±0.39
Power law	PLA40-XG0.2	43.3±0.5		0.13±0.01			14.33±6.90
Power law	PLA40-XG0.4	17.8±0.2		0.14±0.01			15.46±0.46
Power law	PLA40-XG0.8	14.7±0.2		0.16±0.01			36.09±3.61
Power law	PLA15-XG0.4	3.86±0.02		0.20±0.003			3.73±0.70
Cross	PLA40		3.35±0.05	1.83±0.05	11.30±0.10	0.03±0.02	1.29±0.46
Cross	PLA15		9.3±0.3	0.83±0.02	0.090±0.001	0.01±0.0002	0.02±0.01

Table 2.S5. *Sample list and water absorption properties of paper sheets coated with ELE3.0-SDS5 as prepared (PLA15) and after concentration (PLA40) both thickened with XG, applied at 60 °C using hand coaters.*

Entry	Application[1]	Dispersion[2]	XG (wt/vol %)	Coating weight (g/m^2)	Cobb60 (g/m^2)
1	1 x 4 µm	PLA40	0.2	5 ± 1	100 ± 10
2	2 x 4 µm	PLA40	0.2	9.1 ± 0.1	35 ± 17
3	3 x 4 µm	PLA40	0.2	15.8 ± 0.3	27 ± 9
4	4 x 4 µm	PLA40	0.2	16.5 ± 0.9	15 ± 1
5	2 x 15 µm	PLA40	0.2	13.6 ± 0.6	24 ± 6
6	3 x 15 µm	PLA40	0.2	17.5 ± 0.5	7 ± 2
7	1 x 4 µm	PLA15	0.4	4 ± 1	97 ± 5
8	2 x 4 µm	PLA15	0.4	7 ± 1	80 ± 20
9	3 x 4 µm	PLA15	0.4	9 ± 2	50 ± 10
10	4 x 4 µm	PLA15	0.4	13.6 ± 0.6	23 ± 4
11	2 x 15 µm	PLA15	0.4	9 ± 1	40 ± 1
12	3 x 15 µm	PLA15	0.4	13 ± 2	19 ± 5
13	4 x 15 µm	PLA15	0.4	15 ± 1	14 ± 4
14	2 x 4 µm	PLA40	0.4	10 ± 2	32 ± 17
15	3 x 4 µm	PLA40	0.4	15 ± 1	8 ± 4
16	4 x 4 µm	PLA40	0.4	15.9 ± 0.7	2.4 ± 0.7
17	2 x 15 µm	PLA40	0.4	13 ± 1	50 ± 10
18	3 x 15 µm	PLA40	0.4	21 ± 3	2.1 ± 0.4
19	2 x 4 µm	PLA40	0.8	9.8 ± 0.9	3.3 ± 0.4
20	3 x 4 µm	PLA40	0.8	12 ± 1	4.0 ± 0.7
21	4 x 4 µm	PLA40	0.8	15 ± 2	3.4 ± 0.3
22	2 x 15 µm	PLA40	0.8	10.5 ± 0.4	8 ± 1
23	3 x 15 µm	PLA40	0.8	15.3 ± 0.6	3 ± 1

[1] Number of applications x nominal wet film thickness of coating bar; [2] Solid content: PLA40 = 40 ± 5 wt %, PLA15 = 16 ± 3 wt %

Table 2.S6. *Surface energy (γ) as measured by Dyne testing of PLA-coated paper samples*

Application	XG (wt/vol %)	Coating weight (g/m^2)	Surface energy (γ, dyne/cm)
2 x 4 μm	0.2	9.1 ± 0.1	56
3 x 4 μm	0.2	15.8 ± 0.3	50
4 x 4 μm	0.2	16.5 ± 0.9	50 > γ > 40
2 x 4 μm	0.4	10 ± 2	54
3 x 4 μm	0.4	15 ± 1	50 > γ > 40
4 x 4 μm	0.4	15.9 ± 0.7	50 > γ > 40
2 x 4 μm	0.8	9.8 ± 0.9	50 > γ > 40
3 x 4 μm	0.8	12 ± 1	50
4 x 4 μm	0.8	15 ± 2	50 > γ > 40

3. Production of aquaculture socks from recycled poly(lactic acid) and study of their biodegradation properties

3.1 Introduction

Aquaculture is one of the fastest-growing food production sectors, especially in developing countries. It is a less resource-intensive protein-producing industry compared to land-based animal husbandry and if properly managed it can also mitigate the overexploitation of wild fish stocks.[163,164] However, current aquaculture technologies often involve the heavy usage of non-biodegradable plastics that may be dispersed as marine litter. In Italy, for example, aquaculture gear makes up around 5% of beach litter and this dramatically increases in beaches near production sites.[165]

Mussel farming is one of the major forms of aquaculture. Mussels can be produced by either bottom or off-bottom culture, which account respectively for 15% and 85% of production. Bottom culture dredges natural mussel beds and moves them to sheltered areas to grow and harvest. In 'off-bottom' culture mussel seeds are added to socks which are suspended in the water column by poles, rafts or ropes. The main method of off-bottom culture is longline farming, where the socks are suspended from anchored ropes (Figure 3.1).[166]

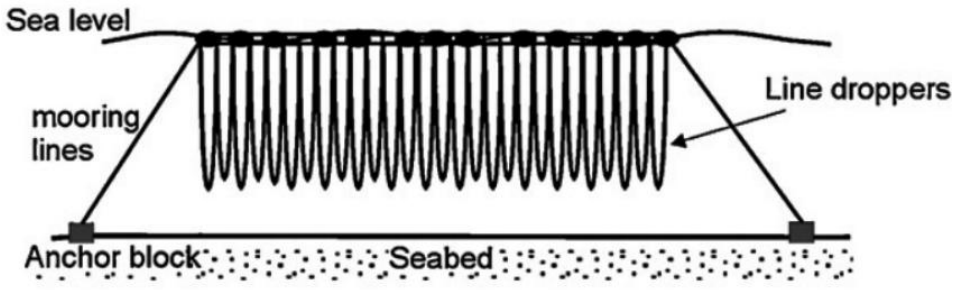

Figure 3.1 Diagram of a longline mussel farming setup, adapted from[167]

The traditional material for aquaculture socks until the 1970s were natural fibers manually knitted by mussel farmers, for example in the Mediterranean these were made from esparto

grass.[168,169] While this method is inherently sustainable, the superior mechanical properties and easy production of plastic netting made it so that natural fiber socks were quickly replaced worldwide by socks made of polypropylene (PP), a cheap, easily processable polymer that is generally very resistant to biodegradation.[170] Biodegradable plastic fibers offer the potential of being a material that can be processed into socks with an ease similar to that of traditional plastics but may be composted at the end of their service life and in the case of some materials may also degrade in the marine environment, if dispersed into it. For the purpose of mussel farming, however, the socks cannot undergo heavy degradation in seawater in the period of use, which for mussel farming is a cycle taking around 4 months,[170] and should degrade only after this period.

The switch to biodegradable materials for mussel farming socks is attracting research attention. Petrocelli et al. tested two different vegetable fibers, hemp and sisal, for the construction of mussel farming socks, finding that hemp was unsuitable due to its quick breakdown in seawater but that sisal was mechanically viable.[170] However, this manually-knitted nets are hard to scale for economical industrial production. Baini et al. characterized various bioplastics for the purpose of mussel farming.[169] The polymers they tested are produced by Novamont and are based on polycaprolactone (PCL) alone or combined with starch or other polyesters in various formulations. They found that these materials gave faster biodegradation on the seafloor rather than in the water column, making them potentially useful as they could serve the purpose of mussel farming without fast degradation but degrade faster if dispersed in the environment and sunk to the sea floor. However, they only tested this materials as dog-bone samples rather than in netting form. More extensive field testing in mussel farming using socks made of similar materials is also being carried out in Italy as part of an EU action, which claims their effectiveness in farming efficiency, but more detailed data is not yet available.[171] Biodegradable seed mussel collectors made from aliphatic polyesters have also been designed in the Netherlands for use in the locally important bottom culture production method.[172]

Bioplastics are also a promising solution in mussel farming because they may be processed using the same machinery already applied to the production of equipment, making industrialization simple. For example, Pavia et al. obtained starch-based aquaculture trays by the same injection molding process used for conventional ones made out of PP.[173]

Poly(lactic acid) (PLA) has seen relatively little study in the field of aquaculture, it has only been used in a few tests for the use in fishing nets,[72,73] but not for use in mussel farming socks. The biodegradation of PLA in seawater is very slow and is not expected to take place during the growth period of mussels, a few months.[33,34,174] On the one hand this means that socks that are lost in the sea would remain a ghost fishing danger for an extended period, on the other hand it also means that PLA itself would not degrade for its use period and

could be composted after being retrieved from the sea. Lost PLA socks might also sink to the bottom of the sea environment due to polymer density being greater than water. While biodegradation at the seawater-sediment interface has been studied for other polymers,[175,176] there is a lack of such data for PLA.

Despite being the lowest-cost and highest-production polymer among biodegradable polyesters, PLA is still significantly more expensive than PP or other conventional polymers used in the aquaculture industry. The use of recycled PLA is in general a potential way of further reducing its cost. Chemical and mechanical recycling are both viable strategies for PLA. Mechanical recycling in particular is well-developed for other thermoplastic polymers and uses well-known technologies such as extrusion and injection molding. For example, Dieterle et al. have estimated that the use of mechanically recycled PLA in cups can reduce their cost and environmental impact by 60%.[177] LCA assessments have actually shown that mechanical recycling is also from an environmental perspective a better end-of-life option than composting for biodegradable plastic objects.[178] However, high temperatures and shear stresses during processing can cause chain scission and oxidation in repeated processing cycles.[179] PLA can potentially withstand many cycles of reprocessing without a strong drop in properties, for example Finnerty et al. were able to reprocess PLA reinforced by natural fiber up to 6 times before observing a drop in mechanical properties.[180] PLA grade strongly influences this, as some grades have been shown to be able to go through up to 10 extrusion cycles with limited drops in polymer properties, while other grades are already strongly degraded after their second processing.[181] Separation of the still minor PLA fraction in the plastic waste stream is also a challenge and systems need to be developed to obtain a pure polymer from consumer waste.[182] For example the washing steps used in the processing of collected plastic waste can compromise the recycling of PLA as it is susceptible to hydrolytic degradation.[183,184] Separation at the source of PLA-heavy waste streams, such as production waste from manufacturers is a way of obtaining cleaner PLA for mechanical recycling.

In this study we analyze the fabrication of mussel socks from mechanically recycled PLA and assess the biodegradability of these socks in various lab-simulated environments. The recycled PLA is a secondary polymer recovered as part of the production process of biodegradable coffee pods. We aim to test the viability of using this material as-is without further processing or additives in an extrusion process used for polypropylene mussel socks. The obtained socks are to be analyzed by various methods (SEC, FTIR, DSC, TGA) to evaluate the degradation of the polymer in this processing step. The biodegradability of this netting will then be tested in an industrial composting environment to verify the viability of this end-of-life option as well as in soil and at the seawater-sediment interface to observe the speed of biodegradation in such environments.

3.2 Materials and methods

Secondary PLA in flake form was recovered from the production waste of GEA® coffee pods produced by Flo S.P.A. previously processed by thermoforming.

Aquaculture socks were produced by processing the secondary PLA at ROM Plastica Srl facilities using an extrusion line typically employed to produce PP mussel socks. The process parameters were those typically used for PP mussel socks production, with minor adjustments to temperature and processing rate. For material comparison, PP socks previously produced at the same extrusion plant were also obtained.

DSC measurements were carried out on a PerkinElmer DSC 8000 calorimeter equipped with an IntraCooler II cooling device (PerkinElmer Inc., Shelton, USA). 5–7 mg of sample in an aluminum open pan was first heated up from room temperature to 200 °C, held isothermally for 5 min, cooled down to −70 °C, held isothermally for 5 min, and heated up again up to 200 °C. Heating and cooling steps were performed at 10 °C/min. The degree of crystallinity (χ_c) of PLA is calculated considering the melting enthalpy ($\Delta H_{m)}$) of 100% α form crystalline PLA to be 143 J/g.[185] It must be noted that in the literature often the old 93 J/g value for 100% crystalline PLA has been used.[186]. The degree of crystallinity (χ_c) of PP is calculated considering the melting enthalpy ($\Delta H_{m)}$) of 100% α form crystalline PP to be 170 J/g.[187]

Thermogravimetric analysis (TGA) was carried out on a TGA 4000 (PerkinElmer Inc.) instrument with Pyris software for data acquisition and analysis. Samples (5–10 mg) were analyzed in an alumina pan at a heating rate of 10 °C/min from 30 to 900 °C under a nitrogen atmosphere (30 mL/min).

Size-exclusion chromatography (SEC) analyses were performed with an instrument set comprised of a Jasco PU-4180 pump (JASCO Corporation, Tokyo, Japan) operating at 0.4 mL/min, two in-series PLgel miniMIXED-D columns (Agilent, Santa Clara, USA), a Jasco CO-4060 column oven, a 20 µL injector, a Jasco RI-4030 refractive index detector, and a Jasco UV-4075 multi-channel UV–Vis detector. The column oven was set at 30 °C, and the eluent used was HPLC-grade chloroform. Polystyrene standards were used for calibration.

Attenuated total reflectance (ATR) analyses of samples were obtained with a universal ATR accessory coupled to an FTIR spectrometer (PerkinElmer Spectrum 100 FTIR). All spectra were recorded in the 4000–600 cm^{-1} range at a 4 cm^{-1} resolution, and 120 scans were accumulated. SpectraGryph 1.2.15 software was used to elaborate the spectra.

Scanning electrode microscopy (SEM) observation was carried out using a GeminiSEM460 microscope from Carl Zeiss AG (Oberkochen, Germany). Samples were coated by sputtering with platinum (2 nm thickness).

Water Holding Capacity (WHC) was calculated by the Keen-Raczkowsky box gravimetric method. Dry sediment was sieved with a 2 mm mesh and compacted in a cylinder with 3.5 cm diameter and 4 cm height with filter paper on the bottom and an open top. The cylinder was immersed in water by 3 cm for 24 hours, then removed from the water and hung until the dripping stopped, then weighed. WHC was taken as the percentage ratio of the weight gain to the dry soil.

A method modified from ISO 14855-1 was adopted to test the biodegradation of material under simulated aerobic home composting condition.[188] To this aim 5 g of mature compost (sourced from Recicla Srl, Copparo, Italy) was mixed with 10 g of perlite (supplied by VWR International, Radnor, USA) and sandwiched between two layers of 15 g of perlite in cylindrical glass vessels (500 mL capacity). Humidity content was adjusted and maintained at 50%. The test samples and the reference material (Whatman grade 1 cellulose filter paper) were placed in the core of the mature compost middle layer at about 40 mg sample/g compost ratios. All the vessels were incubated at 58 °C in the dark and the tests were carried out in triplicate. The CO_2 evolved from test and reference materials was trapped in the vessels by means of 20 mL of 0.5 N NaOH solution contained in a beaker set in each vessel. The head space of each vessel was sufficiently large to provide the microorganisms with oxygen, thus avoiding anoxic conditions. Every 3–10 days CO_2 absorbers were retrieved and replaced with fresh NaOH solution in known aliquots. The retrieved NaOH solutions were titrated with 0.5 N HCl and the amount of adsorbed CO_2 was determined. The percentage of biodegradation is given by the ratio of the CO_2 produced from test material to the maximum theoretical amount of CO_2 that can be produced, derived from the total organic carbon (TOC) content as calculated from molecular structures. The material was assumed to be 100 % made of pure PLA. Additional samples were removed from a test environment before the end of the experiment, in this case no CO_2 absorber was present, and samples were simply kept in the same closed environment as respirometric tests and oxygenated weekly.

A method modified from ISO 19679-1 was adopted to test the biodegradation of material settled on the sea bottom on sandy sediment. 60 g of sandy sediment and 140 mL of seawater were sampled from two different sites in the north Adriatic area (see figure 3.2) and placed within a 500 mL cylindrical glass vessel. 30-40 mg of the test samples and the reference material (Whatman grade 1 cellulose filter paper) were placed lying directly on the sea sediment and blocked in place by a stainless-steel mesh net. All the vessels were incubated at room temperature in the dark and the tests were carried out in triplicate. The

CO_2 evolved from test and reference materials was trapped in the vessels by means of 30 mL of 0.025N $Ba(OH)_2$ solution which were placed within the vessels in a 50 mL glass beaker. Every 3–10 days CO_2 absorbers were retrieved and replaced with fresh $Ba(OH)_2$ solution in known aliquots. The retrieved $Ba(OH)_2$ solutions were titrated with 0.05 N HCl and the amount of adsorbed CO_2 was determined and calculated as per the previous method. Additional samples were removed from a test environment before the end of the experiment, in this case no CO_2 absorber was present, and samples were simply kept in the same closed environment as respirometric tests and oxygenated weekly.

Figure 3.2 Locations of the G and N sampling sites for sediment and seawater.

The soil biodegradation test was carried out according to the ISO-7556 standard. The soil was sampled from a location 5 km SSW of Imola (Italy) as shown in figure 3.3a.

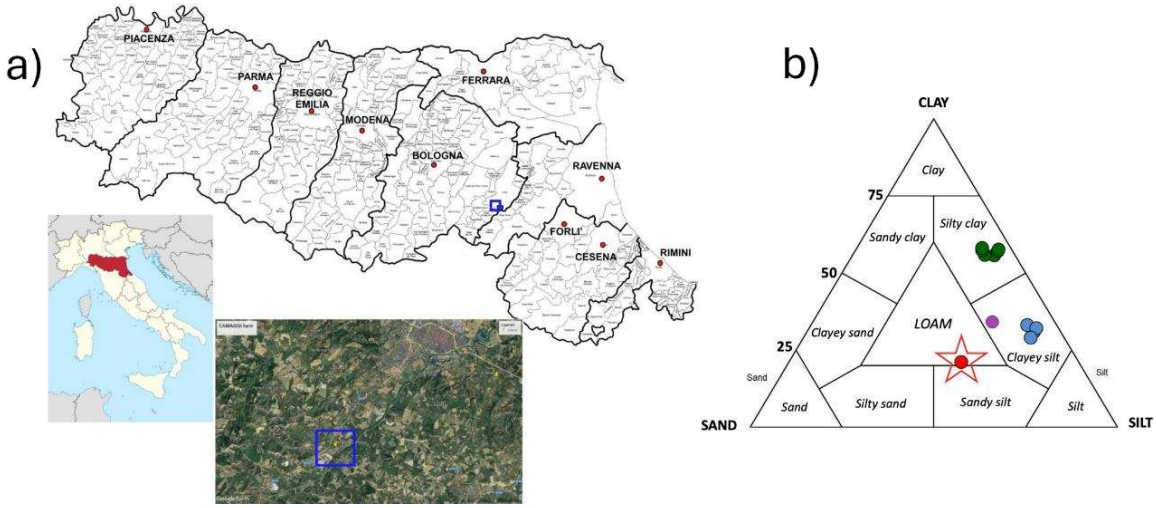

Figure 3.3 a) Location of soil sampling, b) soil classification Shepard diagram for sampled soil (red dot).

The soil is classifiable as calcareous loam (figure 3.3b), moderately alkaline and with a medium-fine texture. Further data is provided in table 3.1.

Table 3.1 Physico-chemical characteristics of the sampled soil used for biodegradation tests.

Parameter	Value
Bulk density (g/cm^3)	1.14 ± 0.06
Organic content (wt. %)	5.2 ± 0.3
pH	7.7 ± 0.1
Electrical conductivity (ms/cm)	0.88 ± 0.05

The soil was dried in the open air, sieved with a 2 mm mesh. The soil was added to a 500 mL container in three layers, the lowest 100 g of pure soil, the middle one was the sample-containing layer of 100 g of soil mixed with 2.5 g of sample, and the upper one again 100 g of soil. Ultrapure water was then added in the quantity necessary to reach 50% of the WHC. A 50 mL beaker containing 25 mL of 0.25M NaOH was used as CO_2 absorber. The containers were kept closed in the dark at room temperature (20 ± 2 °C).

3.3 Results and discussion

Table 3.2 reports the molecular weight data for PLA flakes and compares it to the one that is obtained after a further extrusion process. Two different extrusion runs were carried out, resulting in two different PLA socks, one with wider meshes (sock 1) and the other with narrower meshes (sock 2) (Figure 3.4). Run 1 was accomplished by using flakes just received at the extrusion facility, while run 2 was accomplished after storing the flakes for 1.5 months under room temperature and open air. Both processing steps resulted in a moderate decrease in molecular weight (between 16 and 27 % loss of $\overline{M_w}$), which was higher in the case of the second sock. The difference was attributed to the adsorption of some moisture by the flakes during storage, which results in a higher degradation by hydrolysis. The dispersity of the molecular weight distribution was not found to vary significantly after reprocessing, remaining around a PDI of 2.

Figure 3.4 The two fabricated PLA socks, on the left the wider meshes (Sock 1), on the right the narrower meshes (Sock 2)

Table 3.2 Average molecular mass by SEC measurements for the two PLA socks.

	$\overline{M_n}$ (kDa)	$\overline{M_w}$ (kDa)	PDI
Secondary PLA	109	225	2.05
PLA sock 1	87	188	2.15
PLA sock 2	83	164	1.98

DSC and TGA thermal analyses can give further insight into the effect of the second processing on polymer properties. Table 3.3 reports key data and Figure 3.5 shows the heating scans.

Table 3.3 DSC thermal analysis data for recycled PLA and nets made from it, compared to a PP sock

Sample	T_g (°C)[1]	T_m (°C)[1]	ΔH_m (J/g)[1]	ΔH_m 1st heat (J/g)[1]	χ_c	T_c (°C)[1]	ΔH_c (J/g)[1]	T_{onset} (°C)[2]
Secondary PLA	62.2	178.5	35.2	40.9	0.29	107.4	-29.4	327.9
PLA sock 1	64.7	177.9	42.1	46.8	0.33	105.8	-34.2	316.2
PLA sock 2	64.7	178	41.8	49.1	0.34	105.8	-31.8	n.a.
PP sock	ND	165.2	78.8	79.4	0.47	112.5	-74.3	418.7

[1] Measured by DSC; [2] Measured by TGA

The degree of crystallinity and the melting point of the secondary PLA flakes are quite typical of a semicrystalline PLA with low D- content (< 2%). The capacity of the PLA of recrystallizing during the second heating scan is quite high, with most of the original crystallinity being recovered, suggesting that some additives facilitating nucleation are present within the recycled plastic given that PLA alone has quite slow recrystallization kinetics.

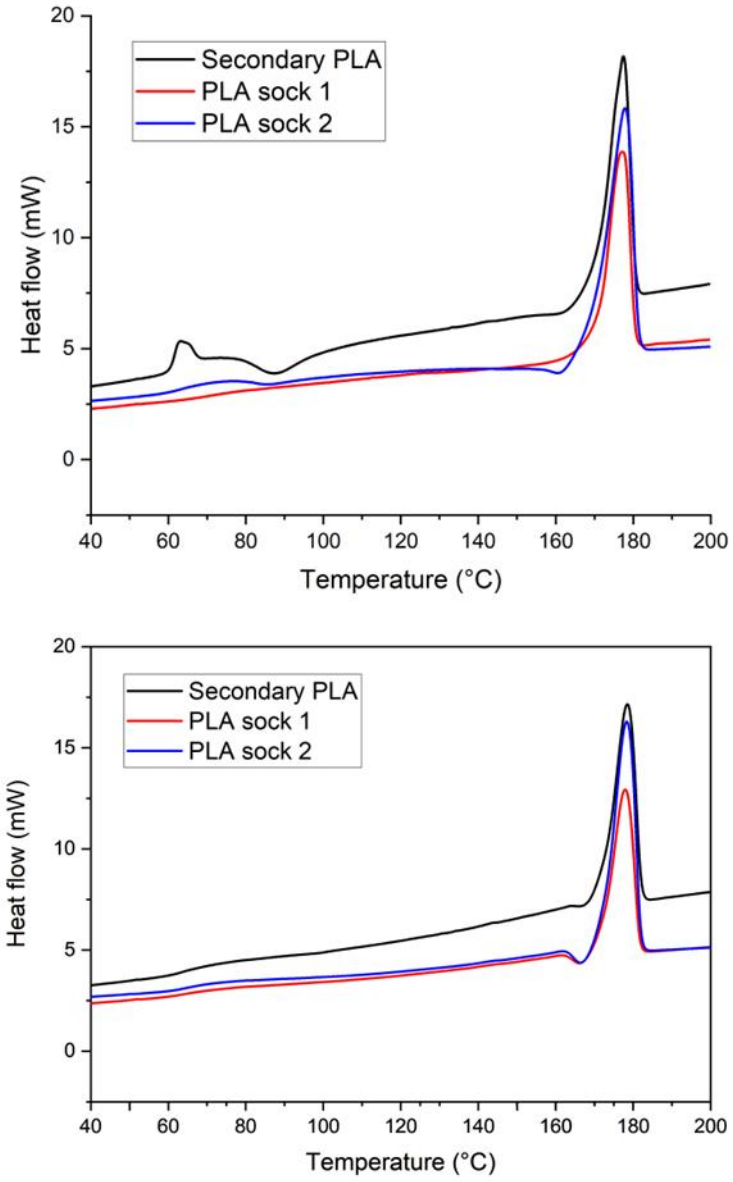

Figure 3.5 DSC scans (endo up) of secondary PLA and the two PLA socks. First heating scan above, second heating scan below.

The most relevant change in thermal properties is the increase in crystallinity in the reprocessed PLA obtained by both extrusion processes. This is observed both by a direct comparison of the secondary PLA and the reprocessed socks in the first DSC heating cycle

as well as after recrystallization in the second heating cycle. Thus, both the crystallinity of the material and its capacity of recrystallization are enhanced by further processing. The increase in crystallinity of PLA with successive recycling cycles has been observed in other studies[180,189] and it's attributable to the chain scission leading to a decrease in molecular weight and thus increased mobility of the polymeric chains which can more easily arrange into thicker crystallites. The thermal degradation of PLA, on the other hand, may also result in a decreased degree of crystallinity if the degradation reactions taking place result in branching or partial crosslinking of the polymer chains due to radical formation.[190] It is thus likely that this kind of degradation is not taking place. The T_g was also observed to slightly increase after the reprocessing. The decrease in molecular weight would be expected to reduce this value, but the stiffening of the material caused by the increase of crystallinity is probably countering this effect, as the molecular weight loss is not heavy enough to strongly influence T_g. A slight decrease in the thermal resistance of reprocessed PLA is also observed, as evidenced by a decrease of 10 °C in TGA onset temperature.

Compared to a conventional PP sock, the one made from PLA has a lower crystallinity degree and is less thermally stable.

Structural changes after reprocessing can also be investigated by FTIR analysis of functional groups. An important change in the carbonyl region (Figure 3.6) is the increase in reprocessed PLAs of a shoulder of the main C=O stretching signal, located at 1718 cm^{-1}. This may be attributable to -COOH endgroups increasing in concentration as chain scission takes place during processing. There was also a slight change in the main C=O stretch peak position which changed from 1748 to 1751 cm^{-1} after reprocessing which may be attributable to increased crystallinity.[191]

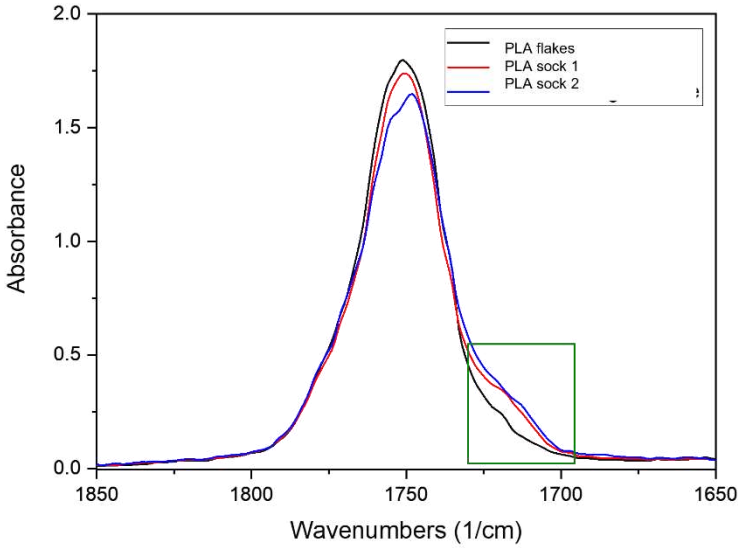

Figure 3.6 FTIR-ATR of the carbonyl region of PLA socks after normalization of the spectra at 1453 cm^{-1}. The 1700-1720 cm^{-1} shoulder is highlighted.

Despite the slightly greater degree of thermal degradation the PLA sock 2 sample, with narrower meshes, was chosen to carry out biodegradation testing due to its more similar shape to commonly used PP socks.

Biodegradation

The behavior of PLA sock pieces was studied in a lab-simulated industrial composting setting for 90 days. The results of respirometric observation are shown in figure 3.7.

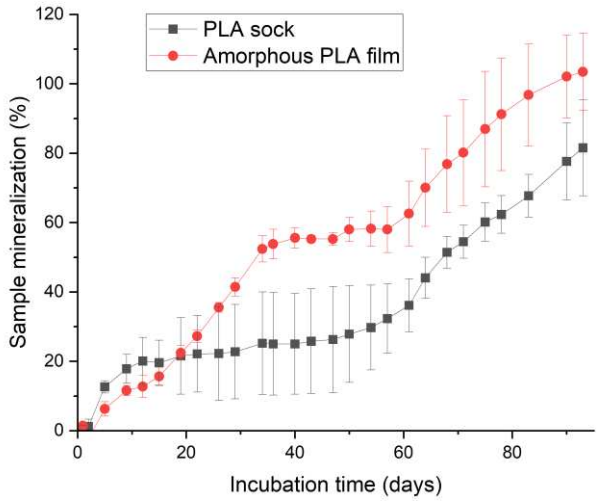

Figure 3.7 Mineralization over time of a PLA sock and an amorphous PLA film in a lab-simulated industrial composting setting at the temperature of 58 °C, as measured by a respirometric method.

The tested PLA sock degraded in two steps, first reaching around 20% mineralization in the first 14 days of testing, then only slowly mineralizing for the following month and then once again growing more rapidly after that, reaching a mineralization over 80% after 90 days. After the end of the measurement sample disintegration was complete and no remains of PLA could be found. Indeed, an amorphous PLA film, which biodegraded faster than the sock due the combination of lack of crystalline phase and greater exposed surface area, served as reference, as it reached 100% biodegradation in 90 days.

Further insight in the biodegradation process of the PLA net is given by SEC measurements carried out within the first 38 days of composting (Table 3.4). It can be noticed that within this period the PLA sock pieces only experienced minor disintegration, with only 15% mass loss being measured after 38 days, but suffered a great loss of molecular weight, as M_w loss was already greater than 50% after 10 days and reached 97% after 38 days. This is consistent with the mineralization measurements: In the initial period of composting, PLA degrades by random hydrolytic chain scission and few soluble low molecular weight fragments suitable for metabolization by microbes are slowly generated, while after the average molecular weight is further decreased there is a final biodegradation phase where metabolizable polymer fragments or monomers are quickly produced and used as food sources.

Table 3.4. Average molecular weight by SEC and thermal analysis for industrial composting of PLA socks

Composting time (days)	$\overline{M_w}$ (kDa)[1]	$\overline{M_w}/\overline{M_{w0}}$	T_m (°C)[2]	ΔH_m 1st heat (J/g)[2]	X_c	T_g (°C)[2]
0	164	1	178.0	41.8	0.29	64.7
10	68.4	0.42	177.4	44.5	0.31	66.2
21	33.6	0.21	175.5	49.9	0.35	58.1
38	4.4	0.03	159.2	52.0	0.36	38.2

1 Measured by SEC 2 Measured by DSC

The preferential biodegradation of the amorphous phase is clearly visible from DSC data gathered in the initial period of composting, as the melting enthalpy and thus the degree of crystallinity constantly increased. The T_g actually increased after 10 days, due to the effect of greater polymer crystallinity, and after that strongly decreased due to the loss of molecular weight. The melting temperature instead remained constant until the molecular weight very strongly decreased and only then started decreasing, thus crystalline structure generally remained constant throughout the initial period of biodegradation.

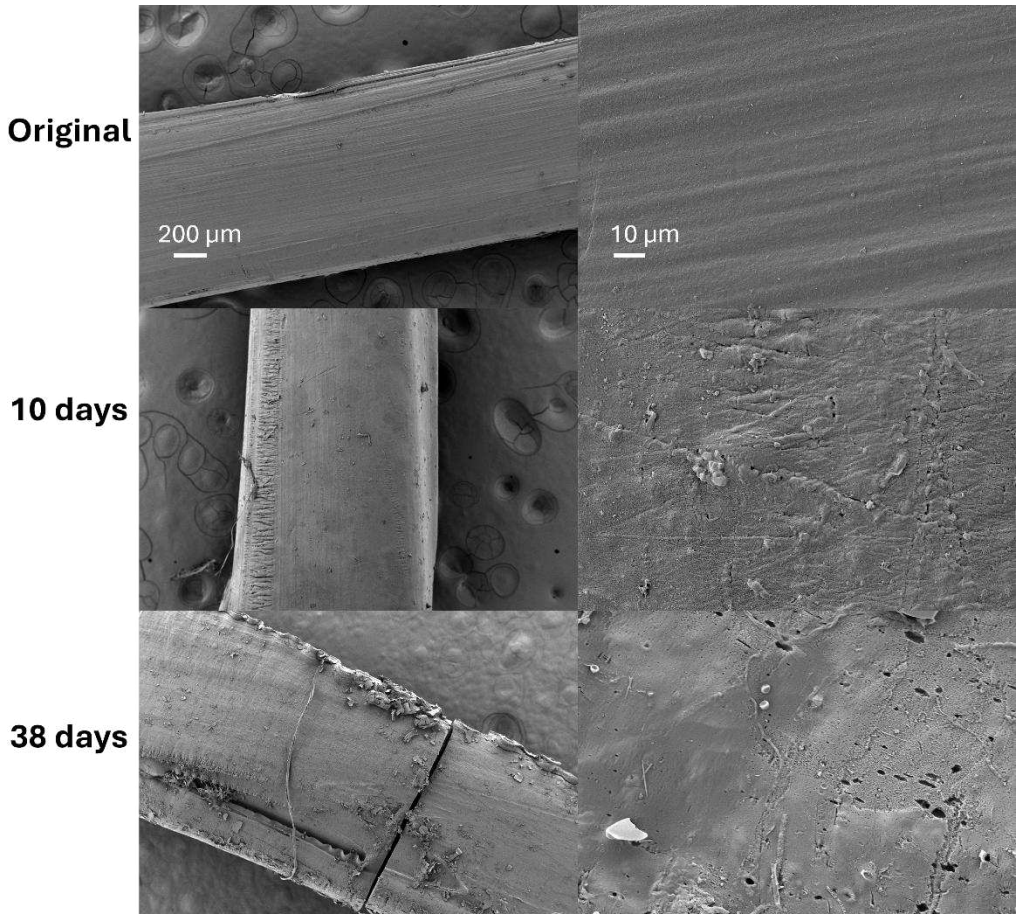

Figure 3.8 SEM images of a sock filament after exposure for various periods in an industrial composting environment at 100 (left) and 5000 (right) magnifications.

Microscopy observation of the sock during industrial composting (figure 3.8) also confirms its progressive degradation, as the surface of the filaments becomes progressively more irregular, porous and colonized by microorganisms. The overall structural integrity of the filaments is however maintained even through the dramatic drop in molecular weight of 38 days of composting and is only lost in subsequent composting.

The socks were also tested for biodegradability at the seawater-sediment interface. This is an interesting setting for an aquaculture sock because they tend to sink to the sea bottom if lost in the environment.[169] Two different sediment and seawater samples were taken for use in these tests (figure 3.2), one from a beach setting (Lido delle Nazioni, N) and one from a coastal lagoon with aquaculture activity (Goro, G).

Mineralization data is only shown for the N marine test (figure 3.9) as the data from the G test was deemed unreliable due to a large unexplained positive drift of sample mineralization incompatible with sample observation. Even in the N test, the uncertainty over data is quite large.

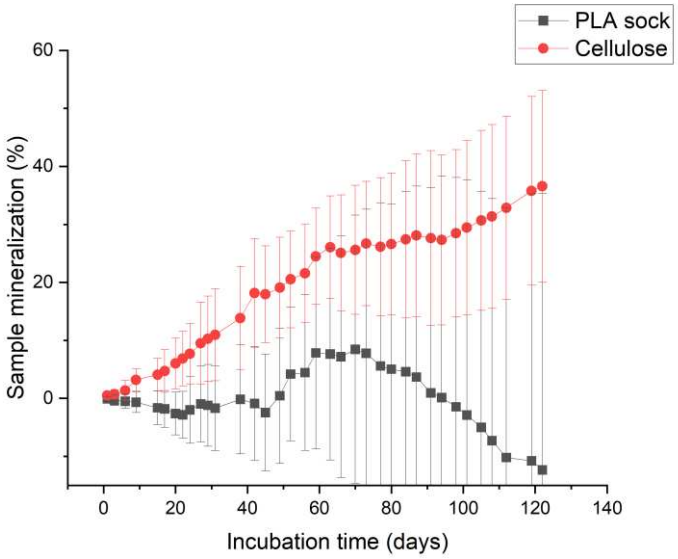

Figure 3.9 Mineralization over time of a PLA sock and cellulose reference a lab-simulated seawater-sediment interface as measured by respirometry.

No clear mineralization of the sample in the N test was observed. Further data for these tests is reported in table 3.5. Disintegration of the sample on the N sediment was also negligible (< 1%), while on the other hand the sample on the G sediment suffered slight disintegration, around 8 %. It is possible that this testifies to a higher availability of biodegrading microorganisms in the coastal lagoon sediment compared to a beach. Microscopy of the samples (figure 3.10) confirms this data by showing that the G sediment

sample displays stronger superficial erosion compared to the N sediment. A drop in molecular weight was measured in both samples but was not very high (13-16% drop in $\overline{M_w}$ after 4-5 months) confirming that only a low level of chain scission has taken place over this period. This value was also quite irregular when monitored over time in the N samples, testifying to a high variability in the speed of molecular weight loss even in a controlled laboratory setting sampled in the same time and place. Crystallinity and T_g values monitored by DSC analysis revealed no significant changes over time, a sign that the amorphous phase is not yet being strongly degraded.

Table 3.5 Data for simulated marine environment biodegradation data for PLA sock fragments. The 0 suffix indicates the original average molecular weight.

[1] Measured by DSC; [2] Measured by SEC

Test time	Sediment	Disintegration (wt %)	ΔH_m 1st heat (J/g)[1]	T_g (°C)[1]	$\overline{M_w}$ (kDa)[2]	$\overline{M_w}/\overline{M_{w0}}$
0	-	-	41.8	64.7	164	1
30	N	0.2	39.9	65.5	142	0.87
60	N	0.5	41.1	66.6	123	0.75
90	N	0.9	39.6	64.4	131	0.90
120	N	0.3	Na	na	137	0.84
150	G	8.3	Na	na	142	0.87

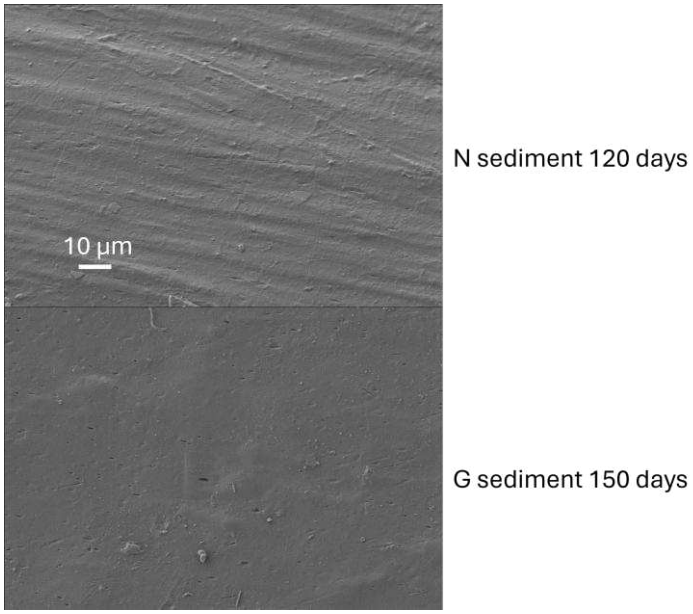

Figure 3.10 SEM observation (2000x magnification) for samples tested in two simulated marine environments, namely N and G.

The sock sample was finally tested in soil for a longer period (1 year). The mineralization as measured via respirometry is shown in figure 3.11. The samples displayed very little biodegradation activity throughout the period, only reaching 2% mineralization after 365 days. It needs to be noted that the mineralization of the cellulose reference stalled after around 4 months raising doubt on the biodegradation activity of the soil after this period. Nevertheless, the biodegradation in soil of the PLA sock in soil is clearly absent or very slow.

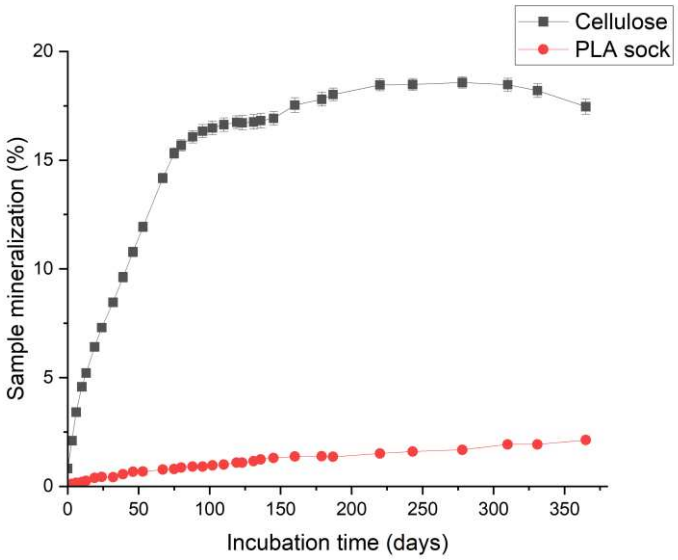

Figure 3.11 Mineralization over time of a PLA sock and cellulose reference a lab-simulated soil environment as measured by respirometry.

The measured weight loss and molecular weight loss are reported in table 3.6. Weight loss after 1 year was around 6%, which is greater than mineralization but still minor, indicating that the disintegration in soil of this material is on the scale of several years, possibly more than a decade. The number-average ($\overline{M_n}$) and weight-average ($\overline{M_w}$) molecular weight were both reduced, indicating that the polymer is suffering a degree of biodegradation within the soil. $\overline{M_n}$ decreased faster than $\overline{M_w}$ and the polydispersity index subsequently increased to 2.7.

Table 3.6 Data for PLA sock fragments in a simulated soil environment after 1 year. The 0 suffix indicates the original average molecular weight.

Mineralization (wt %)	2.1
Disintegration (wt %)	6.3
$\overline{M_n}/\overline{M_n 0}$	0.59
$\overline{M_w}/\overline{M_w 0}$	0.80

Visually, as shown by SEM images (figure 3.12), degradation was quite extensive with large portions of the filaments showing evident macroscopic erosion and even the less damaged portions showing more evident microscopic erosion than those shown by the samples tested in seawater.

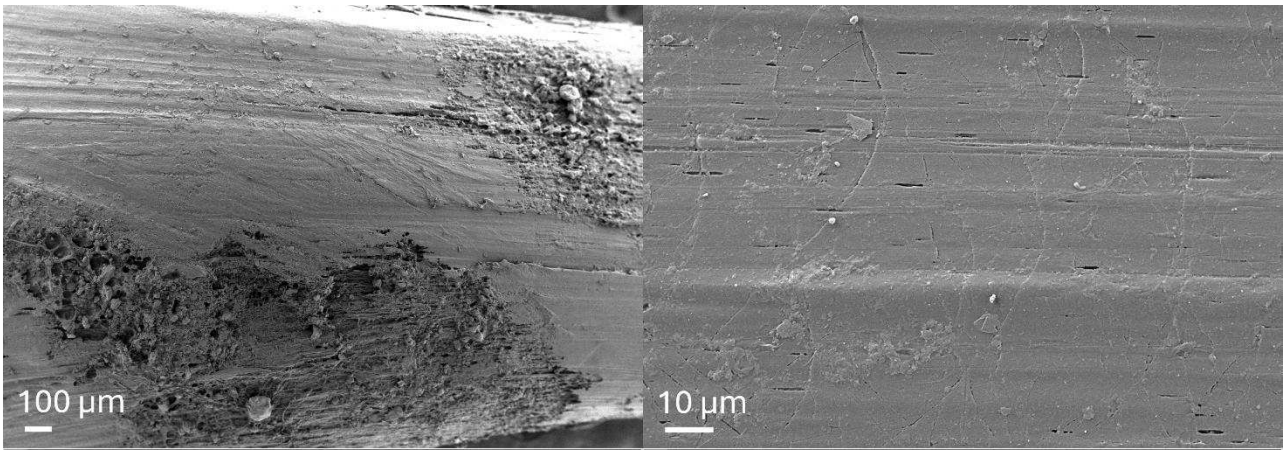

Figure 3.12 SEM images of the surface of PLA sock fragments after testing in a soil environment for a year.

3.3 Conclusions

Recycled PLA from a thermoforming process was successfully reused to produce aquaculture socks using the same equipment and a similar extrusion process as those used for conventional PP socks, without any kind of purification or pre-processing. The PLA suffered a moderate loss in molecular weight during the reprocessing, which could be reduced by more extensive drying before extrusion, but had similar thermal properties and a slightly higher crystallinity degree than the original polymer.

The PLA socks were found to be fully compostable at the industrial composting temperature of 58 °C. Biodegradation properties at the seawater-sediment interface were found to be heavily dependent on the kind of sediment that was used for the tests, with a coastal lagoon environment providing faster biodegradation than a sandy beach one. In any case, the socks were, however, quite slow to disintegrate, with mass loss being at most 8% after 150 days. Soil biodegradation was also found to be very slow, with mass loss being 6% after 1 year, but with faster loss of molecular weight and greater visual disintegration being noticeable compared to the seawater-sediment setting.

Overall, this highlights the versatility of PLA from a processing standpoint, as low-cost recycled polymer can be introduced as-is in an existing process obtaining similar aquaculture gear to conventional one. The overall sustainability of the process is yet to be fully assessed but the compostability of the obtained socks gives a potentially superior end-of-life option compared to PP socks. The reduced degradability of PLA in seawater-sediment and soil environments underlines the need for proper disposal of the material to avoid environmental pollution and ghost fishing concerns.

4. Foaming of amorphous blends of poly(lactic acid) and poly(3-hydroxybutyrate-*co*-4-hydroxybutyrate) with supercritical CO_2 and study of the biodegradation properties of the foamed materials

4.1 Introduction

Polymer foams are one of the most widespread forms in which plastics are employed in daily life, particularly in packaging and construction. Traditional polymers used for this purpose, mainly polystyrene and polypropylene, are based on fossil sources and have many environmental drawbacks, from the consumption of non-renewable resources to environmental pollution. In particular, expanded polystyrene (EPS) is a ubiquitous source of macro- and microplastics in the world's oceans.[192,193]

Bio-based and biodegradable polymers offer an alternative to the use of traditional materials that may solve these problems. Poly(lactic acid) (PLA) currently has by far the highest production capacity among bio-based biodegradable polymers.[14] This is due to its versatility, relatively low cost and easy production compared to alternatives.[194] The fabrication of foamed materials based on PLA has seen intense research in the past quarter century and, although still not one of the main uses of this polymer, it has been introduced in commercial products.[92,93] However, one of the drawbacks of PLA is that its rapid biodegradability (on a scale of 1-3 months for complete mineralization) is only possible in an industrial composting environment, while in home composting or in soil it is far slower, mostly due to the issue of temperatures in these settings being below glass transition (around 60 °C) which limits chain mobility and slows down biodegradation.[30,113] In freshwater and seawater this is

compounded by the lack of biodegrading microorganisms, which limits degradation to simple non-enzymatic hydrolysis and slows it down further.[195–197] Thus, PLA-based materials are generally not certified as home-compostable or seawater-biodegradable.

The environmental biodegradability of PLA has been shown to be enhanced by blending with other polymers such as starch, polycaprolactone or poly(butylene succinate-*co*-adypate).[198,199] The degradation of the more readily biodegradable phase has been shown to not only accelerate the biodegradation of the overall plastic but possibly accelerate the degradation of the PLA phase itself. This has been explained by a number of mechanisms, mainly by the increase of the exposed surface area due to the formation of microvoids, as the more degradable phase is destroyed, as well as the easier formation of biofilms on these surfaces and, if the non-PLA phase is more hydrophilic, by increasing water permeation within the material and thus hydrolysis.[45,198] Polyhydroxyalkanoates (PHAs) in particular are bio-based and biodegradable polyesters that offer superior environmental biodegradability compared to other polyesters, including PLA. However, the low production capacity and high cost of PHAs, associated with their direct production by microorganisms, has thus far limited their adoption as commercial materials. Thus, the use of a PHA as the blend partner of PLA combines the lowering of the cost of the overall material compared to PHA with enhanced biodegradability compared to PLA. Recent research has evaluated the efficacy of such blends in home composting,[63,200] soil[62] and seawater.[201]

The first reported and best known PHA is poly(3-hydroxybutyrate) (PHB) but more recent production has focused on its copolymers with other hydroxyalkanoates such as valerate (PHBV), hydroxyhexanoate (PHBH) and 4-hydroxybutyrate (P34HB) which offer better processability due to lowering of melting point and crystallinity caused by the introduction of a comonomer unit. The latter copolymer has been specifically commercialized as a modifier for other polymers in its amorphous form (4HB content around 30%), which can thus give some PHA properties without introducing a PHA crystalline phase. In particular, the enhanced mechanical and barrier properties of such blend films of PLA and amorphous P34HB have been reported.[202,203]

The foaming of blends of PHA and PLA has been previously explored by several authors. The research has mainly focused on blends of PHBV and semi-crystalline PLA with a PHBV content below 50% using either supercritical or gaseous CO_2. Research has shown effective, structurally tunable foaming of these blends at lower PHA content that became more challenging as PHA content increased.[204–207] Li et al. also recently tested compatibilized blends of PLA and P4HB with good results,[208] while Wang et al. reported the formation of nanocellular foams by the blending and compatibilization of PLA and semi-crystalline P34HB.[209] However, the foaming properties of blends of PLA and amorphous PHA have not yet been reported.

This blending also offers the possibility of easily realizing fully amorphous blends of PHA and amorphous PLA. This is potentially of further interest for enhanced biodegradability, as amorphous PLA biodegrades faster than the crystalline one.[210,211] It also offers a closer analogue to amorphous EPS foams, albeit with a lower temperature limit in practical use due to the lower glass transition. In the case of PLA, crystallinity is in the main dependent on the enantiomer ratio of the two forms of lactic acid (L and D) used in the polymerization feed, with a more isotactic polymer resulting in a higher degree of crystallinity. In commercial uses, an L-rich mixture is commonly used, and the degree of crystallinity decreases as the D content increases. Above 10% of D content, crystallinity is so low and crystallization so slow that PLA is generally considered amorphous.[212]

While the foaming of amorphous PLA has seen less attention than the one of semi-crystalline grades, the fabrication and properties of low-density foams both in batch and extrusion processes using CO_2 as the blowing agent has been reported by multiple authors since the 2000s.[213–216]

In this work we aim to characterize fully amorphous blends of PLA and PHA, without the addition of any other components, studying their morphology by electron microscopy, their thermal properties by DSC and DMA and their rheologic properties by shear rheology measurements. We then progress to obtain expanded materials by batch foaming technique using supercritical CO_2 as the physical blowing agent and to study the effect of pressure and temperature process conditions on the density and morphology of the foams. The biodegradation properties of obtained materials in home composting conditions as well as seawater are then to be studied and compared to pure PLA foam, aiming to characterize the disintegration, the ultimate biodegradation, morphological changes and the selectivity of the biodegradation processes towards the polymeric structures by respirometric, mass loss, electron microscopy, size exclusion chromatography and NMR measurements.

4.2 Materials and methods

Ingeo 4950D amorphous PLA (aPLA) was kindly provided by NatureWorks (Plymouth, USA). This polymer has a D content of around 45%. The measured number-average molecular weight by SEC was 120,000 g/mol with a polydispersity index of 1.75.

PHACT A1000P amorphous PHA (aPHA) was supplied by CJ Biomaterials (Seoul, Republic of Korea). This PHA is a copolymer of 3-hydroxybutyrate and 4-hydroxybutyrate with a 4HB content of around 30%. The measured number-average molecular weight by SEC was 260,000 g/mol with a polydispersity index of 1.60.

The polymers and their blends were always dried for at least 16 hours at 60°C under vacuum before undergoing higher temperature processing or analysis.

Blending

Polymer blends were obtained using a DSM Xplore microcompounder from Xplore Instruments B.V. (Sittard, Netherlands). The blending was performed for 5 minutes under a nitrogen atmosphere with a screw speed of 100 rpm and 185 °C temperature. The total mass of a blend batch was 12 g.

Sample preparation

Samples for foaming and various analyses were obtained by using a hot press (25 kN of force) with the appropriate mold for 3 minutes at 120°C followed by cold pressing for 2 minutes.

Rheology

Shear rheological measurements were carried out on a TA Instruments (New Castle, OH, USA) RDA III rheometer with plate–plate geometry (diameter 25 mm). 1 mm thick disk samples were obtained by hot-pressing. Frequency sweeps were performed at 160-185 °C and a shear stress of γ = 10% in a frequency range of ω = 0.5-500 rad/s. Time sweep experiments were performed at 120-185 °C for 10 min at a shear stress of γ = 10% and a frequency of ω = 1 rad/s.

SEM

Pristine foam samples were observed using a JSM-6510 microscope from Jeol Ltd. (Tokyo, Japan), while samples after biodegradation were observed using a GeminiSEM460 microscope from Carl Zeiss AG (Oberkochen, Germany). In all cases, samples were cryo-cut to observe their section and were coated by sputtering with platinum (2 nm thickness).

Cell morphology was investigated using ImageJ 1.54 analysis software. At least 100 cells per foamed sample were examined by drawing cell perimeters and using them to calculate the area. Mean cell size was then calculated by approximating to spherical cells. By measuring the area in the SEM image in which the cells were measured, the cell density (N_0) was calculated according to the following equation:

$$N_0 = (\frac{n}{A})^{\frac{3}{2}}$$

Where N is the number of cells measured, and A is the total area containing the cells. From this, nucleation density (N_D) was calculated according to the following:

$$N_D = N_0 \cdot \frac{\rho_{polymer}}{\rho_{foam}}$$

Where $\rho_{polymer}$ is the density of the original polymer or blend and ρ_{foam} is the density of the foam. The $\rho_{polymer}$ of pure PLA was 1.25 ± 0.01 g/cm^3, the one of pure aPHA 1.19 ± 0.01 g/cm^3, while the blends had intermediate densities.

TEM

Blend samples were observed using a JEM-2200FS microscope from Jeol Ltd (Tokyo, Japan) at a voltage of 200 kV. Thin section samples were prepared by using a Leica EM UC7 ultramicrotome within a Leica EM FC7 cryo-chamber, both from Leica (Wetzlar, Germany). No staining agent was necessary due to the good natural TEM contrast between PHA and PLA phases. For the purposes of determining dispersed phase size, the acquired images were analyzed with ImageJ 1.54 software using the Analyze Particles function after using FFT bandpass filter processing on 5 images taken in different regions of the sample at a magnification of 124000x. Phase size was calculated as the diameter of a circle with the average measured surface as area.

Foaming

A custom-made autoclave was used. Either melt-pressed samples (10 mm × 10 mm × 1 mm) or granulate beads obtained from the microcompounder (approximately spherical with a diameter of 3-7 mm) were put in the electrically preheated autoclave (40-80 °C). After putting in the samples, supercritical CO_2 was applied using a setup of twin syringe pumps (Isco 260D, Teledyne, Thousand Oaks, CA) at a pressure of 75-140 bar for 30 minutes in isothermal conditions (saturation phase). After saturation, the valve was opened to the atmosphere and the pressure quickly dropped. Samples were retrieved and then tested for properties after at least 1 hour of exposure to ambient temperature and pressure.

Density

The foam density was determined according to the Archimedes principle with a density balance (Mettler Toledo AG245, Columbus, OH).

DSC

Measurements were carried out on a Mettler Toledo DSC 1 (Mettler Toledo, Columbus, OH) on a 2-10 mg sample in an aluminum pan. In standard measurements the samples were heated from 25 to 200 °C, held isothermally at 200 °C for 3 min, cooled down from 200 to −40 °C, held isothermally at −40 °C for 5 min and finally, heated from −40 to 200 °C. All heating and cooling steps were carried out at 10 °C/min. All measurements were carried out using N_2 atmosphere with a flushing rate of 20 mL/min.

DMA

Samples with a geometry of 50 × 10 × 2 mm were prepared by hot pressing and mounted on a DMA (Gabo Eplexor 500N, Netzsch-Gerätebau GmbH, Selb, Germany) working in tension mode. A dynamic strain of 1% at a frequency of 1 Hz with a contact force of 1 N was applied over a temperature range from −40 to 120 °C. For all measurements, a heating rate of 3 °C/min was applied.

Biodegradation

A method modified from ISO 14855-1 was adopted to test the biodegradation of material under simulated aerobic home composting condition.[217] To this aim 5 g of mature compost (ACFA compost supplied by Enomondo, Faenza, Italy) were mixed with 10 g of perlite (supplied by VWR International, Radnor, USA) and sandwiched between two layers of 15 g of perlite in cylindrical glass vessels (500 mL capacity). Humidity content was adjusted and maintained at 50%. The test and reference materials were placed in the core of the mature compost middle layer at about 40 mg sample/g compost ratios. The cellulose used as reference material was in fiber form, sampled from a pure cotton gauze. Foam samples were prepared by cutting into cubic shape approximately 5 mm per side. All the vessels were incubated at 30 °C in the dark and the tests were carried out in triplicate. The CO_2 evolved from test and reference materials was trapped in the vessels by means of 20 mL of 0.5 N NaOH solution contained in a beaker set in each vessel. The head space of each vessel was sufficiently large to provide the microorganisms with oxygen, thus avoiding anoxic conditions. Every 3–10 days CO_2 absorbers were retrieved and replaced with fresh NaOH solution in known aliquots. The retrieved NaOH solutions were titrated with 0.5 N HCl using a SI Analytics Titroline 7000 titrator and the amount of adsorbed CO_2 was determined. The percentage of biodegradation is given by the ratio of the CO_2 produced from test material to the maximum theoretical amount of CO_2 that can be produced, derived from the total organic carbon (TOC) content as calculated from molecular structures. Additional samples were removed from a test environment before the end of the experiment, in this case no CO_2 absorber was present, and samples were simply kept in the same closed environment as respirometric tests and oxygenated weekly.

Marine biodegradation testing was adapted from the ASTM D6691-17 norm. Sea sediment (1 Kg) and seawater (3.5 L) were sampled from coastal lagoon waters from Goro, Ferrara Province, Italy (44.8415 N, 12.2945 E) in June 2025. Seawater and sediment were mixed and then strained through filter paper. 160 mL of the filtered seawater were added to 500 mL test containers, then NH_4Cl (0.5 g/L) and KH_2PO_4 (0.1 g/L) were added to the seawater solution as additional nutrients. Around 40 mg of each sample were cut into approximately cubic 5 mm per side pieces and added to the test containers within a stainless-steel mesh net to be kept underwater. The CO_2 evolved from test and reference materials was trapped in the vessels by means of 20 mL of 0.1 N NaOH solution contained in a beaker set in each

vessel. Every 7–14 days CO_2 absorbers were retrieved and replaced with fresh NaOH solution in known aliquots. The retrieved NaOH solutions were titrated with 0.1 N HCl using a SI Analytics Titroline 7000 titrator and the amount of adsorbed CO_2 was determined. The percentage of biodegradation was calculated in the same way as the composting tests.

NMR

^{1}H Nuclear Magnetic Resonance (NMR) measurements were carried out on a Varian Mercury Plus 400 (Varian Inc., Palo Alto, USA) equipped with an Oxford NMR AS400 MHz autosampler (Oxford Instruments, Abingdon, UK) at room temperature. The sample concentration was approximately 30 g/L in $CDCl_3$. Chemical shifts were referred to TMS as the external standard by using the solvent peak as the internal standard. The molar contents of lactic acid (LA), 3-hydroxybutyrate (3HB) and 4-hydroxybutyrate (4HB) in samples were calculated by taking as references the integrals of the peaks at 1.53 ppm (3H, LA), 1.26 ppm (3H, 3HB) and 4.09 ppm (2H, 4HB).

SEC

Size-exclusion chromatography (SEC) analyses were performed with an instrument set comprised of a Jasco PU-4180 pump (JASCO Corporation, Tokyo, Japan) operating at 0.4 mL/min, two in-series PLgel miniMIXED-D columns (Agilent, Santa Clara, USA), a Jasco CO-4060 column oven, a 20 µL injector, a Jasco RI-4030 refractive index detector, and a Jasco UV-4075 multi-channel UV–Vis detector. The column oven was set at 30 °C, and the eluent used was HPLC-grade chloroform. Polystyrene standards were used for calibration.

4.3 Results and discussion

The blends of aPLA and aPHA are denominated Hxx, where xx is the weight percentage of aPHA in the blend.

The morphology of the blends was observed by TEM imaging and is shown in figure 4.1. In the 10-30% aPHA interval (H10, H20 and H30) that was investigated the PHA was observed in a dispersed phase within the PLA matrix, testifying the immiscibility of the two polymers. The size of this dispersed phase varied between approximately 50 and 1200 nm. The aPHA phases of H10 and H20 were extremely similar in average size at 430-440 nm average phase size, but with a narrower size distribution for H10, while H30 showed an increase to 580 nm of phase size. Compared to a P3HB homopolymer described in previous research

by Takagi et al., the aPHA copolymer displays a smaller phase size, which is instead rather similar to the blend obtained by the same authors using an epoxy-modified PHA as compatibilizer.[218]

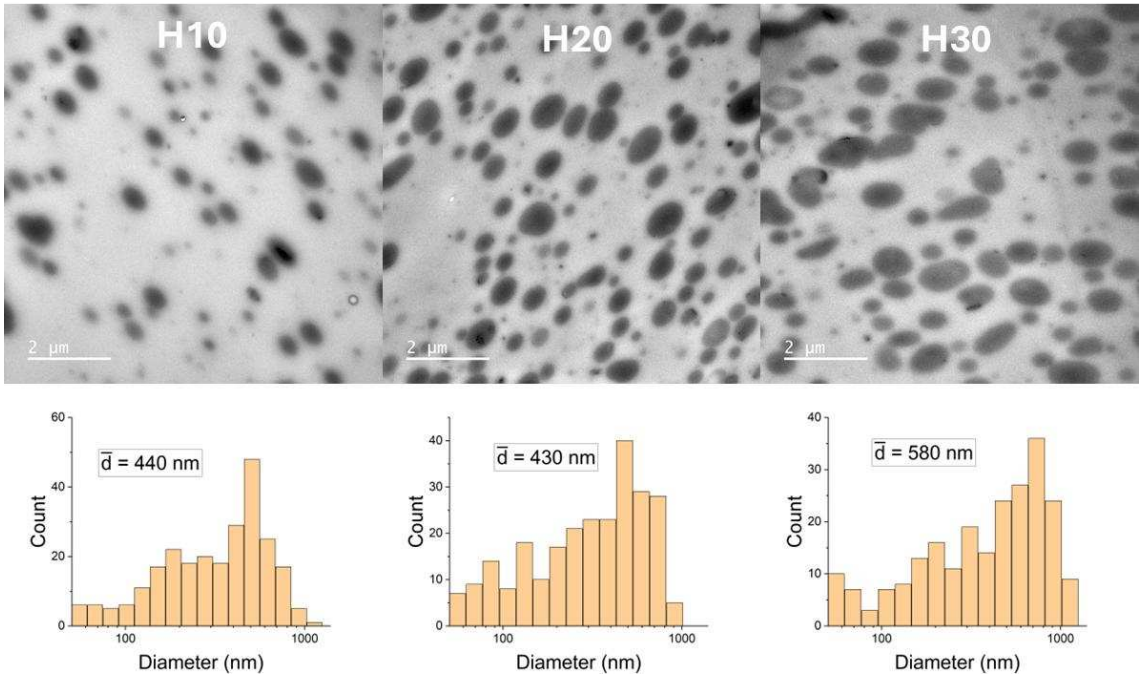

Figure 4.1 TEM imagery of sections of blend samples (above) and their particle size distributions (below)

In thermal analysis (DSC), no melting peak was observed for any sample - pure compounds and blends both in 1st and 2nd heating scans – confirming the amorphous nature of the materials. The immiscibility of the two phases results in two separate T_{gs} (Figure 4.2). Table 4.1 reports the Tgs of the two phases as observed by various techniques (DSC; DMA: tan δ peak and E" peak). The T_g of aPLA (T_{g2}) was 49 °C as measured by DSC, lower than the one typical of more crystalline PLA chains (around 60 °C) due to the high content of D monomeric unit. This temperature did not vary appreciably throughout the composition range of the blends. The T_g of aPHA (T_{g1}) on the other hand was found to vary slightly according to composition, decreasing as aPHA content decreased, as measured by DSC, from -15.9 °C for the pure polymer to -19.5°C for the H10 blend and, as measured by the tan δ DMA peak, from -7.9 °C for the pure polymer to -14.3 °C for H10. Measurements from the E" peak in DMA, on the other hand, did not result in appreciable variations (< 2 °C of difference). This decrease in glass transition temperature of aPHA is consistent with the one reported by Aversa et al. for similar blends with semi-crystalline PLA.[202] It has also been observed for the low-T_g soft phase in a PLA blend by multiple authors both in blends with PHAs[219] as well as different polymers,[220,221] and was explained by Qiu and colleagues as being caused by negative pressure due the differential shrinkage of the two phases as the blend is cooled.

Table 4.1 Thermal analysis data for aPLA/aPHA blends

aPLA (%)	aPHA (%)	DSC		DMA		DSC		DMA	
		T_{g1} (°C)[1]	ΔCp_1 (J/g*K)[1]	T_{g1} E'' (°C)[2]	T_{g1} tanδ (°C)[2]	T_{g2} (°C)[1]	ΔCp_2 (J/g*K)[1]	T_{g2} E'' (°C)[2]	T_{g2} tanδ (°C)[2]
100	0	*	*	*	*	49.2	0.559	61.5	69.1
90	10	-19.5	0.003	-14.3	-14.3	49.4	0.481	59.8	68.4
80	20	-18.0	0.111	-15.1	-13.9	48.3	0.552	61.5	68.7
70	30	-17.7	0.185	-15.2	-13.9	48.6	0.405	59.7	67.6
0	100	-15.9	0.482	-15.7	-7.9	*	*	*	*

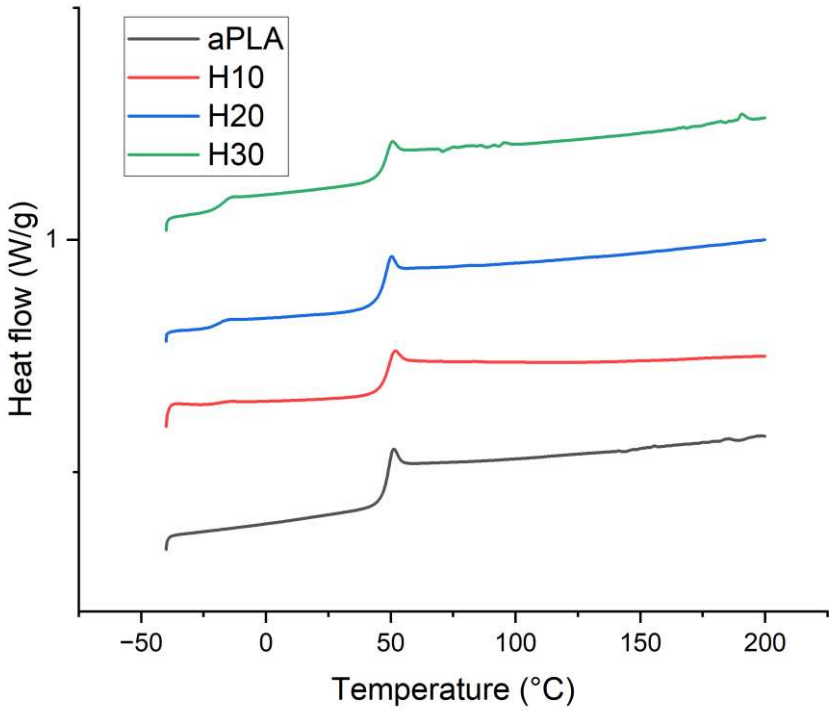

Figure 4.2 Second heating DSC scans (endo up) of amorphous PLA and aPLA/aPHA blends. Curves are offset for clarity.

The rheological properties of aPLA/aPHA blends are shown in Figure 4.3 as measured by strain sweep scans at 180 °C and 160 °C. All compounds show a shear-thinning viscoelastic behavior. aPHA as a pure polymer has significantly greater viscosity than aPLA, primarily due to its greater average molecular weight. The blends follow this trend, with greater aPHA content resulting in a more viscous melt. Compared to the behavior of an ideal polymer blend, the aPLA/APHA blends show a slight negative deviation (Figure 4.4), which is generally explainable by the formation of a low-viscosity interphase between immiscible polymer layers that lowers overall viscosity (interlayer slip).[222]

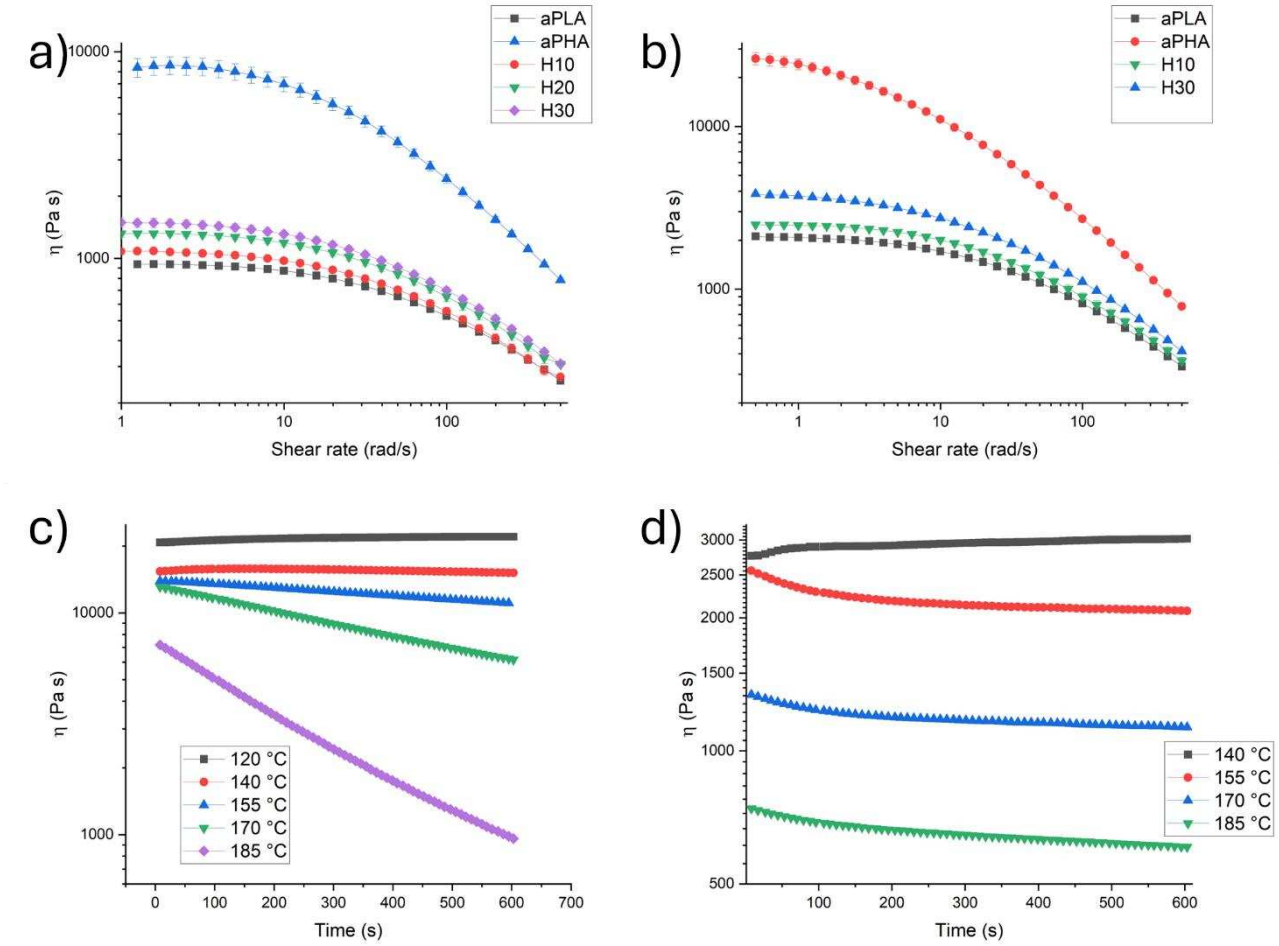

Figure 4.3 Rheology data. On the top strain-sweep viscosity measurements for aPLA, aPHA and their blends at a) 185 °C b) 160 °C. On the bottom time-sweep measurements at various temperatures for c) aPHA and d) aPLA.

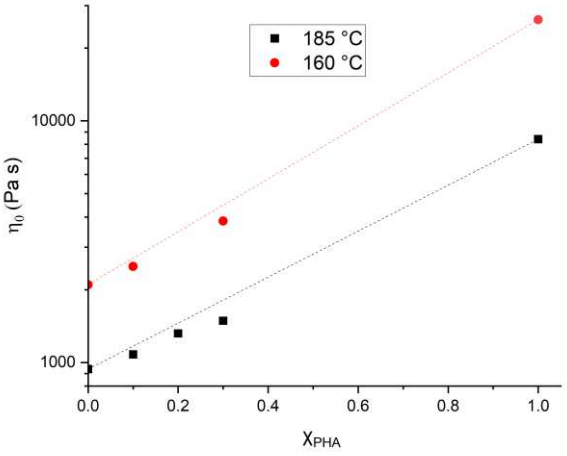

Figure 4.4 Zero-shear viscosity values at 160 and 185 °C of obtained aPLA/aPHA blends and the pure polymers. The dotted line represents the log-additivity dependence of an ideal blend.

At 185 °C, at the lowest shear rates aPHA starts to show a downward trend in viscosity and high dispersity in repeated measures due to thermal degradation, as low shear rate measurements take place later in the sweep. Indeed, aPHA is prone to thermal degradation at lower temperatures compared to PLA, as typical of polyhydroxyalkanoates. We estimated the effect of mixing on molecular weight by two means: rheometer time sweeps of pure polymers and SEC analyses of blends. Table 4.2 reports the decrease in complex viscosity of aPHA and aPLA at 5 and 10 minutes at various temperatures, with the full viscosity curves shown in Figure 4.3. The decrease in viscosity over time begins at 155 °C and becomes very steep at 185 °C. For high molecular weight linear polymers, the decrease in viscosity can be converted to the decrease in molecular weight by the general power law

$$\eta_0 \propto {M_w}^{3.4}$$

Where η_0 is the zero-shear viscosity and M_w is the weight-average molecular weight. Applying this relation to measured values, as shown in table 4.2, leads to the result that the weight-average molecular weight of aPHA is expected to decrease by around 30 % when processed for 5 minutes at 185 °C and below 10 % for the same processing at 160 °C. PLA is generally more thermally resistant than PHA and its expected molecular weight decrease was indeed less than 5 % in all conditions.

Table 4.2 Effect of the thermal degradation of aPHA on the average molecular weight as evaluated from time-sweep viscosity measurements at 120-185 °C.

Processing temperature (°C)	Time (min)	Viscosity decrease (%)	Expected M_w decrease (%)
120	5	0	0
	10	0	0
140	5	0	0
	10	2	1
155	5	10	3
	10	20	6
170	5	32	11
	10	53	20
185	5	67	28
	10	87	45

This can be further investigated in the obtained blends by comparing by SEC their molecular weights with the ones of the same ratios of unprocessed polymers - obtained by directly dissolving the polymers in the desired ratio in SEC solvent (table 4.3). This cannot be a precise measurement due to the different relation of the two polymers to the calibration standards and the large difference in molecular weight of the two components. However, it is evident that the average molecular weight of blends processed at 185 °C is indeed lower

than the one of the solution blended polymers and this becomes more prominent as aPHA content increases. The measured molecular weight of the mechanically blended polymers is also very close to the one of aPLA itself, not changing much with composition. This suggests that aPHA after the thermal degradation of processing ends up with a molecular weight that is quite close – in relation to the SEC calibration curve – to the one of aPLA.

Table 4.3 Weight-average molecular weights of aPLA/aPHA blends by SEC measurements

Samples	H10	H20	H30
Mw after solution blending (kDa)	242	279	331
Mw after mechanical blending (kDa)	215	209	221

Both aPLA and the blends were foamed, while aPHA was assessed after some preliminary trials to not be capable of satisfactory foaming due to excessively low T_g compared to room temperature leading to cell collapse. Pressure was varied from 75 to 140 bar, while foaming temperature was varied from 40 to 100 °C, while saturation time was fixed at 30 minutes, at which time full saturation was assumed. Only supercritical CO_2 was tested and foaming using subcritical CO_2 ($T< 31$ °C or $p_{CO2}< 74$ bar) was not tested. Testing at 75 bar was also more limited than at different pressures due to the irregular structure of foams obtained at this pressure. A full list of tested conditions and properties of the resulting foams is available in table 4.S1. The expansion of the resulting foams is primarily influenced by temperature and p_{CO2} as process variables.[223] When viscosity is higher than the optimum, the resistance of the polymer matrix to the internal pressure of nucleated cells limits their growth and increases the density of the resulting material. When viscosity is lower, on the other hand, the resistance to expansion is too low and the gas tends to diffuse out of the matrix while the cells coalesce into a more open structure. The viscosity of these systems is governed by temperature, an increase of which decreases polymer viscosity, and by the amount of CO_2 dissolved (increased with increasing pressure and decreased by increasing temperature) within the polymer matrix, which through its plasticizing effect decreases viscosity. The behavior of neat aPLA shown in a heatmap in Figure 4.5a can serve as a general example: the highest densities are observed at the highest temperatures and pressures tested, and this can be attributed to insufficient viscosity. As temperature and pressure decrease, the area at which the lowest densities may be obtained is located. A further decrease in these parameters then leads to an increase in density, but this is not as sharp as the one at higher ones, at least in the intervals studied. The combination of temperatures close to the critical temperature and higher pressures also results in denser foam samples; this is consistent with the results of previous research[216] and is attributable to rapid cooling upon pressure drop that freezes the polymer matrix during foaming, limiting cell growth and expansion.

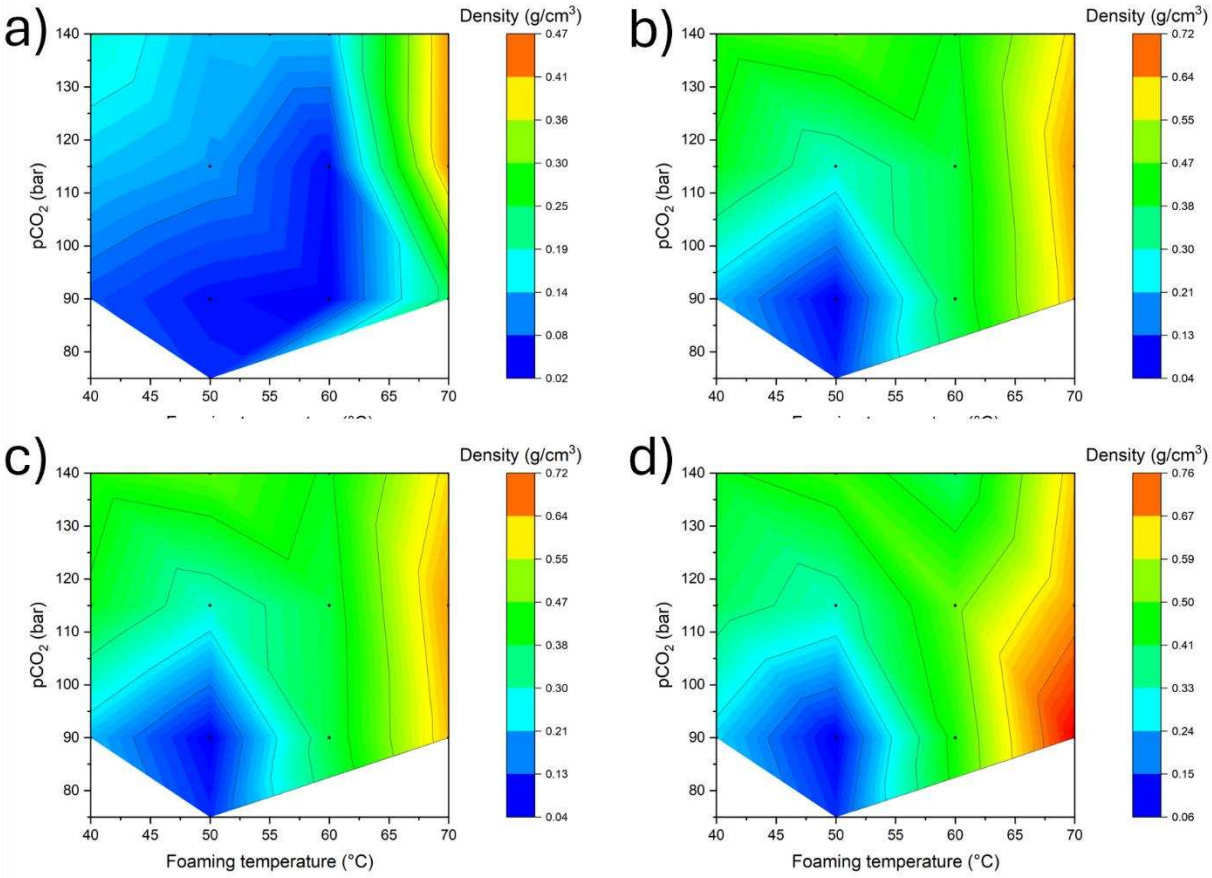

Figure 4.5 Dependence of density of obtained foams on CO_2 pressure and foaming temperature for a) aPLA, b) H10, c) H20, d) H30. Black dots represent experimental data.

It is interesting to compare this foaming behavior to the one of a different grade of amorphous PLA with lower D content (12% D compared to 45%) and consequent higher T_g (55 °C)[216,224]. The temperature window at which the foaming resulted in low density (< 100 g/L) foams is narrower and shifted to lower temperatures for the higher D content polymer (40-60 °C vs 50-110 °C). This effect is larger than what might be expected by the difference in T_g, which is only 6 °C.

When the aPHA component was added, low density foams were obtained at all tested compositions. However, the foaming window at which this low density could be successfully obtained was smaller compared to aPLA. As shown in Figure 4.5b-d, low densities were reached at similar conditions as the ones that lead to the lowest density of aPLA foams (50 °C and 90 bar), but density sharply increases at any deviations from those parameters.

To analyze the morphology of blend foams it is first useful to look at the one of pure amorphous PLA foam in the low-density region of foaming parameters (Figure 4.6). The foam obtained at 50 °C and 90 bar (top row, middle left) has a homogenous cell structure

with a thin skin layer; the average cell size is 80 µm and the overall structure is closed-cell. Raising the pressure to 115 bar has the effect of increasing density while decreasing cell size to 40 µm. The foam structure is still closed-cell but more defective, as more frequent rupture is visible in cell walls. As pressure is further increased to 140 bar the tendency is again towards smaller cells (20 µm), higher density and more defective cells. Cell nucleation density increases by approximately an order of magnitude for each pressure step. Lowering the pressure to 75 bar (top left of Figure 4.6), on the other hand, the structure of the resulting foam is irregular; the cell structure mostly resembles the one found at 90 bar but alternates with areas of higher cell density and low cell size. This is likely caused by the pressure being only slightly higher than the CO_2 critical point (73.8 bar), which leads to a limited driving force for the expansion process and variation in properties in different areas of the foam.[216]

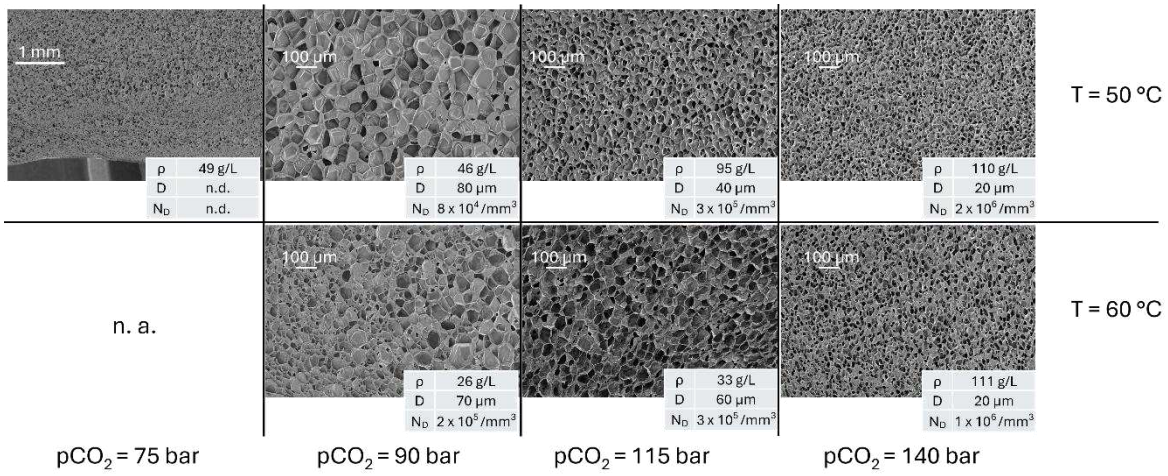

Figure 4.6 SEM images of the cross-section of aPLA foams obtained at different conditions. Density (ρ), cell size (D) and nucleation density (N_D) are reported as key data.

Raising the temperature to 60 °C and varying pressure (Figure 4.6, bottom row), we can observe that at 140 bar the foam structure is very similar to the one obtained at 50 °C, while at lower pressures it is quite different. At 115 bar a low-density foam (33 g/L) with fairly large cells (60 µm) is observed and at 90 bar the lowest density of the foam (26 g/L) is reached. However, compared to the same pressure at 50 °C this foam has a more heterogeneous cell size, with cells more than 100 µm in size coexisting with 10-20 µm sized regions.

When we observe blend foams with 10 % of aPHA content (Figure 4.7, left), the foam obtained at 50 °C and 90 bar is rather similar in structure to the one of pure aPLA at the same conditions. When pressure is increased to 115 bar this changes drastically, as a microcellular (8 µm cell size) foam with increased density (255 g/L) is obtained as a result of nucleation density being almost 2 orders of magnitude greater than the one of aPLA or the same blend at 90 bar. Further raising pressure to 140 bar leads to an even smaller

cellular structure with a lesser degree of foaming. Thus, the presence of aPHA in the blend has the effect of strongly facilitating the nucleation of CO_2 bubbles when pressure is 115 bar or above compared to a pure PLA polymer matrix. Raising the temperature to 60° C another different kind of morphology is present, where nucleation density and cell size (25 µm) is similar to the ones of low-density foams, but the cell walls are much thicker (1-10 µm rather than nanometric thickness) leading to a much higher density (345 g/L).

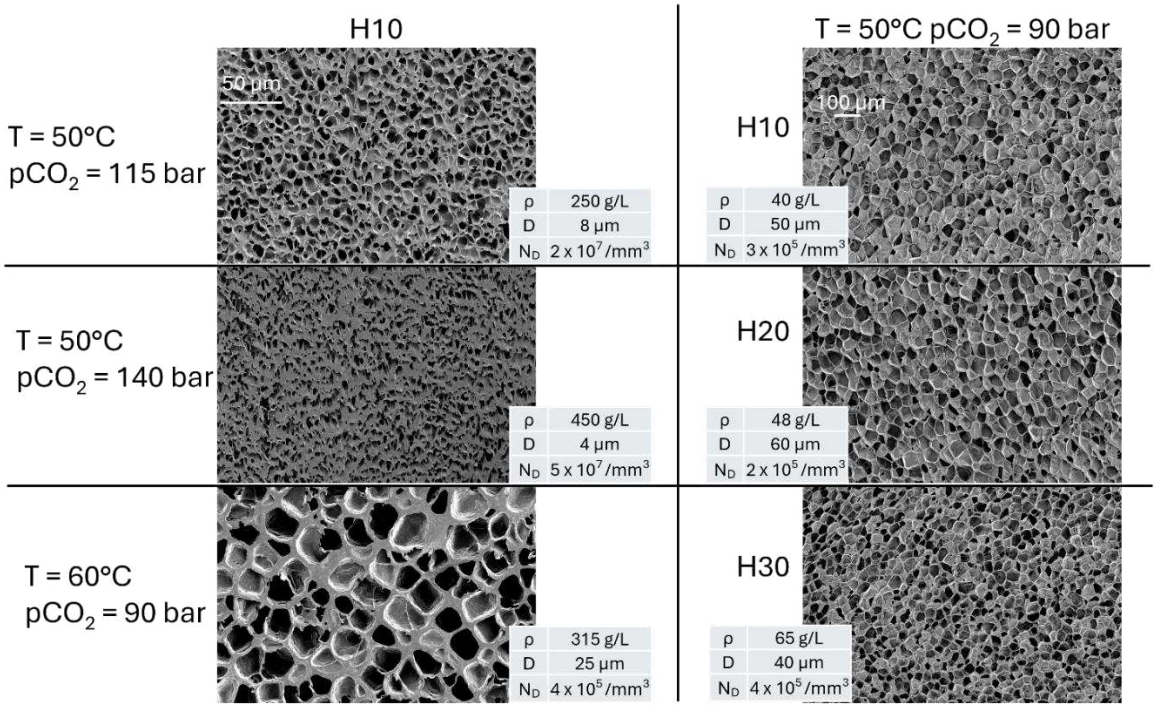

Figure 4.7 SEM images of the cross-section of aPLA/aPHA blend foams obtained at different conditions. Density (ρ), cell size (D) and nucleation density (ND) are reported as key data. On the right row foams are images of foams with the three different compositions obtained at 50°C and 90 bar pCO_2. On the left row H10 foam is observed at different process conditions.

When foaming at 50 °C and 90 bar the nature of blend foams obtained at different blend compositions are extremely similar in all properties, with a slight increase in minimum achievable density and in nucleation density for H30 (Figure 4.7, right). Thus, low density foams with volume expansion ratios equal to at least 20 can be achieved up to 30 % aPHA content working at these conditions. Foaming at these conditions was tested for all compositions on samples in both 1 mm thick sheet and granule (bead) form and was found to lead to well-repeatable properties using up to 1.2 g of beads per autoclave batch.

The biodegradation behavior of these low-density foams was analyzed in lab-simulated home composting conditions working at 30 °C, thus well below the T_g of the PLA component. The foams chosen for the test were the ones obtained for each blend ratio at 90 bar pCO_2 and 50 °C observed in Figure 4.7, using bead foams obtained from granulate. All samples had a density between 0.04 and 0.07 g/L, a closed-cell structure and a pore size between

40 and 80 µm. An aPHA film was also tested for reference of the pure material in these conditions. The mineralization of the samples was measured by respirometry over a 4-month interval and further analysis (weight loss, SEC, NMR, SEM) was carried out on select samples over time as well as on the retrieved final residue after 4 months. Figure 4.8 displays mineralization of the foams over time. We can distinguish between two types of biodegradation behavior depending on composition. Samples containing 20 or 30 % aPHA were measured to quickly begin mineralizing after 10 days of being added to the compost; for the first two months both these samples exhibited a linear growth of mineralization amounting to around 10 %/month, while growing more irregularly after this period, with the 30 % aPHA blend accelerating compared to the 20 % one. On the other hand, samples of pure aPLA or containing 10 % aPHA did not display mineralization for more than two months and only after this period were observed to start biodegradation. The pure aPHA film had a faster biodegradation compared to any of the blends, though slower than the cellulose reference, mineralizing by 60 % within the test period. As the geometry of this sample was different - 0.2 mm of thickness with a density of 1.2 g/cm^3 compared to 5 mm thickness and 0.03-0.06 g/cm^3 of density for foam samples – the results are not necessarily directly comparable. The surface area of the film exposed to biodegradation is larger than the foams and this should accelerate mineralization, though this might change if the inner porous structure of the foams is exposed to microorganisms as degradation progresses, strongly increasing their surface area.

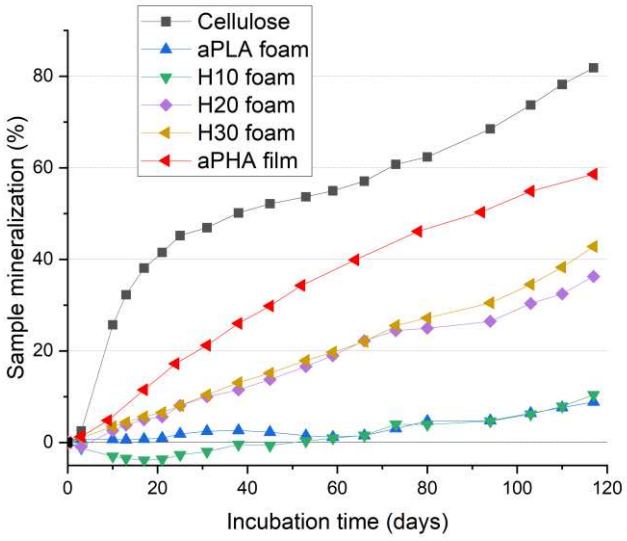

Figure 4.8 Mineralization of various samples in a lab-simulated home-composting setting at the temperature of 30 °C, as measured by respirometric method. The aPHA film plot is reproduced from a separate measurement set but using the same methodology and compost source as the other samples.

These results are not quite as positive on the effect of blending of aPHA with PLA as the ones reported by Han and colleagues[63] which for example resulted in over 60 %

mineralization after 45 days for a sample of blend film containing 30 % aPHA. This may be due to the nature of samples, foam biodegrading slower than a film with comparable composition, or it may simply be due to different testing methodologies, such as differences in the compost used.

Mass loss measured on the retrieved samples (table 4.4) and was found to be in all cases higher than sample mineralization, due to the presence of microplastics as well as soluble oligomers that have not yet been converted to CO_2 but are not retrievable from the test environment. The disintegration of the foam samples after 4 months ranged from 44 % (aPLA) to 84 % (30% aPHA). The variance in mass loss between repeated samples was generally high, highlighting the complexity of the biodegradation process leading to quite different degradation as also shown by the inconsistency in weight loss between the H30 sample retrieved after 45 days and the one retrieved after 90.

We further analyzed the repeating unit content of the non-disintegrated residue by ^{1}H NMR, by which lactate (LA), 3-hydroxybutyrate (3HB) and 4-hydroxybutyrate (4HB) can be distinguished and compared quantitatively. The weight fraction of LA in the fraction that was disintegrated or mineralized ($X_{L(D)}$) may then also be extrapolated by the following relation:

$$X_{L0} = X_{L(R)} \cdot X_R + X_{L(D)} \cdot X_D$$

Where X_{L0} is the weight fraction of lactate in the original mixture, X_R is the residual sample weight and X_D is the missing sample weight that was disintegrated or mineralized. The selective faster biodegradation of the aPHA fraction, which may be expected, would lead to a rapid increase in LA content in the residue and a low content of LA in the disintegrated fraction. On the other hand, this was either not observed or only observed to a reduced degree in most samples. After the end of measurements, only H30 showed an increase in LA content in the residue and a decrease in the disintegrated fraction. H20 after 45 days also showed unusual behavior, with selective degradation of the aPHA fraction and a very PLA-rich residue, again highlighting the complexity of the biodegradation process in repeated samples.

It is evident from these results that the PLA-derived content of the disintegrated fraction is very similar to the one of the original foams in all cases after 4 months of home composting. In absolute terms, the mass loss of PLA alone is as a consequence always higher in the blends compared to the one of pure PLA foam and thus the blending with aPHA enhances the disintegration of the aPLA fraction. However, the monomer ratio cannot be distinguished in the mineralized fraction alone, thus it cannot be conclusively said that blending also enhances PLA mineralization.

The monomeric content of aPHA itself in the residue was also analyzed (table 4.4). In most cases, this was unaltered from the original (69 ± 2% 3HB content) except in samples where

an increase in PLA content was also detected (H30 after 120 days and H20 after 45 days). In these cases, 3HB content compared to 4HB also increased. This suggests that PHA chains richer in 3HB are slower to degrade and thus the 3HB-rich fraction is the last to be left in the residue, but that this difference is not strong enough to be seen in samples that are not in their final stages of biodegradation.

Table 4.4 Mass loss and monomeric content analysis for foam samples after various times of exposure to a simulated domestic composting and seawater environments.

	Mass loss (wt%)			
	Domestic compost			
Time (days)	*0*	*45*	*90*	*120*
aPLA	-	17	37	44 ± 25
H10	-	18	43	65 ± 9
H20	-	27	39	56 ± 19
H30	-	48	17	84 ± 11
	Seawater			
Time (days)	*0*	*60*	*100*	*135*
aPLA	-	0	0	2 ± 2
H10	-	1.3	3.8	9 ± 9
H20	-	5.7	4.0	22 ± 16
H30	-	14.9	23.8	43 ± 2
	LA content in the residue (wt %)[1]			
	Domestic compost			
Time (days)	*0*	*45*	*90*	*120*
H10	88	87	86	87 ± 3
H20	80	94	78	79 ± 1
H30	70	n.a.	75	80 ± 11
	Seawater			
Time (days)	*0*	*60*	*100*	*135*
H10	88	92	92	92 ± 1
H20	80	86	86	89 ± 4
H30	70	91	90	90 ± 2
	LA content in the disintegrated fraction (wt%)			
Time (days)	*0*	*45*	*90*	*120*
H10	-	93	91	89 ± 2
H20	-	41	82	82 ± 2
H30	-	n.a.	49	68 ± 2
Time (days)	-	*60*	*100*	*135*
H10	-	~0	4	48 ± 37
H20	-	~0	~0	48 ± 32
H30	-	~0	7	44 ± 1

[1] Measured by NMR

The evolution of molecular weight and polydispersity of samples of the non-disintegrated foam residue throughout the home composting test is shown in Figure 4.9. All foam samples saw a reduction in molecular weight over time. It is noticeable that the H20 sample removed after 45 days of composting had a sharper reduction in molecular weight compared to the

other members of its data series. This is due, as also observed by monomeric composition, to an unusually selective fast degradation of the aPHA component of this foam sample compared to the others. In the case of the PLA foam samples as well as H10, we also observed that polydispersity remained constant and similar to the pristine polymer for the first 90 days and then sharply increased after that time. This suggests that a uniform chain scission is happening throughout the sample in the initial phase of biodegradation (not associated with mineralization) while later on a more uneven breakdown of the polymer chains, For H20 and H30, PDI was on the other hand observed to decrease in the initial phase of composting and then increase. These samples started mineralizing at the early stages, thus this is likely due to a selective complete biodegradation of shorter polymer chains at the beginning which narrowed the molecular weight distribution, after which an increase in PDI is caused by further advancement in the biodegradation of longer polymer chains. The final molecular weight after 4 months was rather similar (60-75 kDa) for all foam samples, despite the different degrees of mineralization and weight loss. However, it must be taken into account that this measurement is only being done on the residue and does not consider the molecular weight of the disintegrated fraction.

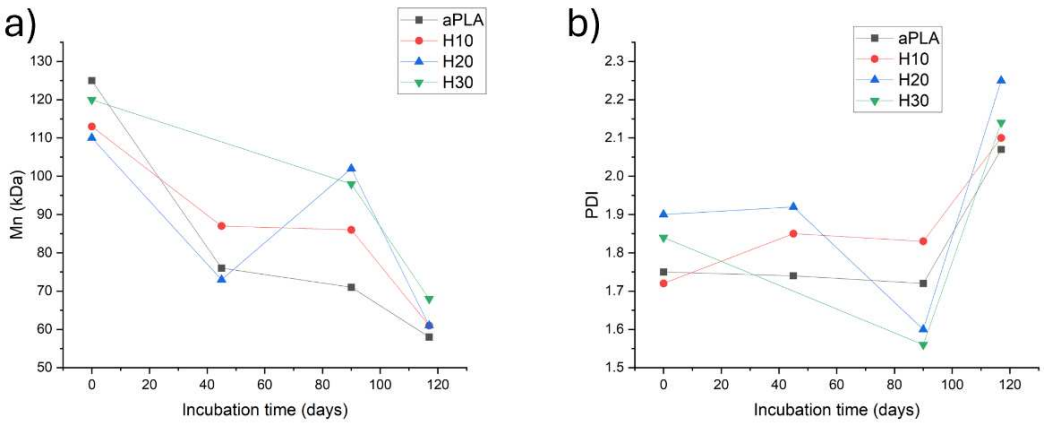

Figure 4.9 SEC measurements of a) number-average molecular weight and b) polydispersity index measured on foam samples after exposure in a simulated home composting environment for increasing period of time.

A morphological analysis of the foam as biodegradation is ongoing can also offer further insight in the mechanism. Figure 4.10 shows SEM images of a section of the inner part of a foam sample at various points after exposure in home composting. Samples taken after 45 days of testing show that the cellular structure of the foam is generally intact, but a general cell shrinkage happened in all samples to a cell size around 20 µm for all compositions. After 90 days all materials are still recognizably cellular, but cell structure is much less regular. In samples retrieved after 120 days, blend composition now defines the structure. While H10 and the pure aPLA foam are still recognizably cellular and closed-cell,

the H30 sample is in the final stage of disintegration and the cellular structure is almost completely lost in the residue, while H20 is at an intermediate stage of cell collapse. This evolution of foam morphology suggests the closed-cell nature of the original foam blocks access to the inner surfaces to microorganisms and biodegradation advances by progressive erosion of the cell walls.[225] The general shrinkage of the cells even in mostly undegraded samples is likely attributable to the mechanical stress of being buried in the damp environment rather than microbial action.

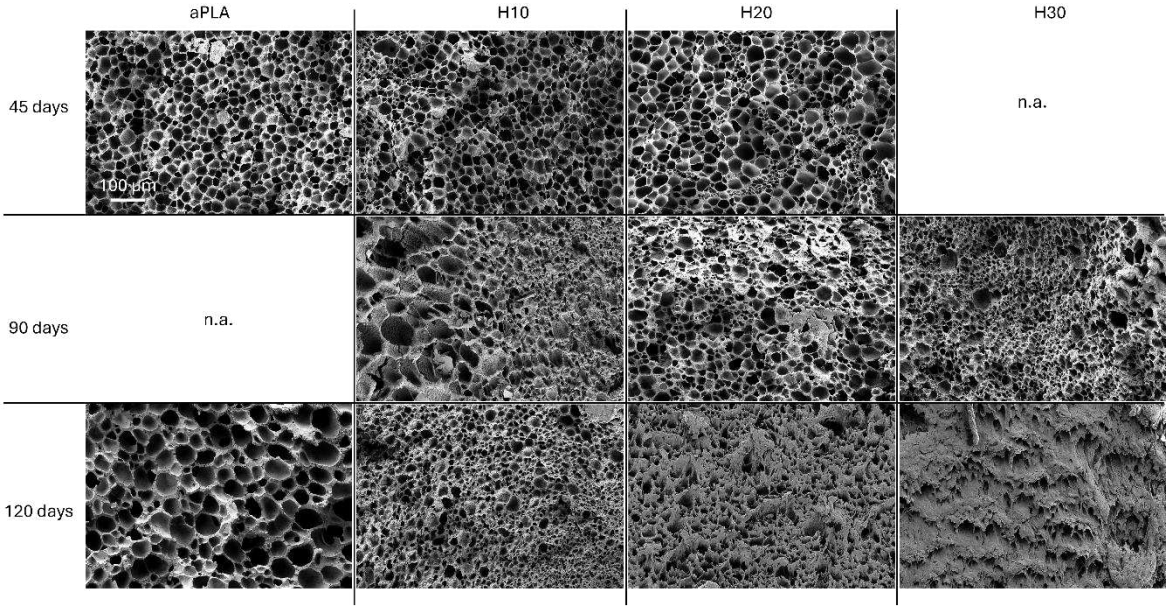

Figure 4.10 SEM images of the inner part of the cross-section of aPLA/aPHA blend foam fragments retrieved after a given time in simulated home composting conditions.

Marine biodegradation was also evaluated in a lab-simulated pelagic environment with the foam fragments being sunk in the water column. The samples selected were obtained using the same conditions used for the home composting test. Mineralization was studied by respirometry and further analysis (weight loss, SEC, NMR, SEM) was carried out on select samples over time as well as on the retrieved final residue after 4.5 months. By mass loss data (table 4.4), H30 displayed by far the fastest decrease over time, reaching 43% by the end of the experiment. By contrast, very little weight loss was measured for aPLA foam The H10 and H20 samples had a weight loss roughly equal to their aPHA content but lost very little weight in the initial part of the experiment and had a high variation between replicated samples. The measurements were carried out in the absence of sea currents, which may lead to greater sample disintegration in an actual marine environment due to mechanical action. Unfortunately, the gathered respirometric data was rather unreliable and could not be used for direct comparison with the weight loss data, with the quality of the data diminishing over time, as observable by the behavior of the cellulose reference (figure 4.S1). Large data errors result for each data point by the small difference between blank and

samples, and these errors cumulate over time since biodegradation is calculated by the total evolved CO_2. Therefore, the data in the early period is the more reliable. Measurement seems indeed to confirm that the H30 sample has by far the fastest biodegradation and that the onset time of this biodegradation is after around 40 days of exposure in seawater.

NMR analysis revealed that, despite overall sample disintegration being much reduced compared to the one observed in domestic composting, in the marine environment the disintegrated portion of the foam was composed nearly entirely of P34HB for the initial 100 days of the experiment, as lactate monomeric unit content sharply increased in all blend foam samples. After 100 days, lactate content in the disintegrated fraction started increasing reaching on average 40-50% for all samples. This highlights an overall biodegradation mechanism by which the PHA fraction of the blend foam is being very selectively degraded, while the PLA fraction is essentially untouched for a period of several months. After this, disintegration of the overall foam starts, though it is still to be determined if an actual biodegradation of the PLA takes place or the removal of most of the PHA simply causes the sample to breakdown more easily.

Table 4.5 Molar percentage of the 3HB comonomer in PHA chains after a given time in simulated home composting or marine environments by NMR analysis. Error values are standard deviations across three different samples.

	3HB (mol%)						
		Compost			Marine		
	Original	45 days	90 days	120 days	60 days	100 days	135 days
H10	69 ± 2	73	74	73 ± 2	72	65	76 ± 6
H20		94	69	69 ± 1	66	66	75 ± 5
H30		nd	69	76 ± 4	67	59	72 ± 9

That this took place despite the foam structure being mostly closed-cell suggests that degrading microorganisms, or more likely extracellular enzymes, were in any case able to have access throughout the foam structure and come into contact with the dispersed aPHA phase. The biodegradation of aPHA phase in cell walls may create pathways for enzymes to propagate through the structure. This is partially confirmed by the observation of the morphological changes of the foams exposed in the simulated marine environment (Figure 4.11). We can notice that the overall cell size of the exposed foams remained very similar to the ones of the pristine foams and no cell size reduction took place, suggesting different mechanical solicitations being present compared to the home composting environment. However, while the structure of the pure PLA foam remained unchanged throughout marine exposure, a greater degree of defects in cell walls appeared in blend foams compared to the original blend foams, increasing with aPHA content. This effect was already observed

for blend films by Han et al. who observed the creation of pores due to the degradation of the aPHA component in PLA/aPHA blend films.[201]

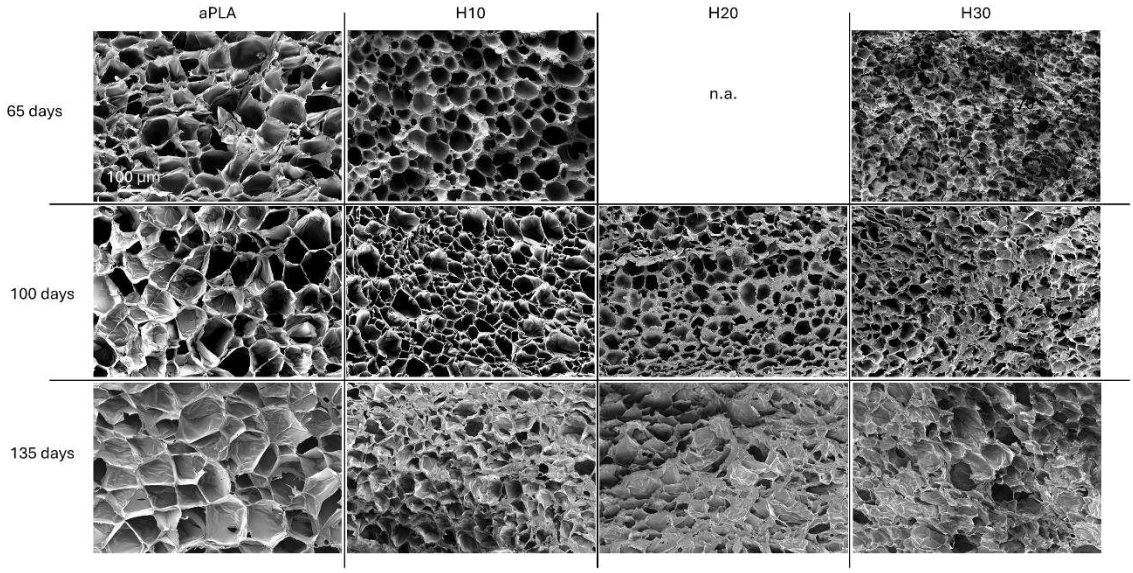

Figure 4.11 SEM images of the inner part of the cross-section of aPLA/aPHA blend foam fragments retrieved after a given time in simulated pelagic marine conditions.

As for the monomeric content of aPHA in the residue (table 4.5), this was, as in home composting mostly unaltered from the original (69 ± 2% 3HB content), a slight decrease was noticed in the early part of the experiment and a slight increase in the later part but neither was significant enough to be indicative of a preference towards either comonomer.

The evolution of molecular weight and polydispersity of samples of the non-disintegrated foam residue throughout the home composting test is shown in Figure 4.12. All foam samples saw a reduction in molecular weight over time, but this was far slower compared to the one observed in domestic composting conditions. The dispersity index (PDI) also moderately increased over this period, meaning that number-average molecular weight decreases faster than weight-average. Notably, the H30 sample, which suffered the greatest weight loss, over 40%, during the test period, and also saw the greatest increase in PLA content and thus loss of aPHA over time, lost less than 10% of its $\overline{M_n}$. This suggests that what is observed by SEC after marine biodegradation testing is essentially the PLA fraction, as most of the PHA fraction has been removed by that point, and confirms that this PLA fraction is only being very slowly decreasing in molecular weight.

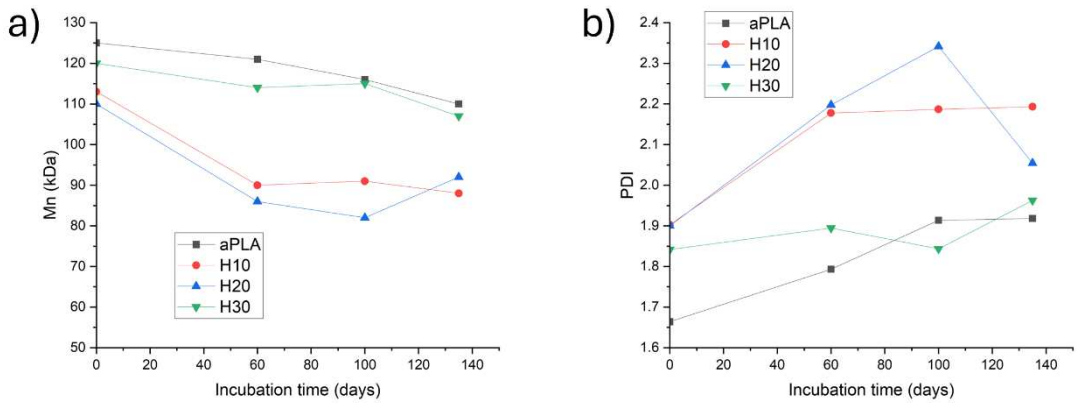

Figure 4.12 a) number-average molecular weight and b) dispersity index (PDI) measured on foam samples by SEC analysis after exposure in a simulated marine environment.

4.4 Conclusions

In this study, blends of amorphous PLA and amorphous P34HB (aPHA) with a 10-30 % content of aPHA were obtained and their morphology and thermo-mechanical properties were investigated, revealing that the mixture at this ratio is not miscible and that the PHA phase is dispersed in the PLA phase with a phase size of 400-600 nm. The blends were fully amorphous, and the glass transition of the PLA phase was not influenced by the presence of the PHA phase, while the latter shifted slightly towards lower temperatures. Viscosity and SEC measurements also showed that the aPHA component is thermally degraded at the mixing temperature, decreasing its molecular weight. The foaming behavior using supercritical CO_2 as the foaming agent was determined for both the pure and blended polymers and the dependence on temperature and pressure of the blends was generally similar to the one of pure PLA, with a narrower window where low-density foams ($\rho < 0.1$ g/m^3) could be obtained. The morphology of low-density foams was in all cases closed-cell with a cell size of 40-80 µm.

By the study of biodegradation of low-density foam in laboratory simulated environments, we determined that the addition of aPHA to the PLA matrix strongly enhanced sample biodegradation in a home composting test at 30 °C when aPHA content was at least 20 %. In this case, we observed that PHA content in exposed samples did not strongly decrease as biodegradation progressed, a sign that PLA biodegradation is enhanced by the presence of the PHA phase. Biodegradation was also observed to progress by surface erosion of the foam, with the cellular structure being conserved until the latter stages of disintegration. However, overall sample biodegradation was still fairly slow, with ultimate biodegradation

being below 50 % after 4 months in all samples, a sign that these foamed materials might not meet more stringent home composting standards. In a marine environment, we observed a much lesser degree of sample disintegration and molecular weight loss compared to home composting and also observed that the degree of mass loss is strongly dependent on aPHA content. We also measured a strong decrease in aPHA content over time, a sign that the PHA phase is selectively degraded by marine microorganisms while the PLA matrix is degraded far more slowly and is effectively left intact for most of the test period. After several months, the PLA matrix from which most aPHA has been already removed also starts disintegrating, but this is likely to be attributable to mechanical disintegration rather than biodegradation.

Overall, these results highlight both the promise and the limitations of using new generation PHAs as additives for other bio-based polymers such as PLA, as the blends were easily processable into high expansion foams and had a good home composting performance, but the PLA component still lacked the ability to quickly degrade in a marine environment.

Acknowledgments

I would like to acknowledge the contributions to this chapter and the following one by the research group and technicians at the Department of Polymer Engineering of the University of Bayreuth who hosted the research on foam preparation. I would also like to thank Alessandro Sisti, who carried out biodegradation studies as part of his M.Sc. thesis.

4.5 Supporting information

Table 4.S1 Full list of foamed samples with process parameters and obtained density

aPLA	aPHA	Sample form	T (°C)	P_{CO2} (bar)	Density (g/cm^3)
100	0	sheet	40	140	0.158
100	0	sheet	50	140	0.11
100	0	sheet	55	140	0.112
100	0	sheet	60	140	0.111
100	0	sheet	70	140	0.4
100	0	sheet	80	140	0.47
100	0	sheet	40	115	0.117

100	0	sheet	50	115	0.095
100	0	sheet	60	115	0.033
100	0	sheet	70	115	0.402
100	0	sheet	40	90	0.064
100	0	sheet	50	90	0.036
100	0	sheet	60	90	0.026
100	0	sheet	70	90	0.207
100	0	sheet	50	75	0.049
100	0	granulate	50	90	0.046
90	10	sheet	40	140	0.413
90	10	sheet	50	140	0.445
90	10	sheet	60	140	0.375
90	10	sheet	70	140	0.57
90	10	sheet	80	140	0.724
90	10	sheet	100	140	1.1
90	10	sheet	40	115	0.373
90	10	sheet	50	115	0.253
90	10	sheet	60	115	0.35
90	10	sheet	70	115	0.615
90	10	sheet	40	90	0.173
90	10	sheet	50	90	0.043
90	10	sheet	60	90	0.345
90	10	sheet	70	90	0.586
90	10	sheet	50	75	0.076
90	10	granulate	50	90	0.033
80	20	sheet	40	140	0.253
80	20	sheet	50	140	0.407
80	20	sheet	55	140	0.438
80	20	sheet	60	140	0.38
80	20	sheet	70	140	0.618
80	20	sheet	80	140	0.617
80	20	sheet	40	115	0.43
80	20	sheet	50	115	0.219
80	20	sheet	60	115	0.426

80	20	sheet	70	115	0.655
80	20	sheet	40	90	0.072
80	20	sheet	50	90	0.048
80	20	sheet	60	90	0.387
80	20	sheet	70	90	0.738
80	20	sheet	50	75	0.108
80	20	granulate	50	90	0.057
70	30	sheet	40	140	0.402
70	30	sheet	50	140	0.456
70	30	sheet	60	140	0.355
70	30	sheet	70	140	0.614
70	30	sheet	40	115	0.359
70	30	sheet	50	115	0.29
70	30	sheet	60	115	0.486
70	30	sheet	70	115	0.65
70	30	sheet	40	90	0.216
70	30	sheet	50	90	0.065
70	30	sheet	60	90	0.437
70	30	sheet	70	90	0.761
70	30	sheet	50	75	0.101
70	30	granulate	50	90	0.057

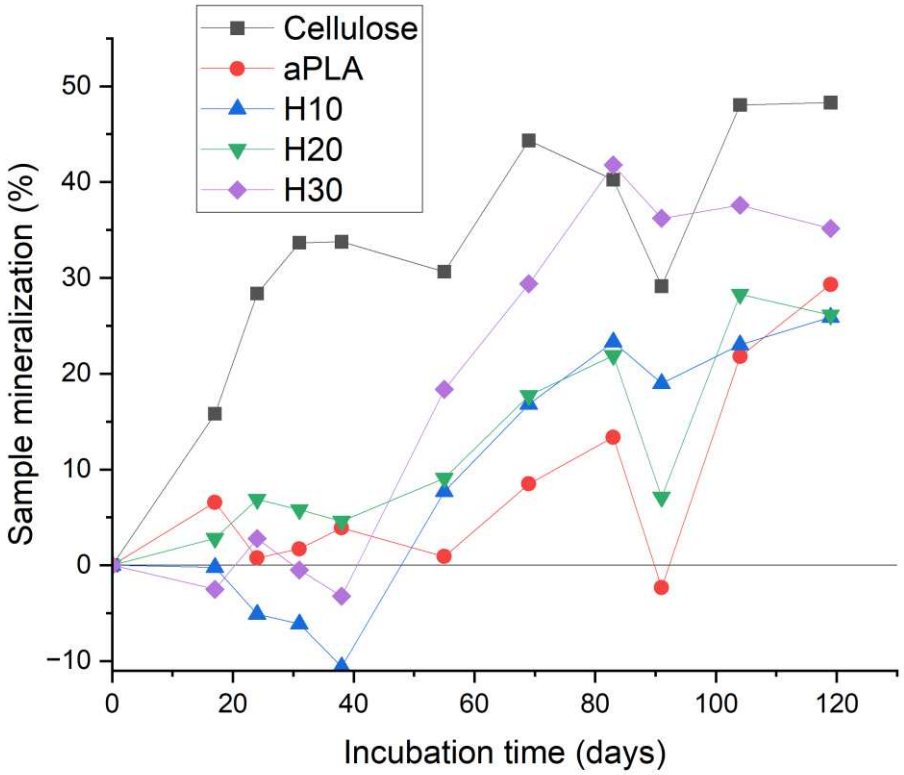

Figure 4.S1 Mineralization of various samples in a lab-simulated pelagic marine setting, as measured by respirometric method.

5. Foaming of blends of semicrystalline poly(lactic acid) and amorphous poly(3-hydroxybutyrate-co-4-hydroxybutyrate) with supercritical CO_2 and study of the biodegradation properties of the foamed materials

5.1 Introduction

In the previous chapter, the potential usefulness of foamed materials obtained from blends of amorphous PLA and amorphous PHA was described. The use of crystalline PLA as part of these blends presents a number of advantages. Crystalline PLA has a wider range of temperatures at which it can be used compared to amorphous PLA. The heat deflection temperature of amorphous PLA is below 60°C, while the one of semicrystalline PLA increases with the degree of crystallinity and can reach above 100°C.[226] Thus for example in food packaging, amorphous or low-crystalline PLA is not suitable for warm food and beverages.[227] Semicrystalline PLA has higher tensile strength, elastic modulus and hardness compared to the amorphous one, which overall makes it a stiffer and more mechanically resistant polymer, it also has better chemical resistance to organic solvents.[126]

Foaming of crystalline polymer is generally a more complex phenomenon than the one of amorphous ones. The presence and nature of crystalline structures before the polymer is saturated with the blowing agent and the interplay of polymer crystallization with the high pressure dissolved gas can lead to drastically different foam structures and properties influenced by the crystallization process.[228,229]

PLA's crystallization kinetics can thus influence the foaming process, as crystal formation can significantly affect cell nucleation and the expansion of foams. Cell nucleation can be promoted by the presence of formed crystals, and the presence of the crystals enhances PLA's melt strength and thus increases PLA's ability to expand by minimizing gas loss and cell coalescence. On the other hand, too high crystallinity induces stiffness in the polymer matrix which will reduce expansion and prevent foaming.[230–232]

The foaming process itself influences PLA crystallinity, as crystallinity kinetics are generally accelerated through the joint effect of gas dissolution enhancing chain mobility.[233] Annealing PLA under CO_2 pressure specifically accelerates cold crystallization but retards melt crystallization.[234]

The blending of PLA with other immiscible polymers has the general effect of enhancing PLA's crystallization kinetics, which is normally slow. This is especially common when the blended polymer is present as a dispersed phase within PLA, as it can effectively act as a heterogeneous nucleating agent promoting the nucleation of PLA crystals at the phase interface, while more complex behavior can be observed if different blend phase structures are present.

For blends with PHAs or with other biodegradable polyesters, for example Aversa et al. studied the non-isothermal cold crystallization of aPHA/PLA blends and observed that amorphous P34HB strongly increased crystallization kinetics of PLA, with aPHA content below 30% being more effective than greater.[202] A similar effect was noticed with the blending of PLA and semicrystalline P34HB.[235] Han et al. also observed that in amorphous P34HB/PLA blends PLA crystallinity in annealed blends was constant while PLA crystallinity in quenched blends increased with PHA content, indicating a greater degree of melt crystallization.[63] Blending of PLA and PCL was shown to enhance the crystallization kinetics of PLA when PCL was present as a dispersed phase, but reduce the overall degree of crystallinity of PLA.[236] Blending with 25% of PBAT also enhanced the isothermal crystallization rate of PLA and this was further enhanced by the addition of plasticizers.[237]

In this work we aim to characterize blends of semicrystalline PLA and amorphous P34HB (aPHA) in the range of 10-50% aPHA content, without the addition of any other components, particularly concentrating on the crystallization properties of PLA and how they are influenced by the blending, observing them both in non-isothermal and isothermal studies by DSC and DMA. The blend morphology will also be characterized by electron microscopy and their rheologic properties by shear rheology measurements. We then aimed to characterize the foaming properties of the blends by batch foaming technique using supercritical CO_2 as the physical blowing agent and studying the effect of sample crystallinity on foam morphology at various saturation temperatures. The biodegradation properties of obtained materials in home composting conditions are then to be studied and

compared to pure PLA foam, aiming to characterize the disintegration, the ultimate biodegradation, morphological changes and the selectivity of the biodegradation processes towards the polymeric structures by respirometric, mass loss, electron microscopy, size exclusion chromatography and NMR measurements.

5.2 Materials and methods

Materials

Ingeo 4032D amorphous PLA (aPLA) was kindly provided by NatureWorks (Plymouth, USA). This polymer has a D- content of around 1.5 %. The measured number-average molecular weight by SEC was 96,000 g/mol with a polydispersity index of 2.0.

PHACT A1000P amorphous PHA (aPHA) was supplied by CJ Biomaterials (Seoul, Republic of Korea). This PHA is a copolymer of 3-hydroxybutyrate and 4-hydroxybutyrate with a 4HB content of around 30%. The measured number-average molecular weight by SEC was 260,000 g/mol with a polydispersity index of 1.60.

The CA1270P masterbatch made up from a blend of the PHACT A1000P aPHA and a semi-crystalline PLA was supplied by CJ Biomaterials (Seoul, Republic of Korea). The weight ratio of the two polymers as measured by NMR was 68/32 PLA/PHA. The PLA in this blend has a D- content of around 4%.

The polymers and their blends were always dried for at least 16 hours at 60 °C under vacuum before undergoing higher temperature processing or analysis unless specified otherwise.

Blending

Polymer blends were obtained using a DSM Xplore microcompounder from Xplore Instruments B.V. (Sittard, Netherlands). The blending was performed for 5 minutes under a nitrogen atmosphere with a screw speed of 100 rpm and 185 °C temperature. The total mass of a blend batch was 12 g.

Sample preparation

Samples for foaming and various analyses were obtained by using a hot press (25 kN of force) with the appropriate mold for 3 minutes at 180 °C followed by cold pressing for 2 minutes.

Foaming

Samples were tested in three forms:

- Bead: granulate beads obtained from the microcompounder (approximately spherical with a diameter of 3-7 mm), which were then annealed by the standard drying procedure before foaming

- Annealed Sheet: melt-pressed sheets (10 mm × 10 mm × 1 mm) obtained by hot pressing, which were then annealed by the standard drying procedure before foaming

- Quenched sheet: melt-pressed sheets (10 mm × 10 mm × 1 mm) obtained by hot pressing, which were used shortly after cooling without being annealed

A custom-made autoclave was used. were put in the electrically preheated autoclave (50-165 °C). After putting in the samples, supercritical CO_2 was applied using a setup of twin syringe pumps (Isco 260D, Teledyne, Thousand Oaks, CA) at a pressure of 90-140 bar for 30 minutes in isothermal conditions (saturation phase). After saturation, the valve was opened to the atmosphere and the pressure quickly dropped. Samples were retrieved and then tested for properties after at least 1 hour of exposure to ambient temperature and pressure.

DSC

Measurements were carried out on a Mettler Toledo DSC 1 (Mettler Toledo, Columbus, OH) on a 2-10 mg sample in an aluminum pan.

In standard measurements the samples were heated from 25 to 200 °C, held isothermally at 200 °C for 3 min, cooled down from 200 to −40 °C, held isothermally at −40 °C for 5 min and finally, heated from −40 to 200 °C. All heating and cooling steps were carried out at 10 °C/min.

In recrystallization tests the samples were first heated from 25 °C to 180 °C at 150 °C/min, held isothermally at 180 °C for 3 min, cooled from 180 °C to 25 °C at 150 °C/min, held isothermally at 25 °C for 3 min, heated from 25 °C to the chosen cold crystallization temperature (T_{CC}) at 150 °C/min, held isothermally at T_{CC} for 25 minutes and finally heated from T_{CC} to 200 °C at 10 °C/min.

All measurements were carried out using N_2 atmosphere with a flushing rate of 20 mL/min. The degree of crystallinity (χ_c) of PLA is calculated considering the melting enthalpy (ΔH_m) of 100% α form crystalline PLA to be 143 J/g.[185] It must be noted that this value is quite different from the older calculations used in most literature sources[186] and this should be taken into account for comparisons.

For Rheology, SEM, TEM, DMA, NMR, biodegradation home composting tests, instruments and methods are reported in Chapter 4.

5.3 Results and discussion

The blends of PLA and aPHA are denominated Hxx, where xx is the weight percentage of aPHA in the blend, while the commercial CA1270P blend is denominated CA. The morphology of the blends was observed by TEM imaging and is shown in figure 5.1. The PHA was in a dispersed phase within the PLA matrix at 10-30% PHA content, while at 50% of PHA content the morphology was co-continuous. This demonstrates the immiscibility of the two polymers in the 10-50% aPHA interval. The average size of this dispersed phase was around 200 nm at an aPHA content of 10-20% and increased to 430 nm when aPHA reached 30%. Comparing H30 and the commercial CA masterbatch, who have a very similar weight ratio between the two polymers, it is interesting to note the very different morphology. The CA blend shows a tendency of the aPHA phase to aggregate into lamellar structures, which coexist in this blend with dispersed 100-200 nm spherical aPHA phases, while in the H30 blend the aPHA tends to form larger spherical phases and not lamellae. This is likely due to a different blending process but may also be related to the lower crystallinity degree of the PLA in the two blends.

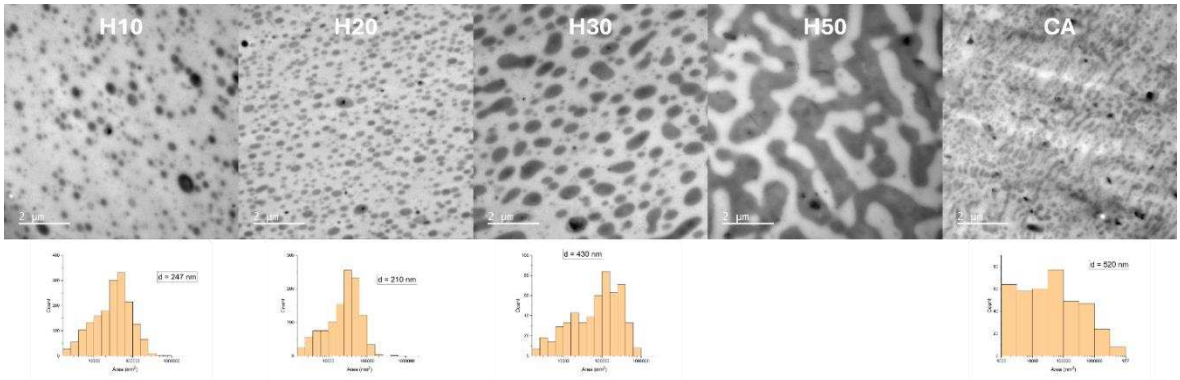

Figure 5.1 TEM imagery of sections of blend samples (above) and their particle size distributions (below)

Compared to the blends between aPHA and amorphous PLA shown in the previous chapter, the blends with semicrystalline PLA display a smaller dispersed phase size at 10-20% aPHA content and a very similar phase size at 30%. This may be related to the lower difference between the viscosity of the two components, as the dispersed phase size depends more on the viscosity ratio rather than on the absolute values.[222]

The rheological properties of aPLA/aPHA blends are shown in figure 5.2 as measured by strain sweep scans at 185 °C. All compounds show a shear-thinning viscoelastic behavior. aPHA as a pure polymer has greater viscosity than PLA, primarily due to its greater average molecular weight. The blends however don't follow this trend, with greater aPHA content resulting in a less viscous melt. This is a negative deviation from the ideal blend behavior, where, as aPHA content increases, the viscosity of the blends would approach the one of the pure polymer. Such a negative deviation is generally explainable by the interlayer slip phenomenon in immiscible blends, by which a low-viscosity interphase is formed between immiscible polymer layers that lowers overall viscosity.[222] A more thorough investigation of the effect of blend ratio on shear rheology would be needed to obtain the full composition range graph. As visible from the zero-shear viscosity plot in figure 5.3, the negative deviation from ideal behavior is quite strong for the blend of these two polymers, compared to the one of amorphous PLA, also negative, shown in the previous chapter. It is unlikely that the difference can be attributed to the difference in the average molecular weight between the two PLAs as this is quite similar so it is more likely attributable to the different tacticity of the two PLAs, since the 4950D PLA is atactic while the 4032D PLA is close to isotactic, which is likely to lead to different interactions between the two phases causing a different kind of interlayer to be present. The CA commercial blend on the other hand had very similar viscosity to the H30 blend with similar composition, thus on the other hand this difference in D-content (4 against 1.5%) did not have a measurable effect on shear rheology.

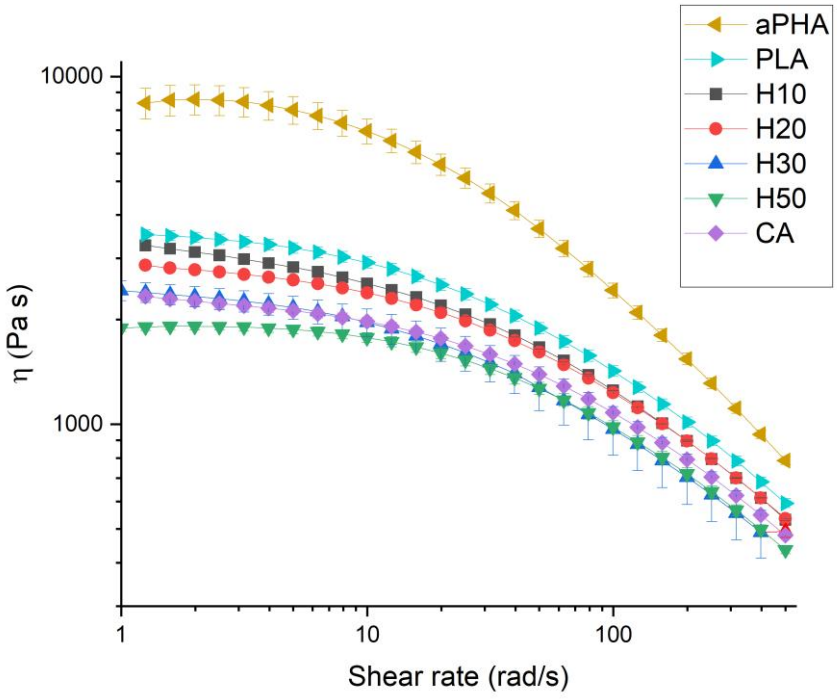

Figure 5.2 Strain-sweep viscosity measurements for PLA, aPHA, their blends and the CA masterbatch at 185 °C.

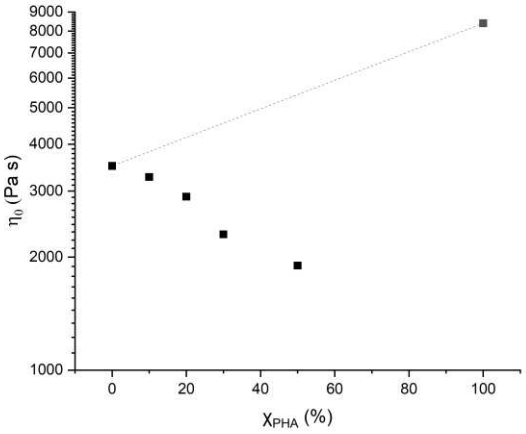

Figure 5.3 Zero-shear viscosity values at 185°C of obtained PLA/aPHA blends and the pure polymers. The dotted line represents the log-additivity dependence of an ideal miscible blend.

The thermal analysis (DSC and DMA) data for the blends is shown in table 5.1. Only the melting peak of PLA was observed both in 1st and 2nd heating scans – confirming the amorphous nature of the PHA and the semicrystalline nature of the PLA. The immiscibility of the two phases resulted in two separate T_gs. The melting temperature (167-171 °C) and the crystallinity degree (χ_c =0.25-0.27) of the PLA phase were not appreciably modified by the blending with aPHA. The T_g of PLA (T_g2) was 60°C as measured by DSC and did not vary appreciably throughout the composition range of the blends by any measurement technique, except for H50, where T_g2 increased by around 10° by DMA measurements. The T_g of aPHA (T_g1) was found to vary slightly according to composition, decreasing as aPHA content decreased, as measured by DSC from -16 °C for the pure polymer to -22 °C for the H10 blend and as measured by the tan δ DMA peak from -8 °C for the pure polymer to -14 °C for H10. Measurements from the E" peak on the other hand did not result in appreciable variations. This is very similar to what we previously observed for blends of aPHA with amorphous PLA and is consistent with previous research on the glass transition of soft low-T_g phases in blends with PLA.[202,220]

Table 5.1 Thermal analysis data for aPLA/aPHA blends. The melting peak measured is the one in the first heating cycle.

	PLA	H10	H20	H30	H50	CA	aPHA
T_g1 (°C)[1]	*	-22.3	-17.1	-20	-17.3	-17.4	-15.9
ΔCp1 (J/g*K)[1]	*	0.004	0.135	0.138	0.268	0.16	0.482
T_g1 E'' (°C)[2]	*	-14.3	-15.1	-15.2	-17.6	-14.7	-15.7
T_g1 tanΔ (°C)[2]	*	-14.3	-13.9	-13.9	-12.9	-13.6	-7.9
T_m (°C)[1]	167	171	168	168	168	149	*
ΔH_m (J/g)[1]	37	33.5	28.3	26.6	17.8	21.3	*
χ_c PLA	0.26	0.27	0.25	0.27	0.25	0.22	*
T_g2 (°C) [1]	60.1	58.9	58.3	59	58.6	56.8	*
ΔCp2 (J/g*K)[1]	0.501	0.457	0.414	0.345	0.283	0.347	*
T_g2 E'' (°C) [2]	61.5	59.8	61.5	59.7	69.8	60.4	*
T_g2 tanΔ (°C) [2]	69.1	68.4	68.7	67.6	78.5	67	*

[1] Measured by DSC [2] Measured by DMA

DSC was also used to investigate the recrystallization properties of the blends. It is already evident from a conventional DSC scan that the presence of the dispersed aPHA phase strongly enhances the recrystallization kinetics of PLA, as on the second DSC heating scan (reported in table 5.2) the degree of crystallinity of pure PLA was only 0.02 while the one of the blends was in all cases 0.21-0.22, quite close to the one measured on the first heating scan on the annealed blends. Most of this recrystallization took place as cold crystallization and a smaller portion as melt crystallization. As batch foaming involves an isothermal saturation step, during which the polymer may undergo recrystallization, it is of interest to estimate the cold crystallization kinetics at various temperatures. The testing was conducted without the CO_2 pressure present in the autoclave; thus, it is not directly descriptive of the behavior during the saturation step but should nevertheless give an indication on the kinetics of the process.

Table 5.2 Degree of crystallinity as calculated from DSC of PLA and PLA/aPHA blends after different thermal treatments. Annealed samples were heated to 60°C for 16 hours, quenched samples were quickly cooled from the melt, the other scans are described in the instrumental section. The net melting peak area value from which X_c is calculated is obtained by the subtraction from the area of the melting peak of the cold crystallization peak if present apart from the 2nd DSC scan X_c value, which is calculated from the melting peak area without subtracting cold crystallization.

Experimental condition	X_c (PLA)					
	PLA	**H10**	**H20**	**H30**	**H50**	**CA**
2nd DSC scan	0.03	0.22	0.22	0.23	0.22	0.04
Annealed	0.26	0.26	0.25	0.27	0.25	0.21
Quenched	0	0.09	0.07	0.08	0.07	0.03
T_{CC} = 75°C	0.01	0.14	0.18	0.13	0.15	0.03
T_{CC} = 90°C	0.02	0.25	0.27	0.26	0.25	0.19
T_{CC} = 105°C	0.08	0.23	0.23	0.23	0.21	0.16
T_{CC} = 120°C	0.16	0.23	0.25	0.25	0.23	0.18
Time to full recystallization (min)						
T_{CC} = 75°C	>25	>25	>25	>25	>25	>25
T_{CC} = 90°C	>25	5	4	5	4	18
T_{CC} = 105°C	>25	2	2	2	2	7
T_{CC} = 120°C	>25	1	1	1	1	5

For this analysis the polymer melt was rapidly cooled to room temperature and then rapidly heated to a cold crystallization temperature (T_{CC}) in the interval of the cold crystallization peak (75-120 °C) observed in a 10 °C/min DSC scan. It was then kept at T_{CC} for 25 minutes, representative of isothermal saturation and then heated again to measure χ_c using the melting peak area. The results are reported in table 5.2. If the isothermal step was not present, the pure PLA remained completely amorphous, while all blends displayed a slight degree of crystallinity (χ_c = 0.03-0.06), increasing with aPHA content and attributable to the capacity of the blends of melt crystallizing even upon fast cooling. The degree of crystallinity of the pure PLA then increased as T_{CC} was increased, but even at 120 °C never reached the values measured on the fully annealed polymer, an indication of a slow cold crystallization process always taking longer than 25 minutes. All blends behaved quite differently from the pure polymer but similar to each other as T_{CC} was increased. At T_{CC} = 75 °C the blends partially recrystallized while at T_{CC} = 90 °C and greater the full recrystallization to values equal to those of the fully annealed blends was observed. Thus,

cold crystallization time was greater than 25 minutes at 75 °C but lower at higher temperatures. The dip in apparent χ_c at T_{CC} = 105 °C is explainable by the presence of a double melting peak (figure 5.4) attributable to the presence of α' crystalline phase, which has a lower melting enthalpy than the α phase and is associated with crystallization temperatures below ~120 °C.[185,238] PLA recrystallized at 75-90 °C was originally in the α' phase but was able to reorganize itself fully in the α phase during the heating scan, while PLA recrystallized at 120 °C was already in the α phase.

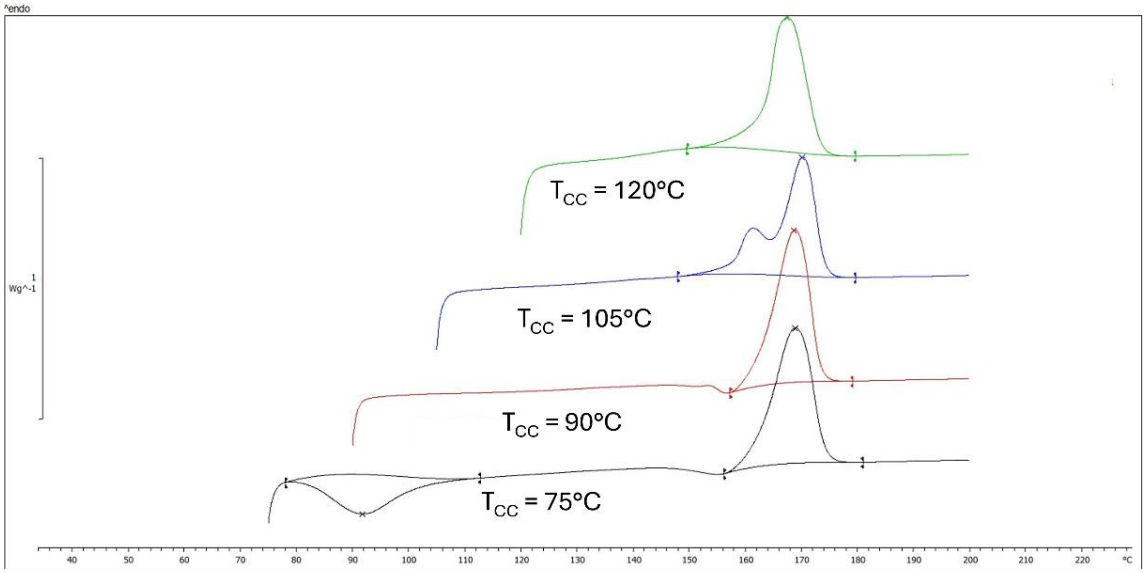

Figure 5.4 DSC heating scan for H30 measured after the isothermal step of recrystallization tests. The other blends show similar curves.

The time of recrystallization was also evaluated (table 5.2, shown in figure 5.5) and was remarkably fast and similar for all blends, taking less than 5 minutes at temperatures of 90 °C or higher. Only at T_{cc} = 75 °C the recrystallization took longer than 25 minutes - the very wide crystallization peak in this case is not distinguishable in the DSC graph. The CA masterbatch by contrast, while still far quicker in cold crystallization than the pure polymer, was significantly slower than the blends obtained from the compounder, which may be due to its lower D- content slowing down crystallization or even due to the lamellar blend morphology.

Overall, the blending of aPHA with semicrystalline PLA enhances the latter's crystallization kinetics in both isothermal and non-isothermal conditions but does not raise the maximum degree of crystallinity that can be reached. A similar behavior in non-isothermal conditions has already been reported for PLA/aPHA blends by Aversa et al.[202], except that they note a decrease in PLA crystallinity as aPHA content reaches 50%, which, instead, we did not observe.

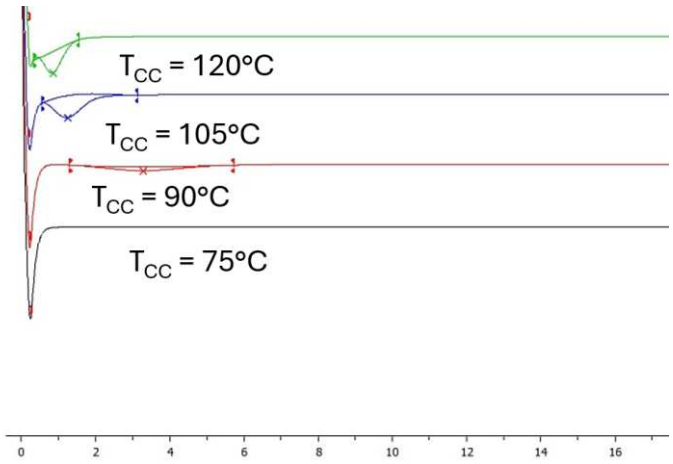

Figure 5.5 Heat flow as a function of time during the isothermal recrystallization step for H30. The other blends show similar curves

Both PLA and the blends were foamed. The main tests were carried out on PLA, the H10, H20 and H30 blends and the CA masterbatch fixing the saturation time at 30 minutes, the CO_2 pressure at 140 bar and varying temperature. More limited testing and no morphology studies were carried out on the H50 blend, for which no foams with density below 0.6 g/cm^3 could be obtained. These will not be discussed in detail and obtained densities are reported in the full sample list in table 5.S1.

To examine the effect of PLA crystallinity, samples were foamed starting from:

- annealed specimens, which are crystallized to their maximum crystallinity degree
- quenched specimens obtained by quick cooling after melting, which are amorphous or only slightly crystalline

Samples were also tested in both bead and sheet shape. The polymers were then saturated isothermally with CO_2 and then depressurized to achieve foaming.

The overall behavior of PLA is shown in figure 5.6. Annealed and quenched samples had very different foaming windows. Annealed PLA achieved only minimal expansion ratios until the temperature reached above 150 °C. This is caused by the polymer having too high a degree of crystallinity to allow for the expansion of the rigid structure. When the polymer starts to melt, which happens at a temperature around 20 °C lower than the peak melting point of the polymer, a progressive drop in crystallinity occurs, allowing the gas bubbles to expand to a certain degree when the pressure drops. As saturation temperature was further raised the density of the obtained foam reached a minimum (157 °C), with a density around 0.2 g/cm^3 and a volume expansion ratio (VER) around 6, and then started increasing again until at 170 °C (the DSC melting peak) it once again reached the density of the pristine polymer. The samples saturated at 170 °C were also visually transparent rather than

opaque like the other samples, a sign that at this temperature all the dissolved CO_2 escaped from the matrix before this could cool, and the final product is free from trapped gas.

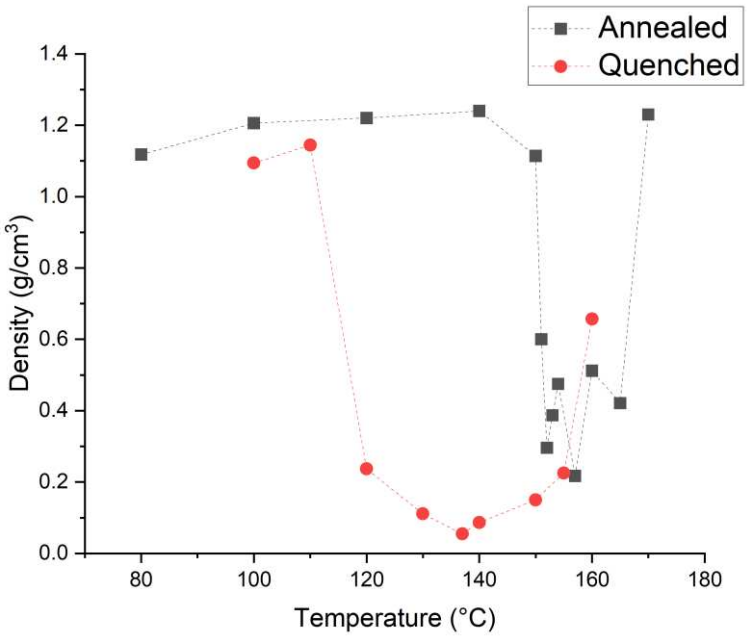

Figure 5.6 Density of obtained foam samples as a function of saturation temperature for annealed and quenched PLA 4032D samples.

By contrast, the quenched PLA is not already crystallized at the start of the experiment, and it is essentially amorphous before the saturation phase, meaning the polymer undergoes recrystallization at the same time as supercritical CO_2 is dissolving within it. The foaming window of the quenched PLA was found to be in the 120-160 °C temperature range, with a maximum expansion ratio and minimum density being found at 137 °C. The maximum volume expansion ratio obtained (VER = 22) was more than three times higher than the one that could be obtained for the annealed PLA (VER = 6). Samples tested at lower saturation temperatures than 120 °C were too rigid to undergo foaming, while samples tested at 165 °C were found to be transparent with no retained CO_2.

Observing the morphology of the foam samples obtained from quenched (figure 5.7) and annealed (figure 5.8) samples, the prevalent cell structure is elongated and varying in shape and size throughout the foam. The cells were generally elongated in the “thickness” direction of the foamed sheet, while locally, around the corners of the foamed sheet regions with a more regular morphology and non-elongated cells were formed. In the samples foamed at 120 °C and then at 140 °C and above another phenomenon is noticed, the presence of unfoamed, fairly large (10-50 μm in size) crystalline spherulites within the foam structure. These objects locally influence the cell structure around them in two ways, first by the

formation of interlamellar very small cells on the outside surface of the spherulite and second, by orienting the elongation of the cells around them outward from the spherulite rather than in the transversal direction. This structure has already been observed in other research and named petal-like or stamen-like and the formation of the elongated cells around the spherulites has been attributed to the exclusion of CO_2 from the crystal growth front.[239,240] In the case of annealed PLA foaming tests (figure 5.8), a similar morphology to the quenched PLA - elongated closed cells, large spherulites - was noticed for the sample foamed at 156 °C, while raising temperature to 160 °C, which is close to the melting point ,the foam assumed a mostly open-cell structure, the cells were still elongated but spherulites were not observed.

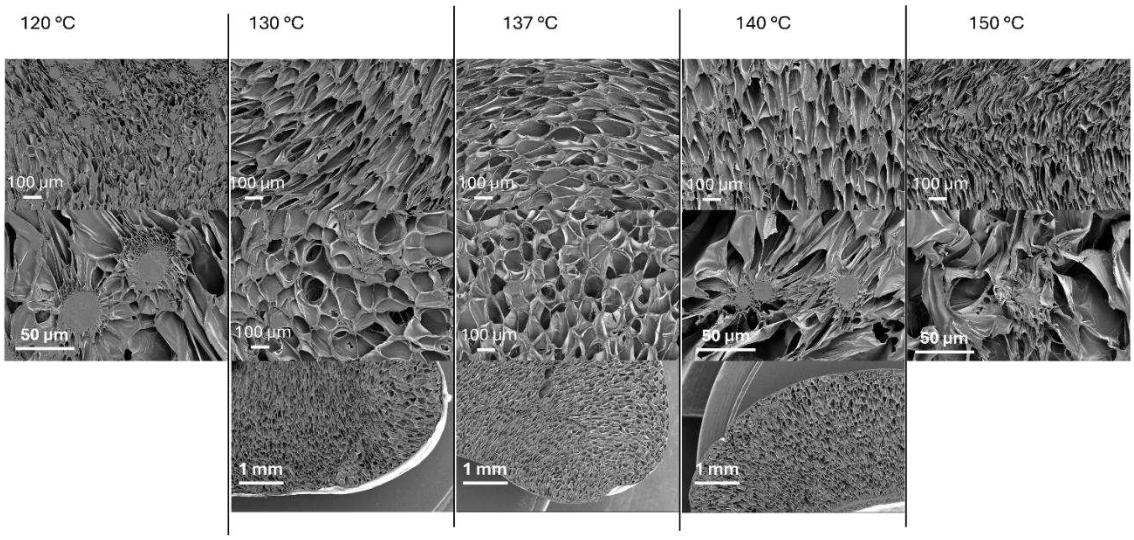

Figure 5.7 SEM images of cross-sections of PLA samples foamed from quenched sheets at various temperatures.

Xu and Huang observed very alike foam morphologies working by a similar batch process on quenched PLA sheets, with the formation of “stamen-like” structures around spherulites and the spherulites changing in size depending on foaming temperature and affecting cell structure.[239] By contrast Li et al., working with our same PLA grade, reached similar expansion ratios at similar temperatures, and did not observe large spherulites. More regular foam morphologies with smaller cells were thus observed. However they used a different pre-treatment process consisting in a partial isothermal recrystallization under CO_2 pressure, which could explain the differences.[241]

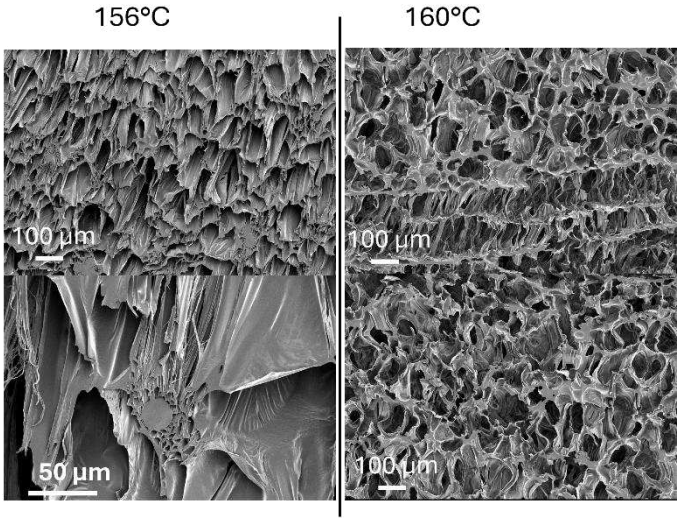

Figure 5.8 SEM images of cross-sections of PLA samples foamed from annealed sheets at various temperatures.

The foaming of the PLA/aPHA blends was also tested, as for the pure PLA, after either an annealing or quenching pretreatment of the samples. The plots of achieved density against temperature are shown in figure 5.9. The foaming window for annealed blends was quite similar to the one observed for PLA: narrow at temperatures slightly lower than the melting peak and minimum density achieved around 155 °C (135°C for the lower-melting CA blend). The results, however, are very different from those previously described in the case of the quenched samples. In this case, no foaming window was noticed that was similar to that of PLA, and the samples remained essentially unfoamed when processed in the 120-160 °C temperature interval. This is attributable to the fast recrystallization of the blends at these temperatures resulting in the maximum degree of crystallinity being reached within a couple of minutes. This occurs before CO_2 can be solubilized within the matrix, effectively then acting the same as the stiff annealed samples. At 160 °C the samples transition directly from opaque (trapped CO_2) to transparent (escaped CO_2) when the crystals cannot form at all due to the melting onset being reached. Another phenomenon that was observed for the annealed blends is that samples in bead shape were capable of foaming to lower densities than the samples in sheet shape, more prominently for H10 and H20 and with reduced effect for H30 and CA. This was not observed for pure PLA or for blend samples foamed in different conditions, in which cases beads and sheets foamed to similar densities to each other.

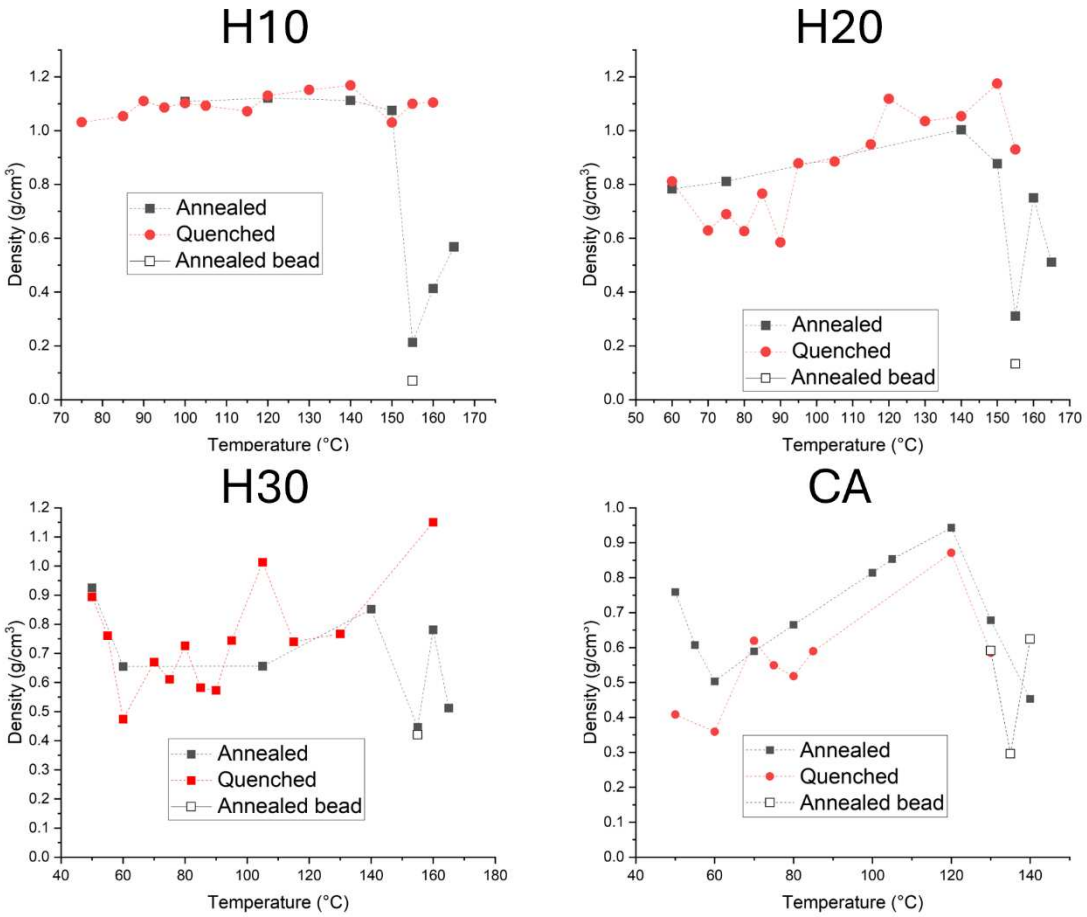

Figure 5.9 Density of obtained foam samples as a function of saturation temperature for annealed and quenched PLA/aPHA samples.

The blend composition also influenced foaming in two important ways, first the minimum achievable density at 155 °C was inversely affected by aPHA content. Second, as aPHA content was increased, a second foaming window started appearing at temperatures below 120 °C. This did not happen for the H10 blend but was observed for the H20 blend and more prominently in the H30 blend. The CA blend, with similar content to H30 also behaved similarly. This low-temperature foaming was observed both in annealed and quenched samples, but quenched ones achieved lower densities. The minimum density for H20 samples in this low-temperature window was higher than the one achievable at close to the melting point, while it was similar for H30 and CA where aPHA content was higher. As aPHA content is increased, the blends become more flexible, with a lower modulus.[202] This makes expansion of the foam easier even if the PLA matrix itself is fully recrystallized, and this is enhanced if the sample starts amorphous and recrystallizes while CO_2 is dissolved within it. Lower temperatures increase the solubility of CO_2 in the polymer matrix,[242] and this may explain why densities decrease with temperature, reaching a minimum and then increasing

again when glass transition is approached and the samples become once again too stiff to expand.

The morphology of the blend foams can be analyzed both in the high-temperature and the low-temperature foaming windows. Compared to PLA foams, the elongated cells phenomenon, as well as the formation of large spherulites, were never observed for the blends, at any temperature and any sample shape. The greater flexibility of the blend materials could allow for better structural relaxation during expansion, as opposed to a pure PLA matrix quickly becoming very stiff upon cooling.

In high-temperature foaming of annealed blends (figure 5.10), the influence of the sample shape is very evident, as sheets foam to smaller cell structures (10-15 μm vs 30-40 μm for beads) caused by larger nucleation densities. The influence of blend composition to density seems to be attributable mostly to cell wall thickness. Beads foamed with a 10-30% aPHA content in fact have similar cell size and nucleation densities, but it was the increase in cell wall thickness, especially prominent for H30 that caused higher densities. The CA blend at 135°C had its own different behavior, as a gradient was formed between a low-density core with larger cells and more compressed high-density and smaller cell sized foam edges.

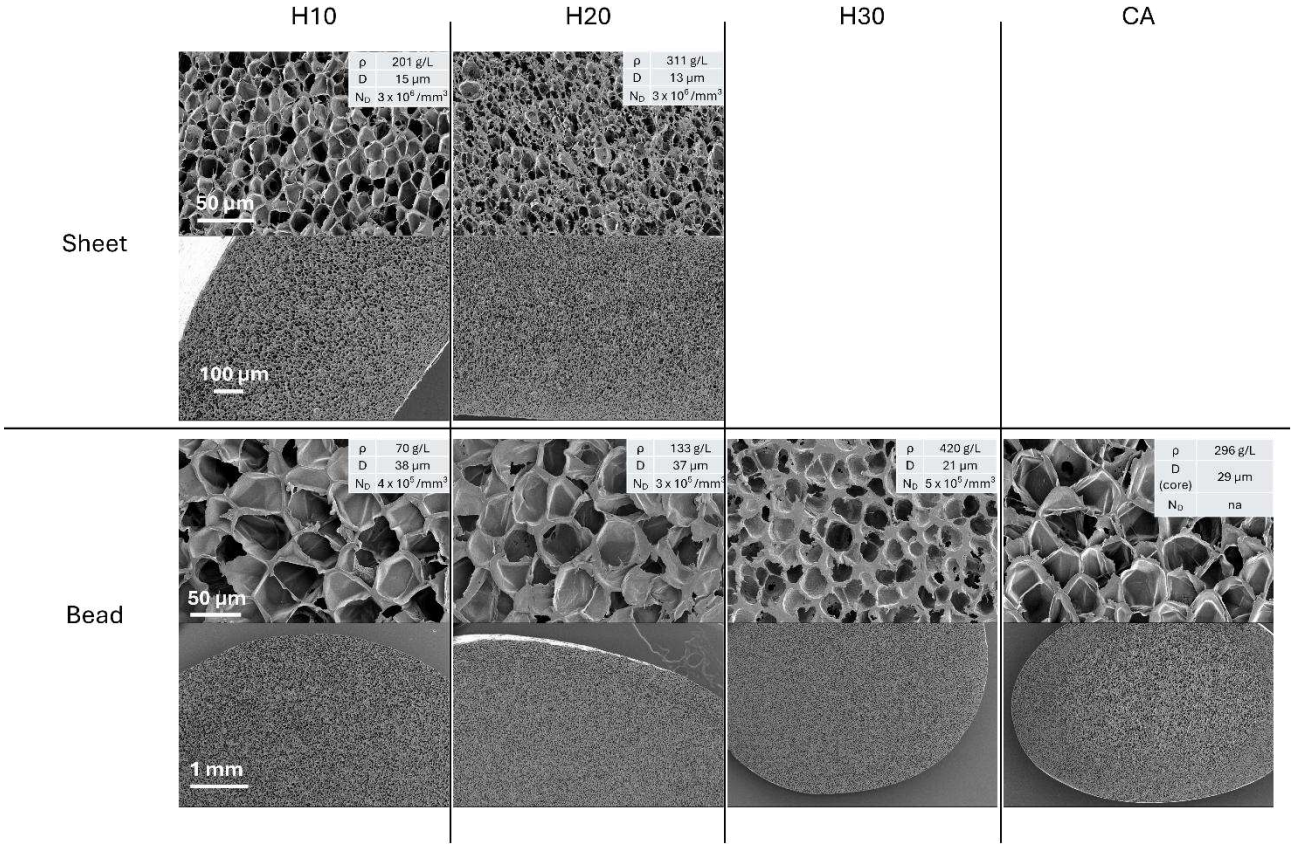

Figure 5.10 SEM images of cross-sections of blend foam samples obtained from annealed samples saturated at 135 °C (CA) or 155 °C (all other samples). Scale bars apply to all images on the same row.

The foams obtained by low temperature foaming - T < 100 °C – of the H30 and CA blends were found to have their own kind morphology, a microcellular one (figure 5.11). Cell sizes were smaller and distributed unevenly throughout the foam structure in bands parallel to the sample skin. While identifying a single cell size describing each foam sample is for this reason challenging, all areas of the observed foams were found to be microcellular with an average cell size < 5 μm, in a context where larger coalesced cells 10-20 μm in size coexist with nanometric ones.

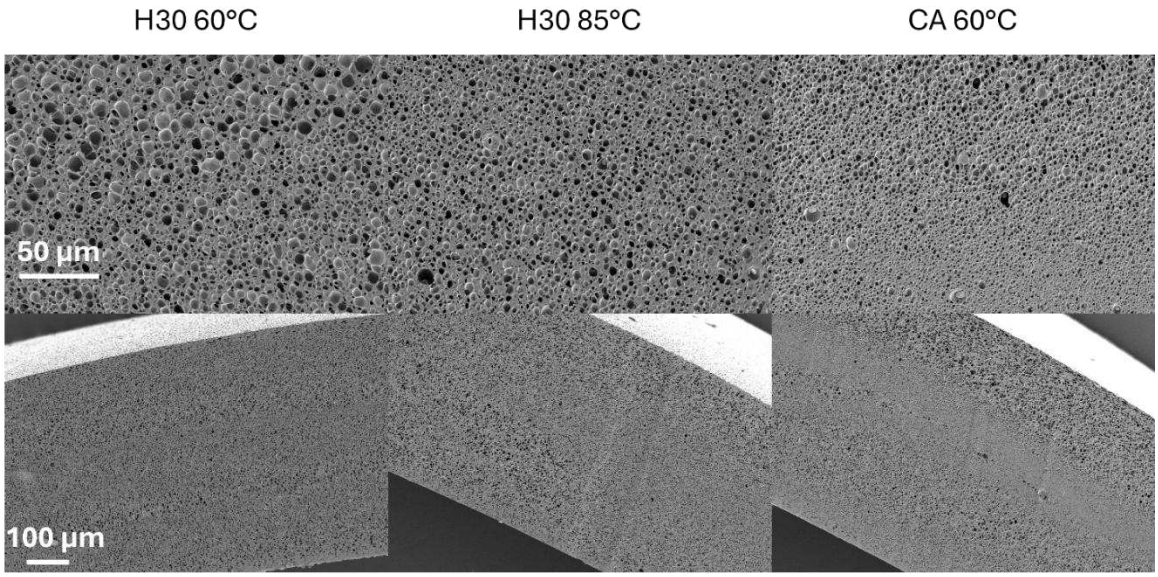

Figure 5.11 SEM images of cross-sections of blend foam samples obtained from quenched samples saturated at the specified temperatures. Scale bars apply to all images on the same row.

The biodegradation behavior of these low-density foams was analyzed in lab-simulated home composting conditions working at 30 °C.The foams chosen for the test were the lowest density available for each composition, which were obtained for H10, H20 and H30 by using bead foams from annealed granulate (bottom row of figure 5.10), and for PLA by foaming quenched sheets at 137 °C (middle column of figure 5.7). Density and cell structure of these samples were thus quite heterogeneous. An aPHA film was also tested for reference of the pure material in these conditions. The mineralization of the samples was measured by respirometry over a 5-month interval and further analysis (weight loss, SEC, NMR, SEM) was carried out on select samples over time as well as on the retrieved final residue after 5 months.

From respirometric data we can distinguish between the behavior of the H20 and H30 samples, which saw some slow biodegradation throughout the test period, and the one of PLA and H10, for which no measurable biodegradation took place. In any case, even the

maximum level of biodegradation of 15-16% for the H20 and H30 samples was quite low, and the materials cannot be considered home compostable. The biodegradation rate for all samples was also far slower than the one measured for the aPHA film, which reached 63% after 5 months. The weight loss measured for the samples (table 5.3) was lower than the results from respirometry, only reaching up to 3-4% weight loss. This suggests that the respirometric data is in this case actually an overestimate, while confirming the slight degree of biodegradation capability conferred by aPHA contents of at least 20%.

SEC measurements (table 5.3) show that the foam made from pure PLA did not decrease at all in molecular weight over the timeframe of the experiment, while all blend foams saw a decrease quantifiable to 20-30% in number-average molecular weight and a moderate increase in polydispersity from around 2 to 2.3-2.5, indicating that a degree of breakdown of the polymeric chains is ongoing for aPHA-containing samples, though it is uncertain to what extent this is due to either of the polymer components of the blend.

Table 5.3 Gravimetric weight loss and SEC data (number-average molecular weight, polydispersity index) gathered for foamed samples of PLA 4032D and blends with aPHA after a given number of days in domestic composting conditions. Values after 150 days are the average of three replicates with standard deviation as error.

Weight loss (wt%)				
Time (days)	*0*	*45*	*115*	*150*
PLA	-	n.a.	0	1.3±0.8
H10	-	0	0.1	0.9±0.8
H20	-	0	0.9	4±2
H30	-	0	0.8	3±2
Mn (kDa)				
Time (days)	*0*	*45*	*115*	*150*
PLA	96	n.a.	100	111 ± 7
H10	103	76	77	68 ± 2
H20	95	67	69	64 ± 7
H30	94	54	70	65 ± 7
PDI				
Time (days)	*0*	*45*	*115*	*150*
PLA	2.01	n.a.	2.06	1.8 ± 0.1
H10	2.06	2.13	2.39	2.53 ± 0.04
H20	2.04	2.15	2.33	2.4 ± 0.1
H30	2.04	2.15	2.24	2.32 ± 0.05

The morphology of the foams incubated in domestic composting conditions is shown in figure 5.12. The overall cell structures of the internal section of the foam were essentially unchanged from the ones of the pristine foams (figures 5.7 and 5.10), confirming that the bulk of the foams was not altered by any biodegradation process.

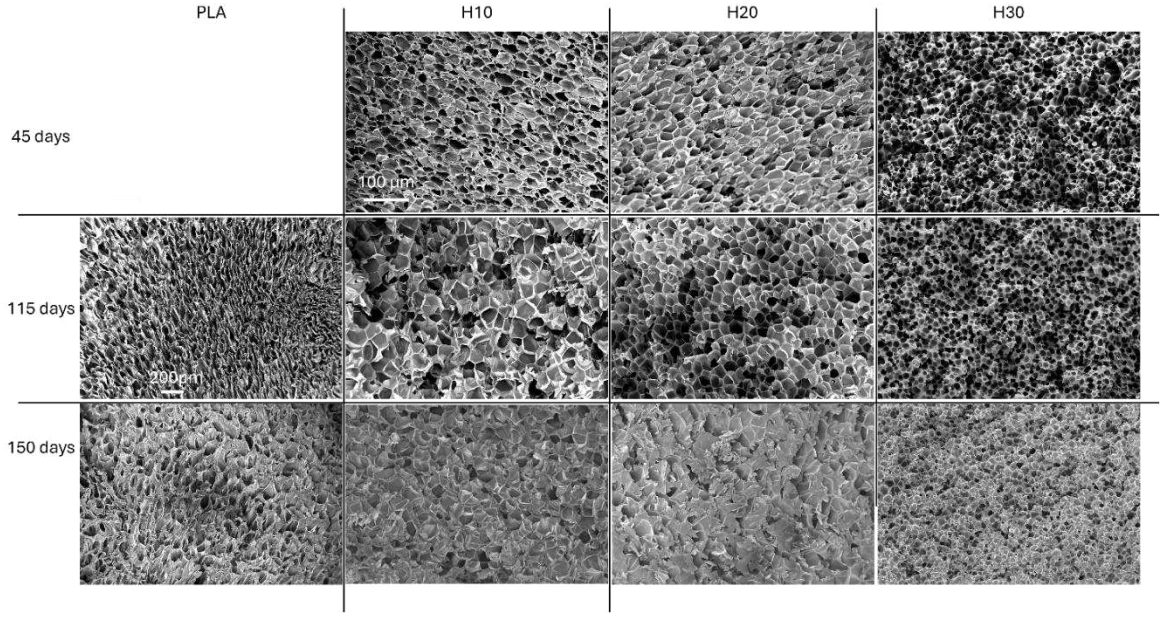

Figure 5.12 SEM images of cross-sections of the foam samples tested for biodegradation in domestic composting conditions after a given exposure time. The scale bar on the left row applies to PLA foam, the scale bar on the upper middle left to all blend foams.

Overall, the results show that there was only a small increase in biodegradation capacity in domestic composting conditions in foams obtained from blends of semi-crystalline PLA and aPHA. This is strikingly different from the results observed for similar foams obtained from blends of aPHA with amorphous PLA (chapter 4), which were degraded in a much more effective way not only in domestic composting but also in seawater. In this case, instead of enhancing the biodegradation properties of PLA, it was the ones of aPHA that were inhibited by being included in the blend. The research of Han et al. on blend films already showed that similar blends of aPHA with semicrystalline PLA have far slower biodegradation than the ones with a more amorphous PLA, but the films were still able to reach around 20% biodegradation within 45 days of measurement with 30% of aPHA content.[63] This different behavior suggests that the particular morphology of a closed-cell foam instead of a film has a further delaying effect on blend biodegradation.

5.4 Conclusions

In this study we obtained blends of semicrystalline PLA and amorphous P34HB (aPHA) with a 10-50 % content of aPHA were obtained and investigated their morphology and thermo-mechanical properties, revealing that the mixture at this ratio is not miscible and that the PHA phase is dispersed in the PLA phase with a phase size of 200-400 nm at 10-30% aPHA content and co-continuous at 50% content. The glass transition of the PLA phase was not influenced by the presence of the PHA phase, while the latter shifted slightly towards lower temperatures. The maximum crystallinity that could be reached by the PLA phase remained unchanged, but its cold crystallization kinetics were strongly accelerated by the presence of the aPHA phase. Shear rheology measurements also showed a strong negative deviation from ideal blend behavior, suggesting the formation of low-viscosity interphase layers in the melt.

The foaming behavior using supercritical CO_2 as the agent in a batch foaming system was determined for both the pure and blended polymers. The chosen PLA had a wider foaming window when used as a mostly amorphous quenched polymer rather than being annealed beforehand. The cell structure was generally elongated, uneven throughout the foam structure and mostly closed-cell. Large spherulites (10-50 μm) orienting the foam structure around them in flower-like structures were also observed in all but the lower-density PLA foams. By contrast the PLA/aPHA blends were unable to foam at all when saturated in quenched form, most likely due to their very fast recrystallization properties. When foamed in the narrow window before melting, however, they were able to form more regular and non-elongated cell structures compared to PLA and did not form large spherulites. The minimum achievable density was higher as aPHA content increased, ranging from 70 g/L for 10% wt. aPHA to 400 g/L for 30% wt. For blends with an aPHA content of 30%, a second foaming window was also observed in the 60-100 °C temperature interval, where microcellular medium-high density (300-600 g/L) foams were obtained.

By the study of biodegradation of blend foams in a domestic composting environment, we observed little degradation in all cases over a 5-month period, although a slight improvement was obtained with the addition of aPHA, which resulted in 3-4% weight loss and a decrease by around a third of the average molecular weight, compared to basically no change of pure PLA. Thus, the biodegradation of the PLA component was, at most, only slightly enhanced and the one of the aPHA component was strongly inhibited.

By comparison with the fully amorphous blends described in chapter 4, the semicrystalline blends thus resulted more challenging to foam to low densities, especially as aPHA content is increased above 20 %, as well as significantly slower in biodegradation in domestic

composting conditions. These factors need to be taken into account for possible usages, to analyze whether they offset the expected advantages in mechanical and thermal resistance of the foams resulting from the crystalline component of the blends.

5.5 Supporting information

Table 5.S1 Full list of foaming trials with obtained densities as a function of saturation temperature, sample shape and pretreatment

Sample	Sample shape	Pretreatment	T (°C)	Density (g/cm^3)
PLA	sheet	Annealed	80	1.118
PLA	sheet	Annealed	100	1.206
PLA	sheet	Annealed	120	1.22
PLA	sheet	Annealed	140	1.24
PLA	sheet	Annealed	150	1.114
PLA	sheet	Annealed	155	0.671
PLA	sheet	Annealed	157	0.217
PLA	sheet	Annealed	165	0.421
PLA	sheet	Quenched	100	1.094
PLA	sheet	Quenched	110	1.144
PLA	sheet	Quenched	120	0.237
PLA	sheet	Quenched	130	0.111
PLA	sheet	Quenched	137	0.055
PLA	sheet	Quenched	140	0.233
PLA	sheet	Quenched	150	0.15
PLA	sheet	Quenched	155	0.225
PLA	bead	Annealed	150	1.1
PLA	bead	Annealed	155	0.33
PLA	bead	Annealed	156	0.225
PLA	bead	Annealed	157	0.430
PLA	bead	Annealed	160	0.512
H10	sheet	Annealed	100	1.108
H10	sheet	Annealed	120	1.121
H10	sheet	Annealed	140	1.112
H10	sheet	Annealed	150	1.075
H10	sheet	Annealed	155	0.213
H10	sheet	Annealed	160	0.413
H10	sheet	Annealed	165	0.568
H10	sheet	Annealed	170	1.21
H10	sheet	Quenched	75	1.031
H10	sheet	Quenched	85	1.053
H10	sheet	Quenched	90	1.11
H10	sheet	Quenched	95	1.086
H10	sheet	Quenched	100	1.102
H10	sheet	Quenched	105	1.092
H10	sheet	Quenched	115	1.072

H10	sheet	Quenched	120	1.13
H10	sheet	Quenched	130	1.151
H10	sheet	Quenched	140	1.168
H10	sheet	Quenched	150	1.03
H10	sheet	Quenched	155	1.1
H10	sheet	Quenched	160	1.2
H10	bead	Annealed	155	0.07
H20	sheet	Annealed	60	0.783
H20	sheet	Annealed	75	0.811
H20	sheet	Annealed	140	1.003
H20	sheet	Annealed	150	0.877
H20	sheet	Annealed	155	0.311
H20	sheet	Annealed	160	0.75
H20	sheet	Annealed	165	0.511
H20	sheet	Annealed	170	1.155
H20	sheet	Quenched	60	0.811
H20	sheet	Quenched	70	0.854
H20	sheet	Quenched	75	0.689
H20	sheet	Quenched	80	0.626
H20	sheet	Quenched	85	0.766
H20	sheet	Quenched	90	0.585
H20	sheet	Quenched	95	0.878
H20	sheet	Quenched	105	0.885
H20	sheet	Quenched	115	0.949
H20	sheet	Quenched	120	1.118
H20	sheet	Quenched	130	1.035
H20	sheet	Quenched	140	1.053
H20	sheet	Quenched	150	1.175
H20	sheet	Quenched	155	0.93
H20	bead	Annealed	155	0.133
H30	sheet	Annealed	50	0.925
H30	sheet	Annealed	60	0.655
H30	sheet	Annealed	105	0.656
H30	sheet	Annealed	140	0.852
H30	sheet	Annealed	155	0.446
H30	sheet	Annealed	160	0.781
H30	sheet	Annealed	165	0.512
H30	sheet	Quenched	50	0.894
H30	sheet	Quenched	55	0.761
H30	sheet	Quenched	60	0.474
H30	sheet	Quenched	70	0.67
H30	sheet	Quenched	75	0.611
H30	sheet	Quenched	80	0.726
H30	sheet	Quenched	85	0.276 or 0.582
H30	sheet	Quenched	90	0.573
H30	sheet	Quenched	95	0.744
H30	sheet	Quenched	105	1.013

H30	sheet	Quenched	115	0.74
H30	sheet	Quenched	130	0.767
H30	sheet	Quenched	160	1.15
H30	bead	Annealed	70	0.854
H30	bead	Annealed	155	0.42
H30	bead	Quenched	60	0.441
H30	bead	Quenched	85	0.56
H30	bead	Quenched	150	0.524
H50	sheet	Annealed	60	0.86
H50	sheet	Annealed	105	0.899
H50	sheet	Quenched	50	0.846
H50	sheet	Quenched	60	0.925
H50	sheet	Quenched	75	0.964
H50	sheet	Quenched	85	0.628
H50	sheet	Quenched	120	0.994
H50	sheet	Quenched	155	0.808
CA	sheet	Annealed	50	0.759
CA	sheet	Annealed	55	0.607
CA	sheet	Annealed	60	0.503
CA	sheet	Annealed	70	0.589
CA	sheet	Annealed	80	0.665
CA	sheet	Annealed	100	0.814
CA	sheet	Annealed	105	0.853
CA	sheet	Annealed	120	0.943
CA	sheet	Annealed	130	0.678
CA	sheet	Annealed	140	0.453
CA	sheet	Quenched	50	0.408
CA	sheet	Quenched	60	0.359
CA	sheet	Quenched	70	0.619
CA	sheet	Quenched	75	0.549
CA	sheet	Quenched	80	0.518
CA	sheet	Quenched	85	0.589
CA	sheet	Quenched	120	0.871
CA	sheet	Quenched	130	0.585
CA	bead	Annealed	130	0.591
CA	bead	Annealed	135	0.296
CA	bead	Annealed	140	0.62

6. Evaluation of cytocompatibility and osteoinductivity of peptide-functionalized poly(lactic acid)-based scaffolds obtained from waterborne dispersions using an in vitro model of Human Adipose-derived stem cells

6.1 Introduction

Bone damage and degenerative diseases caused by various reasons, such as aging, accidents, and sports injuries, are usually treated with metal or biomaterial implants for functional recovery. With the increase in the elderly population and the emergence of complex bone-related diseases, the demand for implants is increasing, as is the demand for the production of high-quality implants with better performance.[243]

The reasons for the success of metal implants in the human body include their high resistance to wear and corrosion and their ability to fuse well with surrounding tissues. Stainless steel, titanium, magnesium, cobalt-chromium, and their alloys are the most commonly used materials in biomedicine.[244]

In particular, titanium alloys, more specifically Ti-6Al-4V alloys, also known as Ti64, are preferred in the field of biomedical applications. Over the years, attention has shifted towards optimizing their performance and biocompatibility. For example, the disparity in mechanical properties, particularly between the hardness and elastic modulus of the Ti64 alloy and human bone, can give rise to a phenomenon known as stress shielding, which can potentially disrupt the natural growth and healing of bone tissue, thereby decreasing the biocompatibility of implants. Furthermore, the absence of intrinsic antibacterial properties in Ti64 alloy often leads to post-implantation bacterial infections, causing a range

of clinical complications and jeopardizing the success of the implant and the well-being of patients. Antibacterial treatments, secondary surgeries, and reimplantation are often necessary to address these issues, significantly increasing costs. Researchers are continually exploring new solutions to overcome or limit these critical issues. One effective approach involves modifying the surface of materials using coatings.[244,245]

One of the roles for which coatings are designed is to improve the biocompatibility of Ti64 implants, promoting cell growth and optimizing their functionality. The surface properties of implants are crucial in determining their biological responses within the body. For example, bone implants must have superior bone formability for proper biological integration. Over the years, various techniques have been used to apply coatings, such as electrophoretic coating, plasma spray, laser deposition, biomimetic deposition, and methods such as sol-gel-based spin-and-dip deposition or spray deposition.[246]

Polymer coatings are important in tissue engineering applications, as the biocompatibility and elasticity of implants are very important properties that can be optimized by applying appropriate coatings. In particular, bone tissue engineering (BTE) therapy is an area of growing interest due to the challenges related to the osseointegration of bioresorbable scaffolds and the management of bone infections. The most commonly used materials for BTE include ceramics, composites, and biodegradable polymers (synthetic and natural), such as poly(glycolic acid) (PGA) and poly(lactides), such as poly(L-lactic acid) (PLLA) and poly(D-lactic acid) (PDLA).[247] Three-dimensional porous scaffolds of PLA have been created for cell cultures of various types, using cell gene therapy for cardiovascular diseases, muscle tissue, bone and cartilage regeneration, and other cardiovascular, neurological, and orthopedic treatments.[248]

PLA coatings and thin films obtained for such purposes in existing research are generally prepared by solvent casting using toxic chlorinated solvents such as dichloromethane and chloroform.[249,250] The waterborne methodology described in the previous chapter is a more sustainable and healthy alternative to these methods while also offering a facile way of including active water-soluble or dispersible compounds within the PLA matrix.

Peptides are, formally, oligomers or polymers consisting of amino acids connected to each other by amide bonds between the carboxyl group of one amino acid and the amino group of the next. Peptides and proteins are the basic molecules for countless biological and physiological processes in living organisms acting as hormones, neurotransmitters, antibodies, enzymes, transporters, and structural components. Osteogenic peptides were discovered in the 1980s, and later their ability to promote bone formation, known as osteogenesis, was recognized.[251]

The first application of bone tissue regeneration can be attributed to Urist, whose research led to the discovery of Bone Morphogenic Proteins (BMPs).[252] These are a group of proteins derived from demineralized bone extracts and are part of the transforming growth factor β (TGF-β) superfamily. They are identified by their ability to initiate ectopic bone formation in adult animals. This unique feature of BMPs has allowed them to be used successfully as therapeutic agents for bone repair. In fact, improving bone regeneration by increasing BMP signaling has become standard practice in spinal fusion surgery and tibial fracture healing. Among these proteins, BMP-2 in particular has been tested and found to induce the formation of new cartilage and bone. It has also been shown that the absence of BMP-2 production by skeletal cells causes significant delays in the formation of secondary ossification centers in each of the endochondral bones of the limb and, as early as two weeks after birth, bones lacking BMP-2 show obvious microfractures. If this damage is not repaired, fracture occurs in a relatively short time.[253,254]

A growing number of studies show that BMPs work in synergy with the vascular endothelial growth factor (VEGF), which acts as a promoter in the formation of blood vessels useful for bone formation (angiogenesis).[255] In fact, during natural bone reconstruction following trauma, angiogenesis and osteogenesis occur one after the other. Initially, angiogenic factors, such as VEGF, are expressed, while osteogenic factors, such as BMP-2, are expressed later to facilitate bone tissue formation. Lack of vascularization is one of the main risk factors for reduced bone healing. Blood vessels not only supply oxygen, but also serve as a conduit for additional osteoblasts, play a positive signaling role in promoting cell differentiation, and are necessary for endochondral ossification. VEGF promotes angiogenesis and is known to indirectly increase bone regeneration through the entry of osteoblast progenitor cells (cells specialized in bone tissue production).

With the advent of synthetic techniques, peptides have become an excellent alternative to the use of growth factors as they can be easily synthesized with low-cost liquid or solid phase procedures. Furthermore, being small in size, they are more stable and less immunogenic. Recent studies have introduced a new peptide as a possible bone metabolic parameter: preptin. Preptin is a peptide hormone consisting of 34 amino acids, derived from the precursor of insulin-like growth factor 2 (pro-IGF2) with bone anabolic and insulin secretion amplification properties.[256,257]

As BMP-2 and VEGF are well known osteogenic and angiogenic factors, their combination with PLA-based materials in various forms (scaffolds, coatings, microspheres etc.) as means of introducing them into biological systems has been amply studied.[258–261] The release of combinations of BMP-2 and VEGF from PLA or PLA-PEG block copolymer scaffolds has also been reported.[262,263] However, to our knowledge the incorporation of the more recently discovered preptin peptide in PLA-based materials has not yet been explored.

The main objective of this chapter is to investigate if the water dispersion developed in this thesis can be used to produce coating for biomedical applications, as well. With this idea in mind as model study we developed advanced polymer coatings for biomedical implants, functionalized with specific peptide sequences to promote osteogenesis, a crucial process for the integration of implants into bone tissue. We aimed to synthesize three peptides generally accepted as osteogenic, hBMP2(73-92), hVEGF(17-25), and hPreptin(26-34), using SPPS technology, purification by High-Performance Liquid Chromatography (HPLC) to ensure high purity, and finally characterization by Ultra-Performance Liquid Chromatography-Mass Spectrometry (UPLC-MS) for precise confirmation of the peptide sequence. We also aimed to add the fluorescent molecules TAMRA and carboxyfluorescein by coupling to obtain alternatively the fluorescent peptides TAMRA-hBMP2(73-92), TAMRA-hPreptin(26-34), and Carboxyfluo-hVEGF(17-25).

The peptides are then to be used to functionalize poly(lactic acid) (PLA)-based polymer films that could potentially be used as coatings for titanium-based orthopedic implants, first by selecting a PLA formulation in aqueous dispersion suitable for obtaining films for biomedical uses. The formulations that have been shown in the previous chapter to be best suitable to obtain such films contain a PEG-PLA-PEG block copolymer (ELE) and sodium dodecyl sulfate (SDS) as surfactants. However, while PEG-PLA-PEG copolymers have already been widely used in the biomedical field and are known to have no toxic effects, SDS can only be used in limited quantities. Thus, PLA dispersions using different combinations of ELE and SDS will be characterized by Dynamic Light Scattering (DLS) to determine particle size and zeta potential, which are fundamental indicators of colloidal stability and particle behavior in solution and thin films will then be prepared using these dispersions and subjected to physical characterization, such as weight, thickness, and surface composition. Finally, the films will be sterilized and used in in vitro cytotoxicity studies. Based on the results, the most suitable formulation from a cytotoxicity point of view will be chosen for the next part of the study, in which the previously synthesized peptides will be added, alone or in a combination of all three peptides, as additives to the PLA aqueous dispersion and thin films will be obtained. The osteogenic potential of these films will then by observed by the expression of RUNX2 genes and osteocalcin.

6.2 Matherials and methods

Poly(lactic acid) Ingeo PLA 4060D (PLA) was supplied by NatureWorks LLC (Minnetonka, MN, USA). PLA 4060D is an amorphous polymer with an L-lactide content of approximately 88 wt%.

Methoxy poly(ethylene glycol) (mPEG) with a nominal number-average molecular weight ($\overline{M_n}$) of 2000 g/mol and a dispersity index of 1.06, L-lactide, sodium dodecyl sulfate (SDS), hexamethylene diisocyanate (HDI), and 4 Å molecular sieves were purchased from Sigma-Aldrich (St. Louis, MO, USA). Prior to use, mPEG was dehydrated by azeotropic distillation under nitrogen flow using anhydrous toluene and a Dean-Stark apparatus, followed by drying under reduced pressure. L-lactide was recrystallized twice from anhydrous ethyl acetate, dried under vacuum, and stored under nitrogen.

Tin(II) 2-ethylhexanoate (Sn(Oct)_2) was obtained from TCI Chemicals (Tokyo, Japan).

Solvents including toluene, ethyl acetate, dichloromethane, diethyl ether, and HPLC-grade chloroform were acquired from Carlo Erba (Milan, Italy). Toluene and ethyl acetate were dried by storage for at least 3 days and up to one month over activated 4 Å molecular sieves (20% w/v), which were activated by heating at 200 °C for 24 hours.

Ultrapure water was produced using a Sartorius Arium Mini water purification system fed with pretreated deionized water.

N-Dimethylformamide (DMF) was obtained from Sigma-Aldrich (France). Acetonitrile (ACN) used for HPLC was purchased from Carlo Erba (Italy) or Sigma-Aldrich (France). Trifluoroacetic acid (TFA), triisopropylsilane (TIS), dichloromethane (DCM), piperidine, diethyl ether, N-methyl-2-pyrrolidone (NMP), PyAOP ((7-azabenzotriazol-1-yloxy)trispyrrolidinophosphonium hexafluorophosphate), N,N′-diisopropylcarbodiimide (DIC), oximino acetate (Oxima), and N-ethyl-diisopropylamine (DIPEA) were all purchased from Sigma-Aldrich (France). HBTU, HATU, protected amino acids, and resins were supplied by Iris Biotech AG (Marktredwitz, Germany).

The following Fmoc-protected amino acids were used: Fmoc-Ala-OH (A), Fmoc-Arg(Pbf)-OH (R), Fmoc-Val-OH (V), Fmoc-Glu(OtBu)-OH (E), Fmoc-Gly-OH (G), Fmoc-Gln(Trt)-OH (Q), Fmoc-Trp(Boc)-OH (W), Fmoc-Ile-OH (I), Fmoc-Ser(tBu)-OH (S), Fmoc-Thr(tBu)-OH (T), Fmoc-Tyr(tBu)-OH (Y), Fmoc-Leu-OH (L), Fmoc-Lys(Boc)-OH (K), and Fmoc-Pro-OH (P). Resins employed included Fmoc-L-Leu Wang TG (loading 0.25 mmol/g), Fmoc-L-Ile Wang TG (loading 0.23 mmol/g), and Fmoc-Rink Amide PEG AM (loading 0.33 mmol/g). TAMRA (5(6)-carboxytetramethylrhodamine) and 5(6)-carboxyfluorescein were obtained from Merck (Germany).

Tools and methods used for cellular studies

Optical density of the supernatant was measured by a Multiskan EX spectrophotometer (Thermo Electron Corporation, Helsinki, Finland).

The Live/Dead Cell dual staining kit for mammalian cells (Calbiochem, Milan, Italy) was used to analyze the viability of hASCs cultured on biomaterials. The Live/Dead test was

performed using a cell-permeable green fluorescent cytocolorant (λ_{ex}. max.: 488 nm; λ_{em}. max.: 518 nm).

Total RNA was isolated using the Rneasy Plus Mini kit (Qiagen, Milan, Italy), according to the manufacturer's instructions, on day 21. The extracted total RNA was quantified using a Nanodrop ND-1000 spectrophotometer (Thermo Scientific, Wilmington, USA). The purified RNA was reverse transcribed into cDNA using the ImProm-II™ Reverse Transcription system (Promega, Milan, Italy). The cDNAs were stored at -80 °C until analysis. Real-time PCR was performed for the detection of RUNX2 in hASC grown on biomaterials with peptides, using the TaqMan™ Gene Expression Assay (FAM) (Hs00231692-RUNX2-FAM, Life Technology, Milan, Italy). All reactions were performed in triplicate. PCR was performed using the CFX96 Touch PCR detection system (Bio-Rad, Hercules, CA, USA). For data analysis, changes in expression of each gene were calculated using the 2-ΔΔCt method, while housekeeping genes used as controls were employed to normalize the results.

Protein extraction was performed using Cell Extraction Buffer (Thermo Fisher Scientific, Milan, Italy) with the addition of 1 mM phenylmethylsulfonyl fluoride and a protease inhibitor cocktail. Total protein concentration was determined using the bicinchoninic acid (BCA) assay, and OCN protein was quantified using the Human Osteocalcin Instant ELISA (Thermo Fisher Scientific, Milan, Italy).

Statistical analyses were performed using Prism8 software (GraphPad 8.0, San Diego, CA, USA). Data obtained from the AlamarBlue test were analyzed using two-way ANOVA and Tukey's test, while statistical analysis of the mean fluorescence intensity, data obtained from real-time PCR, and data obtained from ELISA were analyzed using one-way ANOVA and Tukey's test. A p-value < 0.05 was considered significant.

Digital images were acquired with a fluorescence microscope (TE2000 Nikon s.p.a, Florence, Italy) using ACT-1 and ACT-2 software for DXM1200F digital cameras (Nikon Instruments).

Microwave-assisted solid phase peptide synthesis of hBMP2(73-92), hPreptin(26-34), hVEGF(17-25), TAMRA-hBMP2(73-92), TAMRA-hPreptin(26-34) and FAM-hVEGF(17-25)

All peptides listed in table 6.1 were synthesized and purified in our laboratory with a purity ≥95%. The peptides were synthesized by a fully automated microwave-assisted solid phase peptide synthesis (MW-SPPS), with the peptide synthesizer Liberty Blue (CEM Corporation, Matthews, NC, USA), according to the Fmoc/tBu strategy on a preloaded Wang resin (0,23 mmol/g, 220 mg, 100-200 Mesh) in a 0.05 mmol scale. After resin swelling in DMF, Fmoc-

amino acids were introduced through the following protocol: 1) Fmoc-deprotection in 20% piperidine in DMF; 2) washes (1×) with DMF; 3) Fmoc-deprotection in 20% piperidine in DMF; 4) washes (4×) with DMF; 5) coupling with Fmoc-amino acid (5 eq, 0.2 M in DMF), Oxyma pure (5 eq, 1M in DMF) and DIC (5 eq, 0.5 M in DMF) prepared in separated bottles; 6) washes (1×) with DMF; 7) coupling with Fmoc-amino acid (5 eq, 0.2 M in DMF), Oxyma pure (5 eq, 1M in DMF) and DIC (5 eq, 0.5 M in DMF) prepared in separated bottles; 8) washes (1×) with DMF. Both deprotection and coupling reactions were performed in a Teflon vessel with microwave energy and nitrogen bubbling. Reaction temperatures were monitored by an internal fiberoptic sensor. The resin was exposed to the microwave-assisted cycle described according to the following parameters (Table 6.2):

Table 6.1 List of synthesized compounds and their peptide sequences.

#	Peptide	Peptide sequence
I	**hBMP2(73-92)**	KIPKASSVPTELSAISTLYL
II	**hPreptin(26-34)**	TWKQSTQRL
III	**hVEGF(17-25)**	KLTWQELYQLKYKGI
IV	**TAMRA-hBMP2(73-92)**	TAMRA-KIPKASSVPTELSAISTLYL
V	**TAMRA-hPreptin(26-34)**	TAMRA-TWKQSTQRL
VI	**FAM-hVEGF(17-25)**	FAM-KLTWQELYQLKYKGI

Table 6.2 Steps of microwave-assisted peptide synthesis

Step	Temperature (°C)	Power (W)	Time (s)
Deprotection	25	0	300
Conventional Coupling	25	0	3600
MW Coupling	75	160	15
	90	30	110

For labeling peptides IV and V in Table 6.1 at the N-terminus, the side-chain-protected peptide resins (0.025 mmol) were acylated with TAMRA 2 times at room temperature by HATU (3 eq) and DIEA (4 eq). For labeling peptide VI at the N-terminus, the side-chain-protected peptide resins (0.025 mmol) was acylated with or 5(6)-FAM (3 eq) with PyBOB (3eq) and DIEA (4 eq) overnight. Final cleavage from the resin, with concomitant side chains deprotection was achieved by treatment of resin-bound peptide with a TFA/TIS/H_2O solution (95:2.5:2.5), 1 mL mixture/100 mg of resin. The mixture was stirred for approximately 4 h at

room temperature. The resin was filtered and then rinsed with TFA (2 × 1 mL). The peptide solution was added to the washes, and the product was precipitated from this solution by the addition of ice-cold Et_2O (30 mL). The precipitated material was washed with ice-cold Et_2O (3 x 10 mL) and dried under vacuum. The solid peptide was then dissolved in H_2O (5 mL), cooled in liquid nitrogen and lyophilized. The resulting crude peptides I-VI were purified by semi-preparative Reversed Phase HPLC (RP-HPLC) using a fully automated Waters Preparative System equipped with a Phenomenex Synergi 4u Fusion-RP C18 (150 × 10 mm) column operated at 4 ml/min at 25 °C. The solvent systems used were A (0.1% TFA in H_2O) and B (0.1% TFA in CH_3CN).

The products were characterized by analytical RP-UPLC-ESI-MS (Waters Acquity UPLC coupled to a Waters 3100 ESI-SQD MS) supplied with a Luna Omega PS C18 (1.6 µm, 2.1 × 50 mm) column at 35 °C at 0.6 ml/min with solvent systems A (0.1% TFA in H_2O) and B (0.1% TFA in CH_3CN). Mass spectra were recorded on a simple Quadrupole 3100 MS detector instrument on Electrospray positive mode. The experimental conditions for spectra acquisition in the positive ion mode were: spray voltage=3.0kV, Cone Voltage=20V, Desolvatation Temperature= 400°C, capillary temperature= 250 °C; m/z range= 200–2000. Data were acquired and processed using MassLynx software (Waters, Milford, MA, USA). ESI-MS data are reported in table 6.3.

Table 6.3 Molecular mass of doubly protonated peptides as theoretically calculated and experimentally determined by UPLC-ESI-MS

Peptide	Mass Calculated [M+2H]+	Mass found [M+2H]+
I	1060.26	1060.46
II	956.65	956.45
III	574.66	574.86
IV	1266.48	1266.70
V	1135.81	1136
VI	780.88	781

Synthesis of ELE copolymer

The synthesis is described in chapter 2.

Preparation of waterborne dispersions

The general procedure is the one described in chapter 2. Three dispersions were prepared, denominated PLAxy where x is the concentration of ELE in the aqueous phase and y is the concentration of SDS in the same phase (y=N is used if no SDS is present).

Preparation of PLA films

The films were prepared by solvent casting in a 24-well Petri dish with wells measuring 1 cm in diameter. Each well was filled with 200 µL of dispersion in order to obtain films with a thickness of approximately 200 µm. The dish was then placed in an oven for 2 hours at 60 °C, covered with filter paper to slow down solvent evaporation and prevent surface cracking. For films with peptides, the peptide was dissolved in a 70/30 H_2O:ACN mixture and the solution was added to the wells with a loading of 1% by weight (peptides/PLA), i.e. 37 µL of peptide solution per well in addition to the PLA dispersion.

The peptides tested are:

• TAMRA-hPreptin(26-34)

• hVEGF(17-25)

• TAMRA- hBMP2(73-92)

FT-IR

IR measurements were performed using a PerkinElmer Spectrum 100 FT-IR spectrometer equipped with a Universal ATR accessory. The spectra were acquired by accumulating 8 scans in the range 750-4000 cm^{-1} and processed using SpectraGryph 1.2 software.

Dynamic Light Scattering (DLS)

Particle size and *Z*-potential analyses of the dispersions were performed using the Zetasizer Pro Dynamic Light Scattering (DLS) (Malvern). The samples were diluted to approximately 0.1 g/L of PLA using ultrapure water. Measurements were performed in triplicate at 25 °C and their average was generated using Zetasizer 8.02 software. The size distribution was generated by the same software using the Non-Invasive Back Scatter (NIBS) method, while the *Z*-potential measurements were performed using the Mixed-Mode Measurement phase analysis light scattering (M3-PALS) method.

Gravimetric analysis

To calculate the solid content in the suspensions, 300 mg of the three synthesized suspensions were weighed and then placed in vessels in an oven at 100 °C for 2 hours. The vessels were then weighed, and the solid content was calculated as the percentage ratio between the final mass and the initial mass.

Cell cultures

Human adipose-derived stem cells (hASCs) were used for the in vitro assays. Cryopreserved hASCs (PT-5006) were purchased from Lonza (Milan, Italy). Cells were cultured in Alpha Minimum Essential Medium (α-MEM) (Lonza) supplemented with 10% fetal bovine serum (FBS) (Lonza) and 2% antibiotics (Penicillin/Streptomycin, 10,000

U/mL). Initial seeding density was 5 × 10^3 cells per T25 flask. For experiments, cells were seeded onto the previously described biomaterials in 24-well plates at a density of 2.5 × 10^4 cells per well and maintained at 37 °C with 5% CO_2 until analysis. As a control, hASCs were cultured on tissue culture polystyrene (TCPS) vessels at a seeding density of 5 × 10^3 cells per well.

Prior to cell seeding, scaffolds were sterilized by immersion in 75% ethanol for 2 hours, followed by air drying overnight under a biological safety cabinet.

Ethanol used for sterilizing films containing peptides was analyzed. After the 2-hour incubation of the wells with ethanol, the solvent was removed and evaporated under reduced pressure using a rotary evaporator. The contents of the flasks were analyzed by FT-IR spectroscopy to determine the substances extracted from the films by ethanol. Additionally, the extracts of the two fluorescent peptides, were analyzed using UV-Vis spectroscopy to quantitatively measure the peptides removed from the films.

Alamar Blue assay

The proliferation of hASCs cultured on the scaffolds was assessed using the Alamar Blue metabolic assay (Invitrogen, Milan, Italy). Cells were incubated with 5% (v/v) Alamar Blue reagent in culture medium for 3 hours at 37 °C. To generate a calibration curve, an initial concentration of 1.8 × 10^5 cells was seeded, followed by serial 1:3 dilutions down to 2 × 10^4 cells. The optical density of the supernatant was measured at 570 nm with 620 nm as the reference wavelength using a spectrophotometer (Thermo Electron Corporation, Multiskan EX, Helsinki, Finland). hASC proliferation on the biomaterials was evaluated at days 1, 4, and 7. All experiments were performed in duplicate.

Reverse Transcription qPCR (RT-qPCR)

Total RNA was isolated using the Rneasy Plus Mini kit (Qiagen, Milan, Italy), according to the manufacturer's instructions, on day 21. Total extracted RNA was quantified by using a Nanodrop spectrophotometer (ND-1000; Wilmington, Delaware). Purified RNA was reverse transcribed to cDNA using the ImProm-II™ Reverse Transcription System (Promega, Milano, Italia) . The cDNAs were stored at – 80 °C until the time of analysis. Real time PCR was performed for the detection of RUNX2, using TaqMan™ Gene Expression Assay (FAM) assay (Hs00231692-RUNX2-FAM, Life Tecnology, Milan, Italy) and VEGFR in hASCs grown on biomaterials described above. All reactions were performed in triplicate. PCR was performed by using CFXDuet Touch PCR detection system (Bio-Rad,Hercules, CA,USA). For data analysis, fold changes of each gene expression were calculated by using the 2-ΔΔCt method, whereas housekeeping genes that were employed as controls were used to normalize results.

ELISA test

To demonstrate hASC osteogenic differentiation, the detection and quantification of osteocalcin was carried out. OCN protein expression was analyzed in hASCs grown on the biomaterials at day 21. Protein extraction was performed using Cell extraction Buffer (Thermo Fischer Scientific, Milan, Italy) added to 1 Mm phenyl- methylsulfonylfluoride and a protease inhibitor cocktail. Total protein concentration was determined by bicinchoninic acid assay (BCA) and the OCN protein was quantified using the Human Osteocalcin Instant ELISA as reported (Thermo Fisher Scientific, Milan, Italy).

Alizarin Red staining and quantification of calcium deposits

To assess the ability to stimulate mineralized matrix deposition of functionalized biomaterials after 21 days of culture, staining by Alizarin Red was performed, which allows the assessment of the mineralization of the extracellular matrix of cell cultures by going to highlight calcium phosphate deposits; specifically, in the presence of calcium, Alizarin binds to it to form a visible orange-red pigment. Initially, the cells were washed with PBS 1x and then fixed with 10% formalin for 10 minutes at room temperature. Then the cells were washed again with PBS 1X and incubated for 30 min with a 1% solution of Alizarin Red in distilled water with ammonium hydroxide at pH 4.1 and 0.5 N. Finally, a wash with distilled water was performed before observation of the wells under an optical microscope (Nikon Eclipse TE 2000-E microscope, Nikon Instruments Spa, Florence, Italy). After images were acquired, quantification of calcium deposits was performed by solubilizing the wells with an aqueous solution composed of 20% methanol and 10% acetic acid. The wells were incubated with 1 mL of this solution for 30 min at room temperature, and then a spectrophotometer reading was taken at a wavelength of 450 nm (Thermo Electron Corporation, Multiskan EX model, Helsinki, Finland).

Cytoskeleton organization: vimentin and actin immunostaining

In order to evaluate the influence of functionalized biomaterials on the organization of the cell cytoskeleton, the intermediate (vimentin) and microfilament filaments (actin) of hASCs cultures on materials were studied. Indeed the expression levels of vimentin and actin proteins were analyzed by immunocytochemistry. The cells were placed in culture and analyzed after day 21. Initially, the cells were washed with PBS 1x and then fixed with 4% paraformaldehyde for 20 min at room temperature. Subsequently, the cells were treated with 0. 1% Triton X-100 for 10 min, washed with PBS 1x and incubated with vimentin-specific primary antibody (Vimentin Polyclonal Antibody, ThermoFischer Scientific, Waltham, USA) diluted previously 1: 100 in PBS 1x + 3% BSA; cells grown on PLA, 3% PEG-PLA-PEG, 0.05 SDS and VEGF were incubated with Phalloidin-TRITC (Tetramethylrhodamine Isothiocyanate1 µg/mL) (Sigma-Aldrich, Milan, Italy) diluted 1:1000 in PBS 1x + 3% BSA. for 1 hour at 37 ℃. After this incubation, 3 washes of 5 min each with

PBS 1x were performed and secondary antibody (Donkey Anti-Rabbit IgG (H+L) Higly Cross-Adsorbed Secondary Antibody, Alexa Fluor TM 488; ThermoFischer Scientific, Waltham, USA) diluted in PBS 1x + 3% BSA was incubated on the cells previously incubated with vimentin.

Statistical analysis

The in vitro experiments were performed in triplicate. Statistical analyses were carried out using Prism8 software (Graph Pad 9.0, San Diego, CA, United States). Data obtained from the Alamar Blue assay were analyzed with the two-way ANOVA and Tukey's test, whereas data obtained from Real Time PCR were analyzed with the one-way ANOVA. Data obtained from ELISA were analyzed with the one-way ANOVA and Tukey's test. A value of $p < 0.05$ was considered significant.

6.3 Results and discussion

Three peptides were encapsulated in PLA films: hBMP2(73-92) (KIPKASSVPTELSAISTLYL), hVEGF(17-25) (KLTWQELYQLKYKGI) and a Preptin fragment, hPreptin(26-34) (TWKQSTQRL) (figure 6.1). The resins used for the synthesis were respectively Fmoc-L-Leu Wang TG (loading 0.25 mmol/g), Fmoc-L-Ile-Wang TG (loading 0.23 mmol/g), and Fmoc-Rink-Amide PEG AM (loading 0.33 mmol/g).

The first phase was in all cases the deprotection of Fmoc using 20% pyperidine in DMF followed by standard double coupling cycles at 90 °C using DIC/Oxyme as activators. Following the syntheses the peptide-containing resins were divided into two parts and on one part the coupling of a fluorescent molecule was carried out, for hBMP2 and hPreptin this was TAMRA (emission 580-620 nm(and for hVEGF this was carboxyfluorescein (emission 500-530 nm). Afterwards, the final cleavage was carried out with TFA, using also H_2O/tri-isopropylsylane to eliminate the carbocations originating from deprotection and the peptides were precipitated, lyophilized and then further purified by HPLC.

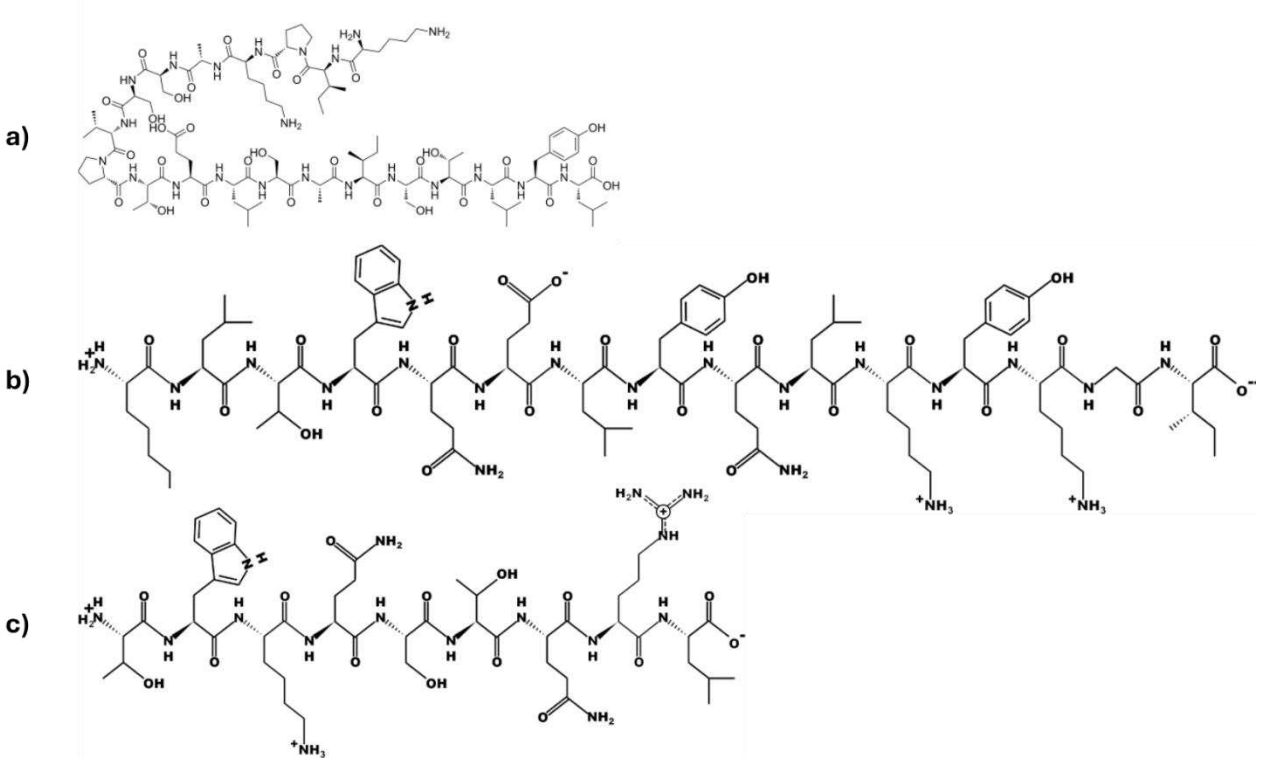

Figure 6.1 Molecular structures of a) hBMP2(73-92) (KIPKASSVPTELSAISTLYL) b) hVEGF(17-25) (KLTWQELYQLKYKGI) and c), hPreptin(26-34) (TWKQSTQRL)

The mPEG-PLA-mPEG block copolymer used as surfactant was synthesized as per chapter 2 and PLA dispersions were obtained. The following formulations were used:

1. PLA3N: 3% ELE

2. PLA3S: 3% ELE + 0.05% SDS

3. PLA2.4S: 2.4% ELE + 0.05% SDS

Table 6.4 describes the key data for the prepared dispersions. Hydrodynamic diameter was smaller for the formulation with the greater content of both surfactants and increased as either ELE or SDS content was decreased, consistently with the properties already observed. The *Z*-potential was negative and indicative of a stable colloid around -50 mV for all formulations. Solids content was greater for the PLA3S formulation, probably due to greater water evaporation during preparation.

Table 6.4 Physical parameters of obtained PLA dispersions

Sample	Solids content (wt %)	Hydrodynamic diameter (nm)[1]	PDI[1]	Z-potential (mV)
PLA3N	15.0	325	0.32	-51
PLA3S	23.0	277	0.24	-48
PLA2.4S	14.4	299	0.24	-47

[1] As determined by DLS Z-average.

Once the polymer films had been prepared, they were sterilized using pure ethanol prior to biological analysis in order to avoid contamination that could alter the results, ensure the accuracy of the data, and maintain standardized test conditions. Sterilization ensures that any biological response observed is due solely to the polymer and not to external contaminants.

It is important to study the effect of this sterilization to ensure that the process effectively eliminates all microorganisms and pathogens without compromising the properties of the material. Since the ethanol used for sterilization is removed from the film as a liquid, it can potentially extract components from the film and thus alter its composition. It was therefore collected, and the presence and nature of any extracted components was analyzed by FT-IR spectroscopy after removing the solvent itself. Figure 6.2 shows the comparison between the IR spectra of the extracts and the IR spectrum of the ELE copolymer. As can be seen, most of the peaks belong to the ELE copolymer, which is certainly the one extracted in the greatest quantity, but there is also a peak at around 1650 cm^{-1}, which is the peak of amide I and indicates that a certain amount of peptides is also extracted.

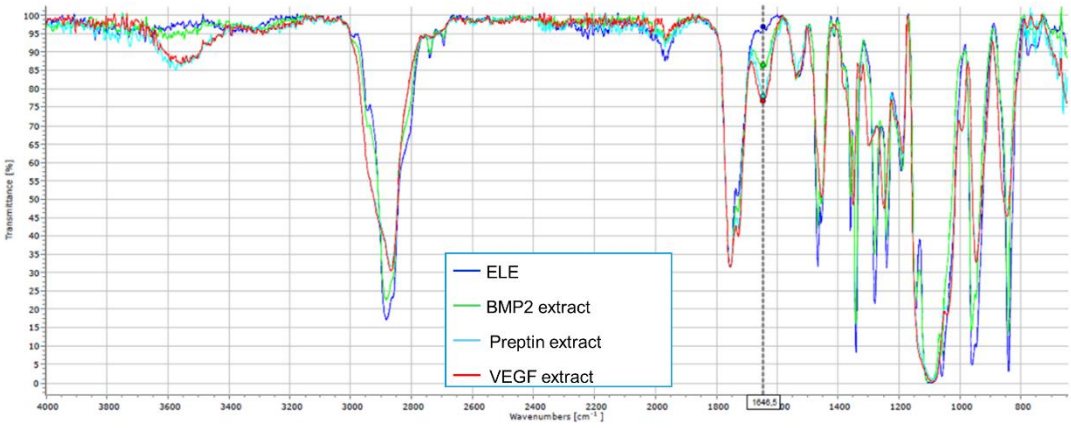

Figure 6.2 ATR-FTIR spectra of ethanol extracts from the sterilization of the three peptides, compared to the one of the ELE surfactant. The Amide I peak is highlighted.

To determine semi-quantitatively how much peptide was extracted from the films, UV-Vis measurements were performed in the case of the two peptides labeled with the fluorescent molecule TAMRA. We measured the absorbance values (A) at the TAMRA excitation wavelength λ= 528 nm and the Lambert-Beer law (with ε_{528}= 37500 cm^{-1} M^{-1} and l=1 cm) was used to calculate the concentration (C) of the peptides in solution.

$A=\varepsilon_{528}\times C\times l$

From the calculated concentration value, the number of moles present in solution was determined, from which it was possible to obtain the mass of the peptide extracted from the eight wells, knowing its molecular weight. The percentage (%) of peptide extracted from a well was calculated knowing the amount of peptide added to each well (0.33 mg). The extraction of peptides after washing with ethanol is therefore also confirmed by UV-Vis analysis, although the quantities extracted remain below 10%. The data are listed in table 6.5. Considering that PLA is insoluble in ethanol and that peptides are extracted in very small quantities, approximately 99% of the extracts consist of ELE copolymer. In the case of extract 1, a total of 27.8 mg of ELE is extracted from the eight wells, equal to approximately 3.5 mg per well. Since the ELE copolymer is present at 3% in the dispersion and approximately 240 mg of dispersion is added to each 200 µL well, each well initially contains approximately 7.2 mg of ELE. The same reasoning can be applied to extract 2, from which it can be deduced that 2.4 mg of ELE was removed from each well. Consequently, we can assume that the amount of ELE in each film is reduced by about half due to the sterilization process. However, the amount of peptides present in the films remains virtually unchanged.

Table 6.5 Quantitative evaluation of peptide extracted from the PLA films by the sterilization process as measured by UV-vis analysis on the two TAMRA-functionalized peptides.

Extract sample	Mass extracted (mg)	Peptide extracted (mg)	% of peptide extracted
TAMRA-hBMP2(73-92)	28	0.023	7
TAMRA-hPreptin(26-34)	19	0.010	3

From among the three dispersions, one formulation was chosen on the basis of the promotion of cellular growth and metabolic activity of the resulting film. The proliferation of human adipose stem cells (hASC) was analyzed by the AlamarBlue test after 1,4 and 7 days on each film and compared to tissue culture polystyrene (TCPS) as control (figure 6.3A). All PLA films displayed a greater cellular proliferation compared to the control (p <

0.05) at all times. After 1 day all 3 films had a similar cell growth, after 4 days PLA3N and PLA3S increased their number of cells compared to PLA 2.4S and after 7 days PLA3S had the greater cellular proliferation of all tested films ($p < 0.001$). A Live&Dead test was also used to evaluate the vitality of the cell cultures at 7 days (figure 6.3B). Fluorescence microscopy shows for all cultures an insignificant quantity of dead cells. The quantification of live cells shows, consistently with the Alamar Blue test, a greater quantity of live cells on PLA3S compared to the other PLA films and a greater quantity of live cells on the two other films, PLA3N and PLA2.4S compared to the control.

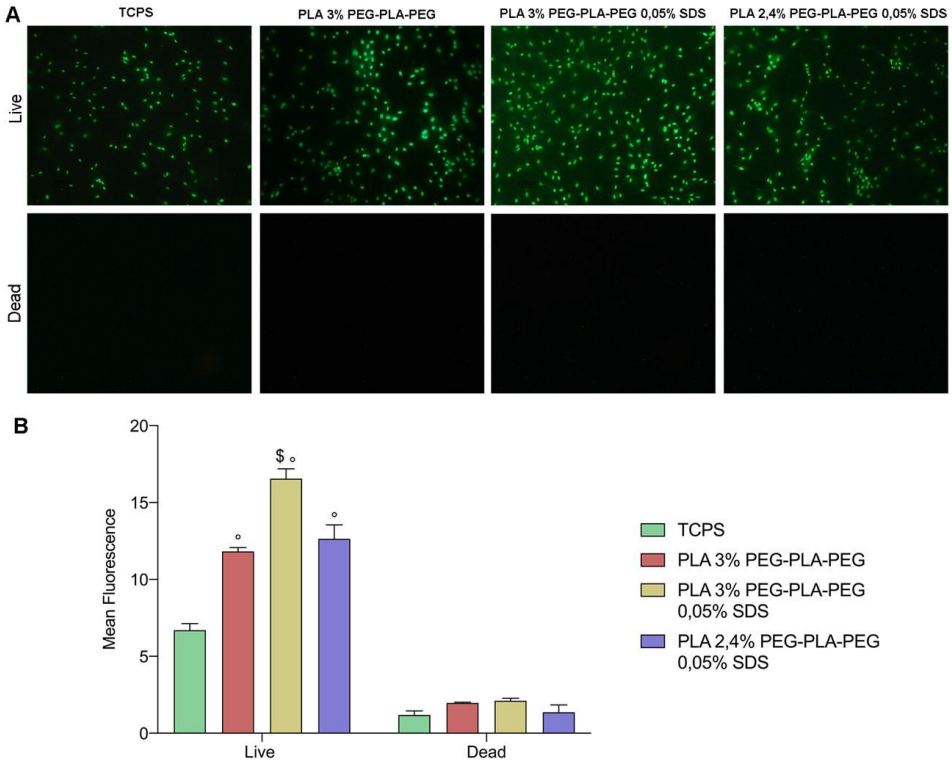

Figure 6.3 A) Live&Dead cell images on PLA films and TCPS. B) Corresponding cell counts; ° is $p < 0.001$ to control, $ is $p < 0.001$ to other films.

On the basis of these results, PLA3S was the formulation chosen for peptide-functionalized films.

The Alamar Blue essay was repeated for the films loaded with 1% of each peptide (PREPTIN, VEGF and BMP2) and compared as control to both TCPS and non-loaded PLA3S (figures 6.4 and 6.5). At day 1 all materials, except the PREPTIN-loaded film show a significant increase in cell proliferation compared to TCPS ($°p < 0.001$). The material functionalized with BMP2 induced the most significant cell proliferation in respect to the material not functionalized with peptides ($*p<0.05$). At day 4, the PLA-based control film and the PREPTIN-loaded one showed a significant cell proliferation increase compared to TCPS ($*p < 0.001$). At day 7, all materials showed a significant increase in cell proliferation

compared to TCPS (°p < 0,001). Furthermore, the materials functionalized with PREPTIN, as well as with all three peptides together showed a significant cell proliferation increase in respect to the control PLA film and the PLA films functionalized with VEGF and BMP2, thus indicating a synergic effect of the peptides. As mentioned before this was already reported for the combination of BMP2 and VEGF.[255,262] The effect is here observed also in the presence of PREPTIN.

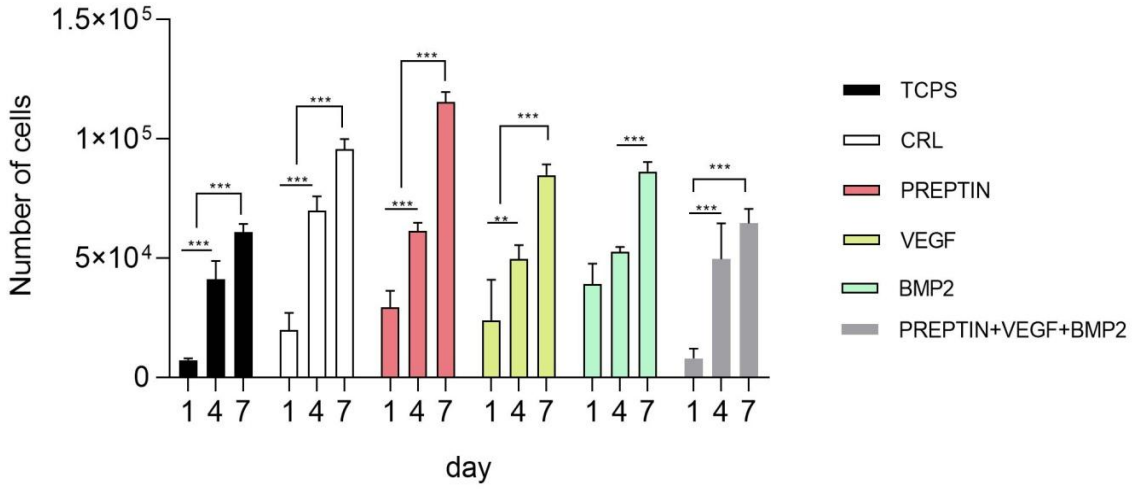

*Figure 6.4 Proliferation of hASC seeded on PLA films and control. i) TCPS, ii) PLA, 3% PEG-PLA-PEG and 0,05% SDS, iii) PLA, 3% PEG-PLA-PEG 0,05% SDS and preptin iv) PLA, 3% PEG-PLA-PEG, 0,05% SDS and VEGF, (v) PLA, 3% PEG-PLA-PEG, 0,05% SDS and BMP2, vi) PLA 3% PEG-PLA-PEG, 0,05% SDS, PREPTIN, VEGF and BMP2. (***p<0.0001; **p<0.001).*

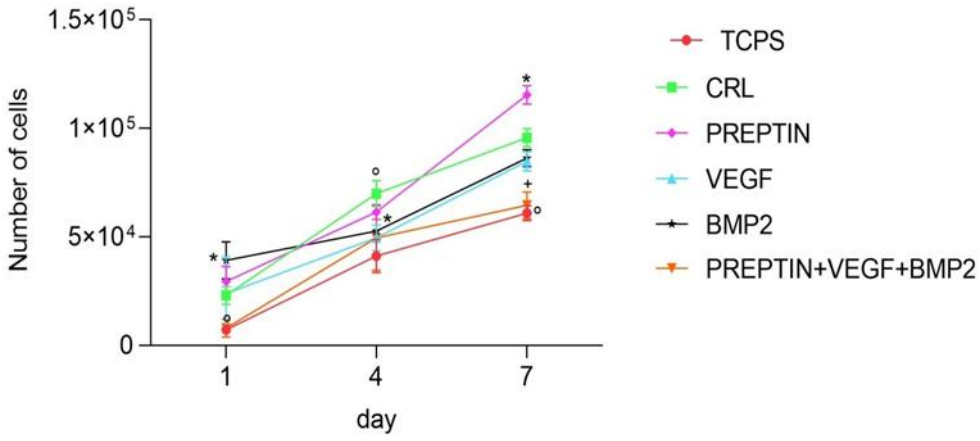

Figure 6.5 Proliferation of hASC seeded on PLA films and control over time.

The cytocompatibility of materials was confirmed by analysis of hASC cytoskeleton architecture. The cytoskeleton architecture of hASCs was evaluated by the technique of immunocytochemistry after 21 days in culture in contact with materials. In particular, the expression of vimentin protein (green) and the distribution of actin filaments (red) were uniform in the cells (figure 6.6). All biomaterials functionalized with preptin and VEGF and BMP2 did not change the cytoskeleton structure of hASCs cells grown on them for 21 days. Some materials appear fluorescent because they are conjugated with TAMRA for PREPTIN and BMP2 materials.

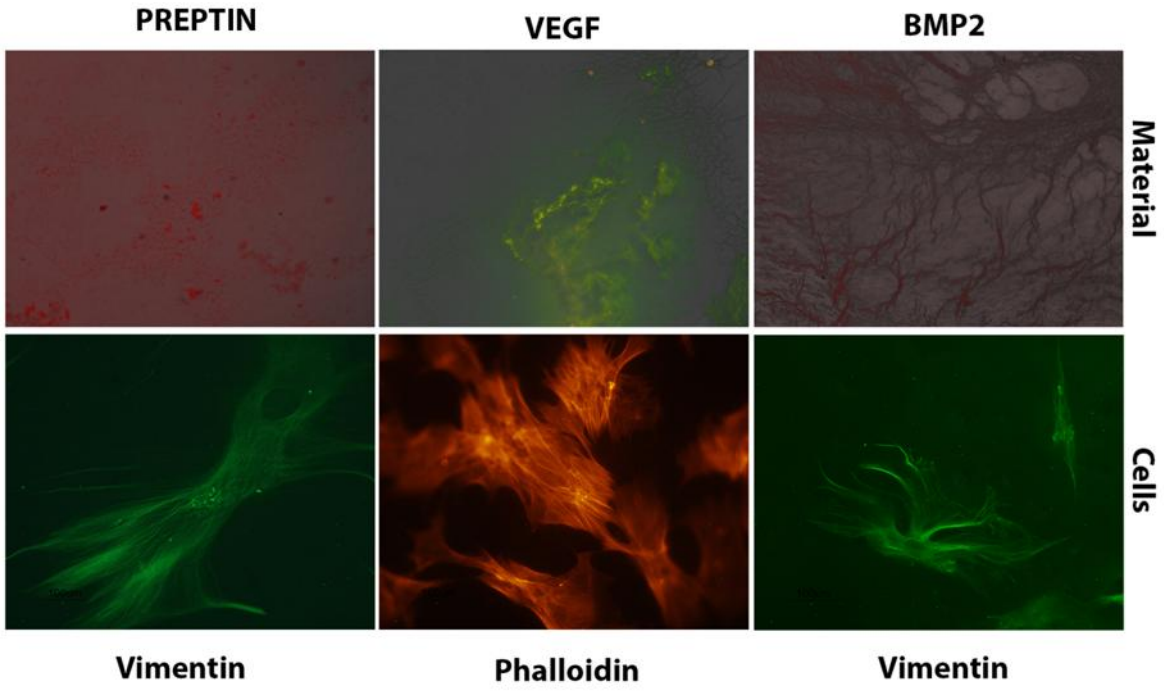

Figure 6.6 Immunostaing of vimentin and actin proteins. Fluorescence microscopy images of green fluorescence-labeled vimentin and red fluorescence-labeled phalloidin-TRITC actin filaments on hASCs grown on functionalized biomaterials at day 21 ii) PLA, 3S and PREPTIN, (iii) PLA 3S and VEGF, (iv) PLA 3S and BMP2.

The capability of the different films of promoting stem cell differentiation into osteoblasts was then tested. The expression of RUNX2 allows the study of osteoblast differentiation and maturation to verify the capability of materials of promoting bone-cell growth. In this case, RUNX2 expression was analyzed after 21 days of cell growth on PLA3S films loaded with peptide (figure 6.7). All loaded films showed greater RUNX2 compared to the control ($p < 0.001$) and were also differentiated from each other, BMP2 triggering greater cell

differentiation compared to PREPTIN ($p < 0.01$) and the latter compared to VEGF ($p < 0.001$).

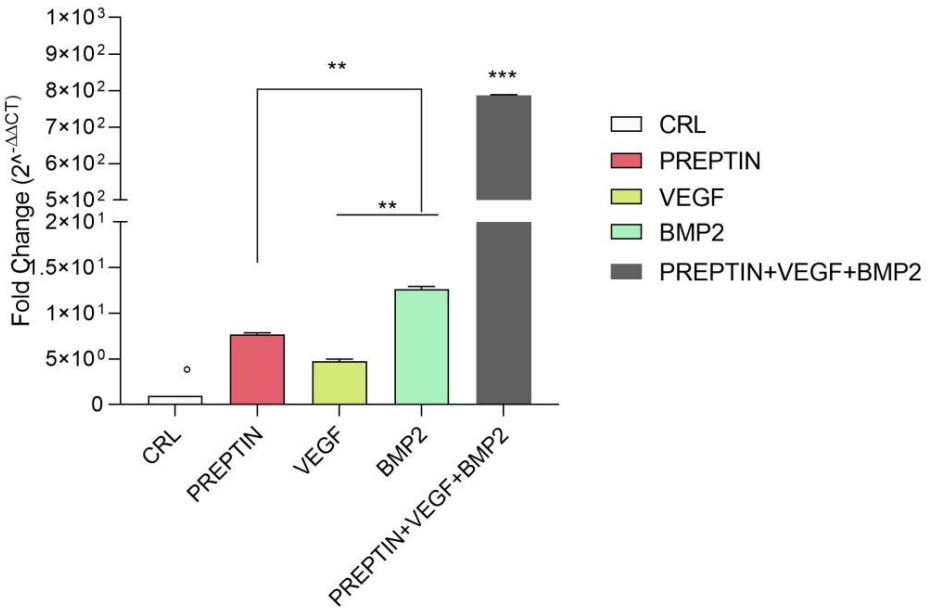

*Figure 6.7 Expression of RUNX2 gene after 21 days on hASC grown on PLA3S film (CRL) and peptide-loaded films. ° and *** is $p < 0.001$ from other samples and ** is $p < 0.01$ from linked sample.*

The expression of osteocalcin protein (OCN) is another useful test. OCN is a bone protein produced by osteoblasts to regulate bone metabolism and mineralization and its expression can be monitored to study the differentiation of mesenchymal stem cells to osteoblasts. OCN expression data is shown in figure 6.8. In contrast to RUNX2 only the PREPTIN-loaded film showed a significant ($p < 0.01$) increase in OCN expression compared to the control and the other two peptide-loaded films after 21 days. VEGF had a similar response to the control and BMP2 had a lower OCN expression.

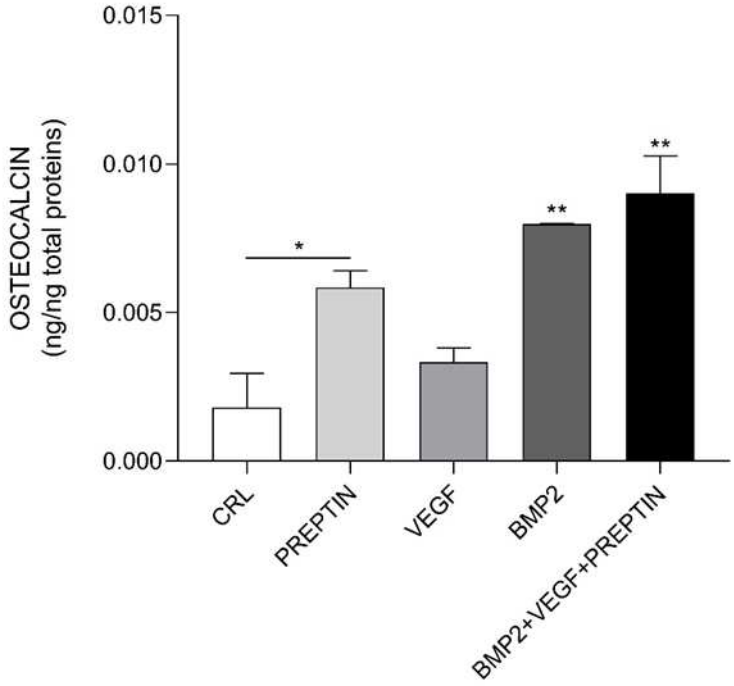

*Figure 6.8 Expression of OCN as a percentage of protein content after 21 days on hASC grown on PLA3S film (CRL) and peptide-loaded films., ** is p < 0.01, * is p < 0.05.*

The expression of VEGFR gene, involved in both angiogenic processes and bone mineralization, was evaluated after 21 days in hASC grown on the materials (figure 6.9). This data shows an increase of VEGFR gene expression in hASCs grown on all the materials functionalized with peptides in respect to hASCs grown on the unfunctionalized PLA film. VEGF, BMP2 and the combination of all three peptides were also more effective in increasing VEGFR gene expression when compared to PREPTIN.

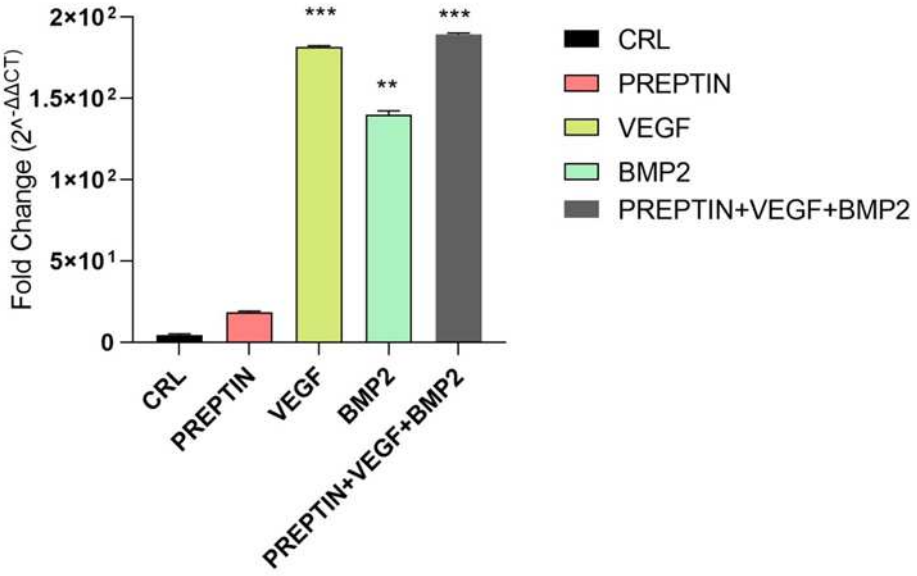

*Figure 6.9 VEGFR gene expression in hASCs grown on functionalized material and TCPS at day 21. i) PLA3S (CRL), (ii) PLA, PLA3S and PREPTIN, (iii) PLA, PLA3S and VEGF, (iv) PLA3S and BMP2, (v PLA3S, PREPTIN, VEGF and BMP2 (**p < 0,01, ***p < 0,001).*

Finally, calcium phosphate deposition was quantified by Alizarin red staining (figure 6.10) and showed more abundant mineralization in the BMP2-containing materials and the three-peptide combination compared to the control and the other peptides.

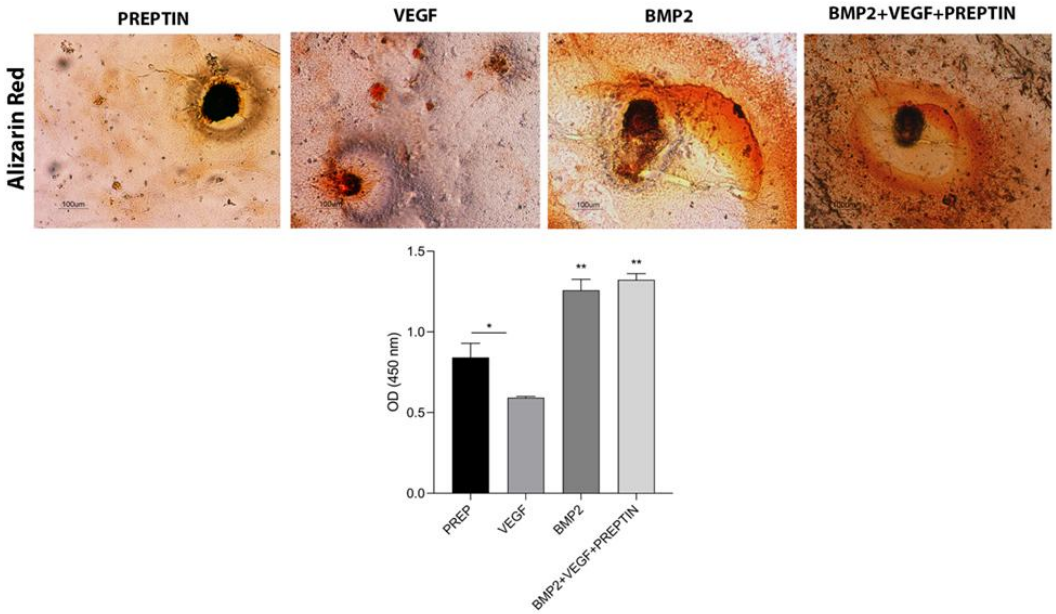

*Figure 6.10 Deposition of calcium phosphates quantified by Alizarin Red staining in hASCs grown on peptide-loaded materials at day 21. *p < 0,05, **p < 0,01.*

6.4 Conclusions

The results obtained in the present study demonstrate the cytocompatibility and osteoinductive efficacy of PLA-based materials functionalized with surfactants (PEG-PLA-PEG block copolymer and SDS) and bioactive peptides (PREPTIN, VEGF, BMP-2) in an in-vitro model of human adipose tissue-derived stem cells (hASCs). All materials proved to be cytocompatible, promoting increasing cell proliferation for a 7-day interval. Notably, the material functionalized with PREPTIN showed a significant increase in cell proliferation compared with both the non-functionalized control and the materials containing VEGF, BMP-2 or the combination of all peptides. Immunocytochemical analysis of the cytoskeleton (vimentin and actin-F) revealed that the functionalized materials do not adversely alter cell architecture, suggesting good mechanical tolerability by hASCs.

Gene expression of the early osteogenesis marker RUNX2 was increased in all functionalized materials compared with control, with a particularly marked peak in the BMP2-containing material, consistent with the known role of this factor in stimulating osteoblastic differentiation. The combination of all three peptides also further enhanced the expression of RUNX2, suggesting a possible synergistic effect. OCN production was significantly increased in hASCs cultured on materials functionalized with the combination of PREPTIN, VEGF and BMP-2, indicating effective progression toward osteoblastic maturation. The VEGFR gene, was also overexpressed in the presence of all peptide materials compared with the control, with higher levels in the groups treated with VEGF, BMP2 or the combination of the three peptides, confirming a pro-angiogenic environment. Calcium phosphate deposition was more abundant in the BMP2-containing materials and the peptide combination. Overall, the results support the use of waterborne functionalized with PREPTIN, VEGF and BMP2 as a potential platform for applications in bone regeneration, offering both structural support and targeted biological stimulation. It can be noted that the material conjugated with the BMP-2 peptide and the material conjugated with all the peptides show the best osteogenic capabilities in the hASC cellular study model. In summary, the present study demonstrated that the water-based dispersions developed in this thesis can also be used to obtain coatings for biomedical applications. Applying the waterborne dispersions of the most promising formulations as coatings on metallic implant substrates rather than free standing films will be the next step of this research.

Acknowledgments

I would like to acknowledge the contributions to this chapter by Giulia Belvito, who carried out many parts of the project as part of her M.Sc. thesis as well as Dr. Elisa Peroni at BioCIS laboratory in Universitè Cergy Paris who directed the peptide synthesis and Prof. Elisa Mazzoni (UniFe) who directed biological tests.

7. Biodegradable poly(lactic acid)/graphene oxide platform obtained from waterborne dispersion for biomolecules sensing

7.1 Introduction

Technological advances have increasingly led to the integration of electrical circuits and devices into plastic products, improving their connectivity and functionality. These events however have exacerbated the problem of electronic waste and the associated issues of difficult recycling and potential toxicity.[264,265]

The enhancement of the recyclability of e-waste or the adoption of biodegradable systems, in conjunction with the implementation of more sustainable and environmentally friendly production methods, are effective solutions to contribute to a more sustainable future, in accordance with the European Green Deal and the United Nations Sustainable Development Goals. Polylactic acid (PLA) is a biodegradable and recyclable polymer that can be derived from renewable sources and is one of the most produced bioplastics in the world, widely used in packaging and biomedical applications. Ecofriendly and multifunctional electronic platforms can be created combining PLA with cutting-edge manufacturing techniques, opening up numerous potential applications in biomedicine, bioelectronic, intelligent food packaging, and sensors.[266,267]

Laser scribed graphene is a process in which a laser is used to induce localized pyrolysis of different carbon substrates in the surface, resulting in the formation of graphene-like structures. This process has been the subject of extensive research, with studies conducted on a range of materials that can be transformed into graphene structures.[268–270] The laser functionalization process modifies the composites, creating extended sp^2 hybridized carbon structures. In contrast to the original polymer, these structures can have excellent electrical properties which allow this technique to be used to realize conductive tracks without the use

of metal. This sustainable and scalable technology would allow the possibility to design and build *ad-hoc* devices with a CO_2 laser on suitable plastic substrates. This approach could offer several advantages over other technologies, such as simplified processes, fewer production stages and, by a proper selection of the plastic substrate, possibility of improved recyclability and biodegradability, due to the reduction in the number of metal-plastic hybrid parts.[271]

One of the approaches normally used for the realization of laser-induced graphene is the inclusion of graphene oxide (GO) into a polymer matrix. Laser treatment induces the local conversion of sp^3 carbon atoms into sp^2 hybridization, thanks to a local pyrolysis of the material, leading to significant increase of the electric conductivity. This approach was effectively used for the realization of conductive polyurethane platforms, applicable for the production of electric circuits, electrochemical sensors and heaters.[271] The non-biodegradability of most polyurethanes constitutes an important drawback, especially when used to produce disposable sensors or bioelectronic devices, due to the massive accumulation of waste.

Among advanced organic materials, PLA/GO composites have emerged as promising materials for interfacing with biological systems.[272,273] This is due to the synergistic combination of biocompatibility and biodegradability of the polymer with the good mechanical strength, high surface area, flexibility and ease of functionalization of graphene nanomaterials, offering enhanced stability and functional versatility for biomedical applications. This implies that the realization of conducting platforms starting from PLA/GO can be applied to numerous biomedical applications, such as the definition of the chemical composition of biological fluids by wearable sensors. A common method for producing PLA/GO composites is solution blending, a process that typically requires the use of toxic and environmentally harmful solvents.[274] The development of alternative methods that reduce or avoid the use of hazardous solvents is highly desirable, and for this reason, in this work we exploit the use of a waterborne dispersion of PLA recently developed for the preparation of the PLA/GO composite.[88,275]

In this work, we study the properties of novel electrodes fabricated by laser scribing eco-friendly PLA/GO platforms; the devices realized are then to be applied to the electrochemical detection of biomarkers in biological fluids. We aim to exploit the electrocatalytic properties of the laser-treated PLA/GO platforms for the detection of several molecules important in human health. The research is particularly focused on the detection of catecholamine neurotransmitters, which are important biomarkers of stress diseases. The correlation between the intensity of the laser fluence adopted for the realization of conductive traces and the physic-chemical properties of the resulting material is to be

studied to achieve a better understanding of the detection of these species in biological fluids.

7.2 Materials and methods

Materials

Poly(lactic acid) Ingeo PLA 4060D (PLA) was kindly provided by NatureWorks LLC (Minnetonka, MN). PLA 4060D is an amorphous polymer with an L-lactide content of around 88 wt%. The preparation of PLA dispersions was adapted from the one described in chapter 2. 0.780 g of ELE was dissolved into 26 mL of ultrapure water at room temperature and 3.740 g of PLA was dissolved in 34 mL of ethyl acetate at 50 °C. The organic phase was added to the aqueous phase in a 100 mL glass beaker at room temperature and homogenized at 0 °C using a Hielscher UP200St ultrasonicator (Hielscher Ultrasonics, Teltow, Germany) equipped with a 14 mm probe, set at 50 % intensity for 30 s and then at 80 % intensity for 90 s. The water/oil emulsions were mechanically stirred under a fume hood until the removal of the organic solvent was complete. The resulting PLA nanoparticles water dispersions exhibited particle sizes in the range of 340-420 nm as measured by DLS.

A GO solution with 4 g/L concentration (particle size: < 10 μm, monolayer content >95%, carbon content: 49−56% from product datasheet) was supplied by Graphenea.

Self-standing films of PLA and PLA/GO were prepared via solvent casting. The GO solution was added dropwise to the PLA dispersion under stirring. The resulting solution was cast onto polystyrene capsules with a diameter of 5.5 cm and left to dry at 60 °C in oven. The weight of the films prepared was around 500 mg. The samples prepared consist of films made up by 83% wt by amorphous PLA and by 17% wt of a PEG-PLA-PEG block copolymer used as surfactant. Graphene oxide was added to the dispersion in three different ratios 0.5, 1 or 2% relative to the solid content (PLA + PEG-PLA-PEG). These samples were named PLA/GO-0.5%, PLA/GO-1% and PLA/GO-2% in the text, while the composite without GO was named PLA/GO-0%.

Characterization techniques

The biodegradation tests were carried out in cylindrical glass vessels (500 mL capacity) containing 5 g mature compost (ACFA compost supplied by Enomondo, Faenza, Italy) mixed with 10 g perlite and sandwiched between two layers of 15 g of perlite. Perlite was used to ensure satisfactory incubation conditions, whereas compost was used mainly as microbial inoculum. The humidity content of both compost and perlite was adjusted to 50%.

The test and reference materials were placed in the core of the mature compost middle layer at about 40 mg/g ratios (200 mg of material). All the vessels were incubated at 58 °C in the dark and the tests were carried out in triplicate. The CO_2 evolved from test and reference was trapped in the vessels by means of 0.5 N NaOH solution contained in a beaker set in each vessel. Every 2-7 days CO_2 absorbers were retrieved and replaced with fresh NaOH solution in known aliquots. The retrieved NaOH solutions were titrated with 0.5 N HCl and the amount of adsorbed CO_2 was determined. The percentage biodegradation is given by the ratio of the CO_2 produced from the test material to the maximum theoretical amount of CO_2 that can be produced from the test material. The maximum theoretical amount of CO_2 produced is calculated from the measured total organic carbon (TOC) content.

DSC measurements were carried out on a PerkinElmer DSC 8000 calorimeter equipped with an IntraCooler II cooling device (PerkinElmer Inc., Shelton, USA). The sample was first heated up from room temperature to 200 °C, held isothermally for 5 min, cooled down to −70 °C, held isothermally for 5 min, and heated up again up to 200 °C. Heating and cooling steps were performed at 10 °C/min.

Thermogravimetric analysis (TGA) was carried out on a TGA 4000 (PerkinElmer Inc.) instrument with Pyris software for data acquisition and analysis. Samples (5–10 mg) were analyzed in an alumina pan at a heating rate of 10 °C/min from 30 to 900 °C under a nitrogen atmosphere (30 mL/min).

For sheet resistance measurements, 3 mm × 10 mm structures were fabricated and connected at the borders with silver paint. The resistance was measured by a two-probe method using a Keithley 2450 Source Meter. Sheet resistance is correlated to measured resistance by the general formula: $RS = R\,W\,L^{-1}$, where R is the resistance across the track; W and L are the track width and length, respectively. By itself, the sheet resistance is not sufficient to understand if the laser treatment, as a function of the laser fluence, speed, line spacing and GO concentration, modifies the resistivity of the matrix or only the thickness of the conductive track. Consequently, an accurate investigation of the thickness of the lasered conductive track was performed by a digital microscope (Olympus BX53 M) and a Scanning electron microscopy (SEM) (ZEISS LEO 1530 FEG), that were used to observe both the surfaces and the cross sections of the modified areas. For SEM pictures the energy of electrons was 5 keV and the signal was acquired using an inlens detector at a working distance of 3−5 mm.

Chemical analysis of the structure was performed with a Raman spectrometer, microRaman Renishaw, using a HeNe laser with a wavelength of 632 nm. Each spectrum is the result of 10 accumulations of 100 seconds.

XRD measurements were performed on a Rigaku SmartLab diffractometer equipped with a rotating-anode Cu source. Two geometries were used: (i) (specular θ–2θ) scans to probe the entire film thickness and (ii) grazing incidence out-of-plane scans (incidence angle 0.2°) to selectively probe the laser-treated surface layer.

Laser treatments

Laser scribing was performed using a Trotec Speedy 360 flexx machine featuring a carbon dioxide (CO_2) laser source with λ = 10.6 μm, a power output of 80 W, a maximum speed of 355 cm/s, and a maximum frequency of 60 kHz. The waist radius *r* is 97 μm. The laser operates in pulsed mode (PWM type) with an optical power output of up to 80 Watt. Laser-scribed tracks were performed by drawing lines of 1 cm of length separated by a distance *d* to form rectangles 3 mm × 10 mm. The laser-shaped rectangles were produced by testing different laser parameters and analyzing how these affect the electrical properties of the material by measuring their respective sheet resistance.

Average laser power (P), laser Fluence (F), scanning speed (S) and line spacing (d) were tested respectively in the range of 4.8-7.2W, 0.54-0.81 J/cm^2, 43−85 mm/s and 25-200 μm. Laser fluence, which is the energy content of the pulse falling on the substrate per unit area, was calculated by the following equation and used as key parameter for laser scribing modification:

$$F = \frac{2 \times P}{Frequency \times \pi r^2}$$

Electrochemical sensors

Electrochemical tests were performed using an Autolab PGSTAT128N (Metrohm). The area of the working electrode (0.09 cm^2) was defined using a hydrophobic and insulating nail on conductive laser tracks (F = 0.54-0.81 J/cm^2, S = 43 mm/s, d = 25 μm), whereas the connection with the potentiostat was established using a silver ink track and a filament of Cu. For preliminary tests, the 3-electrode cell was completed by including an external Pt wire and an Ag/AgCl/KCl (3M) electrode as the counter and the reference electrode, respectively. Further tests for the electrochemical detection of adrenaline were performed with a 3-electrode cell entirely obtained on PLA/GO-2%, by depositing a small amount of Ag paste to fix the potential of the pseudo-reference electrode. The analyses were carried out at room temperature and in equilibrium with the atmosphere, i.e. in the presence of O_2. 100 μL of the test solution was dropped on the PLA/GO surface to perform the analysis.

Commercial CSPE were used as a reference to compare the electrochemical properties of PLA/GO-2% platforms. The potential of the pseudo-reference electrode was fixed in this case by adding 0.1 M KCl to all solutions tested. All the potentials herein reported are finally corrected to a Ag/AgCl/3 M KCl reference to allow the direct comparison with the responses recorded at PLA/GO surfaces.

The electrochemical behaviour of PLA/GO surfaces was first studied by CV, recording voltammetric responses at different scan rates in a 0.5 mM $Fc(OH)_2$, 0.1 M KCl solution. Further tests to evaluate the resistance to charge transfer (R_{CT}) were carried out using EIS by recording the Nyquist plots (i.e. Z'' *vs* Z') in a 1:1 5 mM $[Fe(CN)_6]^{3-/4-}$, 0.1 M KCl solution. These measurements were performed at open-circuit potential, in the 50 mHz – 10 KHz frequency range, using an amplitude of 0.01 V and recording 50 frequencies per decade. In all cases, the Nyquist plots were fitted with a Randles circuit, and the high-frequency region evidenced the typical semicircle, whose diameter gave us a measure of the R_{CT} of the material.

The electrocatalytic performance of PLA/GO surfaces was evaluated towards the oxidation of several organic species present in biological fluids, namely adrenaline, ascorbic acid, NADH, uric acid, tyrosine, L-Dopa, dopamine, and noradrenaline dissolved in artificial sweat. The composition of this solution, resembling the human fluid is 25.5 gL^{-1} KCl, 17.5 gL^{-1} NH_4Cl, 5 gL^{-1} urea, 2.5 gL^{-1} CH_3COOH, final possessing a pH of 4.7 was used in contact with the electrode surfaces. CV traces recorded at a 0.02 Vs^{-1} scan rate were used to preliminary test the electrocatalytic properties of the electrode platform, whereas DPV was used to better assess the applicability of the device in electrochemical sensing. These measurements were performed by applying a modulation amplitude of 0.01 V, a modulation time of 0.1 s, a step potential of 6 mV and 0.020 Vs^{-1} as the scan rate.

7.3 Results and discussion

Self-standing PLA/GO films were prepared by solvent casting from a water dispersion of PLA particles and GO at different concentrations (0.5, 1, and 2%). SEM images of PLA/GO-2% film cross-section (figure 7.1) show a compact structure indicating the good coalescence of PLA particles and the absence of GO interference in the film formation mechanism. Indeed, the morphology of the obtained film is comparable with pure PLA films. The absence of macroscopic GO aggregates in the film section suggests a good distribution of the GO flakes in the PLA/GO composite. This finding is in accordance with the XRD analysis (vide infra), in which the absence of a characteristic GO peak due to the stacking of GO aggregates indicates that the GO nanosheets are well dispersed in the PLA matrix.

The use of mPEG-PLA-mPEG block copolymers to stabilise PLA particles in water has the potential to enhance the interaction between PLA and GO, facilitating the dispersion of GO in the composite. This hypothesis is supported by previous studies, which demonstrated that the interaction between GO and PLA was enhanced by surface grafting GO with poly(ethylene glycol).[276]

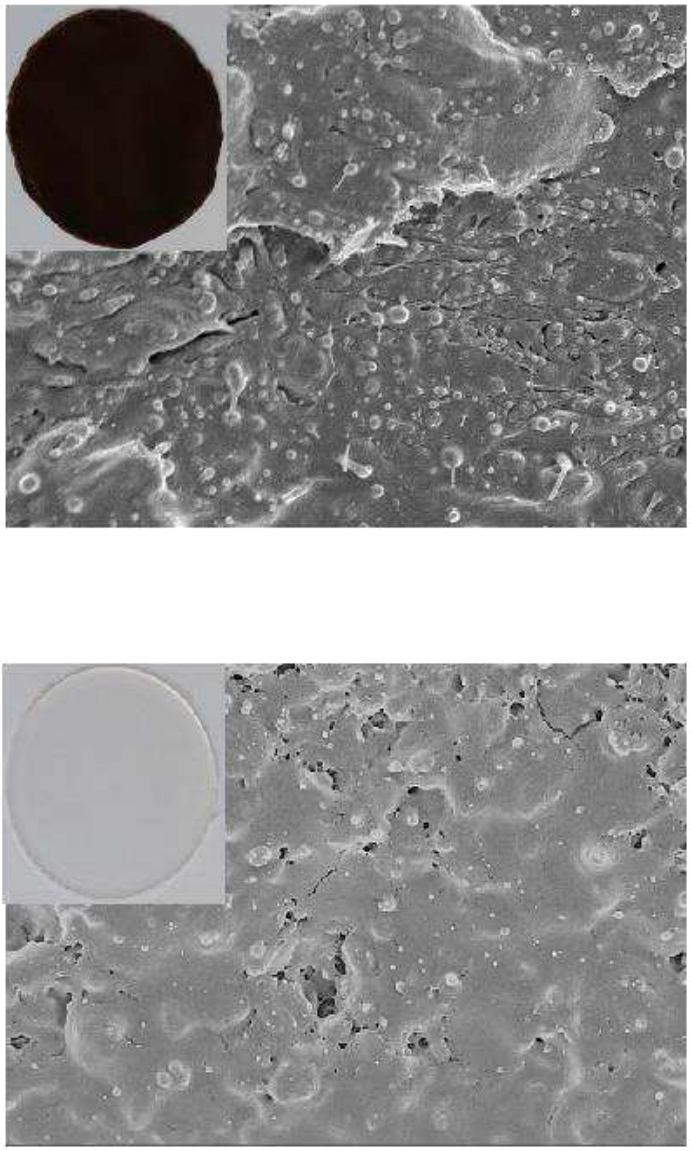

Figure 7.1 SEM images of the surfaces of PLA/GO-2%(above) and PLA without GO (below) films.

TGA (Figure 7.2) evidenced a two-step degradation behaviour. The first, most pronounced, (derivative maximum at 360-370 °C) is related to the PLA matrix and the smaller, partially overlapping, one (derivative maximum at 400-420 °C) is related to the poly(ethylene glycol) (PEG) segments, added as a surfactant, which degrade at a higher temperature, as already observed by Doganci et al.[277] The addition of GO to the films caused a number of effects. First, a small weight loss (< 2%) is noticeable at temperatures < 300 °C, i.e., before the main degradation step begins. This is particularly evident in the samples with higher GO content and can be likely ascribable to the thermal removal of oxygen functional groups massively present in GO.[278] Second, the main degradation onset is shifted to higher temperatures by ~10 °C when GO is added. This indicates a slight thermal stabilization of

PLA by GO that is already maximized at 0.5% GO concentration, as it does not increase at higher GO contents. As observed by several authors,[279–281] this is likely due to the large surface area of the GO nanosheets creating barriers against the escape of volatile gases. On the other hand, the point of maximum degradation rate was shifted slightly upwards (370 *vs* 362 °C) when GO content was 0.5% or 1% but shifted again to lower temperatures (360 °C) when the GO content reached 2%, meaning that with a further increase in GO the degradation reaction is actually accelerated despite its onset being delayed. Additionally, the final residue is reduced from 4% to below 2% when GO is added, indicating a more efficient pyrolysis of the carbon residues when GO is present.

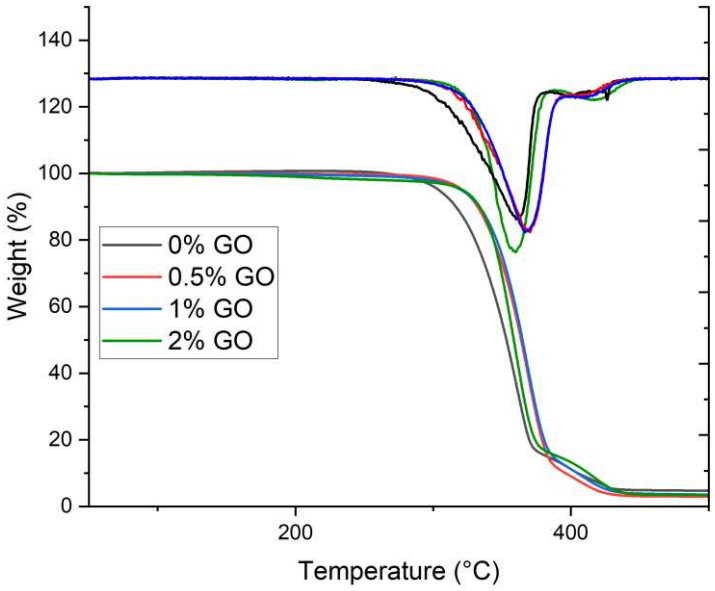

Figure 7.2 TGA measurements for films of PLA loaded with various amounts of GO (below, left scale) and their first derivatives (above).

DSC analysis (figure 7.3) evidenced a single glass transition and no melting peaks due to the amorphous nature of the PLA used. The T_g is substantially lower than the one of the pure PLA that does not include surfactants (25-29 °C *vs* ~ 60 °C) due to the surfactant dissolved within the polymer matrix, which has a soft PEG block that acts as plasticiser. The surfactant was completely miscible in PLA, as no separate glass transition assigned to the PEG component was observed. The GO added to the PLA films had no effect on the glass transition behaviour.

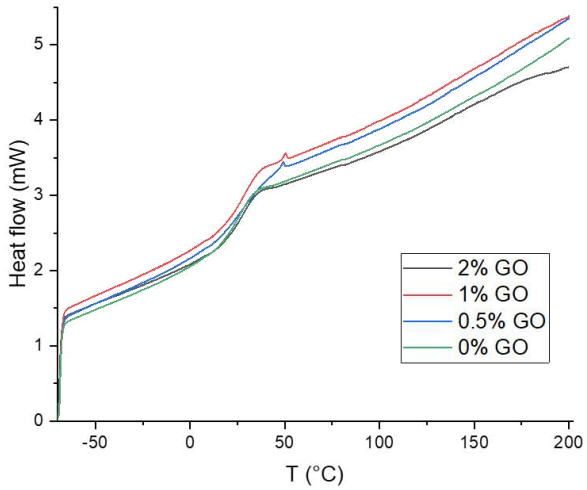

Figure 7.3 DSC thermograms (endo up) of PLA films containing different amounts of GO as observed during the second heating scan.

Biodegradation tests on PLA/GO composites were reported in figure 7.4. All PLA samples (PLA/GO-0%, PLA/GO-0.5%, PLA/GO-1% and PLA/GO-2%) demonstrated rapid biodegradation resulting in 82-93% mineralization in industrial composting conditions after 32 days of observation. After this, the measured biodegradation of all samples continued to slowly increase over time, reaching average values of 100% for all samples, within the experimental error, after 74 days. No remains of the test samples were found in the containers after the test was completed; all of these materials are thus fully disintegrated and biodegraded in composting conditions.

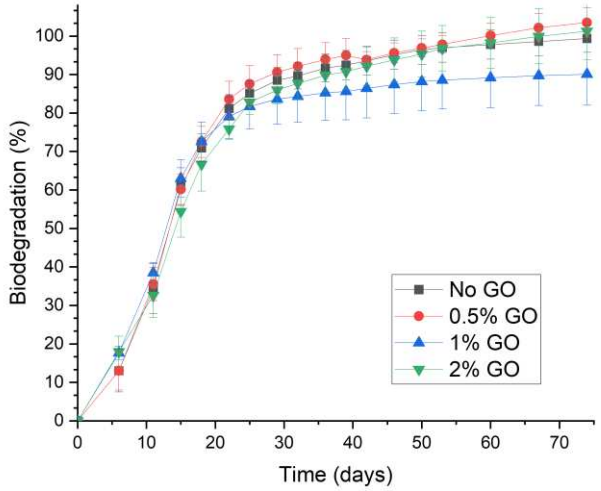

Figure 7.4 Biodegradation over time of PLA films containing various amounts of GO in an industrial composting setting, as measured by respirometry.

Overall, no significant difference in compostability caused by GO addition or the surfactant presence into the films was observed: the sample with 1% GO had somewhat lower ultimate biodegradation values than the other samples but with low statistical significance ($p = 0.1$ at 74 days). The high compostability of all samples also proves that the presence of GO does not interfere with microbial activity. GO composites with biodegradable polymers have actually been previously shown to be capable of accelerating their hydrolytic and enzymatic biodegradation,[282] but in our case the overall shape of the various biodegradation curves was very similar, attesting to no significant effect of GO on biodegradation rates of the material. GO itself is biodegradable and can be metabolized by soil microorganisms to CO_2 and biomass in aerobic conditions.[283]

Laser writing

Conductive pathways were formed by exposing PLA/GO composites containing different concentrations of GO (0%, 0.5%, 1% and 2%) to a pulsed CO_2 laser (figure 7.5 a,b,c). The increase in temperature caused by the laser treatment leads to the reduction of the GO and the degradation of the polymer, forming a network of conductive materials. Figure 7.5d reports the electrical properties of the PLA/GO-0.5%, PLA/GO-1% and PLA/GO-2% composites in function of the laser fluence tested. After laser scribing, the sheet resistance of the three materials decreases by several orders of magnitude compared to the insulating starting composites. The composite with a higher GO concentration (2%) exhibits appreciable sheet resistance (93 $\pm$ 16 Ω/sq) even when treated at low laser fluence (0.59 J/cm^2), a feature that is not evident in other PLA/GO composites containing a lower amount of GO. The lowest achieved sheet resistance is 12 Ω/sq for PLA/GO-2% (Fluence=0.81 J/cm^2), which corresponds to a conductivity of ~21 S/cm considering the thickness of the lasered material (~40 μm). This value is comparable with that of laser-induced graphene obtained from polyimide.[284]

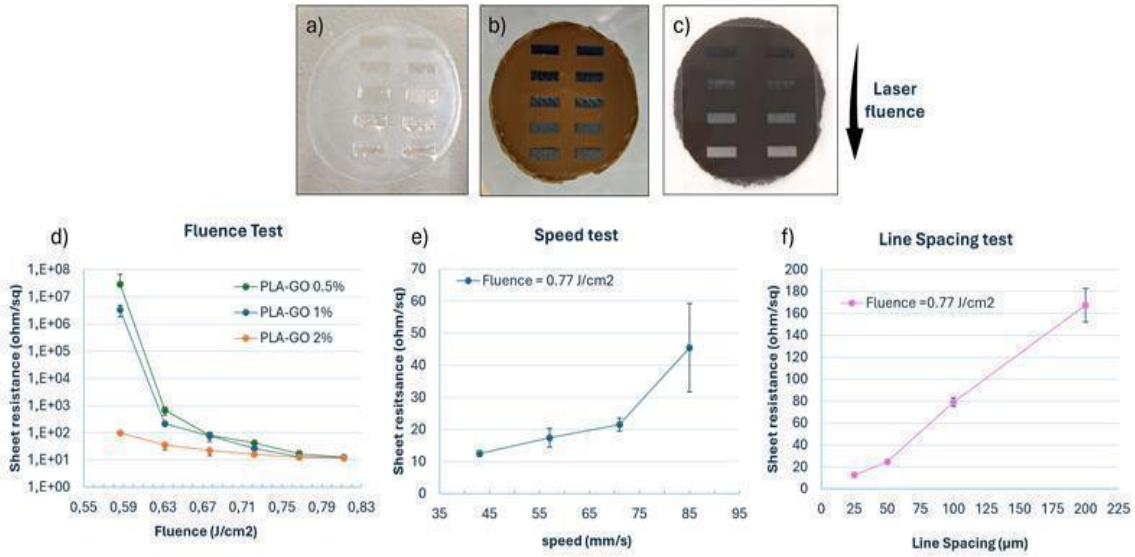

Figure 7.5 Optical picture of PLA/GO membrane patterned by laser irradiation: a) PLA virgin lasered at different laser fluence from 0.54 to 0.72 J/cm^2; b) PLA/GO-1% lasered at different laser fluence from 0.59 to 0.77 J/cm2; c) PLA/GO 2% lasered at different laser fluence from 0.59 to 0.77 J/cm ^{2}. d) Sheet resistance of laser patterned rectangles 3×10 mm as a function of the laser fluence for different PLA/GO concentrations. Sheet resistance of laser patterned rectangles 3×10 mm for PLA/GO 2% at laser Fluence= 0.77 J/cm^2 as a function of e) the scanning speed and f) the line spacing.

Investigating the surface of the PLA/GO-2% after laser treatment at different fluences (figure 7.6), significant morphological changes are revealed once the material becomes conductive, i.e. at laser fluence of 0.59 J/cm^2. The surface of this sample is characterised by the presence of numerous holes measuring up to tens of microns in size accompanied by raised flaps of material. Several droplet-like structures are also visible, which are probably the result of polymer residue softened or decomposed during laser treatment. With an increase in laser fluence, the structures that appear as drops disappear, while the fractures increase along the laser scan direction, revealing a layered organization of the material. The layered structure is most evident in the cross-section of laser-treated materials (figure 7.7), which discloses a morphology analogous to that of a GO film or GO polymer composite after laser treatment shown in different works.[271,285] Similarly to what happens with these materials, the presence of space between layers may be due to the release of gaseous products during GO reduction or polymer degradation, which is caused by an increase in temperature resulting from laser irradiation. In particular, several studies have reported the release of gaseous products such as CO_2 and CO during the decomposition of oxygen-containing functional groups present in GO due to laser reduction or by thermal degradation of PLA.[271] The optical images of the cross section also show that the thickness of the laser-modified area increases with increasing laser fluence tested, reaching a maximum of ~40 µm for a fluence of =0.81 J/cm^2

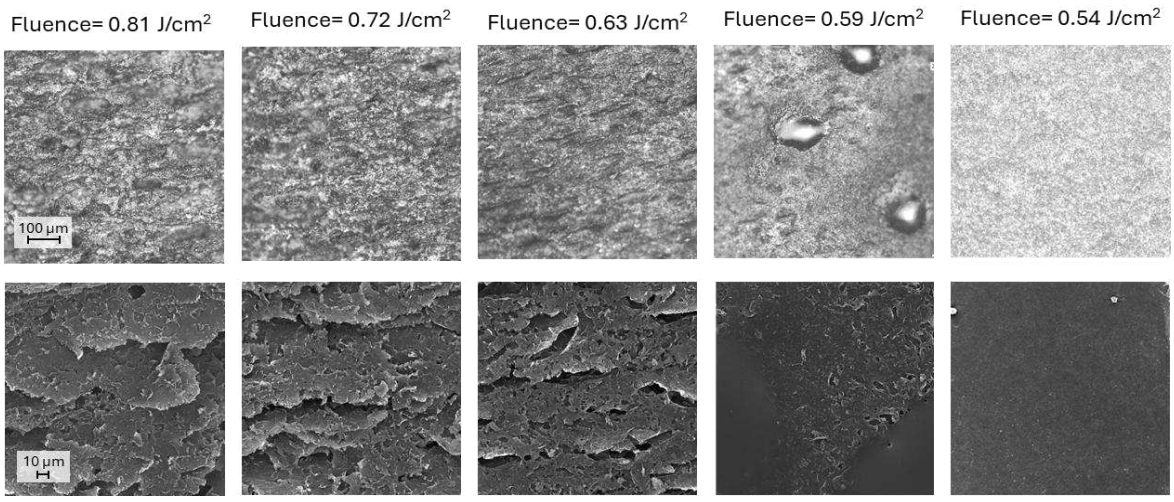

Figure 7.6 On top, microscope optical images of PLA/GO-2% surface lasered at the laser fluence marked above; on bottom, SEM images of PLA/GO-2% surface lasered at respective laser fluence. The scale refers to each image of the series.

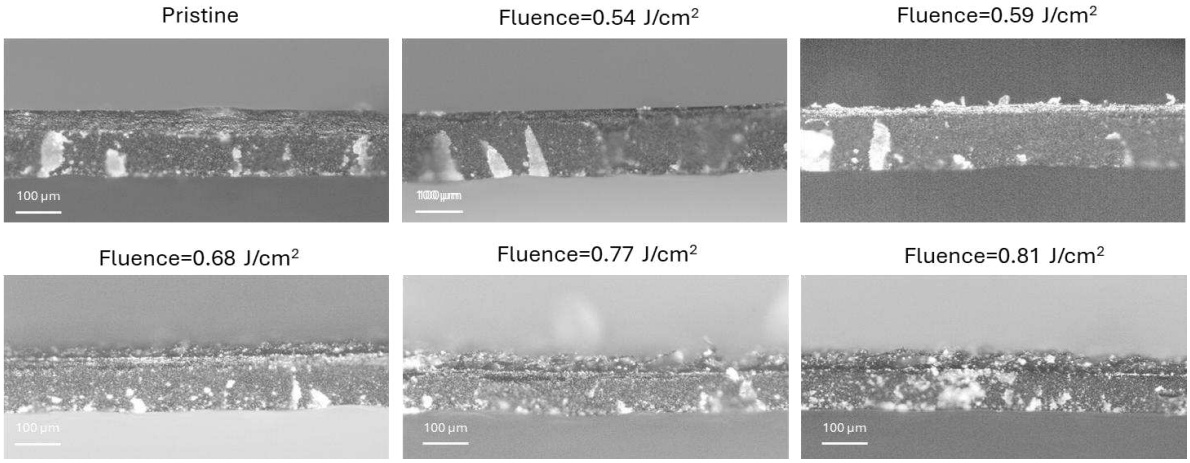

Figure 7.7 Optical microscope images of the cross sections of PLA/GO-2% samples pristine and after laser irradiation at different laser fluences.

Raman spectroscopy (figure 7.8) indicates that laser treatment converts the PLA/GO-2% composite into a low-defective graphitic structure. The Raman spectrum of the sample treated with 0.54 J/cm^2 laser fluence shows two intense peaks at 1332 and 1585 cm^{-1}, which are attributable to the D and G peaks of GO. The increase of laser fluence on the sample causes a significant change in the spectrum with the decrease of I_D/ I_G ratio from 1.16 at 0.54 J/cm^2 to 0.29 at 0.77 J/cm^2 and the growth of an intense 2D peak at 2665 cm^{-1} characteristic of graphitic structures. The I_D/ I_G ratio decreases, testifying to the effective reduction of GO to graphene and the decrease in the number of defects in the graphitic structure. The position of the 2D peak below 2700 cm^{-1} confirms the formation of graphene in agreement with the literature.[286]

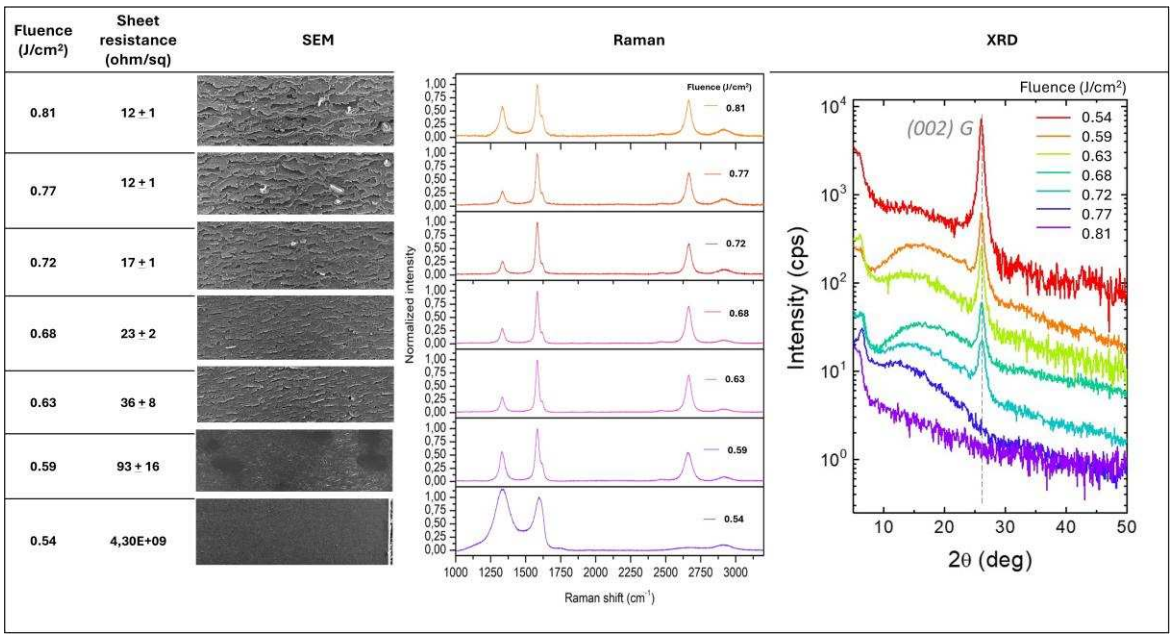

Figure 7.8 Characterization of PLA/GO-2% after laser treatment at different fluences. From the left: sheet resistance, SEM, Raman spectroscopy and grazing incidence X-Ray Diffraction.

In line with SEM and Raman, the XRD patterns (figure 7.8, right) evolve with laser fluence. In the pristine films no GO-related reflections are detected, consistent with a good monodispersion of GO within PLA (absence of layered aggregates in cross-sections). Upon increasing the laser fluence, a diffraction peak appears at $2\theta \approx 26°$ ($d \approx 3.43$ Å), which we assign to graphitic stacking (002) produced by laser writing. This assignment is consistent with prior reports of laser-induced graphene (LIG) from polymeric precursors, where the emergence/broadening of the (002) reflection near 26° is taken as a fingerprint of graphitization.[285]

We propose an explanation of the laser-induced transformation process in PLA/GO composites to better understand the mechanism behind these observations. When exposed to CO_2 laser, PLA/GO converts light energy into thermal energy promoting thermal degradation and graphitization reactions. It seems evident that the GO is responsible for the graphitization reaction. In the absence of GO, laser-treated polymer films exhibit only signs of material softening, without the formation of electrically conductive traces (figure 7.5a). It is evident that the effects of laser treatment on the subject material have had a significant impact on both surface morphology, structure and chemical composition. The heating process is expected to convert insulating GO into electrically conductive RGO by removing its oxygen functional groups and partially restore the percolation pathways of conductive aromatic carbon in the basal plane of GO. Simultaneously several processes could occur for PLA, including softening and thermal degradation of polymer with the formation of gaseous products that leaves the matrix. The rearrangement of carbon atoms

from PLA into an aromatic network with the formation of graphene-like materials is another process that could take place in a similar way to what has been hypothesised in previous studies.[287]

The capability of PLA/GO-2% platforms to be used as electrochemical sensors was first evaluated by using redox active benchmark species, namely 1,1-ferrocenedimethanol - $Fc(OH)_2$ - and the ferro-/ferri-cyanide redox couple ($FeCN^{3+/2+}$). The electrochemical behaviour of these new platforms was compared to that of a more conventional electrode system, namely a commercial CSPE.

Figure 7.9a reports exemplificative cyclovoltammetric (CV) responses recorded in 0.1 M KCl solution in absence and in presence of 0.5 mM $Fc(OH)_2$. The capacitive current (i_c), that generates at the electrode/solution interface by polarizing the electrode at a variable potential, was determined in absence of faradic processes, sampling the current at 0.27 V. A progressive decrease of i_c was observed at increasing laser fluence (Figure 7.9b), reaching a minimum at 0.77 J/cm^2. Interestingly, a further increase in fluence (0.81 J/cm^2) led to a rise in i_c. This trend aligns with Raman spectra, which suggest that higher laser fluences promote the formation of structural defects in the graphitic material. Such defects can enhance surface charge density, thereby increasing the capacitive contribution.

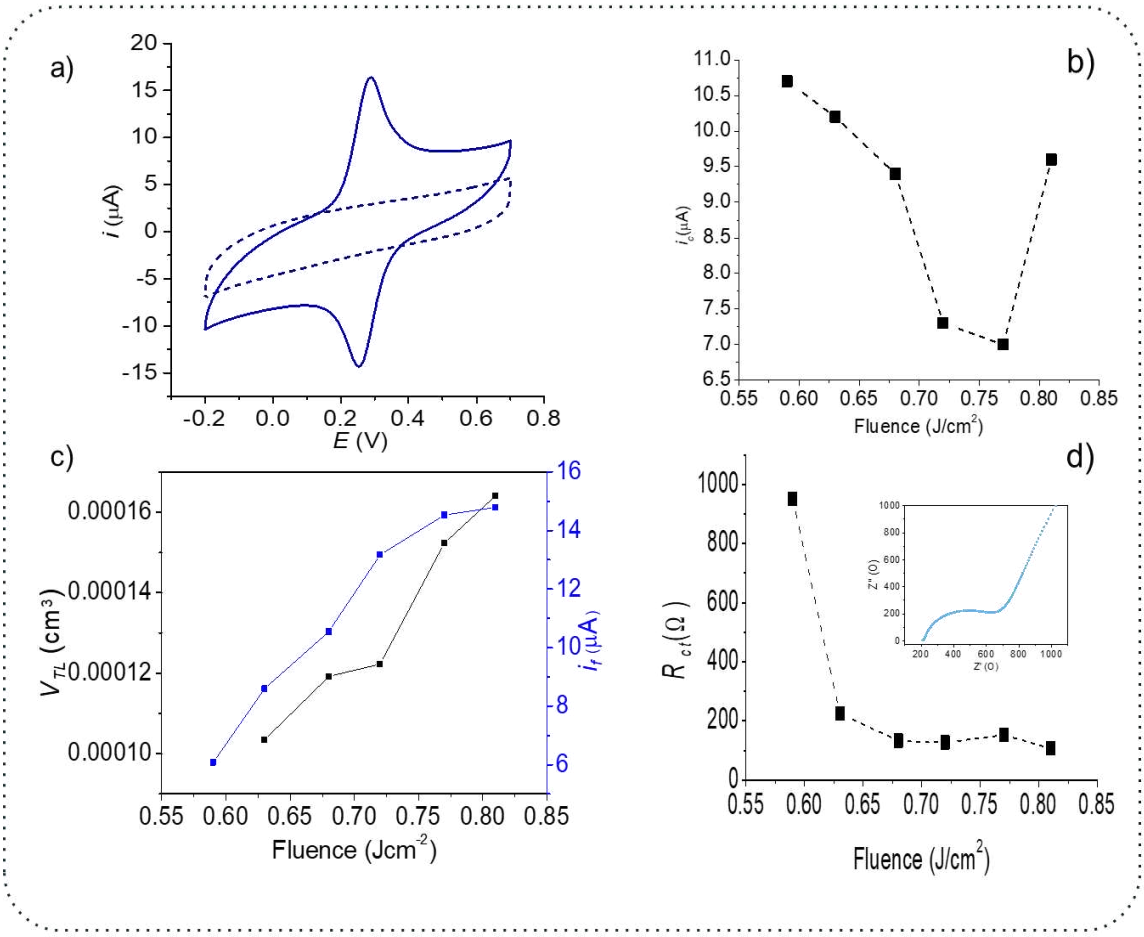

Figure 7.9 a) CV responses recorded at PLA/GO-2%, 0.72 J/cm^2 laser fluence, in 0.1 M KCl in absence (dotted line) and in presence (solid line) of 0.5 mM Fc(OH)$_2$, 0.05 Vs^{-1} potential scan rate. Relevant trend of b) ic recorded in absence of Fc(OH)$_2$ at +0.27 V, c) if and VTL recorded in presence of Fc(OH)$_2$. d) Trend of RCT defined by EIS plots recorded in Fe(CN)$_6^{2+/3+}$ in 0.1 M KCl; an exemplificative response collected with of PLA/GO 2% at fluence of 0.72 J/cm^2 is reported in the inset.

CV responses in presence of $Fc(OH)_2$ show the typical shape expected for a reversible redox species undergoing oxidation at a conductive electrode surface (Figure 7.9a). The difference between the oxidation and the reduction peak potentials, in any case lower than 100 mV, indicates that PLA/GO platforms can be used as electrodes after the laser treatment irrespectively to the laser fluence applied. A more straightforward evaluation of the resistance to charge transfer (R_{CT}) was achieved by electrochemical impedance spectroscopy (EIS), performed using the $FeCN^{3+/2+}$ redox couple (Figure 7.9d). The EIS plot indicates the presence of charge transfer and diffusive processes as expected for this redox couple on an electrochemically inert conductive surface. As observed, the R_{CT} values decrease at increasing laser fluence, reaching minimum values at 0.72 J/cm^2. Except for the platform obtained at the lowest laser fluence (0.59 J/cm^2; R_{CT} = 950 Ω), the values

obtained for all the platforms tested are lower than that obtained with a commercial SPE (R_{CT} = 470 Ω). The dimension of the electroactive surface in platforms obtained in the various conditions was evaluated by considering the faradic contribution to the oxidation peak (i_f) of $Fc(OH)_2$ recorded in CV traces. As observed in figure 7.9c, i_f increases at increasing the laser fluence, reaching a plateau at approximately 0.77 J/cm^2. This trend suggests a correlated increase of the electroactive surface until reaching a threshold.

The electrocatalytic properties of the laser-treated PLA/GO-2% platforms, which are at the basis of the use of these devices as electrochemical sensors, were investigated using electroactive biomolecules relevant to health monitoring. In particular, we tested adrenaline and nicotinamide adenine dinucleotide (NADH), which are important biomarkers of neuronal stimuli, as well as ascorbic and uric acids, normally present in biological fluids (figure 7.10). The increase of the laser fluence from 0.59 to 0.77 J/cm^2 results in electrode platforms characterized by more effective electrocatalytic properties, as evidenced by the shift of the current peak to less positive potentials for ascorbic acid, adrenaline and NADH. This means that the start of electrocatalytic processes, normally due to oxidized moieties present on carbon-based surfaces,[288] allows the detection of these analytes at lower positive potentials and with sharper oxidation peaks as the laser fluency used for scribing is increased, thus improving the sensor selectivity and sensitivity. The correlation between the intensity of the anodic peak and the laser fluence observed for these molecules (Figure 7.10a,b,d) results from a combinatorial effect of the enhancement in electron transfer kinetic due to the electrocatalytic performance and the increasing of the V_{TL} previously described. Vice versa, no correlation was observed for uric acid (figure 7.10c), except for the platform obtained at the lowest laser fluence, i.e. 0.59 J/cm^2, which led to the oxidation of this species at higher potentials and with a broader peak. The poor correlation obtained in this case between the laser fluence and the electrocatalytic properties can probably be ascribed to adsorption of this molecule on the electrode surface.

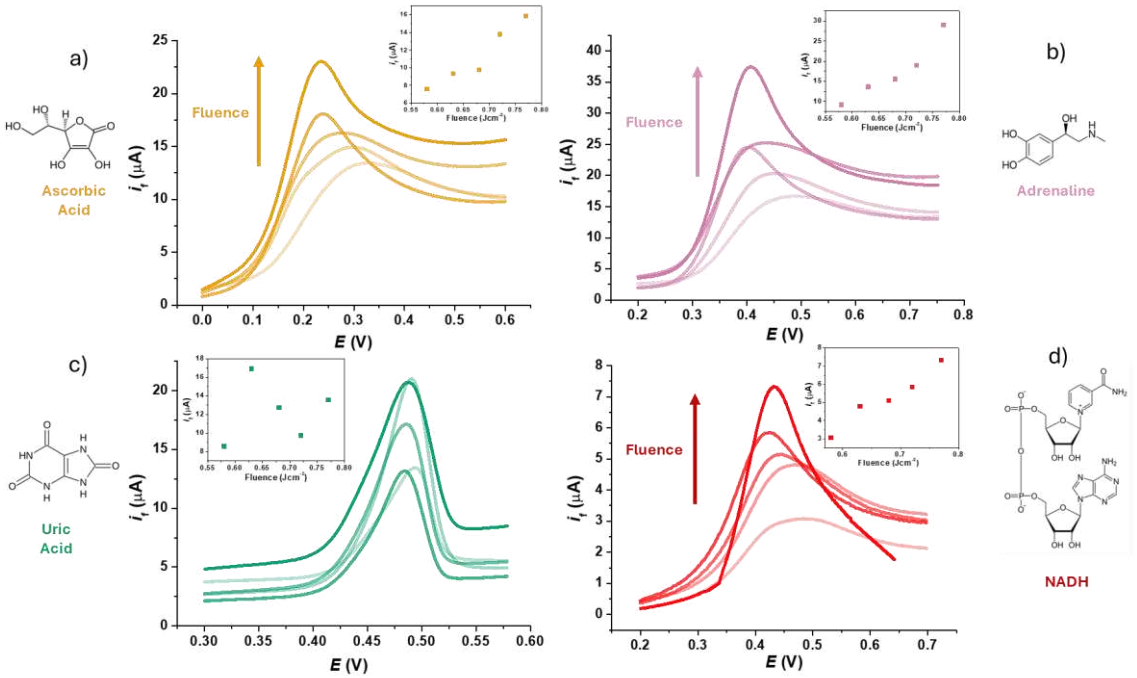

Figure 7.10 Linear Sweep Voltammetry oxidation responses recorded with PLA/GO-2% platforms at various laser fluences in artificial sweat solutions also containing 1 mM a) ascorbic acid, b) adrenaline, c) uric acid, d) NADH in. 0.02 Vs^{-1} potential scan rate. The curves are subtracted for the relevant blank signal.

Based on the promising results observed for adrenaline oxidation and due the importance of the detection of this species for the analysis of neural stimuli, we decided to test the applicability PLA/GO-2% as a sensor for the catecholamine-based neurotransmitters involved in adrenaline biosynthesis, namely Tyrosine (Tyr), L-DOPA, Dopamine (Dop), Noradrenaline (Nor) and Adrenaline (Adr). The platform obtained with a fluence of 0.72 J/cm^2 was selected for these tests, because it combines the best mechanical properties with the best electrocatalytic performance.

Further voltammetric tests were carried out in Differential Pulse Voltammetry (DPV), which is the voltammetric technique most frequently used for electroanalytical purposes. In analogy with the results obtained in CV, the DPV responses are shifted at lower potential values and show a higher peak intensity compared to responses recorded at CSPE (Figure 7.11a-f). In any case, these preliminary investigations indicated a good correlation between the current peak and the concentration of analyte in solution. This is due to negligible fouling or memory effects characterizing PLA/GO platforms. The oxidation peaks observed are 0.737±0.002 V for Tyr, 0.361±0.007 V for L-DOPA, 0.315±0.005 V for Dop, 0.351±0.010 V for Nor and 0.378±0.009 V for Adr (figure 7.11f), indicating the possibility to quantify all these molecules even when present in the same mixture or at least to unravel the response of

adrenaline oxidation with respect to those of the relevant precursors that may be present in the same sample.

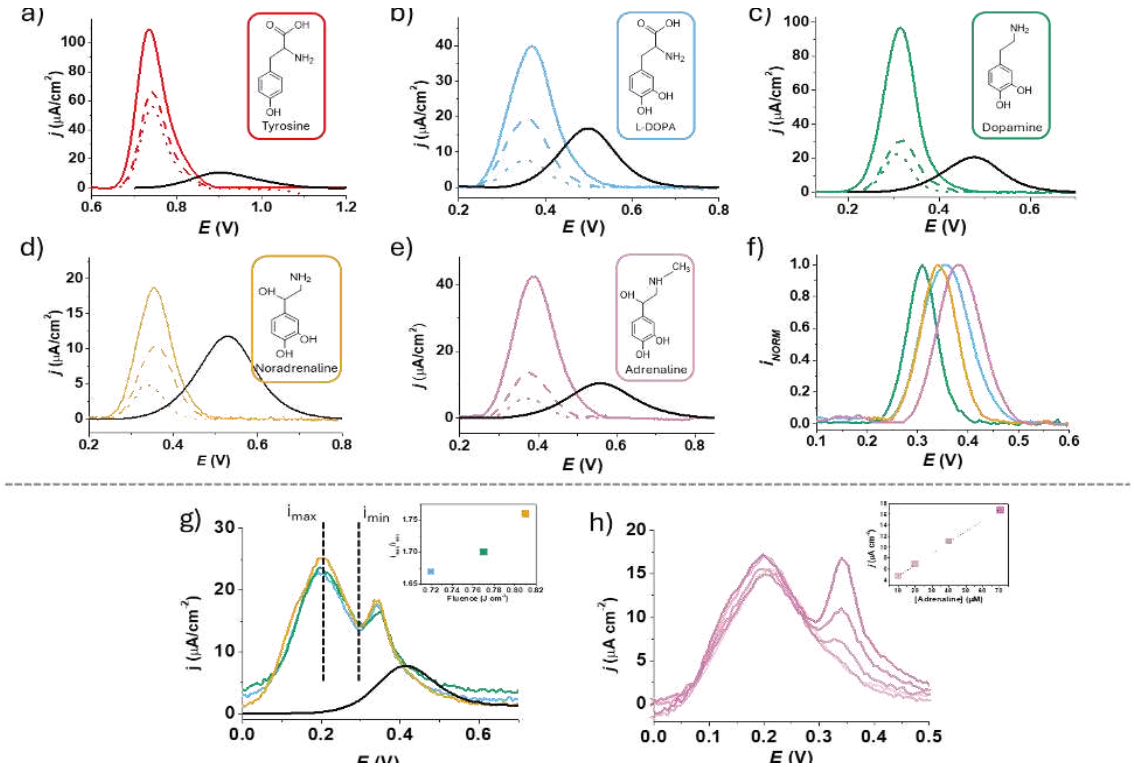

Figure 7.11 DPV responses recorded at PLA/GO-2% in artificial sweat of three different amounts (0.25, 0.5 and 1.0 mM) of the various molecules involved in the biosynthesis of adrenaline: Tyr (a), L-DOPA (b), Dop (c), Nor (d) and Adr (e) compared to responses obtained in solutions containing the analyte at the highest concentration at a CSPE (black curve); f) normalized DPV responses recorded for L-DOPA, Dop, Nor, and Adr at PLA/GO-2% to show the separation among the oxidation peaks. g) DPV responses recorded with PLA/GO-2% (0.72, 0.77, and 0.81 J/cm2 fluence) in artificial sweat containing 50 μM adrenaline and 500 μM ascorbic acid; the inset reports the imax/imin vs. the fluence applied in the realization of the platforms; h) DPV responses recorded in artificial sweat solution containing 0.5 mM ascorbic acid and different amount of adrenaline (10, 20, 40, and 70 μM); the inset reports the trend of anodic peak current recorded at 0.33 V versus adrenaline concentration.

Subsequently, we focused the analysis on the detection of adrenaline. Firstly, we evaluated the platform's performance in terms of repeatability and reproducibility, by performing three calibration plots from 0.1 to 1 mM with the same sensor platform and by repeating this analysis of three PLA/GO platforms obtained with the same laser fluence, namely 0.72 J/cm^2. The relative standard deviation of the sensitivity obtained in these conditions, 4% and 11% respectively, indicate the very good repeatability and reproducibility of the platform tests. As already underlined, massive fouling processes normally badly affecting the repeatability of responses obtained at conventional electrode surfaces, are mitigated by the use of PLA/GO.

Finally, the sensing performance for adrenaline detection was assessed in the presence of a common interfering species present in sweat, namely ascorbic acid, to verify the selectivity of the platform. A mixed solution containing 50 μM adrenaline and 500 μM ascorbic acid was tested with PLA/GO-2% platforms fabricated at three different fluences, namely 0.72, 0.77, and 0.81 J/cm^2. The results obtained were once more compared with analogous responses obtained at the commercial CSPE (figure 7.11g). Beside the analysis of the peak intensity, the capability of the platform to achieve good resolution between the two oxidation processes was quantified by the ratio between the maximum current recorded for ascorbic acid oxidation (i_{max}) and the current recorded in the minimum between the two oxidation processes (i_{min}). As observed, although all PLA/GO platforms tested demonstrated good resolutions between the two responses, better performance was obtained from the platform obtained with the highest fluence. Conversely, commercial SPE shows no capacity to discriminate between adrenaline and ascorbic acid oxidation responses.

Given the promising results obtained for the detection of adrenaline even in presence of ascorbic acid, we recorded the responses in solutions at different concentrations of analyte (0, 10, 20, 40, and 70 μM) and a fixed concentration of the interfering species (0.5 mM) to assess the lack of inference between the two species. As observed from DPV responses recorded in the various solutions (figure 7.11h), the current associated with ascorbic acid oxidation remains constant irrespectively to the concentration of adrenaline and the current peak due to adrenaline oxidation still maintains a linear trend with concentration. These results demonstrate that ascorbic acid does not interfere with the electrochemical detection of adrenaline.

7.4 Conclusions

Self-standing PLA/GO composite films with a homogeneous dispersion of GO nanosheets (up to 2% wt.) were successfully prepared via solvent casting from aqueous dispersions. The use of a PEG-PLA-PEG block copolymer surfactant facilitated good coalescence of PLA particles and integration of GO without macroscopic aggregation. The addition of GO induced a slight thermal stabilization of the PLA matrix, shifting the onset of the main degradation step to higher temperatures, which is attributed to the barrier effect of well-dispersed GO nanosheets. The incorporation of GO did not hinder the compostability of the PLA matrix and all composites demonstrated rapid and complete biodegradation (mineralization and disintegration) under industrial composting conditions, confirming that GO presence is compatible with microbial activity and does not change the material's end-of-life management options.

The composites were effectively converted into highly conductive, graphitic structures upon CO_2 laser irradiation. This process, which involves the thermal reduction of GO and likely the graphitization of PLA, produced Laser-Induced Graphene (LIG) with a sheet resistance as low as 12 Ω/sq, a value comparable to LIG from other polymer precursors. The laser-treated PLA/GO-2% platforms were evaluated as the most conductive and were tested as electrochemical electrodes. The electrodes exhibited low charge transfer resistance and significant electrocatalytic activity and displayed a good ability to detect various biomolecules: ascorbic acid, uric acid, NADH and adrenaline. The platforms further displayed effectiveness in the detection of catecholamine neurotransmitters, including adrenaline and its precursors, showing high reproducibility, resistance to fouling, and, crucially, the ability to selectively detect adrenaline in the presence of a high concentration of the common interferent, ascorbic acid.

In summary, this work successfully demonstrates a versatile and sustainable materials platform. The PLA/GO composites combine full compostability with the advanced functionality of laser-writable graphene electronics, showing particular promise for the development of disposable, high-performance electrochemical sensors for health monitoring and biosensing applications.

8. General conclusions

The research carried out for this thesis work resulted in the preparation of new formulations, of interest for use in the fishing industry, of two kinds of bio-based and biodegradable polyesters, PLA and PHA, by three different techniques: A waterborne dispersion of PLA using a PEG-PLA-PEG block copolymer as surfactant, usable for film and coating applications; a PLA netting which was produced using recycled PLA in an existing extrusion process developed for oil-based conventional polymers; and expanded materials for packaging produced by the foaming of blends of amorphous PHA with either amorphous or semi-crystalline PLA. These overall conclusions only briefly summarize the experimental details of each section, laid out in the respective chapters, and attempt to draw on the common threads between them.

The waterborne dispersions were successfully obtained with a high solids content (around 40%) and a long shelf life (6 months) after optimization of the surfactant ratio, with the addition of a small amount of SDS in addition to the ELE block copolymer proving crucial in decreasing particle size and increasing dispersion stability. After testing the physical properties of xanthan gum as a thickener, the thickened dispersions were coated onto a paper substrate. The coated paper exhibited good barriers to liquid and water vapor, comparable to the performance of solvent-based PLA paper coatings and the paper coated with lower coating weights was able to be fully pulped in water, indicating that it can still be recycled in the paper stream.

The waterborne dispersion that was developed to be used for the coating of paper packaging also revealed itself to be a very useful technique for more specialized and higher-value applications. As the basis for composites including graphene oxide, it could easily be transformed by laser-scribing into an electrochemical sensing platform for biomarkers that is also fully compostable. In the biomedical field, similar films that incapsulated instead peptides were capable of osteogenic activity by promoting the specialization of stem cells into osteoblasts when used as tissue culture surfaces, a promising step for the further objective of using the material as coating for titanium bone implants. Both kinds of material were obtained without the use of organic solvents, but by simple mixing of the additives with previously prepared dispersions, highlighting the versatility and easy application of this technique to innovative research in very diverse fields.

PLA aquaculture socks were successfully obtained from low-cost secondary PLA, by directly feeding the recycled polymer into an existing extrusion process used for polypropylene aquaculture socks. This is an attractive process for the substitution of a

conventional oil-based polymer with a low-cost bio-based one that is also biodegradable in some conditions. In particular, we verified the compostability at 58 °C of the PLA socks, a desirable end-of-life option for material retrieved after mussel harvesting. However, biodegradation tests at the seawater-sediment interface found little degradation over a period of 4-5 months. This is a sign that the PLA socks could also form persistent plastic pollution and a ghost fishing risk if dispersed in the environment, but it also indicates their resistance to prolonged use in the marine environment. Further studies on the field are needed to determine the efficiency of this material for mussel farming, and evaluate the drop in mechanical properties throughout a farming cycle.

The blending of PLA, both an amorphous grade and a semicrystalline one, and amorphous P34HB resulted in immiscible blends where the PHA was the minor component (10-30 wt.%) and was dispersed in a PLA matrix. We aimed to obtain from these blends expanded materials which could be used in packaging applications, such as for substituting EPS fish boxes. The blends were foamed by a batch process using supercritical CO_2 as the physical foaming agent, and after process optimization, low density foams were obtained for all amorphous compositions and for semicrystalline blends up to 20 % PHA. The recrystallization of PLA in the semicrystalline blends was found to be strongly accelerated by the dispersed PHA phase which added challenges to the foaming process.

The biodegradation capabilities in a home composting setting of the blend foams were analyzed and found to be superior to the ones of pure PLA foams, although in semicrystalline foams degradation was still very slow, with the degradation of the PHA phase being slowed down by being dispersed in the crystalline PLA phase. The amorphous blends were also tested in a seawater setting, where the PHA was selectively degraded and removed from the blend while the PLA was generally left unaltered, but a much greater degree of disintegration was obtained as PHA content was increased to 30%. The superior biodegradation capabilities and lower densities at higher aPHA content of the amorphous blends make them particularly interesting for packaging applications where the limited heat resistance is not a factor, such as boxes for storing refrigerated fish.

Overall, the potential and limitations of using biodegradable polyesters as substitution of conventional polymer materials in different fields were highlighted. What was generally evidenced is the great influence of both the environmental conditions and the specific bioplastic formulation that is employed on the rate of biodegradation and consequently the environmental footprint of the produced materials.

9. References

(1) Geyer, R. Chapter 2 - Production, Use, and Fate of Synthetic Polymers. In *Plastic Waste and Recycling*; Letcher, T. M., Ed.; Academic Press, 2020; pp 13–32. https://doi.org/10.1016/B978-0-12-817880-5.00002-5.

(2) Apete, L.; Martin, O. V.; Iacovidou, E. Fishing Plastic Waste: Knowns and Known Unknowns. *Mar. Pollut. Bull.* **2024**, *205*, 116530. https://doi.org/10.1016/j.marpolbul.2024.116530.

(3) Lebreton, L.; Slat, B.; Ferrari, F.; Sainte-Rose, B.; Aitken, J.; Marthouse, R.; Hajbane, S.; Cunsolo, S.; Schwarz, A.; Levivier, A.; Noble, K.; Debeljak, P.; Maral, H.; Schoeneich-Argent, R.; Brambini, R.; Reisser, J. Evidence That the Great Pacific Garbage Patch Is Rapidly Accumulating Plastic. *Sci. Rep.* **2018**, *8* (1), 4666. https://doi.org/10.1038/s41598-018-22939-w.

(4) Lebreton, L.; Royer, S.-J.; Peytavin, A.; Strietman, W. J.; Smeding-Zuurendonk, I.; Egger, M. Industrialised Fishing Nations Largely Contribute to Floating Plastic Pollution in the North Pacific Subtropical Gyre. *Sci. Rep.* **2022**, *12*, 12666. https://doi.org/10.1038/s41598-022-16529-0.

(5) Ceballos-Santos, S.; de Sousa, D. B.; García, P. G.; Laso, J.; Margallo, M.; Aldaco, R. Exploring the Environmental Impacts of Plastic Packaging: A Comprehensive Life Cycle Analysis for Seafood Distribution Crates. *Sci. Total Environ.* **2024**, *951*, 175452. https://doi.org/10.1016/j.scitotenv.2024.175452.

(6) *Assessment of more environmental alternatives to EPS fishboxes (TAUW)*. Fidra. https://www.fidra.org.uk/download/assessment-of-more-environmental-alternatives-to-eps-fishboxes/ (accessed 2025-09-16).

(7) Høiberg, M. A.; Woods, J. S.; Verones, F. Global Distribution of Potential Impact Hotspots for Marine Plastic Debris Entanglement. *Ecol. Indic.* **2022**, *135*, 108509. https://doi.org/10.1016/j.ecolind.2021.108509.

(8) Ziccardi, L. M.; Edgington, A.; Hentz, K.; Kulacki, K. J.; Kane Driscoll, S. Microplastics as Vectors for Bioaccumulation of Hydrophobic Organic Chemicals in the Marine Environment: A State-of-the-science Review. *Environ. Toxicol. Chem.* **2016**, *35* (7), 1667–1676. https://doi.org/10.1002/etc.3461.

(9) Heo, N. W.; Hong, S. H.; Han, G. M.; Hong, S.; Lee, J.; Song, Y. K.; Jang, M.; Shim, W. J. Distribution of Small Plastic Debris in Cross-Section and High Strandline on Heungnam Beach, South Korea. *Ocean Sci. J.* **2013**, *48* (2), 225–233. https://doi.org/10.1007/s12601-013-0019-9.

(10) Vert, M.; Doi, Y.; Hellwich, K.-H.; Hess, M.; Hodge, P.; Kubisa, P.; Rinaudo, M.; Schué, F. Terminology for biorelated polymers and applications (IUPAC Recommendations 2012). *Pure Appl. Chem.* **2012**, *84* (2), 377–410. https://doi.org/10.1351/PAC-REC-10-12-04.

(11) EUBIO_Admin. *Bioplastics*. European Bioplastics e.V. https://www.european-bioplastics.org/bioplastics/ (accessed 2025-09-15).

(12) Lackner, M.; Mukherjee, A.; Koller, M. What Are “Bioplastics”? Defining Renewability, Biosynthesis, Biodegradability, and Biocompatibility. *Polymers* **2023**, *15* (24), 4695. https://doi.org/10.3390/polym15244695.

(13) Krzan, A.; Hemjinda, S.; Miertus, S.; Corti, A.; Chiellini, E. Standardization and Certification in the Area of Environmentally Degradable Plastics. *Polym. Degrad. Stab.* **2006**, *91* (12), 2819–2833. https://doi.org/10.1016/j.polymdegradstab.2006.04.034.

(14) Ishimwe, S. *BIOPLASTICS MARKET DEVELOPMENT UPDATE 2024*. European Bioplastics e.V. https://www.european-bioplastics.org/bioplastics-market-development-update-2024/ (accessed 2025-01-27).

(15) Groot, W.; van Krieken, J.; Sliekersl, O.; de Vos, S. Production and Purification of Lactic Acid and Lactide. In *Poly(Lactic Acid)*; John Wiley & Sons, Ltd, 2022; pp 1–18. https://doi.org/10.1002/9781119767480.ch1.

(16) Gupta, A. P.; Kumar, V. New Emerging Trends in Synthetic Biodegradable Polymers – Polylactide: A Critique. *Eur. Polym. J.* **2007**, *43* (10), 4053–4074. https://doi.org/10.1016/j.eurpolymj.2007.06.045.
(17) Grijpma, D. W.; Pennings, A. J. (Co)Polymers of L-Lactide, 2. Mechanical Properties. *Macromol. Chem. Phys.* **1994**, *195* (5), 1649–1663. https://doi.org/10.1002/macp.1994.021950516.
(18) Nofar, M.; Perego, G.; Cella, G. D. Mechanical Properties. In *Poly(Lactic Acid)*; John Wiley & Sons, Ltd, 2022; pp 169–190. https://doi.org/10.1002/9781119767480.ch10.
(19) Sonchaeng, U.; Iñiguez-Franco, F.; Auras, R.; Selke, S.; Rubino, M.; Lim, L.-T. Poly(Lactic Acid) Mass Transfer Properties. *Prog. Polym. Sci.* **2018**, *86*, 85–121. https://doi.org/10.1016/j.progpolymsci.2018.06.008.
(20) Biswas, S.; Panja, S. S.; Bose, S. Tailored Distribution of Nanoparticles in Bi-Phasic Polymeric Blends as Emerging Materials for Suppressing Electromagnetic Radiation: Challenges and Prospects. *J. Mater. Chem. C* **2018**, *6* (13), 3120–3142. https://doi.org/10.1039/C8TC00002F.
(21) Kathuria, A.; Detyothin, S.; Jaruwattanayon, W.; Selke, S. E. M.; Auras, R. Blends. In *Poly(Lactic Acid)*; John Wiley & Sons, Ltd, 2022; pp 271–339. https://doi.org/10.1002/9781119767480.ch14.
(22) Otero Navas, I.; Kamkar, M.; Arjmand, M.; Sundararaj, U. Morphology Evolution, Molecular Simulation, Electrical Properties, and Rheology of Carbon Nanotube/Polypropylene/Polystyrene Blend Nanocomposites: Effect of Molecular Interaction between Styrene-Butadiene Block Copolymer and Carbon Nanotube. *Polymers* **2021**, *13* (2), 230. https://doi.org/10.3390/polym13020230.
(23) Gajria, A. M.; Davé, V.; Gross, R. A.; P. McCarthy, S. Miscibility and Biodegradability of Blends of Poly(Lactic Acid) and Poly(Vinyl Acetate). *Polymer* **1996**, *37* (3), 437–444. https://doi.org/10.1016/0032-3861(96)82913-2.
(24) Belletti, G.; Ronconi, G.; Mazzanti, V.; Buratti, E.; Marchi, L.; Sotgiu, G.; Calosi, M.; Mollica, F.; Bertoldo, M. Morphology and Mechanical Properties of Poly(Vinyl Alcohol)/Poly(Lactic Acid) Blend Films Prepared from Aqueous Dispersions. *Macromol. Mater. Eng.* **2024**, *309* (1), 2300237. https://doi.org/10.1002/mame.202300237.
(25) Matumba, K. I.; Mokhena, T. C.; Ojijo, V.; Sadiku, E. R.; Ray, S. S. Morphological Characteristics, Properties, and Applications of Polylactide/Poly(ε-Caprolactone) Blends and Their Composites—A Review. *Macromol. Mater. Eng.* **2024**, *309* (8), 2400056. https://doi.org/10.1002/mame.202400056.
(26) Zaaba, N. F.; Jaafar, M. A Review on Degradation Mechanisms of Polylactic Acid: Hydrolytic, Photodegradative, Microbial, and Enzymatic Degradation. *Polym. Eng. Sci.* **2020**, *60* (9), 2061–2075. https://doi.org/10.1002/pen.25511.
(27) Bocchini, S.; Fukushima, K.; Blasio, A. D.; Fina, A.; Frache, A.; Geobaldo, F. Polylactic Acid and Polylactic Acid-Based Nanocomposite Photooxidation. *Biomacromolecules* **2010**, *11* (11), 2919–2926. https://doi.org/10.1021/bm1006773.
(28) Schliecker, G.; Schmidt, C.; Fuchs, S.; Kissel, T. Characterization of a Homologous Series of d,l-Lactic Acid Oligomers; a Mechanistic Study on the Degradation Kinetics in Vitro. *Biomaterials* **2003**, *24* (21), 3835–3844. https://doi.org/10.1016/S0142-9612(03)00243-6.
(29) Tournier, V.; Duquesne, S.; Guillamot, F.; Cramail, H.; Taton, D.; Marty, A.; André, I. Enzymes' Power for Plastics Degradation. *Chem. Rev.* **2023**, *123* (9), 5612–5701. https://doi.org/10.1021/acs.chemrev.2c00644.
(30) Shalem, A.; Yehezkeli, O.; Fishman, A. Enzymatic Degradation of Polylactic Acid (PLA). *Appl. Microbiol. Biotechnol.* **2024**, *108* (1), 413. https://doi.org/10.1007/s00253-024-13212-4.
(31) Qi, X.; Ren, Y.; Wang, X. New Advances in the Biodegradation of Poly(Lactic) Acid. *Int. Biodeterior. Biodegrad.* **2017**, *117*, 215–223. https://doi.org/10.1016/j.ibiod.2017.01.010.
(32) Elsawy, M. A.; Kim, K.-H.; Park, J.-W.; Deep, A. Hydrolytic Degradation of Polylactic Acid (PLA) and Its Composites. *Renew. Sustain. Energy Rev.* **2017**, *79*, 1346–1352. https://doi.org/10.1016/j.rser.2017.05.143.

(33) Krasowska, K.; Heimowska, A. Degradability of Polylactide in Natural Aqueous Environments. *Water* **2023**, *15* (1), 198. https://doi.org/10.3390/w15010198.
(34) Deroiné, M.; Le Duigou, A.; Corre, Y.-M.; Le Gac, P.-Y.; Davies, P.; César, G.; Bruzaud, S. Accelerated Ageing of Polylactide in Aqueous Environments: Comparative Study between Distilled Water and Seawater. *Polym. Degrad. Stab.* **2014**, *108*, 319–329. https://doi.org/10.1016/j.polymdegradstab.2014.01.020.
(35) Hajilou, N.; Mostafayi, S. S.; Yarin, A. L.; Shokuhfar, T. A Comparative Review on Biodegradation of Poly(Lactic Acid) in Soil, Compost, Water, and Wastewater Environments: Incorporating Mathematical Modeling Perspectives. *AppliedChem* **2025**, *5* (1), 1. https://doi.org/10.3390/appliedchem5010001.
(36) Solano, G.; Rojas-Gätjens, D.; Rojas-Jimenez, K.; Chavarría, M.; Romero, R. M. Biodegradation of Plastics at Home Composting Conditions. *Environ. Chall.* **2022**, *7*, 100500. https://doi.org/10.1016/j.envc.2022.100500.
(37) Palsikowski, P. A.; Kuchnier, C. N.; Pinheiro, I. F.; Morales, A. R. Biodegradation in Soil of PLA/PBAT Blends Compatibilized with Chain Extender. *J. Polym. Environ.* **2018**, *26* (1), 330–341. https://doi.org/10.1007/s10924-017-0951-3.
(38) Rudnik, E.; Briassoulis, D. Comparative Biodegradation in Soil Behaviour of Two Biodegradable Polymers Based on Renewable Resources. *J. Polym. Environ.* **2011**, *19* (1), 18–39. https://doi.org/10.1007/s10924-010-0243-7.
(39) Kolstad, J. J.; Vink, E. T. H.; De Wilde, B.; Debeer, L. Assessment of Anaerobic Degradation of Ingeo™ Polylactides under Accelerated Landfill Conditions. *Polym. Degrad. Stab.* **2012**, *97* (7), 1131–1141. https://doi.org/10.1016/j.polymdegradstab.2012.04.003.
(40) Ainali, N. M.; Kalaronis, D.; Evgenidou, E.; Kyzas, G. Z.; Bobori, D. C.; Kaloyianni, M.; Yang, X.; Bikiaris, D. N.; Lambropoulou, D. A. Do Poly(Lactic Acid) Microplastics Instigate a Threat? A Perception for Their Dynamic towards Environmental Pollution and Toxicity. *Sci. Total Environ.* **2022**, *832*, 155014. https://doi.org/10.1016/j.scitotenv.2022.155014.
(41) Ferrández-Montero, A.; Lieblich, M.; González-Carrasco, J. L.; Benavente, R.; Lorenzo, V.; Detsch, R.; Boccaccini, A. R.; Ferrari, B. Development of Biocompatible and Fully Bioabsorbable PLA/Mg Films for Tissue Regeneration Applications. *Acta Biomater.* **2019**, *98*, 114–124. https://doi.org/10.1016/j.actbio.2019.05.026.
(42) Pattanasuttichonlakul, W.; Sombatsompop, N.; Prapagdee, B. Accelerating Biodegradation of PLA Using Microbial Consortium from Dairy Wastewater Sludge Combined with PLA-Degrading Bacterium. *Int. Biodeterior. Biodegrad.* **2018**, *132*, 74–83. https://doi.org/10.1016/j.ibiod.2018.05.014.
(43) Mayekar, P. C.; Auras, R. Accelerating Biodegradation: Enhancing Poly(Lactic Acid) Breakdown at Mesophilic Environmental Conditions with Biostimulants. *Macromol. Rapid Commun.* **2024**, *45* (7), 2300641. https://doi.org/10.1002/marc.202300641.
(44) Guicherd, M.; Ben Khaled, M.; Guéroult, M.; Nomme, J.; Dalibey, M.; Grimaud, F.; Alvarez, P.; Kamionka, E.; Gavalda, S.; Noël, M.; Vuillemin, M.; Amillastre, E.; Labourdette, D.; Cioci, G.; Tournier, V.; Kitpreechavanich, V.; Dubois, P.; André, I.; Duquesne, S.; Marty, A. An Engineered Enzyme Embedded into PLA to Make Self-Biodegradable Plastic. *Nature* **2024**, *631* (8022), 884–890. https://doi.org/10.1038/s41586-024-07709-1.
(45) Easton, Z. H. W.; Essink, M. A. J.; Rodriguez Comas, L.; Wurm, F. R.; Gojzewski, H. Acceleration of Biodegradation Using Polymer Blends and Composites. *Macromol. Chem. Phys.* **2023**, *224* (6), 2200421. https://doi.org/10.1002/macp.202200421.
(46) Bher, A.; Cho, Y.; Auras, R. Boosting Degradation of Biodegradable Polymers. *Macromol. Rapid Commun.* **2023**, *44* (5), 2200769. https://doi.org/10.1002/marc.202200769.
(47) Z. Naser, A.; Deiab, I.; M. Darras, B. Poly(Lactic Acid) (PLA) and Polyhydroxyalkanoates (PHAs), Green Alternatives to Petroleum-Based Plastics: A Review. *RSC Adv.* **2021**, *11* (28), 17151–17196. https://doi.org/10.1039/D1RA02390J.
(48) Dhaini, A.; Hardouin-Duparc, V.; Alaaeddine, A.; Carpentier, J.-F.; Guillaume, S. M. Recent Advances in Polyhydroxyalkanoates Degradation and Chemical Recycling.

Prog. Polym. Sci. **2024**, *149*, 101781. https://doi.org/10.1016/j.progpolymsci.2023.101781.
(49) Liang, X.; Cha, D. K.; Xie, Q. Properties, Production, and Modification of Polyhydroxyalkanoates. *Resour. Conserv. Recycl. Adv.* **2024**, *21*, 200206. https://doi.org/10.1016/j.rcradv.2024.200206.
(50) Laycock, B.; Halley, P.; Pratt, S.; Werker, A.; Lant, P. The Chemomechanical Properties of Microbial Polyhydroxyalkanoates. *Prog. Polym. Sci.* **2014**, *39* (2), 397–442. https://doi.org/10.1016/j.progpolymsci.2013.06.008.
(51) Getino, L.; Martín, J. L.; Chamizo-Ampudia, A. A Review of Polyhydroxyalkanoates: Characterization, Production, and Application from Waste. *Microorganisms* **2024**, *12* (10), 2028. https://doi.org/10.3390/microorganisms12102028.
(52) Koller, M. Chemical and Biochemical Engineering Approaches in Manufacturing Polyhydroxyalkanoate (PHA) Biopolyesters of Tailored Structure with Focus on the Diversity of Building Blocks. *Chem. Biochem. Eng. Q.* **2019**, *32* (4), 413–438. https://doi.org/10.15255/CABEQ.2018.1385.
(53) Carrasco, F.; Dionisi, D.; Martinelli, A.; Majone, M. Thermal Stability of Polyhydroxyalkanoates. *J. Appl. Polym. Sci.* **2006**, *100* (3), 2111–2121. https://doi.org/10.1002/app.23586.
(54) Miu, D.-M.; Eremia, M. C.; Moscovici, M. Polyhydroxyalkanoates (PHAs) as Biomaterials in Tissue Engineering: Production, Isolation, Characterization. *Materials* **2022**, *15* (4), 1410. https://doi.org/10.3390/ma15041410.
(55) Li, Y.; Lei, Y.; Yao, S.; Han, C.; Yu, Y.; Xiao, L. Miscibility, Crystallization, Rheological and Mechanical Properties of Biodegradable Poly(3-Hydroxybutyrate-*Co*-4-Hydroxybutyrate)/Poly(Vinyl Acetate) Blends. *Thermochim. Acta* **2020**, *693*, 178755. https://doi.org/10.1016/j.tca.2020.178755.
(56) *Neat Resins – CJ Biomaterials*. https://cjbiomaterials.com/neat-resins/ (accessed 2025-09-10).
(57) W. Meereboer, K.; Misra, M.; K. Mohanty, A. Review of Recent Advances in the Biodegradability of Polyhydroxyalkanoate (PHA) Bioplastics and Their Composites. *Green Chem.* **2020**, *22* (17), 5519–5558. https://doi.org/10.1039/D0GC01647K.
(58) Paloyan, A.; Tadevosyan, M.; Ghevondyan, D.; Khoyetsyan, L.; Karapetyan, M.; Margaryan, A.; Antranikian, G.; Panosyan, H. Biodegradation of Polyhydroxyalkanoates: Current State and Future Prospects. *Front. Microbiol.* **2025**, *16*. https://doi.org/10.3389/fmicb.2025.1542468.
(59) Vayshbeyn, L. I.; Mastalygina, E. E.; Olkhov, A. A.; Podzorova, M. V. Poly(Lactic Acid)-Based Blends: A Comprehensive Review. *Appl. Sci.* **2023**, *13* (8), 5148. https://doi.org/10.3390/app13085148.
(60) Muniyasamy, S.; Ofosu, O.; John, M.; Anandjiwala, R. Mineralization of Poly(Lactic Acid) (PLA), Poly(3-Hydroxybutyrate-Co-Valerate) (PHBV) and PLA/PHBV Blend in Compost and Soil Environments. *J. Renew. Mater.* **2016**, *4* (2), 133–145. https://doi.org/10.7569/JRM.2016.634104.
(61) Sashiwa, H.; Fukuda, R.; Okura, T.; Sato, S.; Nakayama, A. Microbial Degradation Behavior in Seawater of Polyester Blends Containing Poly(3-Hydroxybutyrate-Co-3-Hydroxyhexanoate) (PHBHHx). *Mar. Drugs* **2018**, *16* (1), 34. https://doi.org/10.3390/md16010034.
(62) Weng, Y.-X.; Wang, L.; Zhang, M.; Wang, X.-L.; Wang, Y.-Z. Biodegradation Behavior of P(3HB,4HB)/PLA Blends in Real Soil Environments. *Polym. Test.* **2013**, *32* (1), 60–70. https://doi.org/10.1016/j.polymertesting.2012.09.014.
(63) Han, G.; Yoon, J.; Lee, C.; Lee, E.; Yoon, K.; Kwak, H. W.; Jin, H.-J. Biodegradation Behavior of Amorphous Polyhydroxyalkanoate-Incorporated Poly(l-Lactic Acid) under Modulated Home-Composting Conditions. *Polym. Test.* **2023**, *126*, 108155. https://doi.org/10.1016/j.polymertesting.2023.108155.
(64) Hong, Y.; Yang, H.-S.; Lee, M. H.; Kim, S.; Park, S. B.; Hwang, S. Y.; Park, J.; Koo, J. M.; Oh, D.; Hwang, D. S. Fishing Gear with Enhanced Drapability and Biodegradability: Artificial, Eco-Friendly Fibers Inspired by the Mussel Byssus. *Chem. Eng. J.* **2024**, *489*, 151388. https://doi.org/10.1016/j.cej.2024.151388.

(65) Grimaldo, E.; Herrmann, B.; Tveit, G. M.; Vollstad, J.; Schei, M. Effect of Using Biodegradable Gill Nets on the Catch Efficiency of Greenland Halibut. *Mar. Coast. Fish.* **2018**, *10* (6), 619–629. https://doi.org/10.1002/mcf2.10058.
(66) Grimaldo, E.; Herrmann, B.; Su, B.; Føre, H. M.; Vollstad, J.; Olsen, L.; Larsen, R. B.; Tatone, I. Comparison of Fishing Efficiency between Biodegradable Gillnets and Conventional Nylon Gillnets. *Fish. Res.* **2019**, *213*, 67–74. https://doi.org/10.1016/j.fishres.2019.01.003.
(67) Cerbule, K.; Grimaldo, E.; Herrmann, B.; Larsen, R. B.; Brčić, J.; Vollstad, J. Can Biodegradable Materials Reduce Plastic Pollution without Decreasing Catch Efficiency in Longline Fishery? *Mar. Pollut. Bull.* **2022**, *178*, 113577. https://doi.org/10.1016/j.marpolbul.2022.113577.
(68) Cerbule, K.; Larsen, R. B.; Vollstad, J.; Alvestad, A. H. Comparison of Fishing Performance of Biodegradable and Nylon Gillnets with Different Twine Diameter. *Reg. Stud. Mar. Sci.* **2025**, *87*, 104247. https://doi.org/10.1016/j.rsma.2025.104247.
(69) Seonghun, K.; Pyungkwan, K.; Seongjae, J.; Kyounghoon, L. Assessment of the Physical Characteristics and Fishing Performance of Gillnets Using Biodegradable Resin (PBS/PBAT and PBSAT) to Reduce Ghost Fishing. *Aquat. Conserv. Mar. Freshw. Ecosyst.* **2020**, *30* (10), 1868–1884. https://doi.org/10.1002/aqc.3354.
(70) Kim, S.; Kim, P.; Lim, J.; An, H.; Suuronen, P. Use of Biodegradable Driftnets to Prevent Ghost Fishing: Physical Properties and Fishing Performance for Yellow Croaker. *Anim. Conserv.* **2016**, *19* (4), 309–319. https://doi.org/10.1111/acv.12256.
(71) Hong, Y.; Yang, H.-S.; Lee, M. H.; Kim, S.; Park, S. B.; Hwang, S. Y.; Park, J.; Koo, J. M.; Oh, D.; Hwang, D. S. Fishing Gear with Enhanced Drapability and Biodegradability: Artificial, Eco-Friendly Fibers Inspired by the Mussel Byssus. *Chem. Eng. J.* **2024**, *489*, 151388. https://doi.org/10.1016/j.cej.2024.151388.
(72) Yu, M.; Tang, Y.; Min, M.; Herrmann, B.; Cerbule, K.; Liu, C.; Dou, Y.; Zhang, L. Comparison of Physical Properties and Fishing Performance between Biodegradable PLA and Conventional PA Trammel Nets in Grey Mullet (*Mugil Cephalus*) and Red-Lip Mullet (*Liza Haematocheila*) Fishery. *Mar. Pollut. Bull.* **2023**, *195*, 115545. https://doi.org/10.1016/j.marpolbul.2023.115545.
(73) AiyanSHU; MinZHANG; WenwenYU; YueWANG; JiangaoSHI; LeiWANG; MinghuaMIN. Comparative Analysis of Physical Performance and Fishing Efficiency between Biodegradable PLA Gill Net and Conventional PA Gill Net. *Mar. Fish.* **2022**, *43* (01), 93–103. https://doi.org/10.3724/SP.J.1004-2490.2021.0110.
(74) Rheinland, T. *TÜV Rheinland | TÜV Rheinland*. https://www.dincertco.de/din-certco/en/main-navigation/products-and-services/certification-of-products/environmental-field/biodegradable-in-marine-environment/ (accessed 2025-09-16).
(75) Karl, C. W.; Bernat, S.; Arstad, B.; Kubowicz, S.; Persson, A.-M. M. R.; Stenerud, G.; Olafsen, K.; Comerford, J.; Grimaldo, E.; Hakvaag, S.; Larsen, R. B. Degradation Behavior of Biodegradable and Conventional Polymers for Gill Nets, Exposed to Accelerated Aging. *ACS Appl. Polym. Mater.* **2025**, *7* (5), 2830–2840. https://doi.org/10.1021/acsapm.4c03333.
(76) Cao, H.; Ding, X.; Ao, S.; Huang, W.; Wang, S.; Li, F.; Li, L.; Li, Y.; Li, B.; Li, Q.; Liu, S. Cellulose-Based Biomass Foams for Food Packaging: Current Trends and Future Challenges. *Trends Food Sci. Technol.* **2025**, *163*, 105185. https://doi.org/10.1016/j.tifs.2025.105185.
(77) Soykeabkaew, N.; Thanomsilp, C.; Suwantong, O. A Review: Starch-Based Composite Foams. *Compos. Part Appl. Sci. Manuf.* **2015**, *78*, 246–263. https://doi.org/10.1016/j.compositesa.2015.08.014.
(78) Tapia-Blácido, D. R.; Aguilar, G. J.; de Andrade, M. T.; Rodrigues-Júnior, M. F.; Guareschi-Martins, F. C. Trends and Challenges of Starch-Based Foams for Use as Food Packaging and Food Container. *Trends Food Sci. Technol.* **2022**, *119*, 257–271. https://doi.org/10.1016/j.tifs.2021.12.005.
(79) *Our Business | Expanded PHBH, KANEKA BIODEGRADABLE POLYMER PHBH® - Mitsui & Co. Italia S.p.A.*

https://www.mitsui.com/it/en/business/performance_materials/1241495_13583.html (accessed 2025-09-16).
(80) Zhou, H.; Hu, D.; Zhu, M.; Xue, K.; Wei, X.; Park, C. B.; Wang, X.; Zhao, L. Review on Poly (Butylene Succinate) Foams: Modifications, Foaming Behaviors and Applications. *Sustain. Mater. Technol.* **2023**, *38*, e00720. https://doi.org/10.1016/j.susmat.2023.e00720.
(81) Sheng, H.; Zhou, Z.; Yan, H.; Yao, Y.; Zhang, L. Shrink-Resistant Poly(Butylene Adipate-Co-Terephthalate) Foam Reinforced with Crystalline Poly(3-Hydroxybutyrate-Co-3-Hydroxyvalerate) Particles. *ACS Appl. Polym. Mater.* **2023**, *5* (9), 7519–7527. https://doi.org/10.1021/acsapm.3c01348.
(82) Cheng, H.-Y.; Yang, Y.-J.; Li, S.-C.; Hong, J.-Y.; Jang, G.-W. Modification and Extrusion Coating of Polylactic Acid Films. *J. Appl. Polym. Sci.* **2015**, *132* (35). https://doi.org/10.1002/app.42472.
(83) Helanto, K.; Talja, R.; Rojas, O. J. Talc Reinforcement of Polylactide and Biodegradable Polyester Blends via Injection-Molding and Pilot-Scale Film Extrusion. *J. Appl. Polym. Sci.* **2021**, *138* (41), 51225. https://doi.org/10.1002/app.51225.
(84) Morris, B. A. Understanding Why Adhesion in Extrusion Coating Decreases With Diminishing Coating Thickness. *J. Plast. Film Sheeting* **2008**, *24* (1), 53–88. https://doi.org/10.1177/8756087908089486.
(85) Rastogi, V. K.; Samyn, P. Bio-Based Coatings for Paper Applications. *Coatings* **2015**, *5* (4), 887–930. https://doi.org/10.3390/coatings5040887.
(86) Gutoff, E. B.; Cohen, E. D. 14 - Water- and Solvent-Based Coating Technology. In *Multilayer Flexible Packaging (Second Edition)*; Wagner, J. R., Ed.; Plastics Design Library; William Andrew Publishing, 2016; pp 205–234. https://doi.org/10.1016/B978-0-323-37100-1.00014-4.
(87) Pieters, K.; H. Mekonnen, T. Progress in Waterborne Polymer Dispersions for Coating Applications: Commercialized Systems and New Trends. *RSC Sustain.* **2024**, *2* (12), 3704–3729. https://doi.org/10.1039/D4SU00267A.
(88) Belletti, G.; Buoso, S.; Ricci, L.; Guillem-Ortiz, A.; Aragón-Gutiérrez, A.; Bortolini, O.; Bertoldo, M. Preparations of Poly(Lactic Acid) Dispersions in Water for Coating Applications. *Polymers* **2021**, *13* (16), 2767. https://doi.org/10.3390/polym13162767.
(89) Okolieocha, C.; Raps, D.; Subramaniam, K.; Altstädt, V. Microcellular to Nanocellular Polymer Foams: Progress (2004–2015) and Future Directions – A Review. *Eur. Polym. J.* **2015**, *73*, 500–519. https://doi.org/10.1016/j.eurpolymj.2015.11.001.
(90) Lee, L. J.; Zeng, C.; Cao, X.; Han, X.; Shen, J.; Xu, G. Polymer Nanocomposite Foams. *Compos. Sci. Technol.* **2005**, *65* (15), 2344–2363. https://doi.org/10.1016/j.compscitech.2005.06.016.
(91) Matuana, L. M. Foaming. In *Poly(Lactic Acid)*; John Wiley & Sons, Ltd, 2022; pp 341–365. https://doi.org/10.1002/9781119767480.ch15.
(92) Nofar, M.; Park, C. B. Poly (Lactic Acid) Foaming. *Prog. Polym. Sci.* **2014**, *39* (10), 1721–1741. https://doi.org/10.1016/j.progpolymsci.2014.04.001.
(93) Standau, T.; Zhao, C.; Murillo Castellón, S.; Bonten, C.; Altstädt, V. Chemical Modification and Foam Processing of Polylactide (PLA). *Polymers* **2019**, *11* (2), 306. https://doi.org/10.3390/polym11020306.
(94) Zhang, X.; Ding, W.; Zhao, N.; Chen, J.; Park, C. B. Effects of Compressed CO2 and Cotton Fibers on the Crystallization and Foaming Behaviors of Polylactide. *Ind. Eng. Chem. Res.* **2018**, *57* (6), 2094–2104. https://doi.org/10.1021/acs.iecr.7b04139.
(95) Taki, K.; Kitano, D.; Ohshima, M. Effect of Growing Crystalline Phase on Bubble Nucleation in Poly(L -Lactide)/CO_2 Batch Foaming. *Ind. Eng. Chem. Res.* **2011**, *50* (6), 3247–3252. https://doi.org/10.1021/ie101637f.
(96) Longo, A.; Di Maio, E.; Di Lorenzo, M. L. Heterogeneous Bubble Nucleation by Homogeneous Crystal Nuclei in Poly(l-Lactic Acid) Foaming. *Macromol. Chem. Phys.* **2022**, *223* (4), 2100428. https://doi.org/10.1002/macp.202100428.
(97) Li, S.; Chen, T.; Liao, X.; Han, W.; Yan, Z.; Li, J.; Li, G. Effect of Macromolecular Chain Movement and the Interchain Interaction on Crystalline Nucleation and Spherulite Growth of Polylactic Acid under High-Pressure CO2. *Macromolecules* **2020**, *53* (1), 312–322. https://doi.org/10.1021/acs.macromol.9b01601.

(98) Chinaglia, S.; Tosin, M.; Degli-Innocenti, F. Biodegradation Rate of Biodegradable Plastics at Molecular Level. *Polym. Degrad. Stab.* **2018**, *147*, 237–244. https://doi.org/10.1016/j.polymdegradstab.2017.12.011.
(99) Skleničková, K.; Abbrent, S.; Halecký, M.; Kočí, V.; Beneš, H. Biodegradability and Ecotoxicity of Polyurethane Foams: A Review. *Crit. Rev. Environ. Sci. Technol.* **2022**, *52* (2), 157–202. https://doi.org/10.1080/10643389.2020.1818496.
(100) Tyagi, P.; Salem, K. S.; Hubbe, M. A.; Pal, L. Advances in Barrier Coatings and Film Technologies for Achieving Sustainable Packaging of Food Products – A Review. *Trends Food Sci. Technol.* **2021**, *115*, 461–485. https://doi.org/10.1016/j.tifs.2021.06.036.
(101) De Temmerman, J.; Vermeir, I.; Slabbinck, H. Eating out of Paper versus Plastic: The Effect of Packaging Material on Consumption. *Food Qual. Prefer.* **2023**, *112*, 105023. https://doi.org/10.1016/j.foodqual.2023.105023.
(102) Kunam, P. K.; Ramakanth, D.; Akhila, K.; Gaikwad, K. K. Bio-Based Materials for Barrier Coatings on Paper Packaging. *Biomass Convers. Biorefinery* **2022**. https://doi.org/10.1007/s13399-022-03241-2.
(103) Khwaldia, K.; Arab-Tehrany, E.; Desobry, S. Biopolymer Coatings on Paper Packaging Materials. *Compr. Rev. Food Sci. Food Saf.* **2010**, *9* (1), 82–91. https://doi.org/10.1111/j.1541-4337.2009.00095.x.
(104) Basak, S.; Dangate, M. S.; Samy, S. Oil- and Water-Resistant Paper Coatings: A Review. *Prog. Org. Coat.* **2024**, *186*, 107938. https://doi.org/10.1016/j.porgcoat.2023.107938.
(105) Nechita, P.; Roman (Iana-Roman), M. Review on Polysaccharides Used in Coatings for Food Packaging Papers. *Coatings* **2020**, *10* (6), 566. https://doi.org/10.3390/coatings10060566.
(106) Nur Hanani, Z. A. Surface Properties of Biodegradable Polymers for Food Packaging. In *Polymers for Food Applications*; Gutiérrez, T. J., Ed.; Springer International Publishing: Cham, 2018; pp 131–147. https://doi.org/10.1007/978-3-319-94625-2_6.
(107) Auras, R.; Harte, B.; Selke, S. An Overview of Polylactides as Packaging Materials. *Macromol. Biosci.* **2004**, *4* (9), 835–864. https://doi.org/10.1002/mabi.200400043.
(108) Mohan, S.; Panneerselvam, K. A Short Review on Mechanical and Barrier Properties of Polylactic Acid-Based Films. *Mater. Today Proc.* **2022**, *56*, 3241–3246. https://doi.org/10.1016/j.matpr.2021.09.375.
(109) Mujtaba, M.; Lipponen, J.; Ojanen, M.; Puttonen, S.; Vaittinen, H. Trends and Challenges in the Development of Bio-Based Barrier Coating Materials for Paper/Cardboard Food Packaging; a Review. *Sci. Total Environ.* **2022**, *851*, 158328. https://doi.org/10.1016/j.scitotenv.2022.158328.
(110) Rhim, J.-W.; Kim, J.-H. Properties of Poly(Lactide)-Coated Paperboard for the Use of 1-Way Paper Cup. *J. Food Sci.* **2009**, *74* (2), E105–E111. https://doi.org/10.1111/j.1750-3841.2009.01073.x.
(111) N, S.; S, A. K.; A, P.; S, G. Studies on Semi-Crystalline Poly Lactic Acid (PLA) as a Hydrophobic Coating Material on Kraft Paper for Imparting Barrier Properties in Coated Abrasive Applications. *Prog. Org. Coat.* **2020**, *145*, 105682. https://doi.org/10.1016/j.porgcoat.2020.105682.
(112) Marano, S.; Laudadio, E.; Minnelli, C.; Stipa, P. Tailoring the Barrier Properties of PLA: A State-of-the-Art Review for Food Packaging Applications. *Polymers* **2022**, *14* (8), 1626. https://doi.org/10.3390/polym14081626.
(113) Karamanlioglu, M.; Preziosi, R.; Robson, G. D. Abiotic and Biotic Environmental Degradation of the Bioplastic Polymer Poly(Lactic Acid): A Review. *Polym. Degrad. Stab.* **2017**, *137*, 122–130. https://doi.org/10.1016/j.polymdegradstab.2017.01.009.
(114) *CPI publishes revised Design for Recyclability Guidelines*. https://paper.org.uk/CPI/CPI/Content/News/Press-Releases/2022/CPI-publishes-revised-Design-for-Recyclability-Guidelines.aspx (accessed 2023-12-20).
(115) Sängerlaub, S.; Brüggemann, M.; Rodler, N.; Jost, V.; Bauer, K. D. Extrusion Coating of Paper with Poly(3-Hydroxybutyrate-Co-3-Hydroxyvalerate) (PHBV)—Packaging

Related Functional Properties. *Coatings* **2019**, *9* (7), 457. https://doi.org/10.3390/coatings9070457.
(116) Shankar, A.; A.k., A. M.; Narayan, R.; Chakrabarty, A. Emulsion Polymerized Styrene Acrylic/Nanocellulose Composite Coating to Improve the Strength and Hydrophobicity of Kraft Paper. *Prog. Org. Coat.* **2023**, *182*, 107634. https://doi.org/10.1016/j.porgcoat.2023.107634.
(117) Aguirreurreta, Z.; de la Cal, J. C.; Leiza, J. R. Preparation of High Solids Content Waterborne Acrylic Coatings Using Polymerizable Surfactants to Improve Water Sensitivity. *Prog. Org. Coat.* **2017**, *112*, 200–209. https://doi.org/10.1016/j.porgcoat.2017.06.028.
(118) Hamdani, S. S.; Emch, H.; Isherwood, J.; Khan, A.; Kumar, V.; Alford, A.; Wyman, I.; Sharma, R.; Mayekar, P.; Bher, A.; Auras, R.; Rabnawaz, M. Waterborne Poly(Butylene Succinate)-Coated Paper for Sustainable Packaging Applications. *ACS Appl. Polym. Mater.* **2023**, *5* (10), 7705–7717. https://doi.org/10.1021/acsapm.3c00846.
(119) Pieters, K.; Mekonnen, T. H. Stable Aqueous Dispersions of Poly(3-Hydroxybutyrate-Co-3-Hydroxyvalerate) (PHBV) Polymer for Barrier Paper Coating. *Prog. Org. Coat.* **2024**, *187*, 108101. https://doi.org/10.1016/j.porgcoat.2023.108101.
(120) *Polylactide Resin Emulsions - LANDY PL Series*. https://www.miyoshi-yushi.co.jp/en/business-information/pdf/06_landyPL_en202210.pdf (accessed 2023-07-25).
(121) Yamamoto, S.; Kasukabe, Y.; YAMASHITA, C.; Tanaka, T.; Nagatani, N. Polylactic Acid-Containing Aqueous Dispersion. US10987299B2, April 27, 2021. https://patents.google.com/patent/US10987299B2/en (accessed 2023-04-18).
(122) HIPPS, S. J.; Cai, H.; GAY, E. R.; COLLINS, T. M.; HOMOELLE, J. B. Aqueous-Based Hydrolytically Stable Dispersion of a Biodegradable Polymer. WO2017151595A1, September 8, 2017. https://patents.google.com/patent/WO2017151595A1/en (accessed 2023-04-18).
(123) Bandera, D.; Meyer, V. R.; Prevost, D.; Zimmermann, T.; Boesel, L. F. Polylactide/Montmorillonite Hybrid Latex as a Barrier Coating for Paper Applications. *Polymers* **2016**, *8* (3), 75. https://doi.org/10.3390/polym8030075.
(124) Buoso, S.; Belletti, G.; Ragno, D.; Castelvetro, V.; Bertoldo, M. Rheological Response of Polylactic Acid Dispersions in Water with Xanthan Gum. *ACS Omega* **2022**, *7* (15), 12536–12548. https://doi.org/10.1021/acsomega.1c05382.
(125) Abdenour, C.; Eesaee, M.; Stuppa, C.; Chabot, B.; Barnabé, S.; Bley, J.; Tolnai, B.; Guy, N.; Nguyen-Tri, P. Water Vapor and Air Barrier Performance of Sustainable Paper Coatings Based on PLA and Xanthan Gum. *Mater. Today Commun.* **2023**, *36*, 106626. https://doi.org/10.1016/j.mtcomm.2023.106626.
(126) Farah, S.; Anderson, D. G.; Langer, R. Physical and Mechanical Properties of PLA, and Their Functions in Widespread Applications — A Comprehensive Review. *Adv. Drug Deliv. Rev.* **2016**, *107*, 367–392. https://doi.org/10.1016/j.addr.2016.06.012.
(127) Cohn, D.; Younes, H. Biodegradable PEO/PLA Block Copolymers. *J. Biomed. Mater. Res.* **1988**, *22* (11), 993–1009. https://doi.org/10.1002/jbm.820221104.
(128) Miyamoto, S.; Takaoka, K.; Okada, T.; Yoshikawa, H.; Hashimoto, J.; Suzuki, S.; Ono, K. Polylactic Acid-Polyethylene Glycol Block Copolymer: A New Biodegradable Synthetic Carrier for Bone Morphogenetic Protein. *Clin. Orthop.* **1993**, *294*, 333–343. https://doi.org/10.1097/00003086-199309000-00050.
(129) Perinelli, D. R.; Cespi, M.; Bonacucina, G.; Palmieri, G. F. PEGylated Polylactide (PLA) and Poly (Lactic-Co-Glycolic Acid) (PLGA) Copolymers for the Design of Drug Delivery Systems. *J. Pharm. Investig.* **2019**, *49* (4), 443–458. https://doi.org/10.1007/s40005-019-00442-2.
(130) Chaos, A.; Sangroniz, A.; Fernández, J.; del Río, J.; Iriarte, M.; Sarasua, J. R.; Etxeberria, A. Plasticization of Poly(Lactide) with Poly(Ethylene Glycol): Low Weight Plasticizer vs Triblock Copolymers. Effect on Free Volume and Barrier Properties. *J. Appl. Polym. Sci.* **2020**, *137* (28), 48868. https://doi.org/10.1002/app.48868.
(131) Yodthong Baimark; Rungseesantivanon, W.; Prakymoramas, N. Improvement in Crystallization and Toughness of Poly(L-Lactide) by Melt Blending with Poly(L-Lactide)-b-Polyethylene Glycol-b-Poly(L-Lactide) in the Presence of Chain Extender.

Polym. Sci. Ser. A **2021**, *63* (1), S34–S45. https://doi.org/10.1134/S0965545X22030051.
(132) Rodriguez, E. J.; Marcos, B.; Huneault, M. A. Hydrolysis of Polylactide in Aqueous Media. *J. Appl. Polym. Sci.* **2016**, *133* (44). https://doi.org/10.1002/app.44152.
(133) Porfyris, A.; Vasilakos, S.; Zotiadis, C.; Papaspyrides, C.; Moser, K.; Van der Schueren, L.; Buyle, G.; Pavlidou, S.; Vouyiouka, S. Accelerated Ageing and Hydrolytic Stabilization of Poly(Lactic Acid) (PLA) under Humidity and Temperature Conditioning. *Polym. Test.* **2018**, *68*, 315–332. https://doi.org/10.1016/j.polymertesting.2018.04.018.
(134) Limsukon, W.; Auras, R.; Selke, S. Hydrolytic Degradation and Lifetime Prediction of Poly(Lactic Acid) Modified with a Multifunctional Epoxy-Based Chain Extender. *Polym. Test.* **2019**, *80*, 106108. https://doi.org/10.1016/j.polymertesting.2019.106108.
(135) Jeong, B.; Bae, Y. H.; Lee, D. S.; Kim, S. W. Biodegradable Block Copolymers as Injectable Drug-Delivery Systems. *Nature* **1997**, *388* (6645), 860–862. https://doi.org/10.1038/42218.
(136) Bollenbach, L.; Buske, J.; Mäder, K.; Garidel, P. Poloxamer 188 as Surfactant in Biological Formulations – An Alternative for Polysorbate 20/80? *Int. J. Pharm.* **2022**, *620*, 121706. https://doi.org/10.1016/j.ijpharm.2022.121706.
(137) Guo, X.; Rong, Z.; Ying, X. Calculation of Hydrophile–Lipophile Balance for Polyethoxylated Surfactants by Group Contribution Method. *J. Colloid Interface Sci.* **2006**, *298* (1), 441–450. https://doi.org/10.1016/j.jcis.2005.12.009.
(138) van Zyl, A. J. P.; Wet-Roos, D. de; Sanderson, R. D.; Klumperman, B. The Role of Surfactant in Controlling Particle Size and Stability in the Miniemulsion Polymerization of Polymeric Nanocapsules. *Eur. Polym. J.* **2004**, *40* (12), 2717–2725. https://doi.org/10.1016/j.eurpolymj.2004.07.021.
(139) Hecht, L. L.; Wagner, C.; Landfester, K.; Schuchmann, H. P. Surfactant Concentration Regime in Miniemulsion Polymerization for the Formation of MMA Nanodroplets by High-Pressure Homogenization. *Langmuir* **2011**, *27* (6), 2279–2285. https://doi.org/10.1021/la104480s.
(140) McPhee, W.; Tam, K. C.; Pelton, R. Poly(N-Isopropylacrylamide) Latices Prepared with Sodium Dodecyl Sulfate. *J. Colloid Interface Sci.* **1993**, *156* (1), 24–30. https://doi.org/10.1006/jcis.1993.1075.
(141) Rocca-Smith, J. R.; Whyte, O.; Brachais, C.-H.; Champion, D.; Piasente, F.; Marcuzzo, E.; Sensidoni, A.; Debeaufort, F.; Karbowiak, T. Beyond Biodegradability of Poly(Lactic Acid): Physical and Chemical Stability in Humid Environments. *ACS Sustain. Chem. Eng.* **2017**, *5* (3), 2751–2762. https://doi.org/10.1021/acssuschemeng.6b03088.
(142) Kumar, A.; Dixit, C. K. 3 - Methods for Characterization of Nanoparticles. In *Advances in Nanomedicine for the Delivery of Therapeutic Nucleic Acids*; Nimesh, S., Chandra, R., Gupta, N., Eds.; Woodhead Publishing, 2017; pp 43–58. https://doi.org/10.1016/B978-0-08-100557-6.00003-1.
(143) Toussaint, A.; De Wilde, M.; Molenaar, F.; Mulvihill, J. Calculation of Tg and MFFT Depression Due to Added Coalescing Agents. *Prog. Org. Coat.* **1997**, *30* (3), 179–184. https://doi.org/10.1016/S0300-9440(96)00685-6.
(144) Dron, S. M.; Bohorquez, S. J.; Mestach, D.; Paulis, M. Reducing the Amount of Coalescing Aid in High Performance Waterborne Polymeric Coatings. *Eur. Polym. J.* **2022**, *170*, 111175. https://doi.org/10.1016/j.eurpolymj.2022.111175.
(145) Nicholson, J. W. Waterborne Coatings. In *Surface Coatings—2*; Wilson, A. D., Nicholson, J. W., Prosser, H. J., Eds.; Springer Netherlands: Dordrecht, 1988; pp 1–38. https://doi.org/10.1007/978-94-009-1351-6_1.
(146) Protzman, T. F.; Brown, G. L. An Apparatus for the Determination of the Minimum Film Temperature of Polymer Emulsions. *J. Appl. Polym. Sci.* **1960**, *4* (10), 81–85. https://doi.org/10.1002/app.1960.070041012.
(147) Zhao, C. L.; Holl, Y.; Pith, T.; Lambla, M. FTIR-ATR Spectroscopic Determination of the Distribution of Surfactants in Latex Films. *Colloid Polym. Sci.* **1987**, *265* (9), 823–829. https://doi.org/10.1007/BF01418459.

(148) Scalarone, D.; Lazzari, M.; Castelvetro, V.; Chiantore, O. *Surface Monitoring of Surfactant Phase Separation and Stability in Waterborne Acrylic Coatings*. ACS Publications. https://doi.org/10.1021/cm0714077.
(149) Xu, G. H.; Dong, J.; Severtson, S. J.; Houtman, C. J.; Gwin, L. E. Modifications of Surfactant Distributions and Surface Morphologies in Latex Films Due to Moisture Exposure. *J. Phys. Chem. B* **2009**, *113* (30), 10189–10195. https://doi.org/10.1021/jp902716b.
(150) Petri, D. F. S. Xanthan Gum: A Versatile Biopolymer for Biomedical and Technological Applications. *J. Appl. Polym. Sci.* **2015**, *132* (23). https://doi.org/10.1002/app.42035.
(151) Borch, J. Thermodynamics of Polymer-Paper Adhesion: A Review. *J. Adhes. Sci. Technol.* **1991**, *5* (7), 523–541. https://doi.org/10.1163/156856191X00729.
(152) Kuusipalo, J.; Savolainen, A. Adhesion Phenomena in (Co)Extrusion Coating of Paper and Paperboard. *J. Adhes. Sci. Technol.* **1997**. https://doi.org/10.1163/156856197X00877.
(153) Zhao, B.; Pelton, R.; Bartzoka, V. Peeling Pressure Sensitive Tape from Paper. In *Advances in Paper Science and Technology, Transactions of the 13th Fundamental Research Symposium, Cambridge*; Fundamental Research Committee Manchester, 2005; pp 827–850.
(154) Alanen, E. Adhesion Characterization of Extrusion Coated Paperboards. Masters Thesis, Tampere University, 2023. https://trepo.tuni.fi/bitstream/handle/10024/146535/AlanenElli.pdf?sequence=2 (accessed 2024-05-07).
(155) Archaviboonyobul, T.; Jinkarn, T.; Sane, S.; Chariyachotilert, S.; Kongcharoenkiat, S. Water Resistance and Barrier Properties Improvement of Paperboard by Poly(Lactic Acid) Electrospraying. *Packag. Technol. Sci.* **2014**, *27* (5), 341–352. https://doi.org/10.1002/pts.2034.
(156) Sundar, N.; Stanley, S. J.; Kumar, S. A.; Keerthana, P.; Kumar, G. A. Development of Dual Purpose, Industrially Important PLA–PEG Based Coated Abrasives and Packaging Materials. *J. Appl. Polym. Sci.* **2021**, *138* (21), 50495. https://doi.org/10.1002/app.50495.
(157) Auras, R. A.; Harte, B.; Selke, S.; Hernandez, R. Mechanical, Physical, and Barrier Properties of Poly(Lactide) Films. *J. Plast. Film Sheeting* **2003**, *19* (2), 123–135. https://doi.org/10.1177/8756087903039702.
(158) González-López, M. E.; Calva-Estrada, S. de J.; Gradilla-Hernández, M. S.; Barajas-Álvarez, P. Current Trends in Biopolymers for Food Packaging: A Review. *Front. Sustain. Food Syst.* **2023**, *7*.
(159) Rong, X.; Keif, M. A Study of PLA Printability with Flexography. *59th Annu. Tech. Assoc. Graph. Arts Tech. Conf. Proc. Pittsburgh PA* **2007**.
(160) Aydemir, C.; Altay, B. N.; Akyol, M. Surface Analysis of Polymer Films for Wettability and Ink Adhesion. *Color Res. Appl.* **2021**, *46* (2), 489–499. https://doi.org/10.1002/col.22579.
(161) Jordá-Vilaplana, A.; Fombuena, V.; García-García, D.; Samper, M. D.; Sánchez-Nácher, L. Surface Modification of Polylactic Acid (PLA) by Air Atmospheric Plasma Treatment. *Eur. Polym. J.* **2014**, *58*, 23–33. https://doi.org/10.1016/j.eurpolymj.2014.06.002.
(162) Zhang, H.; Bussini, D.; Hortal, M.; Elegir, G.; Mendes, J.; Jordá Beneyto, M. PLA Coated Paper Containing Active Inorganic Nanoparticles: Material Characterization and Fate of Nanoparticles in the Paper Recycling Process. *Waste Manag.* **2016**, *52*, 339–345. https://doi.org/10.1016/j.wasman.2016.03.045.
(163) Stevens, J. R.; Newton, R. W.; Tlusty, M.; Little, D. C. The Rise of Aquaculture By-Products: Increasing Food Production, Value, and Sustainability through Strategic Utilisation. *Mar. Policy* **2018**, *90*, 115–124. https://doi.org/10.1016/j.marpol.2017.12.027.
(164) Suplicy, F. M. A Review of the Multiple Benefits of Mussel Farming. *Rev. Aquac.* **2020**, *12* (1), 204–223. https://doi.org/10.1111/raq.12313.

(165) Fortibuoni, T.; Amadesi, B.; Vlachogianni, T. Composition and Abundance of Macrolitter along the Italian Coastline: The First Baseline Assessment within the European Marine Strategy Framework Directive. *Environ. Pollut.* **2021**, *268*, 115886. https://doi.org/10.1016/j.envpol.2020.115886.
(166) Mascorda Cabre, L.; Hosegood, P.; Attrill, M. J.; Bridger, D.; Sheehan, E. V. Offshore Longline Mussel Farms: A Review of Oceanographic and Ecological Interactions to Inform Future Research Needs, Policy and Management. *Rev. Aquac.* **2021**, *13* (4), 1864–1887. https://doi.org/10.1111/raq.12549.
(167) Stevens, C.; Plew, D.; Hartstein, N.; Fredriksson, D. The Physics of Open-Water Shellfish Aquaculture. *Aquac. Eng.* **2008**, *38* (3), 145–160. https://doi.org/10.1016/j.aquaeng.2008.01.006.
(168) Menzel, W. *Estuarine and Marine Bivalve Mollusk Culture*; CRC Press: Boca Raton, 2018. https://doi.org/10.1201/9781351071918.
(169) Baini, M.; Fossi, M. C.; Innocenti, F. D.; Chinaglia, S.; Tosin, M.; Pecchiari, M.; Panti, C. Degradation of Plastic Materials in the Marine Environment: A Mussel Farm as a Case Study for the Development of Alternative Mussel Nets. *J. Clean. Prod.* **2024**, *450*, 141825. https://doi.org/10.1016/j.jclepro.2024.141825.
(170) Petrocelli, A.; Portacci, G.; Gasperis, E. D.; Cecere, E. Preliminary Results of Plastic Substitution in Mussel Farming with Natural Vegetal Fibers. In *2021 International Workshop on Metrology for the Sea; Learning to Measure Sea Health Parameters (MetroSea)*; 2021; pp 366–370. https://doi.org/10.1109/MetroSea52177.2021.9611562.
(171) *Il Progetto - Life Muscles*. https://lifemuscles.eu/en/il-progetto/ (accessed 2025-11-24).
(172) van den Bogaart, L. A.; Schotanus, J.; Capelle, J. J.; Bouma, T. J. Comparing Traditional vs. Biodegradable Seed Mussel Collectors (SMCs) for Seed Settlement, Seed Density, and Seed Growth: Effect of Deployment Depth and Location. *Aquac. Eng.* **2023**, *102*, 102344. https://doi.org/10.1016/j.aquaeng.2023.102344.
(173) Pavia, F. C.; Brucato, V.; Mistretta, M. C.; Botta, L.; Mantia, F. P. L.; Pavia, F. C.; Brucato, V.; Mistretta, M. C.; Botta, L.; Mantia, F. P. L. A Biodegradable, Bio-Based Polymer for the Production of Tools for Aquaculture: Processing, Properties and Biodegradation in Sea Water. *Polymers* **2023**, *15* (4). https://doi.org/10.3390/polym15040927.
(174) Nakayama, A.; Yamano, N.; Kawasaki, N. Biodegradation in Seawater of Aliphatic Polyesters. *Polym. Degrad. Stab.* **2019**, *166*, 290–299. https://doi.org/10.1016/j.polymdegradstab.2019.06.006.
(175) Caravella, A.; Lettieri, R.; Vezza, R.; Gatto, E. Aerobic Biodegradation at a Seawater-Sediment Interface of a New Bioplastic 100% Based on Natural Polymers. *ACS Sustain. Resour. Manag.* **2024**, *1* (6), 1099–1111. https://doi.org/10.1021/acssusresmgt.4c00029.
(176) Briassoulis, D.; Pikasi, A.; Papardaki, N. G.; Mistriotis, A. Aerobic Biodegradation of Bio-Based Plastics in the Seawater/Sediment Interface (Sublittoral) Marine Environment of the Coastal Zone – Test Method under Controlled Laboratory Conditions. *Sci. Total Environ.* **2020**, *722*, 137748. https://doi.org/10.1016/j.scitotenv.2020.137748.
(177) Dieterle, M.; Ginter, J. Life Cycle (Gap) Analysis for Advanced Material Recycling of PLA Cups. *Procedia CIRP* **2022**, *105*, 13–18. https://doi.org/10.1016/j.procir.2022.02.003.
(178) Piemonte, V. Bioplastic Wastes: The Best Final Disposition for Energy Saving. *J. Polym. Environ.* **2011**, *19* (4), 988–994. https://doi.org/10.1007/s10924-011-0343-z.
(179) Badia, J. D.; Ribes-Greus, A. Mechanical Recycling of Polylactide, Upgrading Trends and Combination of Valorization Techniques. *Eur. Polym. J.* **2016**, *84*, 22–39. https://doi.org/10.1016/j.eurpolymj.2016.09.005.
(180) Finnerty, J.; Rowe, S.; Howard, T.; Connolly, S.; Doran, C.; Devine, D. M.; Gately, N. M.; Chyzna, V.; Portela, A.; Bezerra, G. S. N.; McDonald, P.; Colbert, D. M. Effect of Mechanical Recycling on the Mechanical Properties of PLA-Based Natural Fiber-

Reinforced Composites. *J. Compos. Sci.* **2023**, *7* (4), 141. https://doi.org/10.3390/jcs7040141.
(181) Ramos-Hernández, T.; Robledo-Ortíz, J. R.; González-López, M. E.; del Campo, A. S. M.; González-Núñez, R.; Rodrigue, D.; Pérez Fonseca, A. A. Mechanical Recycling of PLA: Effect of Weathering, Extrusion Cycles, and Chain Extender. *J. Appl. Polym. Sci.* **2023**, *140* (16), e53759. https://doi.org/10.1002/app.53759.
(182) Soroudi, A.; Jakubowicz, I. Recycling of Bioplastics, Their Blends and Biocomposites: A Review. *Eur. Polym. J.* **2013**, *49* (10), 2839–2858. https://doi.org/10.1016/j.eurpolymj.2013.07.025.
(183) Beltrán, F. R.; Lorenzo, V.; de la Orden, M. U.; Martínez-Urreaga, J. Effect of Different Mechanical Recycling Processes on the Hydrolytic Degradation of Poly(l-Lactic Acid). *Polym. Degrad. Stab.* **2016**, *133*, 339–348. https://doi.org/10.1016/j.polymdegradstab.2016.09.018.
(184) Beltrán, F. R.; Ortega, E.; Solvoll, A. M.; Lorenzo, V.; de la Orden, M. U.; Martínez Urreaga, J. Effects of Aging and Different Mechanical Recycling Processes on the Structure and Properties of Poly(Lactic Acid)-Clay Nanocomposites. *J. Polym. Environ.* **2018**, *26* (5), 2142–2152. https://doi.org/10.1007/s10924-017-1117-z.
(185) Righetti, M. C.; Gazzano, M.; Di Lorenzo, M. L.; Androsch, R. Enthalpy of Melting of A′- and α-Crystals of Poly(l-Lactic Acid). *Eur. Polym. J.* **2015**, *70*, 215–220. https://doi.org/10.1016/j.eurpolymj.2015.07.024.
(186) Fischer, E. W.; Sterzel, H. J.; Wegner, G. Investigation of the Structure of Solution Grown Crystals of Lactide Copolymers by Means of Chemical Reactions. *Kolloid-Z. Z. Für Polym.* **1973**, *251* (11), 980–990. https://doi.org/10.1007/BF01498927.
(187) Lanyi, F. J.; Wenzke, N.; Kaschta, J.; Schubert, D. W. On the Determination of the Enthalpy of Fusion of α-Crystalline Isotactic Polypropylene Using Differential Scanning Calorimetry, X-Ray Diffraction, and Fourier-Transform Infrared Spectroscopy: An Old Story Revisited. *Adv. Eng. Mater.* **2020**, *22* (9), 1900796. https://doi.org/10.1002/adem.201900796.
(188) Chiellini, E.; Corti, A. A Simple Method Suitable to Test the Ultimate Biodegradability of Environmentally Degradable Polymers. *Macromol. Symp.* **2003**, *197* (1), 381–396. https://doi.org/10.1002/masy.200350733.
(189) Lee, D.; Lee, Y.; Kim, I.; Hwang, K.; Kim, N. Thermal and Mechanical Degradation of Recycled Polylactic Acid Filaments for Three-Dimensional Printing Applications. *Polymers* **2022**, *14* (24), 5385. https://doi.org/10.3390/polym14245385.
(190) Shojaeiarani, J.; Bajwa, D. S.; Rehovsky, C.; Bajwa, S. G.; Vahidi, G. Deterioration in the Physico-Mechanical and Thermal Properties of Biopolymers Due to Reprocessing. *Polymers* **2019**, *11* (1), 58. https://doi.org/10.3390/polym11010058.
(191) Takkalkar, P.; Tobin, M. J.; Vongsvivut, J.; Mukherjee, T.; Nizamuddin, S.; Griffin, G.; Kao, N. Structural, Thermal, Rheological and Optical Properties of Poly(Lactic Acid) Films Prepared through Solvent Casting and Melt Processing Techniques. *J. Taiwan Inst. Chem. Eng.* **2019**, *104*, 293–300. https://doi.org/10.1016/j.jtice.2019.08.018.
(192) Turner, A. Foamed Polystyrene in the Marine Environment: Sources, Additives, Transport, Behavior, and Impacts. *Environ. Sci. Technol.* **2020**, *54* (17), 10411–10420. https://doi.org/10.1021/acs.est.0c03221.
(193) Corbau, C.; Buoninsegni, J.; Olivo, E.; Vaccaro, C.; Nardin, W.; Simeoni, U. Understanding through Drone Image Analysis the Interactions between Geomorphology, Vegetation and Marine Debris along a Sandy Spit. *Mar. Pollut. Bull.* **2023**, *187*, 114515. https://doi.org/10.1016/j.marpolbul.2022.114515.
(194) Taib, N.-A. A. B.; Rahman, M. R.; Huda, D.; Kuok, K. K.; Hamdan, S.; Bakri, M. K. B.; Julaihi, M. R. M. B.; Khan, A. A Review on Poly Lactic Acid (PLA) as a Biodegradable Polymer. *Polym. Bull.* **2023**, *80* (2), 1179–1213. https://doi.org/10.1007/s00289-022-04160-y.
(195) Wang, G.-X.; Huang, D.; Ji, J.-H.; Völker, C.; Wurm, F. R. Seawater-Degradable Polymers—Fighting the Marine Plastic Pollution. *Adv. Sci.* **2021**, *8* (1), 2001121. https://doi.org/10.1002/advs.202001121.

(196) Lors, C.; Leleux, P.; Park, C. H. State of the Art on Biodegradability of Bio-Based Plastics Containing Polylactic Acid. *Front. Mater.* **2025**, *11*. https://doi.org/10.3389/fmats.2024.1476484.
(197) Viel, T.; Liotta, I.; Avolio, R.; Errico, M. E.; Manfra, L.; Libralato, G.; Zupo, V.; Costantini, M.; Cocca, M. The Fate of Biodegradable Polyesters in the Marine Environment. *Polym. Degrad. Stab.* **2025**, *241*, 111539. https://doi.org/10.1016/j.polymdegradstab.2025.111539.
(198) Mayekar, P. C.; Limsukon, W.; Bher, A.; Auras, R. Breaking It Down: How Thermoplastic Starch Enhances Poly(Lactic Acid) Biodegradation in Compost─A Comparative Analysis of Reactive Blends. *ACS Sustain. Chem. Eng.* **2023**, *11* (26), 9729–9737. https://doi.org/10.1021/acssuschemeng.3c01676.
(199) Van de Perre, D.; Serbruyns, L.; Coltelli, M.-B.; Gigante, V.; Aliotta, L.; Lazzeri, A.; Geerinck, R.; Verstichel, S. Tuning Biodegradation of Poly (Lactic Acid) (PLA) at Mild Temperature by Blending with Poly (Butylene Succinate-Co-Adipate) (PBSA) or Polycaprolactone (PCL). *Materials* **2024**, *17* (22), 5436. https://doi.org/10.3390/ma17225436.
(200) Fogašová, M.; Figalla, S.; Danišová, L.; Medlenová, E.; Hlaváčiková, S.; Vanovčanová, Z.; Omaníková, L.; Baco, A.; Horváth, V.; Mikolajová, M.; Feranc, J.; Bočkaj, J.; Plavec, R.; Alexy, P.; Repiská, M.; Přikryl, R.; Kontárová, S.; Báreková, A.; Sláviková, M.; Koutný, M.; Fayyazbakhsh, A.; Kadlečková, M. PLA/PHB-Based Materials Fully Biodegradable under Both Industrial and Home-Composting Conditions. *Polymers* **2022**, *14* (19), 4113. https://doi.org/10.3390/polym14194113.
(201) Han, G.; Yoon, J.; Hwang, J.; Lee, C.; Lee, E.; Yoon, K.; Kwak, H. W.; Jin, H.-J. Promoted Biodegradation Behavior of Poly(L-Lactic Acid) in Seawater Conditions through Blending Amorphous Polyhydroxyalkanoate. *Macromol. Res.* **2024**, *32* (5), 393–399. https://doi.org/10.1007/s13233-023-00239-1.
(202) Aversa, C.; Barletta, M.; Koca, N. Processing PLA/P(3HB)(4HB) Blends for the Manufacture of Highly Transparent, Gas Barrier and Fully Bio-Based Films for Compostable Packaging Applications. *J. Appl. Polym. Sci.* **2023**, *140* (13), e53669. https://doi.org/10.1002/app.53669.
(203) Koca, N.; Aversa, C.; Barletta, M. Blown Film Extrusion of Poly(Lactic)Acid/Poly(3-Hydroxybutyrate-4-Hydroxybutyrate) Blends for Improved Toughness and Processability. *Polym. Eng. Sci.* **2023**, *63* (10), 3300–3312. https://doi.org/10.1002/pen.26445.
(204) Richards, E.; Rizvi, R.; Chow, A.; Naguib, H. Biodegradable Composite Foams of PLA and PHBV Using Subcritical CO2. *J. Polym. Environ.* **2008**, *16* (4), 258–266. https://doi.org/10.1007/s10924-008-0110-y.
(205) Brütting, C.; Dreier, J.; Bonten, C.; Altstädt, V.; Ruckdäschel, H. Sustainable Immiscible Polylactic Acid (PLA) and Poly(3-Hydroxybutyrate-Co-3-Hydroxyvalerate) (PHBV) Blends: Crystallization and Foaming Behavior. *ACS Sustain. Chem. Eng.* **2023**, *11* (17), 6676–6687. https://doi.org/10.1021/acssuschemeng.3c00199.
(206) Brütting, C.; Dreier, J.; Bonten, C.; Ruckdäschel, H. Biobased Immiscible Polylactic Acid (PLA): Poly(3-Hydroxybutyrate-Co-3-Hydroxyvalerate) (PHBV) Blends: Impact of Rheological and Non-Isothermal Crystallization on the Bead Foaming Behavior. *J. Polym. Environ.* **2024**. https://doi.org/10.1007/s10924-024-03186-9.
(207) Yang, H.; Xu, G.; Li, J.; Wang, L.; Yu, K.; Yan, J.; Zhang, S.; Zhou, H. Fabrication of Bio-Based Biodegradable Poly(Lactic Acid) (PLA) and Poly(3-Hydroxybutyrate-*Co*-3-Hydroxyvalerate) (PHBV) Composite Foams for Highly Efficient Oil-Water Separation. *Int. J. Biol. Macromol.* **2024**, *257*, 128750. https://doi.org/10.1016/j.ijbiomac.2023.128750.
(208) Li, M.; Chen, X.; Feng, Q.; Fan, W.; Ding, Y.; Kan, Z.; Li, Z. Tailoring the Mechanical Properties and Foaming Behaviors of PLA/P4HB Blends by Using P4HB-g-GMA as Compatibilizer. *J. Polym. Sci.* **2025**, *63* (1), 204–212. https://doi.org/10.1002/pol.20240750.
(209) Wang, Y.; Chai, Y.; Wang, L.; Zhang, G.; Yu, K.; Sun, X.; Ji, E. Lightweight and High Performance Nano-Cellular Poly(Lactic Acid)/Poly(3-Hydroxybutyrate-Co-4-

Hydroxybutyrate) Foams Characterized by High Volume Expansion Ratio. *Polym. Test.* **2025**, *150*, 108920. https://doi.org/10.1016/j.polymertesting.2025.108920.
(210) Pantani, R.; Sorrentino, A. Influence of Crystallinity on the Biodegradation Rate of Injection-Moulded Poly(Lactic Acid) Samples in Controlled Composting Conditions. *Polym. Degrad. Stab.* **2013**, *98* (5), 1089–1096. https://doi.org/10.1016/j.polymdegradstab.2013.01.005.
(211) Sedničková, M.; Pekařová, S.; Kucharczyk, P.; Bočkaj, J.; Janigová, I.; Kleinová, A.; Jochec-Mošková, D.; Omaníková, L.; Perďochová, D.; Koutný, M.; Sedlařík, V.; Alexy, P.; Chodák, I. Changes of Physical Properties of PLA-Based Blends during Early Stage of Biodegradation in Compost. *Int. J. Biol. Macromol.* **2018**, *113*, 434–442. https://doi.org/10.1016/j.ijbiomac.2018.02.078.
(212) Saeidlou, S.; Huneault, M. A.; Li, H.; Park, C. B. Poly(Lactic Acid) Crystallization. *Prog. Polym. Sci.* **2012**, *37* (12), 1657–1677. https://doi.org/10.1016/j.progpolymsci.2012.07.005.
(213) Reignier, J.; Gendron, R.; Champagne, M. F. Extrusion Foaming of Poly(Lactic Acid) Blown with CO_2 : Toward 100% Green Material. *Cell. Polym.* **2007**, *26* (2), 83–115. https://doi.org/10.1177/026248930702600202.
(214) Mihai, M.; Huneault, M. A.; Favis, B. D. Crystallinity Development in Cellular Poly(Lactic Acid) in the Presence of Supercritical Carbon Dioxide. *J. Appl. Polym. Sci.* **2009**, *113* (5), 2920–2932. https://doi.org/10.1002/app.30338.
(215) Standau, T.; Long, H.; Murillo Castellón, S.; Brütting, C.; Bonten, C.; Altstädt, V. Evaluation of the Zero Shear Viscosity, the D-Content and Processing Conditions as Foam Relevant Parameters for Autoclave Foaming of Standard Polylactide (PLA). *Materials* **2020**, *13* (6), 1371. https://doi.org/10.3390/ma13061371.
(216) Dippold, M.; Ruckdäschel, H. Influence of Pressure-Induced Temperature Drop on the Foaming Behavior of Amorphous Polylactide (PLA) during Autoclave Foaming with Supercritical CO2. *J. Supercrit. Fluids* **2022**, *190*, 105734. https://doi.org/10.1016/j.supflu.2022.105734.
(217) Chiellini, E.; Corti, A.; Del Sarto, G.; D'Antone, S. Oxo-Biodegradable Polymers – Effect of Hydrolysis Degree on Biodegradation Behaviour of Poly(Vinyl Alcohol). *Polym. Degrad. Stab.* **2006**, *91* (12), 3397–3406. https://doi.org/10.1016/j.polymdegradstab.2006.05.021.
(218) Takagi, Y.; Yasuda, R.; Yamaoka, M.; Yamane, T. Morphologies and Mechanical Properties of Polylactide Blends with Medium Chain Length Poly(3-Hydroxyalkanoate) and Chemically Modified Poly(3-Hydroxyalkanoate). *J. Appl. Polym. Sci.* **2004**, *93* (5), 2363–2369. https://doi.org/10.1002/app.20734.
(219) Jiang, N.; Abe, H. Miscibility and Morphology Study on Crystalline/Crystalline Partially Miscible Polymer Blends of 6-Arm Poly(l-Lactide) and Poly(3-Hydroxybutyrate-*Co*-3-Hydroxyvalerate). *Polymer* **2015**, *60*, 260–266. https://doi.org/10.1016/j.polymer.2015.01.060.
(220) Qiu, J.; Xing, C.; Cao, X.; Wang, H.; Wang, L.; Zhao, L.; Li, Y. Miscibility and Double Glass Transition Temperature Depression of Poly(l-Lactic Acid) (PLLA)/Poly(Oxymethylene) (POM) Blends. *Macromolecules* **2013**, *46* (14), 5806–5814. https://doi.org/10.1021/ma401084y.
(221) Qu, Y.; Chen, Y.; Ling, X.; Wu, J.; Hong, J.; Wang, H.; Li, Y. Reactive Micro-Crosslinked Elastomer for Supertoughened Polylactide. *Macromolecules* **2022**, *55* (17), 7711–7723. https://doi.org/10.1021/acs.macromol.2c00824.
(222) Utracki, L. A. Rheology of Polymer Blends. In *Encyclopedia of Polymer Blends*; Isayev, A. I., Ed.; Wiley, 2011; pp 27–108. https://doi.org/10.1002/9783527805242.ch2.
(223) Gao, D.; Wang, J.; Wang, Y.; Zhang, P. Effect of Melt Viscosity on the Cell Morphology and Properties of Poly(Lactic Acid) Foams. *J. Cell. Plast.* **2016**, *52* (2), 175–187. https://doi.org/10.1177/0021955X14566210.
(224) Brütting, C.; Dreier, J.; Bonten, C.; Altstädt, V.; Ruckdäschel, H. Amorphous Polylactide Bead Foam–Effect of Talc and Chain Extension on Foaming Behavior and Compression Properties. *J. Renew. Mater.* **2021**, *9* (11), 1859–1868. https://doi.org/10.32604/jrm.2021.016244.

(225) Skleničková, K.; Abbrent, S.; Halecký, M.; Kočí, V.; Beneš, H. Biodegradability and Ecotoxicity of Polyurethane Foams: A Review. *Crit. Rev. Environ. Sci. Technol.* **2022**, *52* (2), 157–202. https://doi.org/10.1080/10643389.2020.1818496.
(226) Tábi, T.; Ageyeva, T.; Kovács, J. G. Improving the Ductility and Heat Deflection Temperature of Injection Molded Poly(Lactic Acid) Products: A Comprehensive Review. *Polym. Test.* **2021**, *101*, 107282. https://doi.org/10.1016/j.polymertesting.2021.107282.
(227) Ghasemlou, M.; Barrow, C. J.; Adhikari, B. The Future of Bioplastics in Food Packaging: An Industrial Perspective. *Food Packag. Shelf Life* **2024**, *43*, 101279. https://doi.org/10.1016/j.fpsl.2024.101279.
(228) Jiang, X.-L.; Liu, T.; Xu, Z.-M.; Zhao, L.; Hu, G.-H.; Yuan, W.-K. Effects of Crystal Structure on the Foaming of Isotactic Polypropylene Using Supercritical Carbon Dioxide as a Foaming Agent. *J. Supercrit. Fluids* **2009**, *48* (2), 167–175. https://doi.org/10.1016/j.supflu.2008.10.006.
(229) Zhang, X.; Li, B.; Wang, X.; Li, K.; Wang, G.; Chen, J.; Park, C. B. Modification of iPP Microcellular Foaming Behavior by Thermal History Control and Nucleating Agent at Compressed CO2. *J. Supercrit. Fluids* **2018**, *133*, 383–392. https://doi.org/10.1016/j.supflu.2017.11.003.
(230) Nofar, M.; Tabatabaei, A.; Park, C. B. Effects of Nano-/Micro-Sized Additives on the Crystallization Behaviors of PLA and PLA/CO2 Mixtures. *Polymer* **2013**, *54* (9), 2382–2391. https://doi.org/10.1016/j.polymer.2013.02.049.
(231) Taki, K.; Kitano, D.; Ohshima, M. Effect of Growing Crystalline Phase on Bubble Nucleation in Poly(L-Lactide)/CO2 Batch Foaming. *Ind. Eng. Chem. Res.* **2011**, *50* (6), 3247–3252. https://doi.org/10.1021/ie101637f.
(232) Wang, J.; Zhu, W.; Zhang, H.; Park, C. B. Continuous Processing of Low-Density, Microcellular Poly(Lactic Acid) Foams with Controlled Cell Morphology and Crystallinity. *Chem. Eng. Sci.* **2012**, *75*, 390–399. https://doi.org/10.1016/j.ces.2012.02.051.
(233) Yang, Y.; Li, X.; Zhang, Q.; Xia, C.; Chen, C.; Chen, X.; Yu, P. Foaming of Poly(Lactic Acid) with Supercritical CO2: The Combined Effect of Crystallinity and Crystalline Morphology on Cellular Structure. *J. Supercrit. Fluids* **2019**, *145*, 122–132. https://doi.org/10.1016/j.supflu.2018.12.006.
(234) Yu, L.; Liu, H.; Dean, K. Thermal Behaviour of Poly(Lactic Acid) in Contact with Compressed Carbon Dioxide. *Polym. Int.* **2009**, *58* (4), 368–372. https://doi.org/10.1002/pi.2540.
(235) Li, H.; Lu, X.; Yang, H.; Hu, J. Non-Isothermal Crystallization of P(3HB-Co-4HB)/PLA Blends. *J. Therm. Anal. Calorim.* **2015**, *122* (2), 817–829. https://doi.org/10.1007/s10973-015-4824-5.
(236) Somsunan, R.; Mainoiy, N. Isothermal and Non-Isothermal Crystallization Kinetics of PLA/PBS Blends with Talc as Nucleating Agent. *J. Therm. Anal. Calorim.* **2020**, *139* (3), 1941–1948. https://doi.org/10.1007/s10973-019-08631-9.
(237) Quero, E.; Müller, A. J.; Signori, F.; Coltelli, M.-B.; Bronco, S. Isothermal Cold-Crystallization of PLA/PBAT Blends With and Without the Addition of Acetyl Tributyl Citrate. *Macromol. Chem. Phys.* **2012**, *213* (1), 36–48. https://doi.org/10.1002/macp.201100437.
(238) Tábi, T.; Hajba, S.; Kovács, J. G. Effect of Crystalline Forms (A′ and α) of Poly(Lactic Acid) on Its Mechanical, Thermo-Mechanical, Heat Deflection Temperature and Creep Properties. *Eur. Polym. J.* **2016**, *82*, 232–243. https://doi.org/10.1016/j.eurpolymj.2016.07.024.
(239) Xu, L.-Q.; Huang, H.-X. Foaming of Poly(Lactic Acid) Using Supercritical Carbon Dioxide as Foaming Agent: Influence of Crystallinity and Spherulite Size on Cell Structure and Expansion Ratio. *Ind. Eng. Chem. Res.* **2014**, *53* (6), 2277–2286. https://doi.org/10.1021/ie403594t.
(240) Yu, K.; Wang, D.; Hou, J.; Zhang, X.; Chen, J. Fabrication of Poly(Lactic Acid) Foam with High Expansion Ratio and Oriented Cellular Structure by Restricting Cold Crystallization. *Int. J. Biol. Macromol.* **2023**, *251*, 126463. https://doi.org/10.1016/j.ijbiomac.2023.126463.

(241) Li, B.; Zhao, G.; Wang, G.; Zhang, L.; Gong, J. Fabrication of High-Expansion Microcellular PLA Foams Based on Pre-Isothermal Cold Crystallization and Supercritical CO2 Foaming. *Polym. Degrad. Stab.* **2018**, *156*, 75–88. https://doi.org/10.1016/j.polymdegradstab.2018.08.009.
(242) Nofar, M.; Zhu, W.; Park, C. B. Effect of Dissolved CO2 on the Crystallization Behavior of Linear and Branched PLA. *Polymer* **2012**, *53* (15), 3341–3353. https://doi.org/10.1016/j.polymer.2012.04.054.
(243) Hankenson, K. D.; Gagne, K.; Shaughnessy, M. Extracellular Signaling Molecules to Promote Fracture Healing and Bone Regeneration. *Adv. Drug Deliv. Rev.* **2015**, *94*, 3–12. https://doi.org/10.1016/j.addr.2015.09.008.
(244) Kumar, A.; Singh, G. Surface Modification of Ti6Al4V Alloy via Advanced Coatings: Mechanical, Tribological, Corrosion, Wetting, and Biocompatibility Studies. *J. Alloys Compd.* **2024**, *989*, 174418. https://doi.org/10.1016/j.jallcom.2024.174418.
(245) Wei, G.; Tan, M.; Attarilar, S.; Li, J.; Uglov, V. V.; Wang, B.; Liu, J.; Lu, L.; Wang, L. An Overview of Surface Modification, A Way toward Fabrication of Nascent Biomedical Ti–6Al–4V Alloys. *J. Mater. Res. Technol.* **2023**, *24*, 5896–5921. https://doi.org/10.1016/j.jmrt.2023.04.046.
(246) Priyadarshini, B.; Rama, M.; Chetan; Vijayalakshmi, U. Bioactive Coating as a Surface Modification Technique for Biocompatible Metallic Implants: A Review. *J. Asian Ceram. Soc.* **2019**, *7* (4), 397–406. https://doi.org/10.1080/21870764.2019.1669861.
(247) Farah, S.; Anderson, D. G.; Langer, R. Physical and Mechanical Properties of PLA, and Their Functions in Widespread Applications — A Comprehensive Review. *Adv. Drug Deliv. Rev.* **2016**, *107*, 367–392. https://doi.org/10.1016/j.addr.2016.06.012.
(248) Smith, J. R.; Lamprou, D. A. Polymer Coatings for Biomedical Applications: A Review. *Trans. IMF* **2014**, *92* (1), 9–19. https://doi.org/10.1179/0020296713Z.000000000157.
(249) Aydin, M. S.; Nicolae, C.-V.; Campodoni, E.; Mohamed-Ahmed, S.; Kadousaraei, M. J.; Yassin, M. A.; Gjerde, C.; Sandri, M.; Stancu, I.-C.; Rashad, A.; Mustafa, K. Osteogenic Potential of 3D-Printed Porous Poly(Lactide-Co-Trimethylene Carbonate) Scaffolds Coated with Mg-Doped Hydroxyapatite. *ACS Appl. Mater. Interfaces* **2025**, *17* (21), 31411–31433. https://doi.org/10.1021/acsami.5c03945.
(250) Rojas, R.; Zanín, J. P.; Martínez, R.; Gil, G. A. Self-Standing Films of Medical Grade PLA/PEG Copolymers for Guided Bone Regeneration. *Mater.* **2025**, *8*, 100561. https://doi.org/10.1016/j.nxmate.2025.100561.
(251) Jabbari, E. Osteogenic Peptides in Bone Regeneration. *Curr. Pharm. Des.* **2013**, *19* (19), 3391–3402. https://doi.org/10.2174/1381612811319190006.
(252) Urist, M. R.; Mikulski, A. J. A Soluble Bone Morphogenetic Protein Extracted from Bone Matrix with a Mixed Aqueous and Nonaqueous Solvent. *Proc. Soc. Exp. Biol. Med. Soc. Exp. Biol. Med. N. Y. N* **1979**, *162* (1), 48–53. https://doi.org/10.3181/00379727-162-40616.
(253) Rosen, V. BMP2 Signaling in Bone Development and Repair. *Cytokine Growth Factor Rev.* **2009**, *20* (5–6), 475–480. https://doi.org/10.1016/j.cytogfr.2009.10.018.
(254) Wozney, J. M. The Bone Morphogenetic Protein Family and Osteogenesis. *Mol. Reprod. Dev.* **1992**, *32* (2), 160–167. https://doi.org/10.1002/mrd.1080320212.
(255) Szwed-Georgiou, A.; Płociński, P.; Kupikowska-Stobba, B.; Urbaniak, M. M.; Rusek-Wala, P.; Szustakiewicz, K.; Piszko, P.; Krupa, A.; Biernat, M.; Gazińska, M.; Kasprzak, M.; Nawrotek, K.; Mira, N. P.; Rudnicka, K. Bioactive Materials for Bone Regeneration: Biomolecules and Delivery Systems. *ACS Biomater. Sci. Eng.* **2023**, *9* (9), 5222–5254. https://doi.org/10.1021/acsbiomaterials.3c00609.
(256) Ungureanu, M.-C.; Bilha, S. C.; Hogas, M.; Velicescu, C.; Leustean, L.; Teodoriu, L. C.; Preda, C. Preptin: A New Bone Metabolic Parameter? *Metabolites* **2023**, *13* (9), 991. https://doi.org/10.3390/metabo13090991.
(257) Lubos, M.; Mrázková, L.; Gwozdiaková, P.; Pícha, J.; Buděšínský, M.; Jiráček, J.; Kaminský, J.; Žáková, L. Functional Stapled Fragments of Human Preptin of Minimised Length. *Org. Biomol. Chem.* **2022**, *20* (12), 2446–2454. https://doi.org/10.1039/D1OB02193A.

(258) Polan, J. L.; Morse, B.; Wetherold, S.; Villanueva-Vedia, R. E.; Phelix, C.; Barera-Roderiquiz, E.; Waggoner, D.; Goswami, N.; Munoz, O.; Agrawal, C. M.; Bailey, S. R. VEGF Analysis Induced by Endothelialized Gas-Plasma Treated d,l-PLA Scaffolds. *Cardiovasc. Radiat. Med.* **2002**, *3* (3), 176–182. https://doi.org/10.1016/S1522-1865(03)00100-8.
(259) De la Riva, B.; Nowak, C.; Sánchez, E.; Hernández, A.; Schulz-Siegmund, M.; Pec, M. K.; Delgado, A.; Évora, C. VEGF-Controlled Release within a Bone Defect from Alginate/Chitosan/PLA-H Scaffolds. *Eur. J. Pharm. Biopharm.* **2009**, *73* (1), 50–58. https://doi.org/10.1016/j.ejpb.2009.04.014.
(260) Cha, M.; Jin, Y.-Z.; Park, J. W.; Lee, K. M.; Han, S. H.; Choi, B. S.; Lee, J. H. Three-Dimensional Printed Polylactic Acid Scaffold Integrated with BMP-2 Laden Hydrogel for Precise Bone Regeneration. *Biomater. Res.* **2021**, *25* (1), 35. https://doi.org/10.1186/s40824-021-00233-7.
(261) Wang, M.; Dai, T.; Wang, W.; OuYang, J. BMP-2 Loaded Bioactive PLLA/PCL Blended Nanofibers for Synergistic Influences on Osteogenic Differentiation of Rat Bone Marrow-Derived Mesenchymal Stem Cells via TGF-β/Smad2/3 Signaling Pathway. *J. Drug Deliv. Sci. Technol.* **2025**, *105*, 106639. https://doi.org/10.1016/j.jddst.2025.106639.
(262) Eğri, S.; Eczacıoğlu, N. Sequential VEGF and BMP-2 Releasing PLA-PEG-PLA Scaffolds for Bone Tissue Engineering: I. Design and in Vitro Tests. *Artif. Cells Nanomedicine Biotechnol.* **2017**, *45* (2), 321–329. https://doi.org/10.3109/21691401.2016.1147454.
(263) Sun, H.; Dong, J.; Wang, Y.; Shen, S.; Shi, Y.; Zhang, L.; Zhao, J.; Sun, X.; Jiang, Q. Polydopamine-Coated Poly(l-Lactide) Nanofibers with Controlled Release of VEGF and BMP-2 as a Regenerative Periosteum. *ACS Biomater. Sci. Eng.* **2021**, *7* (10), 4883–4897. https://doi.org/10.1021/acsbiomaterials.1c00246.
(264) Liu, K.; Tan, Q.; Yu, J.; Wang, M. A Global Perspective on E-Waste Recycling. *Circ. Econ.* **2023**, *2* (1), 100028. https://doi.org/10.1016/j.cec.2023.100028.
(265) Parvez, S. M.; Jahan, F.; Brune, M.-N.; Gorman, J. F.; Rahman, M. J.; Carpenter, D.; Islam, Z.; Rahman, M.; Aich, N.; Knibbs, L. D.; Sly, P. D. Health Consequences of Exposure to E-Waste: An Updated Systematic Review. *Lancet Planet. Health* **2021**, *5* (12), e905–e920. https://doi.org/10.1016/S2542-5196(21)00263-1.
(266) Zhang, D.; Hou, J.; Long, H.; Wang, M.; Wen, Z.; Yang, W.; Pan, H.; Xia, L.; Xu, W. High-Performance Degradable PLA-Based Sensors with Enhanced Strain Sensing and Triboelectric Power Generation for Wearable Devices. *ACS Sens.* **2025**. https://doi.org/10.1021/acssensors.5c02723.
(267) Qian, F.; Jia, R.; Cheng, M.; Chaudhary, A.; Melhi, S.; Mekkey, S. D.; Zhu, N.; Wang, C.; Razak, F.; Xu, X.; Yan, C.; Bao, X.; Jiang, Q.; Wang, J.; Hu, M. An Overview of Polylactic Acid (PLA) Nanocomposites for Sensors. *Adv. Compos. Hybrid Mater.* **2024**, *7* (3), 75. https://doi.org/10.1007/s42114-024-00887-6.
(268) Griffiths, K.; Dale, C.; Hedley, J.; D. Kowal, M.; B. Kaner, R.; Keegan, N. Laser-Scribed Graphene Presents an Opportunity to Print a New Generation of Disposable Electrochemical Sensors. *Nanoscale* **2014**, *6* (22), 13613–13622. https://doi.org/10.1039/C4NR04221B.
(269) Ye, R.; James, D. K.; Tour, J. M. Laser-Induced Graphene: From Discovery to Translation. *Adv. Mater.* **2019**, *31* (1), 1803621. https://doi.org/10.1002/adma.201803621.
(270) Lau, K. Y.; Qiu, J. Broad Applications of Sensors Based on Laser-Scribed Graphene. *Light Sci. Appl.* **2023**, *12* (1), 168. https://doi.org/10.1038/s41377-023-01210-6.
(271) Parkula, V.; Licata, A.; Valorosi, F.; Kovtun, A.; Scidà, A.; Ruani, G.; Liscio, F.; Zanardi, C.; Candini, A.; Bertocchi, F.; Cristiano, F.; Brunella, V.; Cesano, F.; Sarotto, E.; Martorana, B.; Treossi, E.; Palermo, V. Laser-Patterned Polyurethane Composites with Graphene, Graphene Oxide, and Aramid Fibers for the Production of Electric Circuits, Sensors, and Heaters. *ACS Appl. Nano Mater.* **2024**, *7* (15), 18077–18088. https://doi.org/10.1021/acsanm.4c04059.

(272) Silva, M.; Alves, N. M.; Paiva, M. C. Graphene-Polymer Nanocomposites for Biomedical Applications. *Polym. Adv. Technol.* **2018**, *29* (2), 687–700. https://doi.org/10.1002/pat.4164.
(273) Adekoya, G. J.; Ezika, A. C.; Adekoya, O. C.; Sadiku, E. R.; Hamam, Y.; Ray, S. S. Recent Advancements in Biomedical Application of Polylactic Acid/Graphene Nanocomposites: An Overview. *BMEMat* **2023**, *1* (4), e12042. https://doi.org/10.1002/bmm2.12042.
(274) Ajaj, Y.; AL-Salman, H. N. K.; Hussein, A. M.; Khaleel Jamee, M.; Abdullaev, S.; Omran, A. A.; Morad Karim, M.; Abdulwahid, A. S.; Mahmoud, Z. H.; kianfar, E. Effect and Investigating of Graphene Nanoparticles on Mechanical, Physical Properties of Polylactic Acid Polymer. *Case Stud. Chem. Environ. Eng.* **2024**, *9*, 100612. https://doi.org/10.1016/j.cscee.2024.100612.
(275) Calosi, M.; D'Ilorio, A.; Buratti, E.; Cortesi, R.; Franco, S.; Angelini, R.; Bertoldo, M. Preparation of High-Solid PLA Waterborne Dispersions with PEG-PLA-PEG Block Copolymer as Surfactant and Their Use as Hydrophobic Coating on Paper. *Prog. Org. Coat.* **2024**, *193*, 108541. https://doi.org/10.1016/j.porgcoat.2024.108541.
(276) Zhang, C.; Wang, L.; Zhai, T.; Wang, X.; Dan, Y.; Turng, L.-S. The Surface Grafting of Graphene Oxide with Poly(Ethylene Glycol) as a Reinforcement for Poly(Lactic Acid) Nanocomposite Scaffolds for Potential Tissue Engineering Applications. *J. Mech. Behav. Biomed. Mater.* **2016**, *53*, 403–413. https://doi.org/10.1016/j.jmbbm.2015.08.043.
(277) Dandan Doganci, M.; Doganci, E.; Balci, H.; Cetin, M. Antibacterial and Cytotoxic Performance of Methenamine-Based Poly(Lactic Acid)/Poly(Ethylene Glycol) (PLA/PEG) Composite Films. *J. Appl. Polym. Sci.* **2024**, *141* (21), e55412. https://doi.org/10.1002/app.55412.
(278) Farivar, F.; Yap, P. L.; Hassan, K.; Tung, T. T.; Tran, D. N. H.; Pollard, A. J.; Losic, D. Unlocking Thermogravimetric Analysis (TGA) in the Fight against "Fake Graphene" Materials. *Carbon* **2021**, *179*, 505–513. https://doi.org/10.1016/j.carbon.2021.04.064.
(279) Gong, M.; Zhao, Q.; Dai, L.; Li, Y.; Jiang, T. Fabrication of Polylactic Acid/Hydroxyapatite/Graphene Oxide Composite and Their Thermal Stability, Hydrophobic and Mechanical Properties. *J. Asian Ceram. Soc.* **2017**, *5* (2), 160–168. https://doi.org/10.1016/j.jascer.2017.04.001.
(280) Zheng, L.; Zhen, W. Preparation and Characterization of Amidated Graphene Oxide and Its Effect on the Performance of Poly(Lactic Acid). *Iran. Polym. J.* **2018**, *27* (4), 239–252. https://doi.org/10.1007/s13726-018-0604-y.
(281) Yu, Y.; Ma, C.; Zhang, H.; Zhang, Y.; Fang, Z.; Song, R.; Lin, Z.; Feng, J.; Song, P. Combination Effects of a Bio-Based Fire Retardant and Functionalized Graphene Oxide on a Fire Retardant and Mechanical Properties of Polylactide. *Mater. Today Chem.* **2023**, *30*, 101565. https://doi.org/10.1016/j.mtchem.2023.101565.
(282) Tayouri, M. I.; Estaji, S.; Mousavi, S. R.; Salkhi Khasraghi, S.; Jahanmardi, R.; Nouranian, S.; Arjmand, M.; Khonakdar, H. A. Degradation of Polymer Nanocomposites Filled with Graphene Oxide and Reduced Graphene Oxide Nanoparticles: A Review of Current Status. *Polym. Degrad. Stab.* **2022**, *206*, 110179. https://doi.org/10.1016/j.polymdegradstab.2022.110179.
(283) Vranic, S.; Kurapati, R.; Kostarelos, K.; Bianco, A. Biological and Environmental Degradation of Two-Dimensional Materials. *Nat. Rev. Chem.* **2025**, *9* (3), 173–184. https://doi.org/10.1038/s41570-024-00680-5.
(284) Lin, J.; Peng, Z.; Liu, Y.; Ruiz-Zepeda, F.; Ye, R.; Samuel, E. L. G.; Yacaman, M. J.; Yakobson, B. I.; Tour, J. M. Laser-Induced Porous Graphene Films from Commercial Polymers. *Nat. Commun.* **2014**, *5* (1), 5714. https://doi.org/10.1038/ncomms6714.
(285) El-Kady, M. F.; Strong, V.; Dubin, S.; Kaner, R. B. Laser Scribing of High-Performance and Flexible Graphene-Based Electrochemical Capacitors. *Science* **2012**, *335* (6074), 1326–1330. https://doi.org/10.1126/science.1216744.
(286) Ferrari, A. C.; Meyer, J. C.; Scardaci, V.; Casiraghi, C.; Lazzeri, M.; Mauri, F.; Piscanec, S.; Jiang, D.; Novoselov, K. S.; Roth, S.; Geim, A. K. Raman Spectrum of Graphene and Graphene Layers. *Phys. Rev. Lett.* **2006**, *97* (18), 187401. https://doi.org/10.1103/PhysRevLett.97.187401.

(287) Funayama, R.; Hayashi, S.; Terakawa, M. Laser-Induced Graphitization of Lignin/PLLA Composite Sheets for Biodegradable Triboelectric Nanogenerators. *ACS Sustain. Chem. Eng.* **2023**, *11* (7), 3114–3122. https://doi.org/10.1021/acssuschemeng.2c07510.
(288) Aguiar-Hualde, J.-M.; Magnin, Y.; Amara, H.; Bichara, C. Probing the Role of Carbon Solubility in Transition Metal Catalyzing Single-Walled Carbon Nanotubes Growth. *Carbon* **2017**, *120*, 226–232. https://doi.org/10.1016/j.carbon.2017.05.035.